

Investigation of the Hydromechanical Effects of Lithostatic Unloading in Open-pit Mines

Author: Christopher Philip Soeller

Persistent link: <http://hdl.handle.net/2345/bc-ir:107281>

This work is posted on [eScholarship@BC](#),
Boston College University Libraries.

Boston College Electronic Thesis or Dissertation, 2016

Copyright is held by the author, with all rights reserved, unless otherwise noted.

Boston College

Morrissey School of Arts & Sciences

Graduate School

Department of Earth and Environmental Sciences

INVESTIGATION OF THE HYDROMECHANICAL EFFECTS OF
LITHOSTATIC UNLOADING IN OPEN-PIT MINES

a thesis

by

CHRISTOPHER PHILIP SOELLER

Submitted in partial fulfillment of the requirements

for the degree of

Master of Science

November 2016

Investigation of the Hydromechanical Effects of Lithostatic Unloading in Open-Pit Mines

By: Christopher P. Soeller

Advisor: Alfredo Urzua, Ph.D.

Abstract

The stability of open-pit mine walls and other geotechnical infrastructure is a function of geometry, material properties and groundwater conditions (pore pressure distribution). A portion of failures are attributed to the effect of pore water pressures within the mine wall slopes. The objective of this research was to investigate the interaction between the increments/decrements of stresses that occur during the lithostatic unloading/excavation of the pit and the increments/decrements of pore water pressures. This interaction can be described by the theory of linear poroelasticity, which incorporates the coupling between changes in fluid pressure and changes in stress in porous media. The results of this thesis are displayed in the form of contour charts and graphs.

Table of Contents

Table of Contents	iv
Acknowledgements	v
List of Tables	vi
List of Figures	vii
Chapter 1: Introduction	1
1.1 Objectives	5
Chapter 2: Background	6
2.1 Undrained Response	13
2.2 Transient (Drained) Response.....	17
2.3 Steady-State (Drained) Response	21
Chapter 3: Methodology	22
3.1 One-Dimensional Finite Element Analyses.....	23
3.2 Two-Dimensional Finite Element Analyses	25
3.3 Range of Parameter Values.....	29
3.4 Undrained, Seepage, Coupled, and Steady-State Analyses	30
3.5 Specific Procedures for Solving for the Undrained Response.....	31
Chapter 4: Results	31
4.1 Distribution of Octahedral Stresses	32
4.2 Results from the 1-D Confined Flow Analyses	34
4.3 Results from the 2-D Confined Flow Rectangular-Strip Excavation Analyses.....	40
4.4 Results from the 2-D Unconfined Trapezoid-Shaped Excavation Analyses	54
Chapter 5: Discussion	73
Chapter 6: Conclusions and Future Research	77
References Cited	81
Appendix A: Additional 1-D Confined Flow Results	83
Appendix B: Additional 2-D Confined Flow Results	106
Appendix C: Additional 2-D Unconfined Flow Results	151

Acknowledgements

I would like to thank Alfredo Urzua for helping with every phase of this thesis, from first suggesting the general idea to suggesting revisions for the final draft. I would also like to thank John Christian, Vincent Murphy, and Marco Bocardin for their comments and suggestions for improving this thesis. Finally, I also thank Professor Alan Kafka for reviewing this thesis.

I would like to thank Aakash Ahmed, James Haklar, Austin Hopkins, Ellen Kristiansen, and Vanessa Napoli for being a great support team during graduate school. I would also like to thank all of the other graduate students and professors in the BC Earth and Environmental Sciences for their help.

Finally, I would like to thank my parents, my brother, Peter, and my friends for providing me with support while finishing this thesis.

List of Tables

Table 2.1: Range of vertical compressibilities.....	16
Table 3.1: Ranges of parameter values for 1-D and 2-D analyses.....	31
Table 4.1: Analysis 1.1 - excavations and dimensions	33
Table 4.2: Analysis 2.1 - ranges of parameter values	34
Table 4.3: Analysis 2.2 - ranges of parameter values	38
Table 4.4: Analysis 3.1 - ranges of parameter values	41
Table 4.5: Analysis 3.2 - ranges of parameter values	45
Table 4.6: Analysis 3.3 - ranges of parameter values	52
Table 4.7: Analysis 4.1 - ranges of parameter values	55
Table 4.8: Analysis 4.2 - ranges of parameter values	58
Table 4.9: Analysis 4.3 - ranges of parameter values	69

List of Figures

Figure 1.1: Open pit mine	1
Figure 1.2: Hydromechanical coupling analogy with piston and spring	4
Figure 2.1: Diagram of volumetric strain	8
Figure 2.2: Diagram of storage at constant stress	11
Figure 2.3: Flowchart of hydromechanical responses and parameters	13
Figure 2.4: Values of hydraulic diffusivity	19
Figure 3.1: 1-D confined flow model - finite element mesh.....	24
Figure 3.2: 1-D confined flow model - boundary conditions	25
Figure 3.3: 2-D confined flow model - finite element mesh.....	26
Figure 3.4: 2-D confined flow model - boundary conditions	27
Figure 3.5: 2-D unconfined flow model - finite element mesh.....	28
Figure 3.6: 2-D unconfined flow model - excavations	28
Figure 3.7: 2-D unconfined flow model - boundary conditions	29
Figure 4.1: Analysis 1.1 - octahedral stresses at center	33
Figure 4.2: Analysis 1.1 - octahedral stresses at corner.....	34
Figure 4.3: Analysis 2.1 - pore pressures for initial and undrained responses	35
Figure 4.4: Analysis 2.1 - pore pressures for transient and steady-state responses	36
Figure 4.5: Analysis 2.1 - total heads for initial and undrained responses	37
Figure 4.6: Analysis 2.1 - total heads for transient and steady-state responses.....	38
Figure 4.7: Analysis 2.2 - pore pressures for a high diffusion coefficient.....	39
Figure 4.8: Analysis 2.2 - pore pressures for a moderate diffusion coefficient.....	39
Figure 4.9: Analysis 2.2 - pore pressures for a low diffusion coefficient.....	40
Figure 4.10: Analysis 3.1 - pore pressures for initial and undrained responses	41
Figure 4.11: Analysis 3.1 - pore pressures for transient and steady-state responses	42
Figure 4.12: Analysis 3.1 - total heads for initial and undrained responses	43
Figure 4.13: Analysis 3.1 - total heads for transient and steady-state responses.....	44
Figure 4.14: Analysis 3.1 - comparison between transient responses	44
Figure 4.15: Analysis 3.2 - pore pressures for a high diffusion coefficient.....	45
Figure 4.16: Analysis 3.2 - pore pressures for a moderate diffusion coefficient.....	46

Figure 4.17: Analysis 3.2 - pore pressures for a low diffusion coefficient.....	46
Figure 4.18: Analysis 3.2 - total heads for a low diffusion coefficient	47
Figure 4.19: Analysis 3.2 - total heads for a moderate diffusion coefficient.....	48
Figure 4.20: Analysis 3.2 - total heads for a low diffusion coefficient	48
Figure 4.21: Analysis 3.2 - hydraulic gradients for a low diffusion coefficient.....	50
Figure 4.22: Analysis 3.2 - hydraulic gradients for a moderate diffusion coefficient	50
Figure 4.23: Analysis 3.2 - hydraulic gradients for a high diffusion coefficient.....	51
Figure 4.24: Analysis 3.2 - discharges for different diffusion coefficients	52
Figure 4.25: Analysis 3.3 - pore pressures for swelling/heave analysis	53
Figure 4.26: Analysis 3.3 - total heads for swelling/heave analysis	54
Figure 4.27: Analysis 4.1 - pore pressures for initial and undrained responses	55
Figure 4.28: Analysis 4.1 - pore pressures for transient and steady-state responses	56
Figure 4.29: Analysis 4.1 - total heads for initial and undrained responses	57
Figure 4.30: Analysis 4.1 - total heads for transient and steady-state responses.....	57
Figure 4.31: Analysis 4.1 - comparison between transient responses	58
Figure 4.32: Analysis 4.2 - measurement locations around pit.....	59
Figure 4.33: Analysis 4.2 - pore pressures at center	60
Figure 4.34: Analysis 4.2 - pore pressures at corner.....	61
Figure 4.35: Analysis 4.2 - pore pressures at point outside	62
Figure 4.36: Analysis 4.2 - comparison of analyses at center	63
Figure 4.37: Analysis 4.2 - comparison of analyses at corner	64
Figure 4.38: Analysis 4.2 - comparison of analyses at point outside	64
Figure 4.39: Analysis 4.2 - hydraulic gradients at center	65
Figure 4.40: Analysis 4.2 - hydraulic gradients at corner.....	66
Figure 4.41: Analysis 4.2 - hydraulic gradients at point outside	67
Figure 4.42: Analysis 4.2 - discharges for different diffusion coefficients	68
Figure 4.43: Analysis 4.3 - measurement locations around pit.....	69
Figure 4.44: Analysis 4.3 - total stress paths	70
Figure 4.45: Analysis 4.3 - effective stress paths for Node A	71
Figure 4.46: Analysis 4.3 - effective stress paths for Node B	72
Figure 4.47: Analysis 4.3 - effective stress paths for Node C	73

Chapter 1: Introduction

Open-pit mining is the process of removing large amounts of geologic material from near the surface of the Earth's crust in order to acquire ores. The removal of this material, by blasting methods, creates a condition of lithostatic unloading, where both the solid material and the water within it are removed simultaneously, or nearly so. On the other hand, hydrostatic unloading refers to the removal of just the water, usually by pumping. Open-pit mines are very large excavations that can reach diameters up to approximately 3,500 meters and depths approaching 1,000 meters (Stacey et al., 2003). Figure 1.1 shows a typical open-pit mine labeled with the names of its main parts.



Figure 1.1: An image of a typical open-pit mine with main parts labeled. (Urzua, 2012).

If an open-pit mine is to be excavated below the water table, the groundwater flow regime must be investigated. The two major groundwater issues that open-pit miners are most concerned with are (1) the amount of groundwater discharging into the pit, and (2) the pore-water pressures in the overall pit slope and bench walls. A large

amount of groundwater discharge into the pit may result in higher costs for the mine due to groundwater pumping, management, treatment, and disposal. High pore water pressures are also of a concern due to their effects on the stability of the overall pit slope and the bench walls.

The important effect of pore pressure on the stability of slopes was recognized by Karl Terzaghi with his effective stress principle (Terzaghi, Peck, and Mesri 1996). Terzaghi demonstrated that this effect could be expressed by a modified form of the Mohr-Coulomb failure criterion:

$$\tau = c' + \sigma' \tan(\phi') \quad (1)$$

where,

$$\sigma' = \sigma - u \quad (2)$$

and where τ is the shear strength, c' is the effective cohesion, and ϕ' is the effective angle of internal friction, σ' is effective stress, σ is total stress, and u is pore fluid pressure. The stability of slopes is a function of loading or demand, and the capacity or strength of the rock mass to resist the demand. If the shear stress (demand) exceeds the shear strength (capacity) the slope will fail along its critical surface (Lambe and Whitman, 1969). It is clear from equations 1 and 2 that an increase in pore water pressure will result in decreased shear strength of the slope material and a decrease in pore water pressure will result in increased shear strength of the slope material. Consequently, determining an accurate pore water pressure distribution is important for slope stability calculations at an open-pit mine.

Given these issues concerning groundwater discharge and high pore water pressures, groundwater models are routinely developed during the construction of an

open-pit mine. These models are used to estimate the amount of dewatering required to decrease the amount of discharge into the pit and to lower the pore water pressures in the mine wall slopes. A groundwater model for an open-pit mine can be quite complex and include material properties and processes such as anisotropy, heterogeneity, flow through fractures, infiltration, etc. Even though these models can be complex and inclusive of many properties and processes, many ignore an important effect: the hydromechanical response of the excavation; that is, the effect the lithostatic unloading has on pore water pressures, heads, hydraulic gradients, and groundwater discharge (Sullivan, 2007).

Pore fluids affect the deformation of porous media by bearing loads or the removal of loads through an increase or decrease of the pore fluid pressure, and the deformation of the porous media affects the pore pressure of the fluid by altering pore volume, as the solid grains comprising the porous media rearrange themselves (Neuzil, 2003). Thus, there is a two-way mechanical-hydraulic interaction between the pore water and the porous media. In the Earth Sciences, this coupling between the mechanical effects of the solid media and the hydraulic effects of the pore water is called either hydromechanical coupling or poroelasticity (Rutqvist and Stephansson, 2003). Figure 1.2 depicts a one-dimensional hydromechanical coupling analogy involving a piston and a spring to illustrate hydromechanical coupling effects.

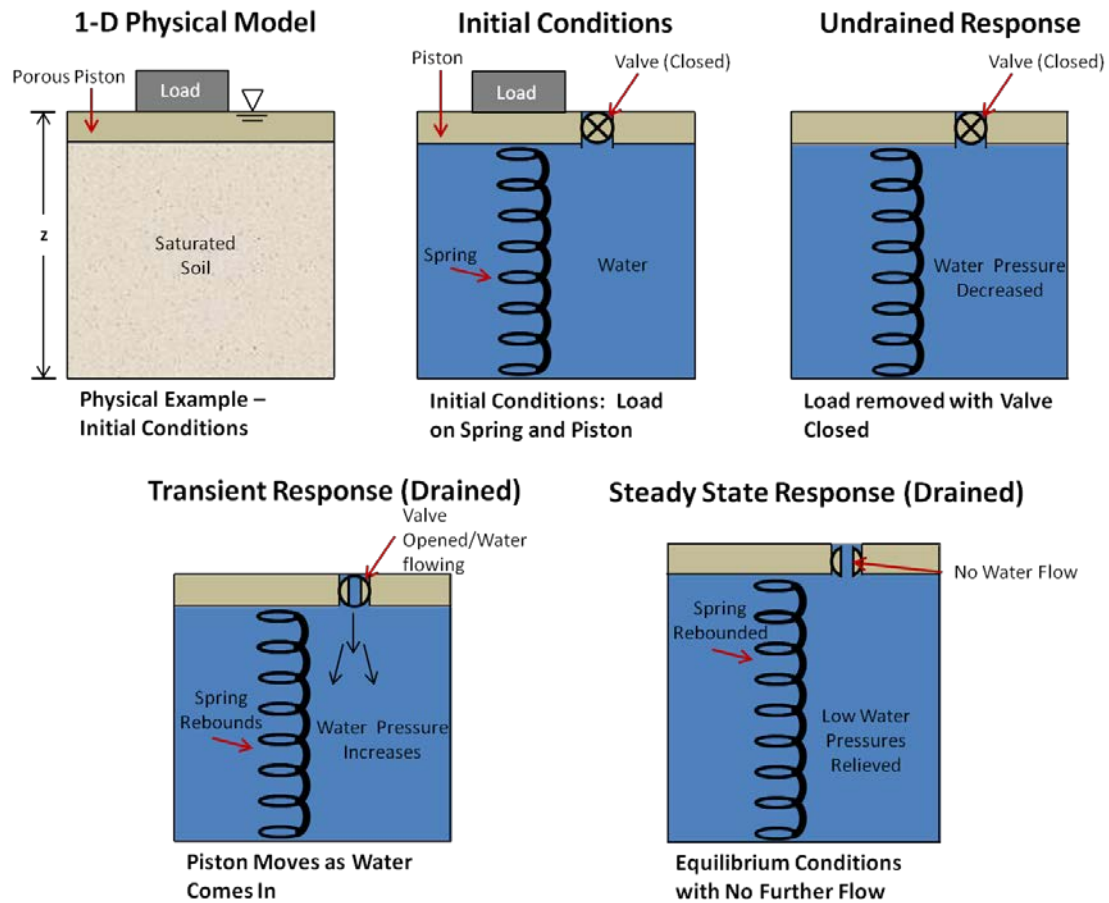


Figure 1.2: Diagram depicting a piston and spring analogy for the hydromechanical unloading process (Modified from Figure 2.5 in Lambe & Whitman, 1969).

Hydromechanical coupling is a well understood phenomenon in geologic materials. For example, Van der Kamp and Gale (1983) studied the effects of earth tides and barometric loading on fluid saturated porous materials, and Bell and Nur (1978) studied the effects of reservoir-filling-induced pore pressures on the stress regimes within geologic materials beneath the reservoir. However, the study of the hydromechanical coupling effects of lithostatic unloading in open-pit mines is rather limited. Sullivan (2007) gives a brief overview of the hydromechanical effects of unloading in mines including a decrease in pore water pressures and the increased permeability (swelling) of the material that may result in a zone around the excavation. Hazzard et al. (2011)

developed a guideline for hydrogeological modeling of large open-pit mines. Their approach consisted of defining a dimensionless excavation rate composed of a volumetric mining rate (per unit model thickness) and a diffusion coefficient composed of hydraulic conductivity and a storativity parameter. Through numerical analyses they found values of the dimensionless excavation rate that determined whether a steady-state analysis, an uncoupled analysis, a coupled analysis, or an undrained analysis should be performed for a given open-pit mine. It was found that mines with materials with high diffusion coefficients and a slow excavation rate could use a steady-state analysis. For mines with low diffusion coefficients or high excavation rates, a fully coupled model was found to be the most accurate (Hazzard et al., 2011). Regarding other large geotechnical excavations, excess negative pore water pressures (pressures below hydrostatic) were measured by Lutton and Banks (1970) in shales underneath the slopes on the sides of the Panama Canal, 70 years after its excavation. In the domain of geological processes, Neuzil and Pollock (1983) presented a numerical analysis of erosional unloading which suggested that, theoretically, excess negative pore water pressures could be found in shales or argillites even after a period of five million years. These two specific examples indicate that lithostatic unloading can generate excess negative pore water pressures that do not completely dissipate to hydrostatic conditions even over relatively long periods of time.

1.1 Objectives

The first objective of this thesis is to investigate the hydromechanical response of the lithostatic unloading in an open-pit mine. Simple one-dimensional (1-D) and two-dimensional (2-D) numerical analyses were performed to illustrate the effects that lithostatic unloading has upon the stress distributions, resultant pore water pressure

distributions, and groundwater flow regimes within an open-pit mine. The second objective of this thesis is to take the information gained from these analyses and develop a simplified groundwater modeling methodology that accounts for the hydromechanical effects of the lithostatic unloading. The results of this thesis are presented in a series of contour cross-sections and graphs depicting the effects of the hydromechanical response on stress distributions, pore water pressures, heads, hydraulic gradients, and discharge.

Chapter 2: Background

Hydromechanical coupling concepts were initially developed separately in the fields of soil mechanics, petroleum engineering, and hydrogeology. These concepts were developed to describe processes such as consolidation, subsidence due to fluid extraction, and the elastic storage of aquifers (Wang, 2000). Within the discipline of soil mechanics, Terzaghi developed a theory of 1-D consolidation in the 1920s, but it was not until 1941 that a general theory of three dimensional (3-D) consolidation (now called the theory of linear poroelasticity) was developed by Maurice A. Biot (Biot, 1941). Biot showed that Terzaghi's theory was a special case of Biot's general theory. Papers in the decades that followed demonstrated that many solutions to specific problems in petroleum engineering and hydrogeology could also be derived from Biot's general theory (Wang, 2000).

The equations that Biot developed form the foundation for the numerical simulations completed in this thesis. The four key variables in linear poroelasticity theory are stress, strain, pore water pressure, and a dimensionless variable called the *increment of fluid content* that accounts for any change in the amount of water within the pores of the medium. For a small change in each of the four variables compared to a

given reference state, the constitutive relations between these variables for a fully saturated, homogenous medium subjected to an isotropic applied stress field are given by the following two equations:

$$\epsilon = a_{11}\sigma + a_{12}u \quad (3)$$

$$\zeta = a_{21}\sigma + a_{22}u \quad (4)$$

where, ϵ is volumetric strain, σ represents an applied total stress field, u is pore water pressure, ζ is the increment of fluid content, and a_{ij} are four generic poroelastic coefficients (Wang, 2000). Volumetric strain is defined as the fractional volume change of the entire medium:

$$\epsilon = \frac{\Delta V}{V} \quad (5)$$

where V is the bulk volume of the representative elementary volume (REV), not of either the solid or fluid phase within the REV. The REV is a specified volume of the medium under analysis that consists of a sufficient amount of void space such that a volume of average porosity approaches a stable limit (Bear, 1972). The volumetric strain is taken to be positive in expansion and negative in contraction. Figure 2.1 depicts the concept of volumetric strain.

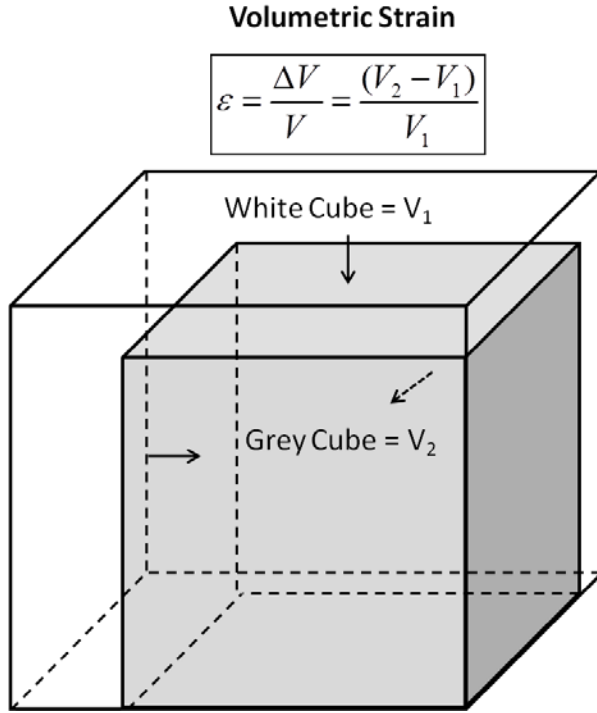


Figure 2.1: Depiction of volumetric strain for a compressed cube.

The increment of fluid content is defined as the volume of fluid added to or removed from a control volume of the medium per unit control volume, and so it is a dimensionless variable. A control volume is the reference volume for which a poroelastic problem is defined. The equation for the increment of fluid content can be given as:

$$\zeta = \frac{m_f - m_{f_0}}{\rho_{f_0}} \quad (6)$$

where m_f is the fluid mass content, m_{f_0} is the fluid mass content in a reference state, and ρ_{f_0} is the density of the fluid in a reference state. Rice and Cleary (1976) defined fluid mass content as the fluid mass per unit control volume. Consequently, a change in the fluid mass content for the given density of the fluid in the reference state is equivalent to the volume of fluid exchanged with the control volume per unit control volume (Wang, 2000).

Equation 3 indicates that changes in applied stress and pore water pressure will produce a fractional volume change of the material. Equation 4 indicates that changes in applied stress and pore water pressure must result in fluid added to or removed from storage within the medium (Wang, 2000). The two equations are coupled together through the stress and pore water pressure variables. The four generic coefficients a_{ij} in equations 3 and 4 represent the four poroelastic moduli that relate strains and the increment of fluid content to stresses and pore water pressure. These poroelastic moduli are defined as ratios of variables for a given constraint on the control volume, and are defined by the following four equations:

$$a_{11} = \left. \frac{\delta \epsilon}{\delta \sigma} \right|_{u=0} = \frac{1}{K} \quad (7)$$

$$a_{12} = \left. \frac{\delta \epsilon}{\delta u} \right|_{\sigma=0} = \frac{1}{H} \quad (8)$$

$$a_{21} = \left. \frac{\delta \zeta}{\delta \sigma} \right|_{u=0} = \frac{1}{H_1} \quad (9)$$

$$a_{22} = \left. \frac{\delta \zeta}{\delta u} \right|_{\sigma=0} = \frac{1}{R} \quad (10)$$

The coefficient $\frac{1}{K}$ is the drained bulk compressibility of the entire medium (composed of both the solid matrix and the fluid), both $\frac{1}{H}$ and $\frac{1}{H_1}$ represent the compressibility of the solid matrix (interchangeably called the solid skeleton), and $\frac{1}{R}$ is a specific storage coefficient that is measured at constant stress. Compressibility is the measure of the change in volume of a material caused by a given change in pore water pressure or stress. The drained bulk compressibility, $\frac{1}{K}$, is a measure of the volumetric strain of the entire medium for a given change in applied stress while holding pore water pressure constant

(drained conditions). The coefficient $\frac{1}{H}$ is referred to by Wang (2000) as the poroelastic expansion coefficient and it describes how much the bulk volume of the medium changes for a given change in pore water pressure while holding stress constant. The coefficient $\frac{1}{H_1}$ is equivalent to coefficient $\frac{1}{H}$ because of potential energy considerations as shown in Biot (1941) and Wang (2000). This equivalence means that the volumetric expansion of the medium at constant stress due to a change in pore water pressure, represented by coefficient $\frac{1}{H}$, is equal to the volume of fluid removed from the control volume of the medium at constant pore water pressure due to a change in applied stress, represented by coefficient $\frac{1}{H_1}$ (Wang, 2000). The coefficient $\frac{1}{R}$ is the ratio of the change in the volume of fluid added to storage per unit control volume to the change in pore water pressure. It is therefore a specific storage coefficient measured under conditions of constant applied stress (Wang, 2000). Figure 2.2 depicts the physical meaning of the specific storage coefficient, $\frac{1}{R}$.

Storage at Constant Stress

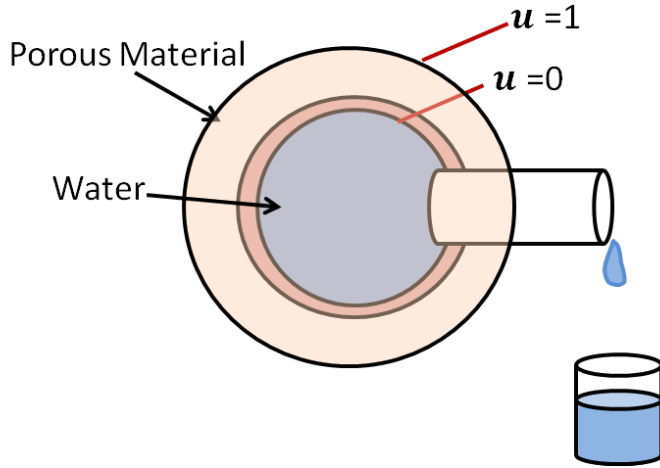


Figure 2.2: Depiction of water released from storage due to the compressibilities of the porous material and of the water as pore water pressure, u decreases. Modified after Wang (2000).

With the four generic coefficients defined, equations 6 through 9 can be combined with equations 3 and 4 to yield:

$$\epsilon = \frac{1}{K}\sigma + \frac{1}{H}u \quad (11)$$

$$\zeta = \frac{1}{H}\sigma + \frac{1}{R}u \quad (12)$$

Equations 11 and 12 describe the interactions between small changes of stress, strain, pore water pressure and the increment of fluid content relative to a given reference state for each variable. In order to describe fluid flow that occurs due to the applied stress field, additional equations are needed. The governing equations for fluid flow in a three dimensional (3-D) fully saturated poroelastic medium can be formulated from eleven constitutive equations: six equations for strain components, one equation for the pore water pressure component, three force equilibrium equations, and a pressure

diffusion equation that is obtained by combining Darcy's Law with the equation for conservation of fluid mass (Wang, 2000).

Darcy's Law, a relationship between the quantity of flow through a porous medium, the hydraulic head differential, and the properties of a porous medium was developed empirically by Henry Darcy in 1856, and is given as:

$$Q = kiA \quad (13)$$

where, Q is discharge, k is hydraulic conductivity, i is the hydraulic gradient, and A is the cross-sectional area of the material in which the flow goes through. The hydraulic gradient is the change in total head, h_t , over drainage path length, L ,

$$i = \frac{\partial h_t}{L} \quad (14)$$

where,

$$h_t = h_p + h_e \quad (15)$$

where, h_p is pressure head and h_e is elevation head. Equations 13, 14, and 15 show that the driving force of groundwater flow is the gradient in pressure head (pressure energy per unit weight) and elevation head (elevation energy per unit weight) over a specified distance.

The coupling between the force equilibrium equations and the fluid-flow equation is the result of the pore water pressure variable appearing in the force equilibrium equations and total stress variable appearing in the fluid-flow equation. A shear modulus constant also appears in the equations to account for shear strains. A complete derivation of the coupled equations of linear poroelasticity is presented in Wang, 2000; Detournay & Chang, 1993; Rice and Cleary, 1976; or Biot, 1941.

2.1 Undrained Response

The hydromechanical response to lithostatic unloading can be conceptually divided into three separate responses: (1) the undrained response, (2) the transient (drained) response, and (3) the steady-state (drained) response. Figure 2.3 is a chart that lists the mechanical and hydraulic parameters that govern each of these responses. Each of these responses is also a function of the geometry of the excavations. Immediately after the excavation, at time $t = 0$, there is no fluid flow or volume change of the material and so the increment of fluid content is constant. As there is no fluid flow this response is considered to be “undrained” and it is the ratio of the change in induced pore pressure to the change in the octahedral normal stress as a result of external loading or unloading. Octahedral normal stress is equal to the average of the normal stresses in the x-direction, y-direction and z-direction.

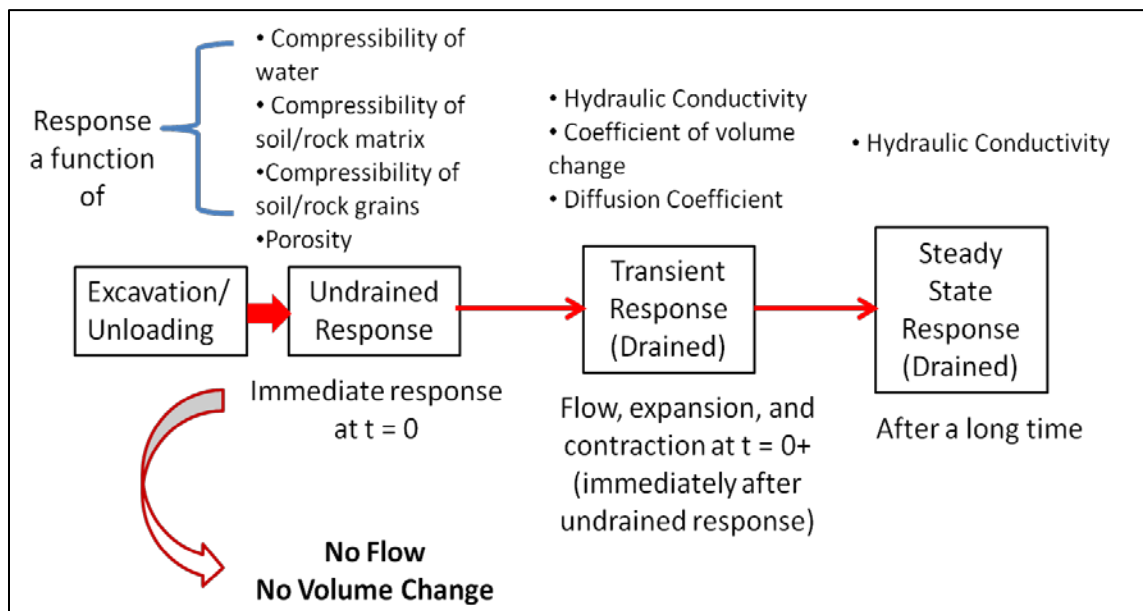


Figure 2.3: A flow chart listing the parameters that govern each of the three hydromechanical responses.

As seen in Figure 2.3, the undrained response is a function of the compressibilities of the pore fluid (liquid and gas phases), solid matrix (interchangeably

called the solid skeleton), solid grains, and the effective porosity of the formation. The solid grains are assumed to be incompressible in this thesis, because for soils and fractured rocks, the compressibility of the solid grains is much less than the compressibility of the solid matrix (Lambe and Whitman, 1969). Though, for unfractured rock this assumption is not accurate, as these rocks have very low compressibility (Rice and Cleary, 1976; Van der Kamp and Gale, 1983). There are different types of compressibility, depending upon the defined conditions of the REV. The compressibility of the medium is defined differently for 1-D conditions (either uniaxial compressibility or constrained compressibility) than it is for 2-D or 3-D conditions (bulk compressibility) as for 1-D conditions only the vertical strain is taken into account. Therefore, the differences in compressibility lead to several different undrained parameters depending on whether dealing with either 1-D or 2-D/3-D conditions. For 1-D conditions, the undrained response is governed by pore pressure parameter C (Lambe and Whitman, 1969):

$$C = \frac{\Delta u}{\Delta \sigma_z} = \frac{1}{1 + n(C_w/C_{c1})} \quad (16)$$

Where $\Delta \sigma_z$ is the increment in vertical stress, C_w is the compressibility of water, C_{c1} is the constrained compressibility of the medium, and n is the porosity of the medium. For 2-D/3-D analyses, C_{c1} must be replaced by the bulk compressibility, C_b , which gives pore pressure parameter B (Lambe and Whitman, 1969):

$$B = \frac{\Delta u}{\Delta \sigma} = \frac{1}{1 + n(C_w/C_b)} \quad (17)$$

If the analysis is of a very stiff rock (a relatively incompressible medium), then the compressibility of the solid grains, C_s , should be taken into account and so Skempton's coefficient, β , must be used (Rice and Cleary, 1976):

$$\beta = \frac{\Delta u}{\frac{\Delta \sigma_{kk}}{3}} = \frac{(C_b - C_s)}{(C_b - C_s) + n(C_w - C_s)} \quad (18)$$

where $\Delta \frac{\sigma_{kk}}{3}$ is the increment or decrement of octahedral normal stress. It can be shown that if the solid grains are assumed to be incompressible, $C_s = 0$, then Skempton's coefficient reverts to pore pressure parameter B. The change in pore water pressure due to the unloading in 2-D or 3-D analyses is given by solving either equation 17 or 18 for the increment in pore water pressure:

$$\Delta u = \Delta \frac{(\sigma_{xx} + \sigma_{yy} + \sigma_{zz})}{3} \beta \quad (19)$$

As horizontal strains are not equal to zero in 2-D or 3-D analyses, octahedral normal stresses must be used in the calculation of the undrained response for 2-D or 3-D analyses. If the analysis is 1-D, then the increment of vertical stress can be used in place of the increment of octahedral normal stress.

Equations 15-17 show that for a given porosity and assuming the solid grains are incompressible, the magnitude of the undrained response is dependent upon the difference between the compressibility of the medium and the compressibility of water. Table 2.1 shows the compressibilities of various types of unconsolidated deposits and rocks as compared to the compressibility of water.

Porous Material	Vertical Compressibility (1/kPa)
Plastic clay	2.09×10^{-3} - 2.62×10^{-4}
Stiff clay	2.62×10^{-4} - 1.31×10^{-4}
Medium hard clay	1.31×10^{-4} - 6.99×10^{-5}
Loose sand	1.05×10^{-3} - 5.24×10^{-5}
Dense sand	2.09×10^{-5} - 1.31×10^{-5}
Dense sandy gravel	1.04×10^{-5} - 5.24×10^{-6}
Rock, fractured, jointed	6.99×10^{-6} - 3.34×10^{-7}
Rock, intact	Less than 3.34×10^{-7}
Water	5.05×10^{-7} - 4.83×10^{-7}

Table 2.1: List of compressibilities for various unconsolidated deposits and rocks. Adapted from Batu (1998); original data from Domenico and Mifflin (1965).

Table 2.1 and equations 15-17 demonstrate that the more compressible the medium is compared to water, the closer the undrained pore pressure parameter is to one (1), and that the less compressible the medium is compared to water, the closer the undrained pore pressure parameter is to zero (0). Therefore, the values of the three undrained pore water pressure parameters must each lie between zero and unity. The physical meaning behind these parameters is that they indicate how the removal of stress during unloading is distributed between the solid matrix and the pore fluid (liquid and gas phases). For highly compressible and fully saturated solid materials, such as a saturated clay or sand (see Table 2.1), the value of these parameters tends toward one (1), meaning

that the pressure of the relatively incompressible water responds to the entire change in stress. For materials that are less compressible, such as intact igneous rock, and filled with a highly compressible pore fluid, (such as gas/air), these parameters tend toward zero (0), because the solid skeleton supports some or all of the removal of stress. To summarize, the undrained response of the lithostatic unloading governs the magnitude of the generation of excess negative pore water pressures, immediately after unloading.

2.2 Transient (Drained) Response

Following the immediate undrained response, the transient (drained) response begins and, with time, increases from zero. During this response, water flows into the medium to relieve the excess negative pore water pressures generated by the undrained response. If only vertical stresses, vertical strains, and vertical flow are considered (1-D conditions), the vertical total stress is constant, and the material is homogenous and isotropic, then the transient response in terms of pore water pressures can be described by the uniaxial fluid diffusion equation:

$$\frac{\partial u'}{\partial t} - c_v \frac{\partial^2 u'}{\partial z^2} = 0 \quad (20)$$

where u' is the excess pore water pressure, t is time, c_v is the diffusion coefficient (interchangeably called the coefficient of consolidation or hydraulic diffusivity), and z is depth. The diffusion coefficient can be expressed as:

$$c_v = \frac{k}{S_s} = \frac{k}{\gamma_w m_v} \quad (21)$$

Equation 20 indicates that the diffusion coefficient is comprised of the hydraulic conductivity, k , and uniaxial specific storage, S_s (equal to the unit weight of water, γ_w , times the coefficient of volume change, m_v). The physical meaning of the diffusion

coefficient is that it governs the time it takes for the excess negative pore water pressures to dissipate. The diffusion coefficient is directly proportional to hydraulic conductivity and inversely proportional to specific storage. A higher hydraulic conductivity allows for faster conductance of fluid, and therefore a higher diffusion coefficient, whereas a larger specific storage coefficient requires more fluid to be moved per unit time, resulting in a lower diffusion coefficient (Wang, 2000). Uniaxial specific storage, as defined in hydrogeology, is the change in fluid pressure due to a drop in total head and is expressed in terms of compressibilities as:

$$S_s = \gamma_w(C_{c1} + nC_w) \quad (22)$$

If water is assumed to be virtually incompressible, $C_w = 0$, as it is in soil mechanics, then $S_s = \gamma_w m_v$, assuming the material is fully saturated so that $m_v = C_{c1}$.

Hydraulic conductivity (or intrinsic permeability) can also vary over many orders of magnitude among various unconsolidated deposits and rocks. Specific storage can vary over several orders of magnitude as it is dependent upon the range of compressibilities shown in Table 2.1. As the diffusion coefficient is composed of both the hydraulic conductivity and specific storage parameters, it can vary over 16 orders of magnitude. Roeloffs (1996) compiled a chart (Figure 2.4) showing a large range of estimated values for the diffusion coefficient with data from both laboratory and in-situ (field) measurements of different unconsolidated deposits and rocks. Li (1984/85) found that the in-situ measurements of the diffusion coefficient for crystalline rocks were at least three to four orders of magnitude higher than the laboratory measurements. Li suggested that this discrepancy arises because the size of the laboratory samples preclude the inclusion of discontinuities such as fractures or joints. On the other hand, Neuzil

(1986) notes that there is an abundance of evidence for large regions of low-permeability geologic materials that have a lack of fractures or fractures that are not connected or transmissive. These findings illustrate the importance of fractures as conduits for fluid flow in crystalline rock, and it is well accepted in the literature that the diffusion coefficients for crystalline rocks are largely controlled by the degree and the nature of the fracturing within the rock masses.

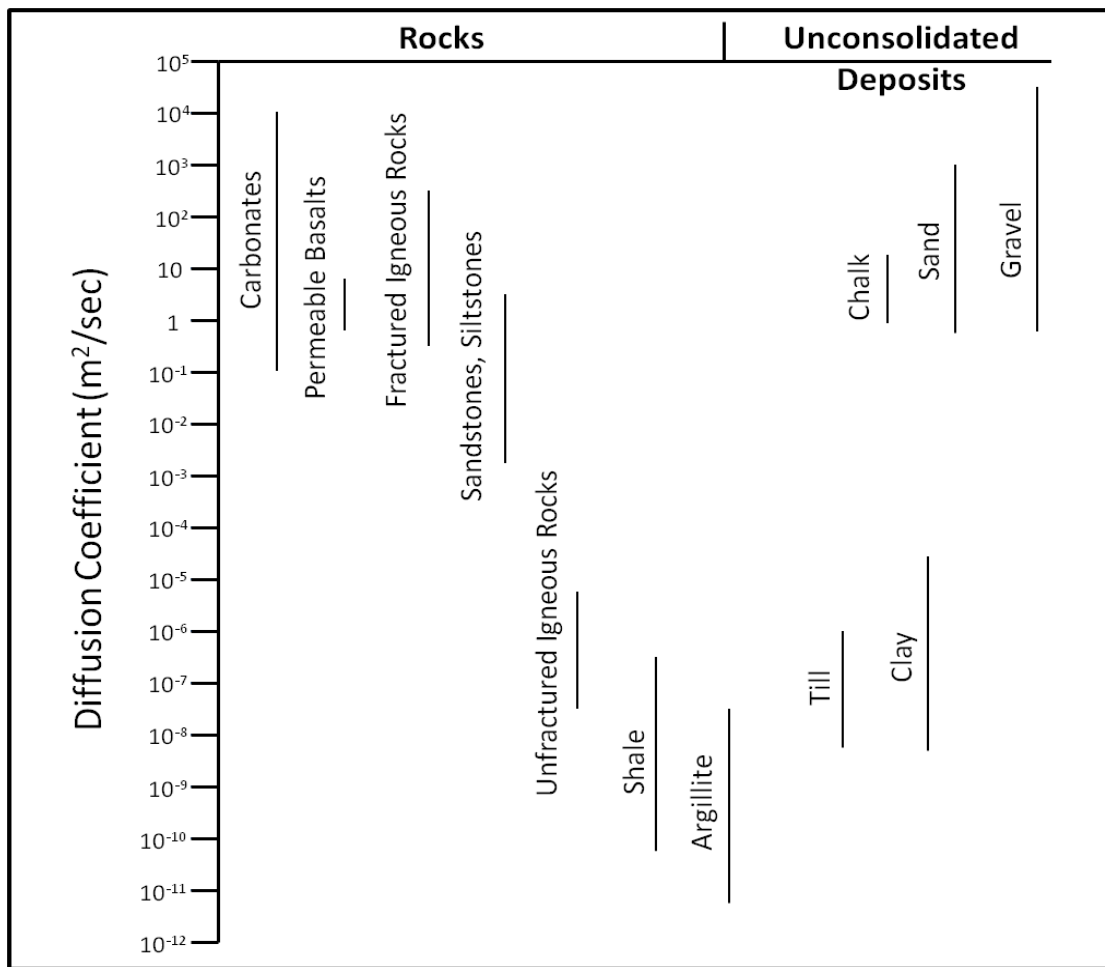


Figure 2.4: Chart depicting ranges of values for the diffusion coefficient for different geologic materials. These ranges were determined by both laboratory and field measurements and are not limiting as they only include a small number of measurements. Adapted from Roeloffs (1996).

Equation 16 describes the diffusion of excess pore water pressures after only one excavation (conditions of constant vertical stress). To fully describe the entire unloading process with multiple excavations for 1-D conditions, the right side of equation 16 can include a change in total stress over time term as shown below:

$$\frac{\partial u'}{\partial t} - c_v \frac{\partial^2 u'}{\partial z^2} = \frac{\partial \sigma_v}{\partial t} \quad (23)$$

where σ_v is total vertical stress. If the term $\frac{\partial \sigma_v}{\partial t}$ is less than zero then equation 23 governs the 1-D unloading process for multiple excavations. To describe the entire unloading process in two or three dimensions, horizontal strains cannot be assumed to be equal to zero (Neuzil, 2003). Consequently, the uniaxial specific storage term in the denominator of the c_v parameter (see equation 21) in equation 23 must be replaced with a 3-D specific storage coefficient, and the vertical stress must be replaced by the octahedral normal stress, as shown below:

$$\frac{\partial u'}{\partial t} - c_v \nabla^2 u' = \frac{\partial \frac{\sigma_{kk}}{3}}{\partial t} \quad (24)$$

where $\nabla^2 u' = \frac{\partial^2 u'}{\partial x^2} + \frac{\partial^2 u'}{\partial y^2} + \frac{\partial^2 u'}{\partial z^2}$. The 3-D specific storage coefficient is the uniaxial specific storage coefficient with bulk compressibility replacing uniaxial compressibility:

$$S_s^* = \gamma_w (C_b + nC_w) \quad (25)$$

If the geologic mass being analyzed is relatively incompressible then the compressibility of the solid grains will need to be taken into account and so equation 24 becomes:

$$S_s^{**} = \gamma_w [(C_b - C_s) + n(C_w - C_s)] \quad (26)$$

where S_s^{**} is the 3-D specific storage coefficient including the compressibilities of the solid grains.

The most general transient fluid diffusion equation for a poroelastic, homogenous, and isotropic medium is given by equation 23 with the 3-D specific storage parameter (equation 25) in the denominator of the diffusion coefficient. Assumptions of incompressible solid grains, 1-D conditions (where only vertical stress, vertical strains, and vertical flow are considered), and constant vertical stress will yield the simpler 1-D transient fluid diffusion equation given by equation 20. Relaxing the assumption of constant vertical stress will yield equation 23, and of course, relaxing all of the other assumptions will yield equation 24.

2.3 Steady-State (Drained) Response

After a long time, the excess negative pore water pressures generated by the undrained response will have completely dissipated by the end of the transient response and the groundwater flow will approach a steady-state. Theoretically, the transient response lasts forever, but for virtually all geotechnical applications the transient response (and therefore consolidation or swelling) can be assumed to end at a certain time (Lambe and Whitman, 1969). The condition at the end of the transient response is referred to as the steady-state response, and it is dependent on the hydraulic conductivity of the geologic material. Since there is no change in pore water pressure over time in the steady-state response, it is governed by Laplace's equation for a 1-D, homogenous and isotropic medium:

$$k \frac{\partial^2 u}{\partial z^2} = 0 \rightarrow \frac{\partial^2 u}{\partial z^2} = 0 \quad (27)$$

For a 3-D homogenous and isotropic medium, equation 24 is simply extended to the other two coordinate directions:

$$\frac{\partial^2 u}{\partial x^2} + \frac{\partial^2 u}{\partial y^2} + \frac{\partial^2 u}{\partial z^2} = 0 \quad (28)$$

Note that the terms $\frac{\partial \sigma_v}{\partial t}$ or $\frac{\partial \frac{\sigma_{kk}}{3}}{\partial t}$ are not present in the steady-state equations, as change in stress over time is equal to zero, and so these equations are uncoupled. The process of solving the undrained, transient, and steady-state equations for the lithostatic unloading problem is explained in the next chapter.

While the theory of linear poroelasticity provides a sound theoretical basis for the analyses performed in this thesis, its major limitation is that it should only be applied to geologic materials that behave elastically. Many geologic materials do not behave elastically because they undergo irreversible deformations (Neuzil, 2003). The reader is referred to Neuzil (2003) for an in-depth discussion on the limitations of linear poroelasticity, and generalizations of this theory for geotechnical and geological applications involving nonlinear elastic, elastoplastic, and viscoelastic materials.

Chapter 3: Methodology

Analytical or closed-form solutions are not easily achievable for poroelastic problems involving 2-D or 3-D excavations with complicated geometries, such as a trapezoid-shaped excavation (Wang, 2000). Consequently, for the purposes of this thesis, a series of simple 1-D and 2-D numerical analyses were performed to investigate the hydromechanical response of lithostatic unloading. The 1-D and 2-D numerical analyses were performed using the technique of finite elements. The finite element software programs SEEP/W and SIGMA/W were used to perform these analyses. For an

explanation of the finite element methods as applied to modeling groundwater flow, the reader is referred to Mercer and Faust, 1980.

The main assumptions for the finite element analyses in this study are as follows:

- (1) The material is homogenous and isotropic;
- (2) The material is fully saturated at all times;
- (3) The material can be modeled as an equivalent porous medium;
- (4) The material can be mechanically modeled as linearly elastic, that is, there exists a linear relation between stress and strain for the material;
- (5) The compressibility of the solid grains within the material is negligible;
- (6) The amount of dissolved gas in the pore fluid is negligible;
- (7) Infiltration, evaporation, and runoff processes are ignored; and
- (8) Hydraulic conductivity and specific storage are constant.

To investigate the possible effects of this last assumption on the results of this study, results are included below from a specific analysis where hydraulic conductivity is allowed to vary over time due to swelling.

While these assumptions may appear limiting, the analyses that comprise this thesis are conceptual and are not based on explicit experimental or field results from a specific open-pit mine. Thus, these assumptions are justified given the purpose of this thesis, which is to provide a clear, conceptual overview of the hydromechanical effects of lithostatic unloading in open-pit mines.

3.1 One-Dimensional Finite Element Analyses

The procedure for constructing the 1-D finite element numerical analysis first involved setting up the geometry and finite element mesh of the profile. An example of a

1-D finite element analysis is shown in Figure 3.1. The finite element mesh was specified with 50-meter by 50-meter elements comprising a 1,000 meter high profile.

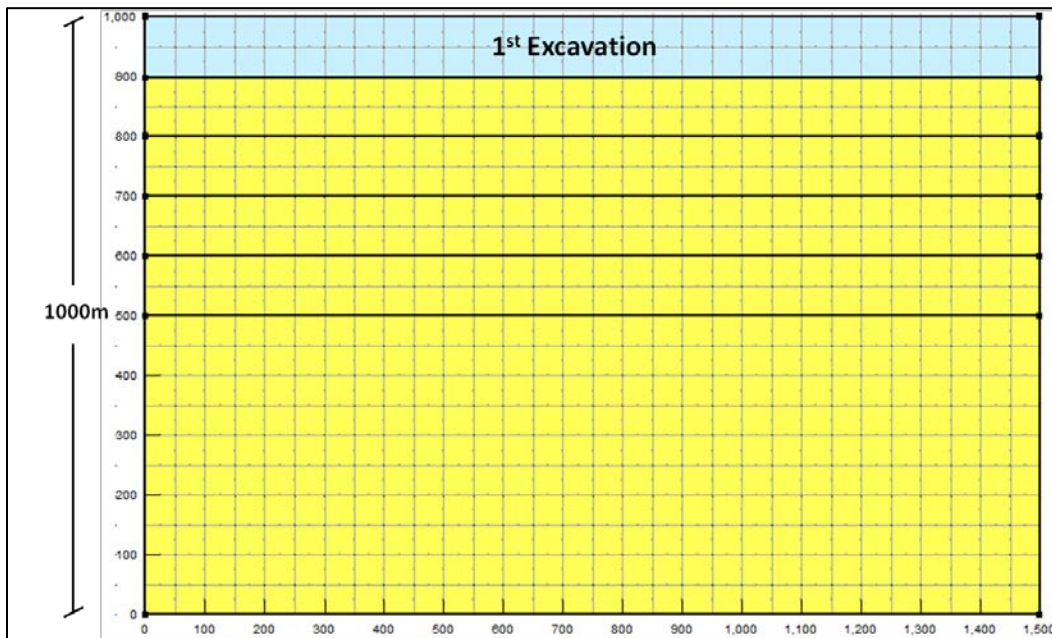


Figure 3.1: A 1-D numerical model with 50m by 50m elements comprising the grid. The height of the profile is 1,000m, while the width of the profile is arbitrary as it is a 1-D model. The excavation is 100m in height.

The boundary conditions for each analysis vary depending upon its specific geometry (i.e. 1-D or 2-D). Both hydraulic and mechanical boundary conditions must be specified to solve a coupled analysis. The boundary conditions for the 1-D analyses are labeled in Figure 3.2. The hydraulic boundary condition at the top of the profile is a zero pressure head condition. The mechanical boundary conditions are fixed displacement in the x direction for both sides of the profile and fixed displacement in both the x and y directions at the bottom of the profile.

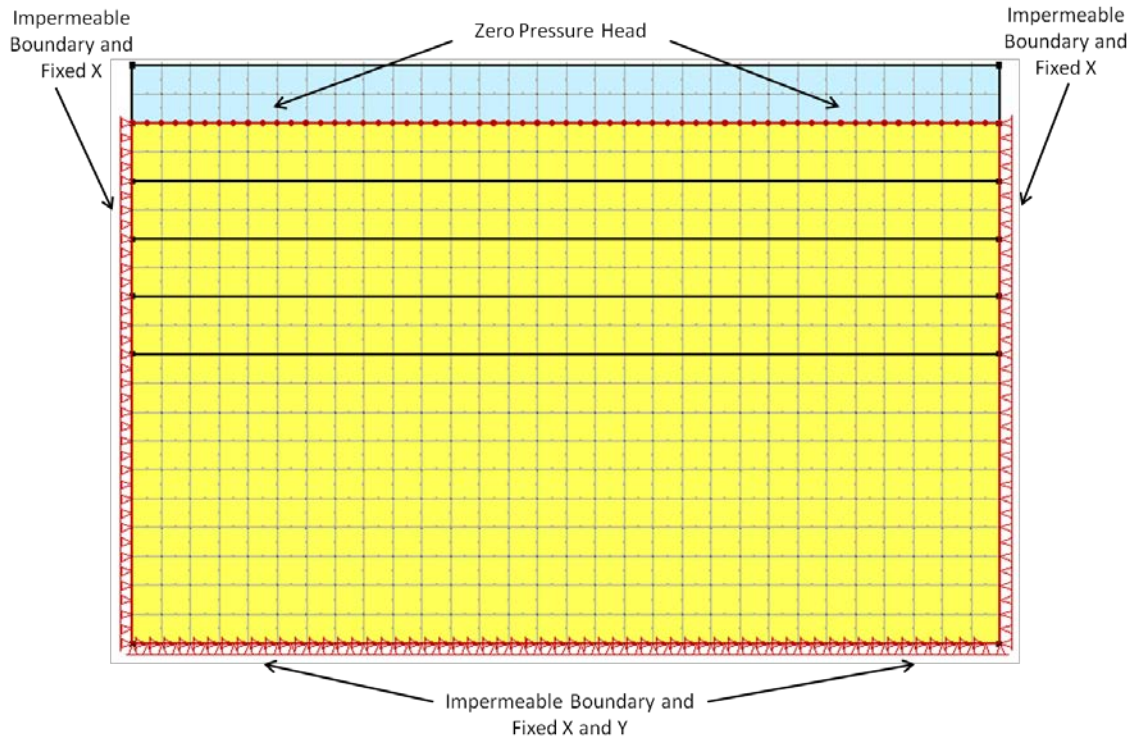


Figure 3.2: A 1-D numerical model with hydraulic and stress boundary conditions labeled.

3.2 Two-Dimensional Finite Element Analyses

The 2-D finite element analyses were split up into two major categories of analyses based on two different excavation geometries. The first category consisted of a simple rectangular-strip excavation geometry. The second category consisted of a more realistic trapezoid-shaped excavation geometry.

The rectangular-strip excavation analyses model the removal of a 500-meter by 100-meter deep rectangular block of geologic material. The side boundaries of this model are at a distance three times the excavation width and the bottom boundary is at a distance six times the excavation width. The finite element mesh is comprised of 50-meter by 50-meter elements near the excavations and 100-meter by 100-meter elements far from the excavations. Figure 3.3 depicts the dimensions and finite element mesh of a 2-D rectangular-strip excavation analysis with two excavation blocks. The geometry of

this analysis could also be completed as a symmetric analysis about the center of the 500-meter wide excavation.

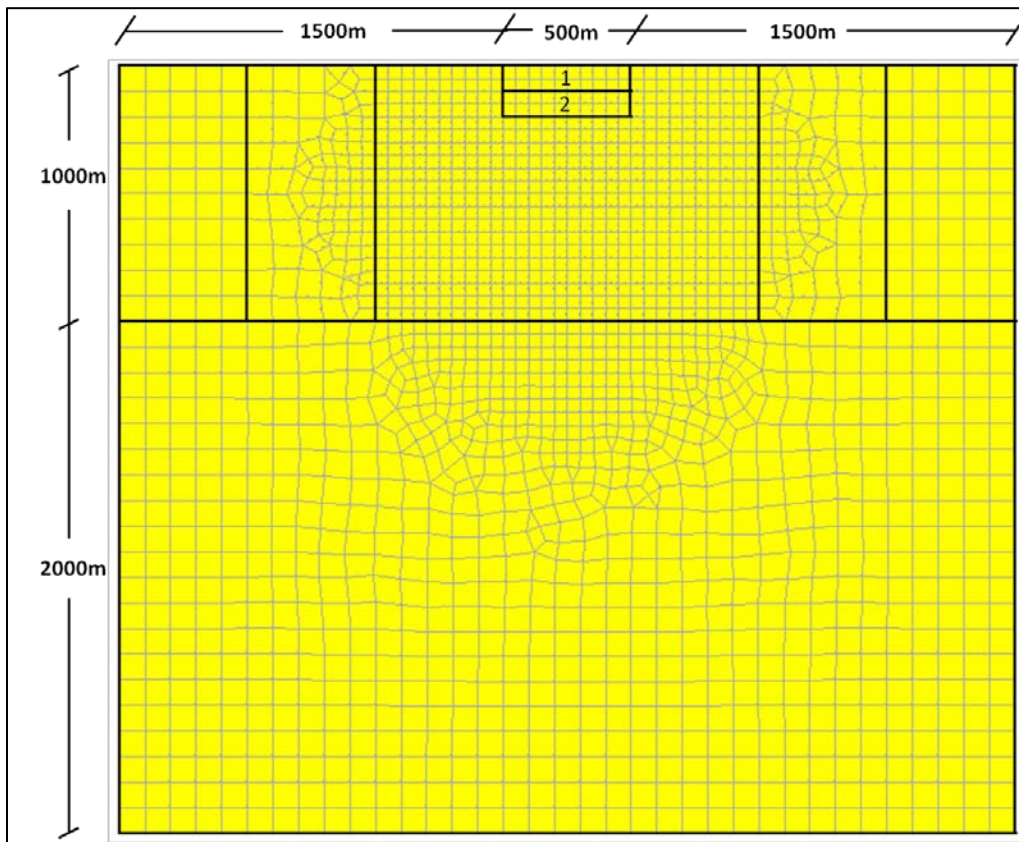


Figure 3.3: Image depicting mesh size and dimensions for a 2-D rectangular-strip excavation analysis.

The 2-D rectangular-strip excavation analyses have similar boundary conditions to the 1-D analyses, except for two major differences. First, the 2-D analyses have constant head boundaries on each side of the profile, although these sides could be impermeable boundaries as well, and the change in the results would be negligible. Second, the sides of the actual excavation have impermeable boundaries. Figure 3.4 depicts the boundary conditions for the 2-D rectangular-strip excavation analyses.

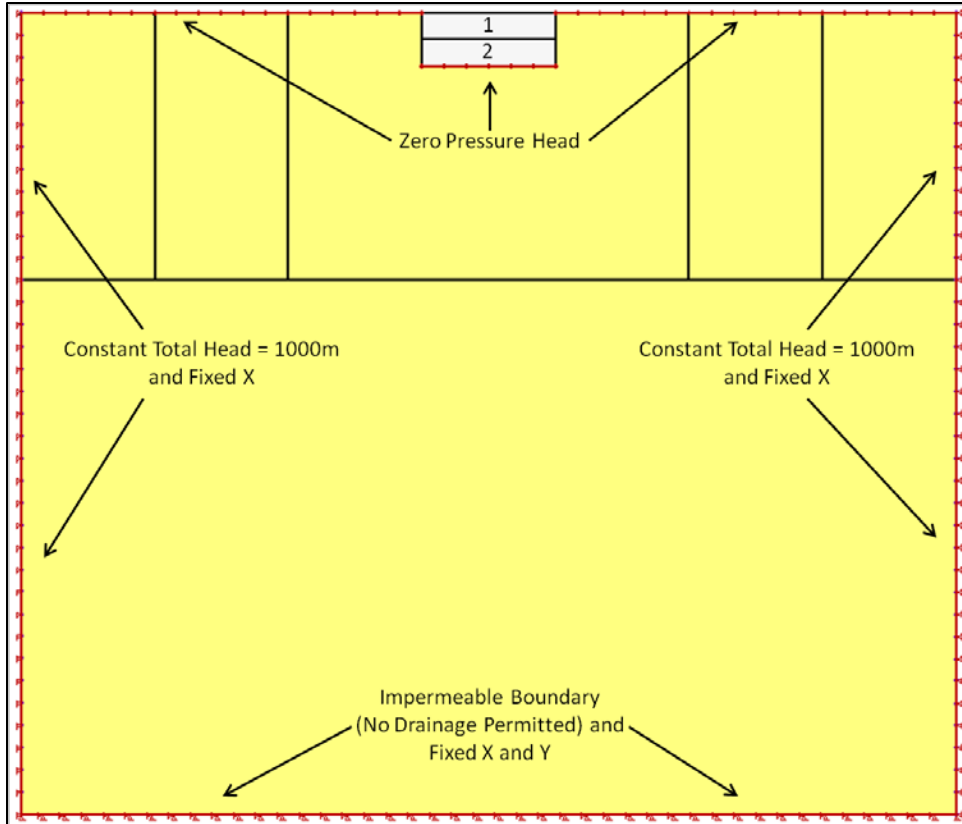


Figure 3.4: Boundary conditions for the 2-D rectangular-strip excavation analyses.

The 2-D trapezoid-shaped excavation analyses were modeled with a symmetrical geometry about the center of the pit, as shown in Figure 3.5; a zoomed-in image of the excavation dimensions is shown in Figure 3.6. A total of ten excavations are modeled with this analysis. These ten excavations were divided into two groups, the first five (numbered 1-5) are large, flat, trapezoid-shaped excavations, that are excavated every 360 days (approximately one year) and the second group of five (numbered 6-10) are smaller trapezoid-block excavations, that are excavated every 180 days (approximately one half of a year). Both excavation groups are comprised of excavations at a 45-degree angle with respect to the ground surface.

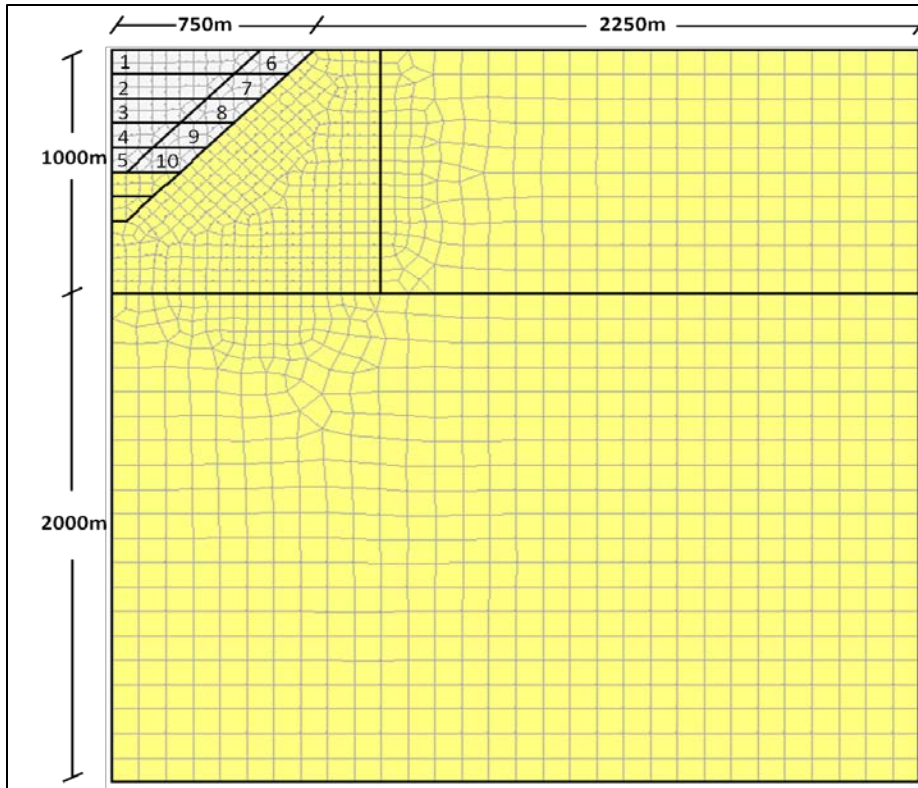


Figure 3.5: Dimensions and mesh for the 2-D trapezoid excavation analyses.

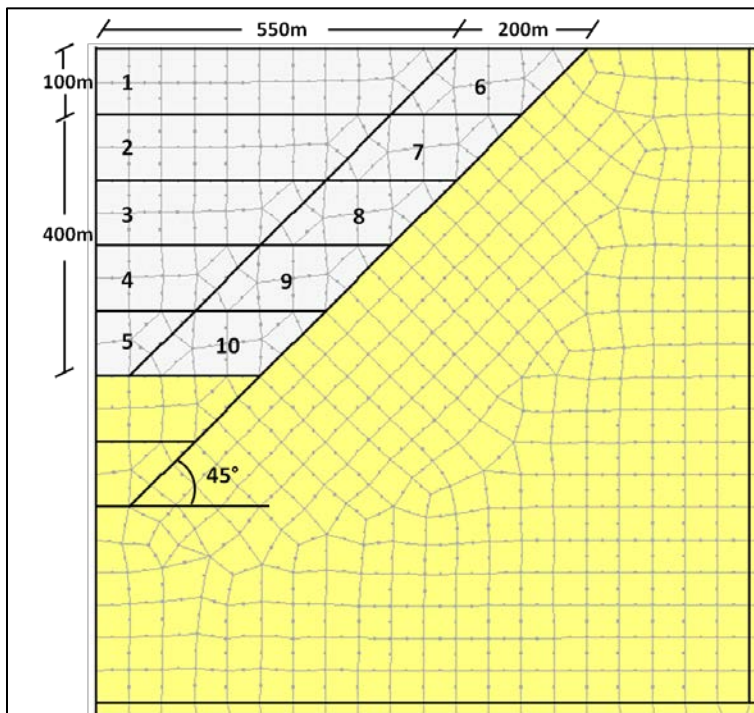


Figure 3.6: Zoomed in view of the excavations shown in figure 3.5.

Regarding boundary conditions, the 2-D trapezoid-shaped excavation model has a major difference from the 2-D rectangular-strip excavation model. The trapezoid-shaped excavation model has a no-flow boundary condition with a potential seepage face review condition on the face of the excavation, as shown in Figure 3.7. The left side of the profile is an impermeable boundary and fixed displacement in the x direction, to simulate the symmetry of the excavation. The bottom of the profile is an impermeable flow boundary and fixed displacement in both the x and y directions.

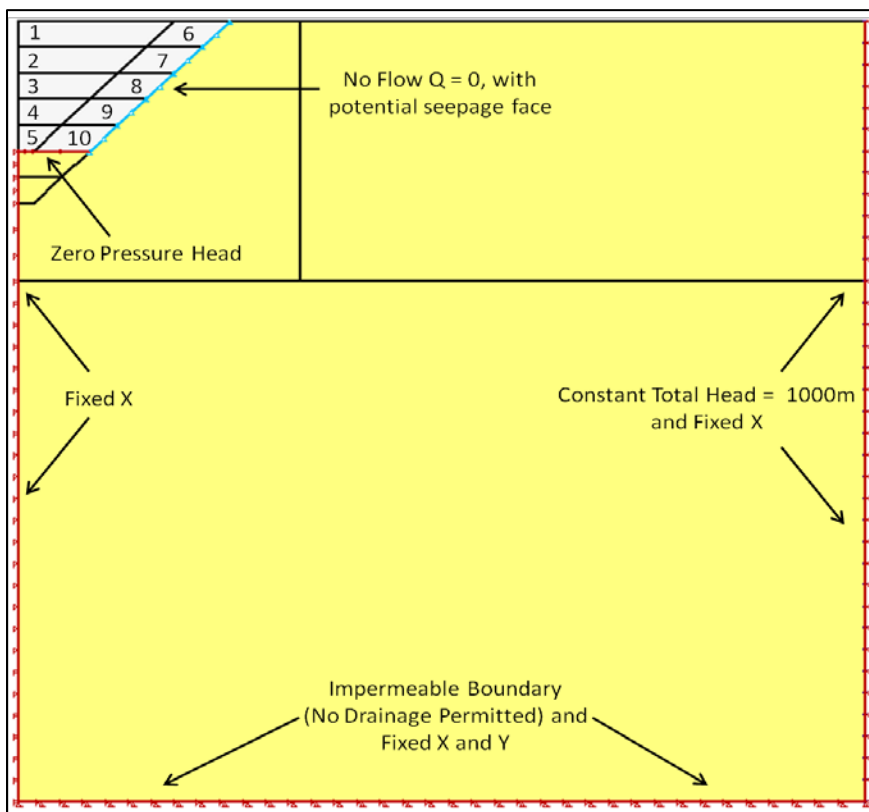


Figure 3.7: Boundary conditions for the trapezoid-shaped excavation analyses.

3.3 Range of Parameter Values

After the excavation geometry and finite element mesh were set up, the values of the material parameters were specified to complete the numerical model. The material parameters specified in SIGMA/W and/or SEEP/W included C_{c1} , the constrained

compressibility, or E , Young's Modulus; ν , Poisson's ratio; m_v , the coefficient of volume change; k , the hydraulic conductivity; c_v , the diffusion coefficient; γ_w , the unit weight of water; and γ_s , the unit weight of the soil/rock. Refer back to Chapter 2 for a detailed discussion on the parameters governing the undrained, transient, and steady-state hydromechanical responses of lithostatic unloading. The values for the parameters used in the both the 1-D and 2-D analyses were chosen based on two major considerations: (1) to provide results that could be readily checked by hand and easily interpreted, and (2) to make the values representative of a compressible soil/fractured rock mass. A list of the ranges of parameter values used in these analyses is given in Table 3.1.

Parameter	C_{c1} or E (kPa)	ν	m_v (1/kPa)	k (m/s)	c_v (m ² /s)	γ_w (kN/m ³)	γ_s (kN/m ³)
Value	10 ⁵ - 10 ⁶	1/3	10 ⁻⁵ - 10 ⁻⁶	10 ⁻⁷ - 10 ⁻⁹	10 ⁻² - 10 ⁻⁴	10	20

Table 3.1: Table of the ranges of parameter values used in the 1-D and 2-D finite element analyses.

3.4 Undrained, Seepage, Coupled, and Steady-State Analyses

In addition to subdividing the analyses in terms of their dimensions (1-D, 2-D) or excavation shape (rectangle, trapezoid, etc.), the analyses can also be subdivided into the different hydromechanical responses they model: undrained analyses, transient seepage analyses, transient coupled analyses, and steady-state (drained) analyses. The undrained analyses model the undrained response, the transient coupled analyses model the transient (drained) response and the steady-state analyses model the steady-state (drained) response. The transient seepage analyses are uncoupled as they model only the groundwater seepage that occurs because of the difference in total head that develops due to the lowering of the ground surface due to the excavation. The hydromechanical effects

of the lithostatic unloading are not captured in the transient seepage analyses. These analyses were performed to show the differences between an uncoupled transient analysis and a coupled transient analysis.

3.5 Specific Procedures for Solving for the Undrained Response

The undrained analysis is a coupled analysis and so the transient seepage analyses and the steady-state analyses are not dependent upon the undrained response. The undrained analysis must be manually specified in SIGMA/W as a load response ratio. Consequently, the calculation of the pore pressure parameter C , pore pressure parameter B , or Skempton's coefficient must be calculated and then used as the load response ratio (interchangeable called the loading efficiency). For the purposes of this thesis, the load response ratio was entered as 1.0 for all analyses, meaning that the pore fluid always supported 100 percent of the removal of the load in each analysis.

Chapter 4: Results

The results from the 1-D and the 2-D numerical analyses indicate that the hydromechanical response of the lithostatic unloading affects octahedral stresses, pore water pressures/pressure heads, total heads, hydraulic gradients, and discharges in various ways. A general overview of the hydromechanical coupling effects of the lithostatic unloading is provided below. First, during the undrained response, the lithostatic unloading causes the octahedral stresses to decrease generating excess negative pore water pressures and therefore a decrease in the pore water pressures. Pressure head decreases, and, if elevation head is constant, the total head decreases by the same amount as the decrease in pressure head. The total head decrease causes the hydraulic gradient to

increase. Discharge is zero during the undrained response. All of these changes are instantaneous.

During the transient (drained) response, the excess negative pore water pressures dissipate at a rate governed by the diffusion coefficient. The pore water pressures therefore increase with time as the excess negative pore water pressures dissipate and consequently pressure head and total head increase over time. The increase in total head is accompanied by a decrease in the hydraulic gradients with time. These transient changes all converge to a set of new steady-state (drained) conditions.

4.1 Distribution of Octahedral Stresses

The decrement of octahedral normal stress for a 1-D lithostatic unloading analysis is equivalent to the decrement in vertical stress, σ_{zz} , for all depths. For 2-D and 3-D analyses the distribution of octahedral normal stresses is different than for the 1-D analyses because the increment/decrement of vertical stress is not equal to the increments/decrements of the horizontal stresses, σ_{xx} and σ_{yy} , at all depths. Analysis 1.1. involved modeling three different types of excavations with dimensions and geometry, as shown in Table 4.1. In this analysis, the removal of 100 meters of material from a 1,100 meter high profile generates a decrement of octahedral normal stress in the profile, from 0 meters elevation to 1,000 meters. The decrements are normalized to the magnitude of the unloading force, for example, a 0.9 decrement of a 2,000 kPa unloading force is equal to 1,800 kPa. Figures 4.1 and 4.2 show normalized comparisons of the decrements of octahedral normal stresses for these excavations with the 1-D analysis at the center of the excavation and at the corner of the excavation, respectively. For example, at an elevation of 800 meters under the center of the excavation, the normalized

decrement is 0.55 for the long rectangular strip, 0.42 for the square excavation and 0.38 for the circular excavation.

Excavation	Long Rectangular Strip	Square	Circular (3-D)
Dimensions	500m x 9,000m	500m x 500m	500m Diameter

Table 4.1: Table of the excavations and their dimensions in meters (m), for Analysis 1.1.

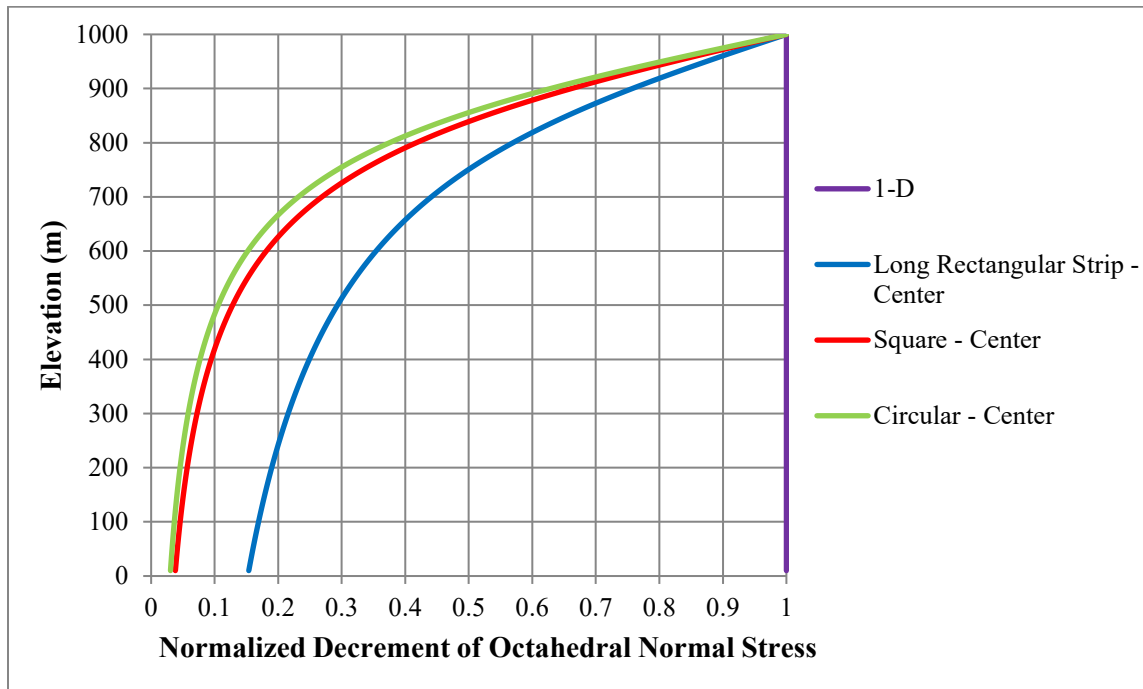


Figure 4.1: Analysis 1.1. Normalized decrements of octahedral normal stress at the center of the excavations due to the lithostatic unloading.

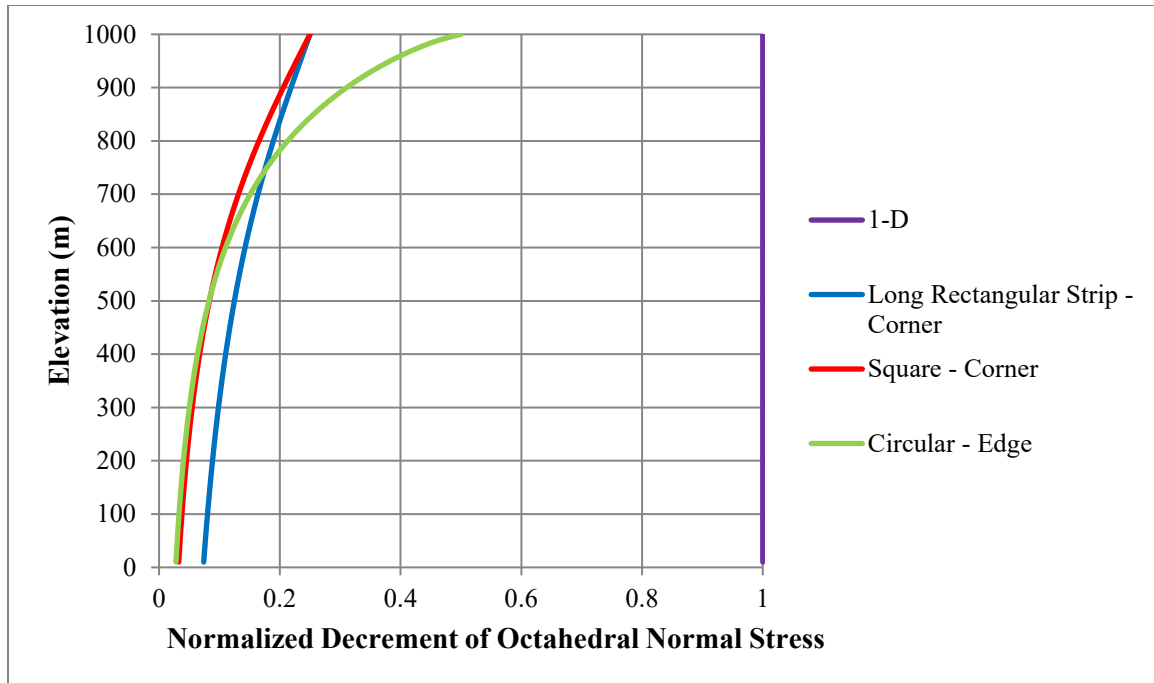


Figure 4.2: Analysis 1.1. Normalized decrements of octahedral normal stress at the corner of the excavations due to the lithostatic unloading.

4.2 Results from the 1-D Confined Flow Analyses

The results from the 1-D finite element analyses are shown in various contour cross sections and graphs. The set of parameter values used in the first analysis (Analysis 2.1) is given in Table 4.2. Analysis 2.1 modeled the lithostatic unloading of 100 meters of geologic material, and the effects this unloading had on pore water pressures and total head in the form of contour cross sections.

Parameter	E (kPa)	ν	m_v (1/kPa)	k (m/s)	c_v (m ² /s)	γ_w (kN/m ³)	γ_s (kN/m ³)	Load Response Ratio
Value	10^6	1/3	10^{-6}	10^{-8}	10^{-3}	10	20	1.0

Table 4.2: Table of the ranges of parameter values used in Analysis 2.1.

Given a geologic material with a unit weight of 20 kN/m³, the lithostatic unloading modeled in Analysis 2.1 resulted in a decrease in pore water pressures of 2,000 kPa throughout the profile, from the initial conditions as shown in Figure 4.3. This

decrease in pore water pressures by 2,000 kPa is equivalent to the generation of an increment of 2,000 kPa excess negative pore water pressure.

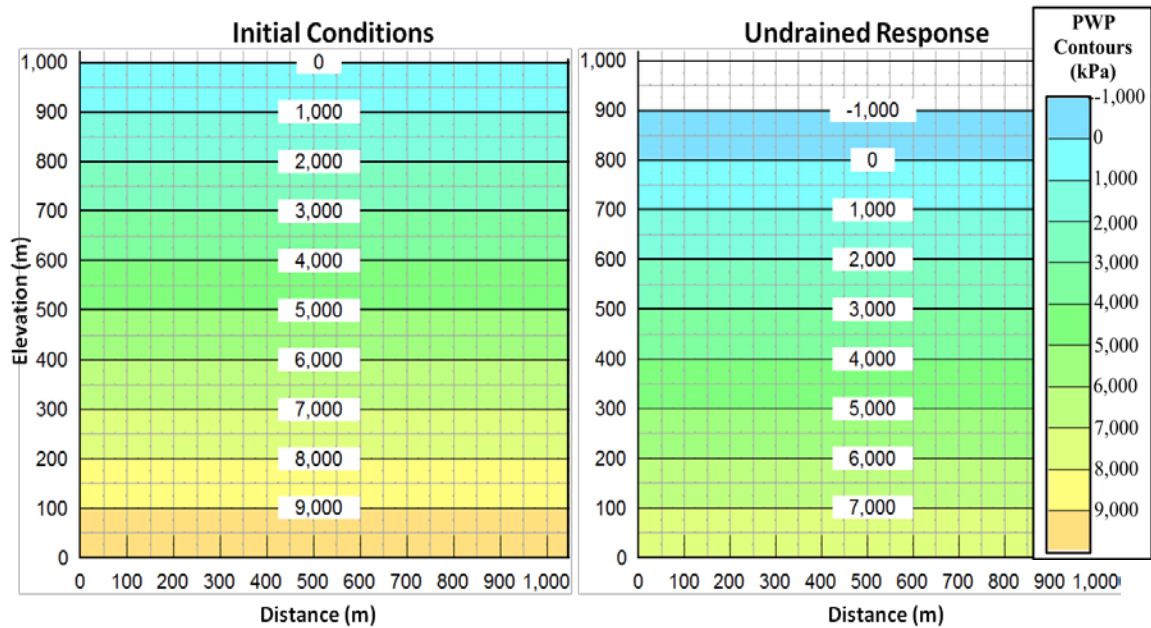


Figure 4.3: Analysis 2.1. Pore water pressure (PWP) contours for initial conditions and the undrained response.

During the transient response of Analysis 2.1 these excess negative pore water pressures dissipated and the pore water pressures increased to a new steady-state distribution. Figure 4.4 shows pore water pressures and hydraulic velocity vectors during the transient response at a time of 90 days after the excavation as they increase to the new steady-state distribution.

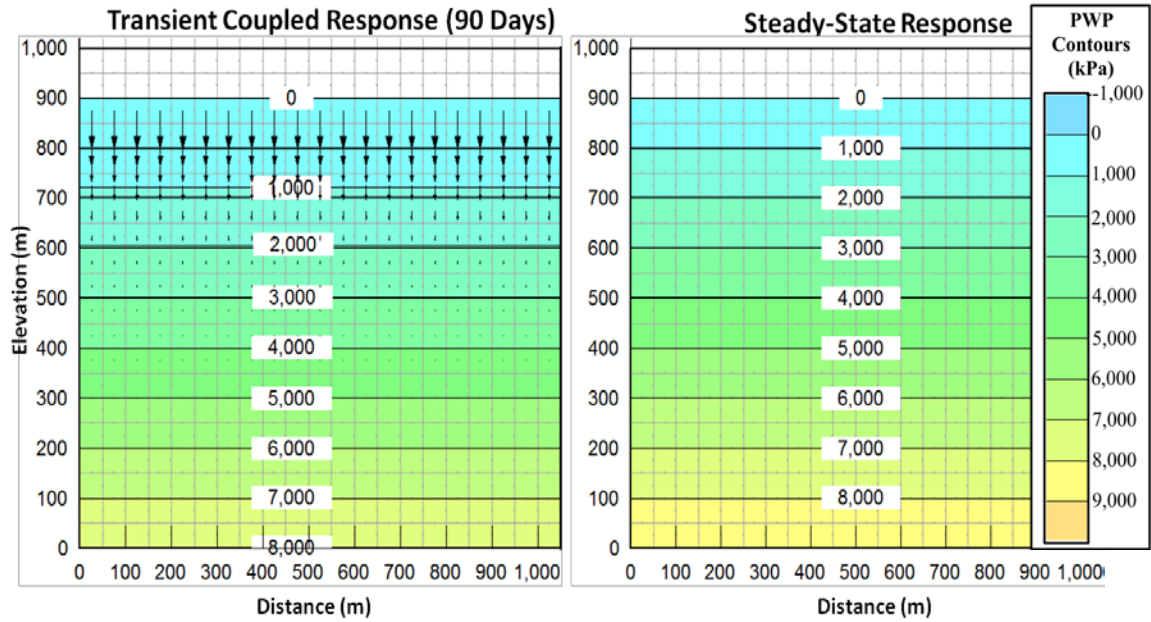


Figure 4.4: Analysis 2.1. Pore water pressure (PWP) contours and hydraulic velocity vectors for the transient response and the steady-state response.

In terms of total head during the undrained response, the lithostatic unloading causes the total head to drop by 200 meters from 1,000 meters as shown in Figure 4.5. The total head decreases by 200 meters throughout the entire profile so the entire profile has a total head distribution equal to 800 meters.

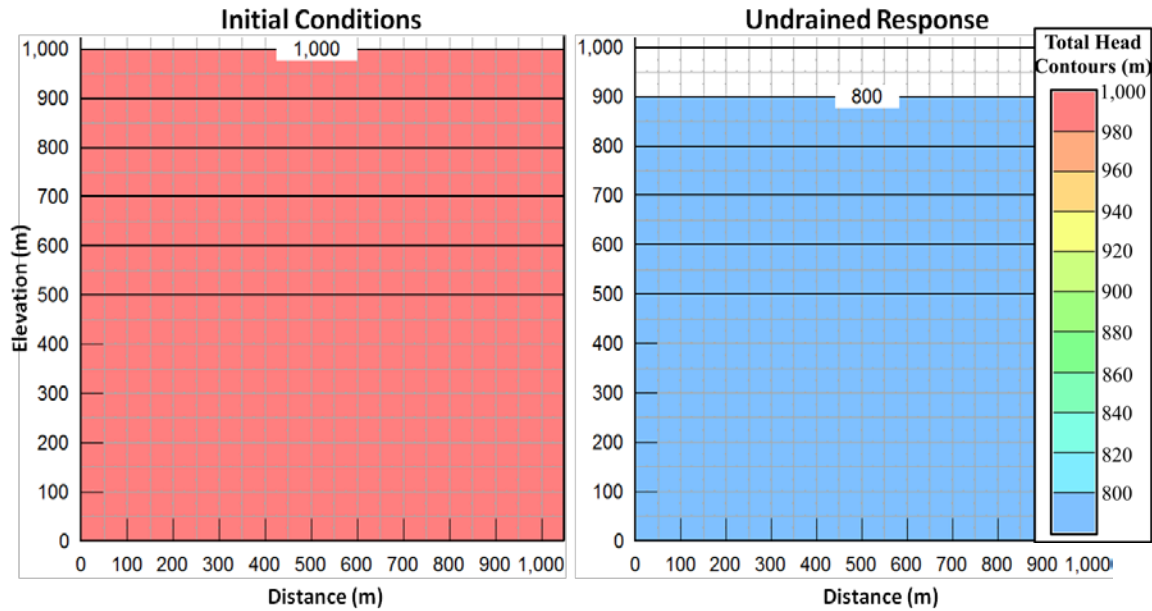


Figure 4.5: Analysis 2.1. Total head contours for initial conditions and the undrained response.

During the transient response, a gradient in total head appears as groundwater flows vertically downward from the ground surface which has a total head of 900 meters. As the profile for Analysis 2.1 has an impermeable bottom, groundwater is only flowing down from the top boundary of the profile. Figure 4.6 shows this total head distribution at a time of 90 days as it goes over time to a new steady-state distribution of a total head of 900 meters throughout the entire profile.

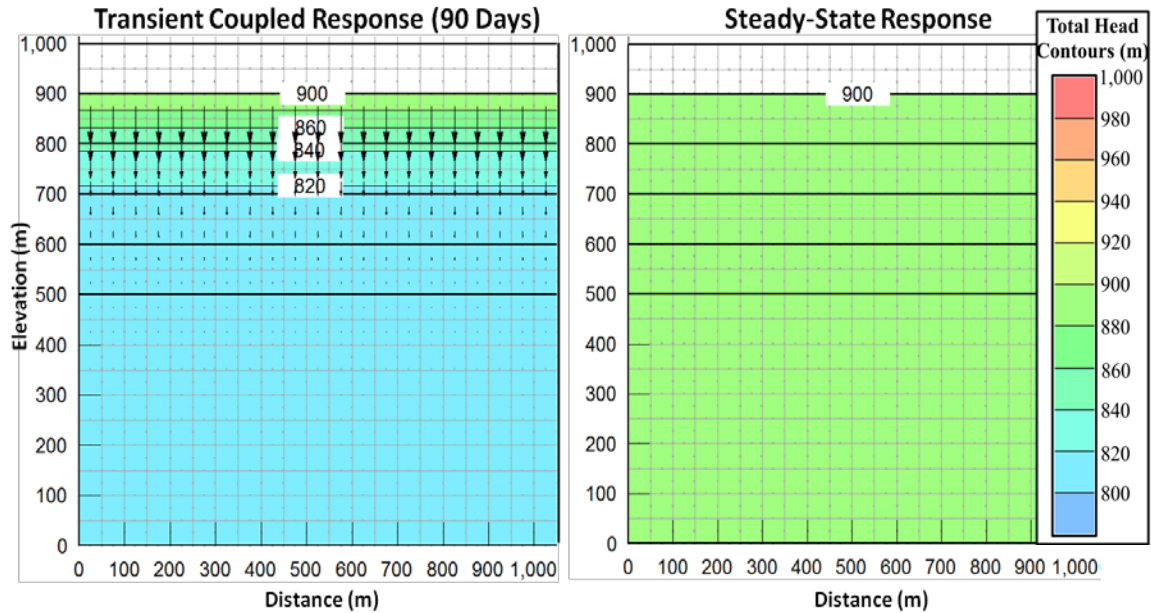


Figure 4.6: Analysis 2.1. Total head contours and hydraulic velocity vectors for the transient coupled response and the steady-state response.

The previous results from Analysis 2.1 show only a single excavation and pore water pressures that reach steady-state conditions. Results from Analysis 2.2, in the form of graphs, show how pore water pressures change after two excavations with a time interval of 360 days (approximately one year) between excavations. Table 4.3 gives the parameter values that were used for Analysis 2.2.

Parameter	E (kPa)	ν	m_v (1/kPa)	k (m/s)	c_v (m ² /s)	γ_w (kN/m ³)	γ_s (kN/m ³)	Load Response Ratio
Value	10^6	1/3	10^{-6}	10^{-7} - 10^{-9}	10^{-2} - 10^{-4}	10	20	1.0

Table 4.3: Table of the parameter values used in Analysis 2.2.

Figures 4.7, 4.8 and 4.9 show the pore water pressure distribution increasing over time towards a new steady-state for the first excavation. These results show, however, that depending on the magnitude of the diffusion coefficient, the pore water pressures do not necessarily reach steady-state conditions before the next excavation occurs. The

lower the diffusion coefficient, the more slowly the pore water pressures distributions move toward steady-state conditions.

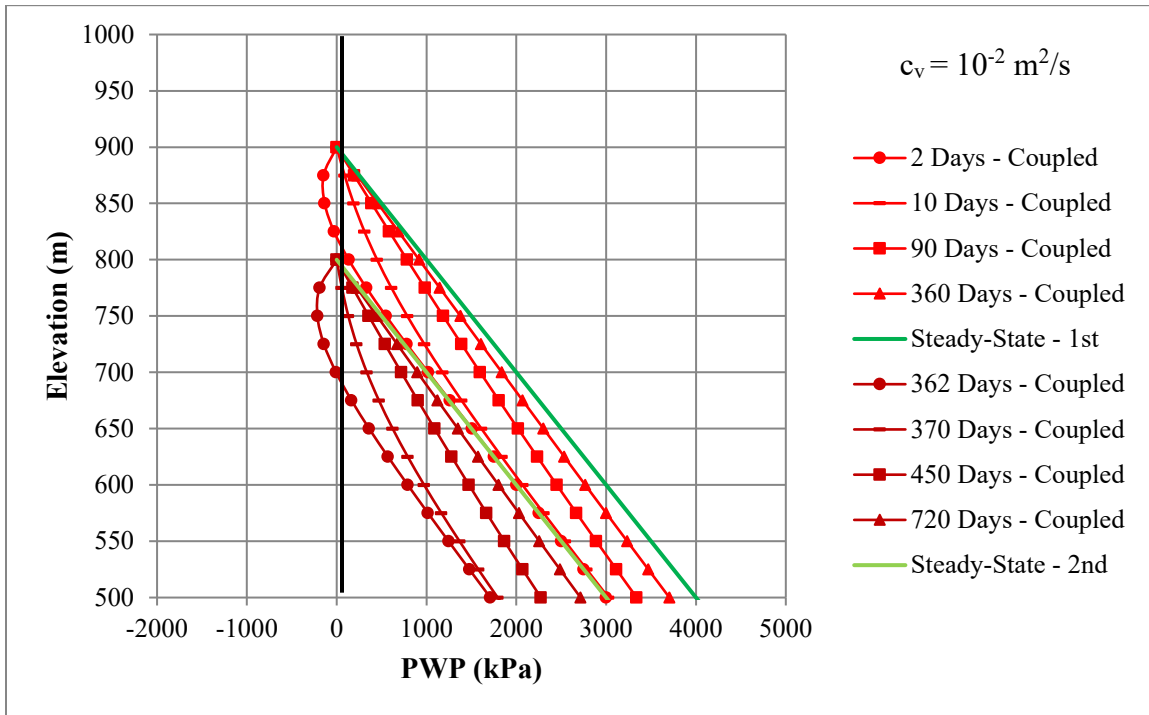


Figure 4.7: Analysis 2.2. Pore water pressure (PWP) distributions for two excavations.

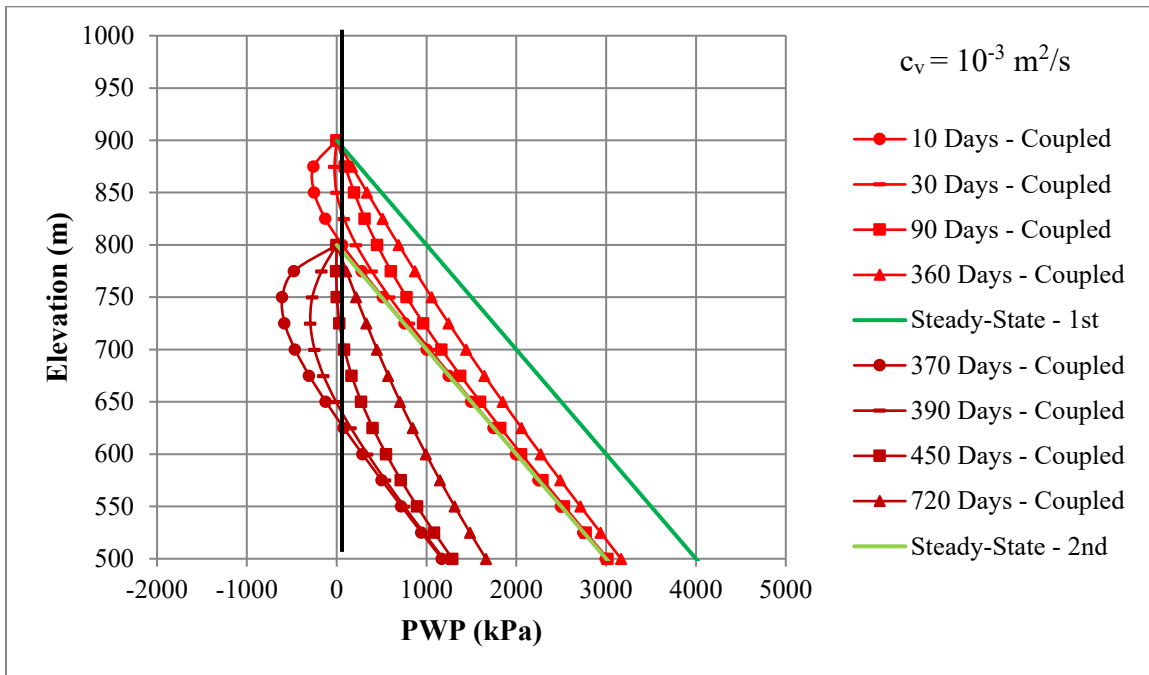


Figure 4.8: Analysis 2.2. Pore water pressure (PWP) distributions for two excavations and a lower diffusion coefficient.

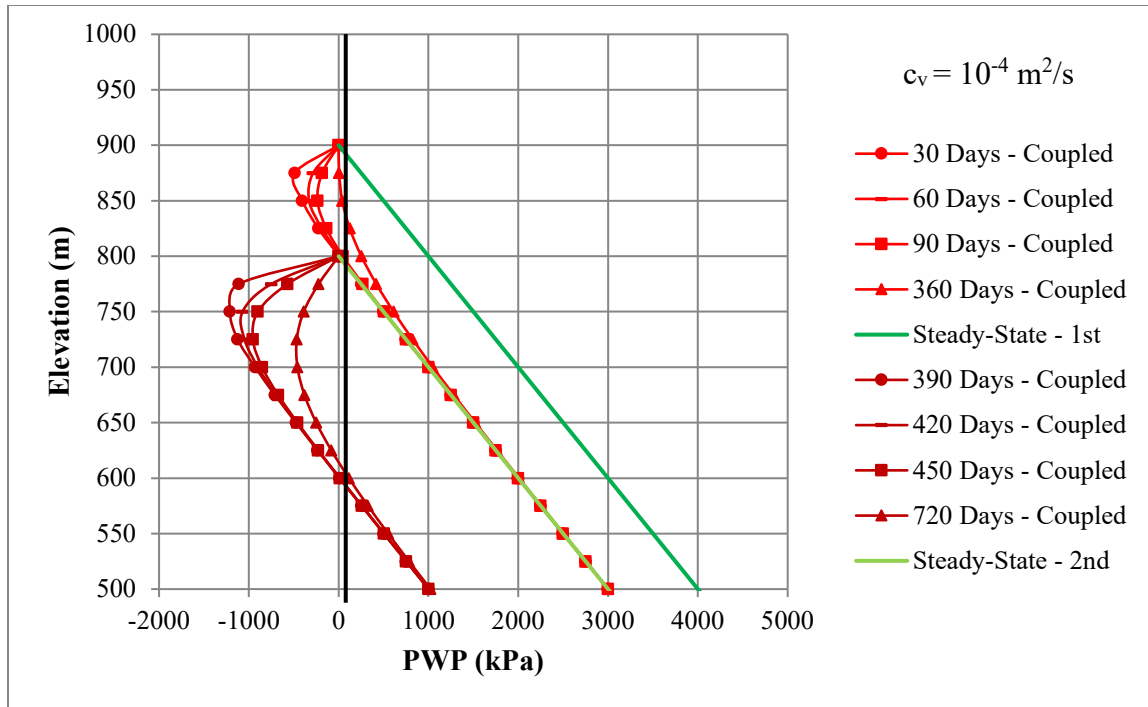


Figure 4.9: Analysis 2.2. Pore water pressure (PWP) distributions for two excavations and a low diffusion coefficient.

Additional pore water pressure and total head results from the 1-D confined flow rectangular-strip excavation analyses are included in Appendix A for reference. The additional results include a full sequence of pore water pressure and total head contour charts for the three different diffusion coefficients (10^{-2} , 10^{-3} , and 10^{-4} m²/s) and graphs of total head for two excavations for each of the diffusion coefficients.

4.3 Results from the 2-D Confined Flow Rectangular-Strip Excavation Analyses

The results from the 2-D rectangular-strip excavation analyses provide insights into the interaction between the transient seepage response and the transient coupled response. These analyses model 2-D confined flow. Here, the groundwater flow is driven both by the change in total head due to the excavation and by the hydromechanical effects of the lithostatic unloading. The set of parameter values used in the following

analysis, Analysis 3.1, which show pore water pressures and total heads in the form of contour charts, is displayed in Table 4.4.

Parameter	E (kPa)	ν	m_v (1/kPa)	k (m/s)	c_v (m ² /s)	γ_w (kN/m ³)	γ_s (kN/m ³)	Load Response Ratio
Value	10 ⁶	1/3	10 ⁻⁶	10 ⁻⁸	10 ⁻³	10	20	1.0

Table 4.4: Table of the parameter values used in Analysis 3.1.

The undrained response to the lithostatic unloading and its effect on the initial pore water pressure distribution is shown in Figure 4.10. The pore water pressures decrease the most below the center of the excavation and the least outside of the excavation, and the decrease is less the greater the depth below the excavation.

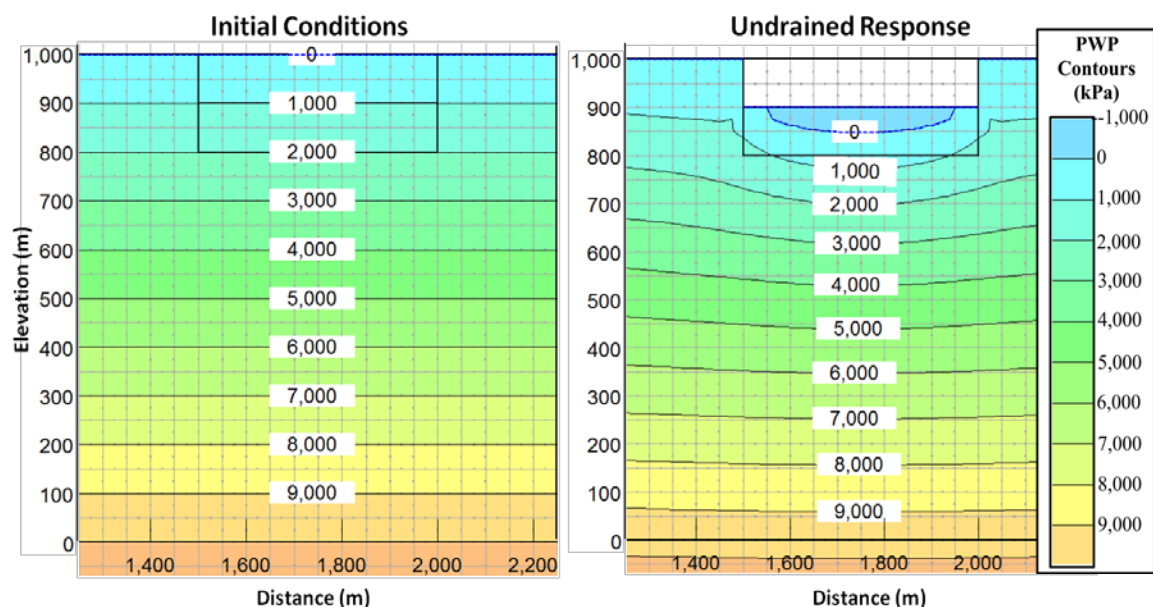


Figure 4.10: Analysis 3.1. Pore water pressure (PWP) contours for initial conditions and the undrained response.

Figure 4.11 displays the transient coupled response and the steady-state response. During the transient coupled response the negative excess pore water pressures generated during the undrained response dissipate resulting in an increase of pore water pressures over time to a new steady-state. The hydraulic velocity vectors indicate a groundwater

stagnation zone developing about 50 meters below the excavation, during the transient coupled response. The groundwater stagnation zone then disappears as the pore water pressures increase to a new steady-state distribution.

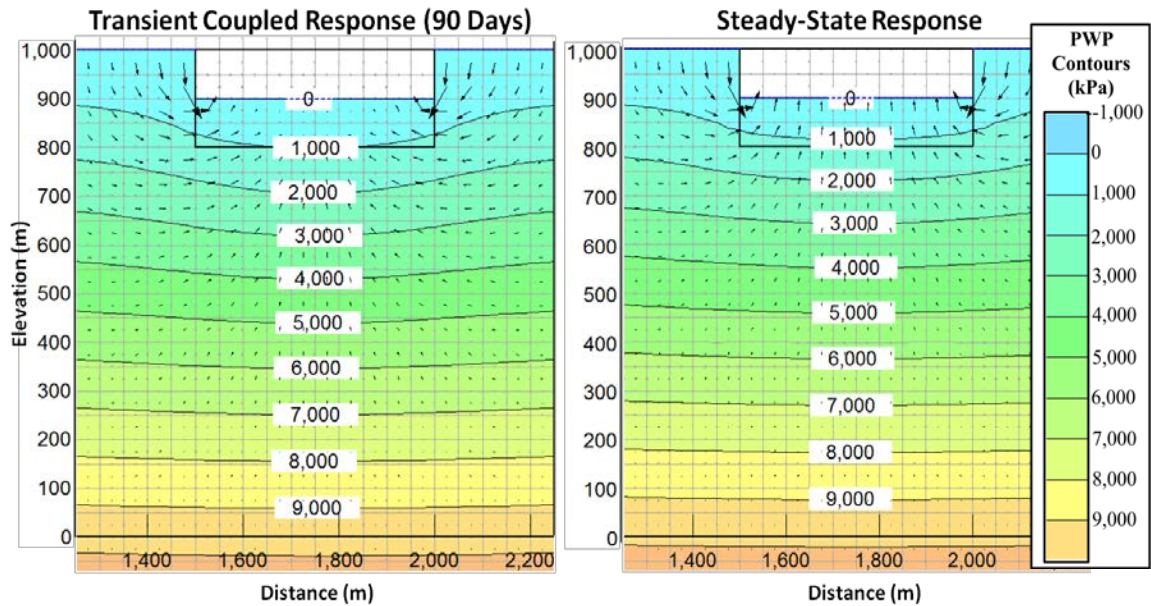


Figure 4.11: Analysis 3.1. Pore water pressure (PWP) contours and hydraulic velocity vectors (black arrows) for the transient coupled response and the steady-state response.

The initial conditions, in terms of total head, are the same everywhere in the profile, so, initially, there is no flow within the profile. The undrained response results in an instantaneous decrease in total head as shown in Figure 4.12.

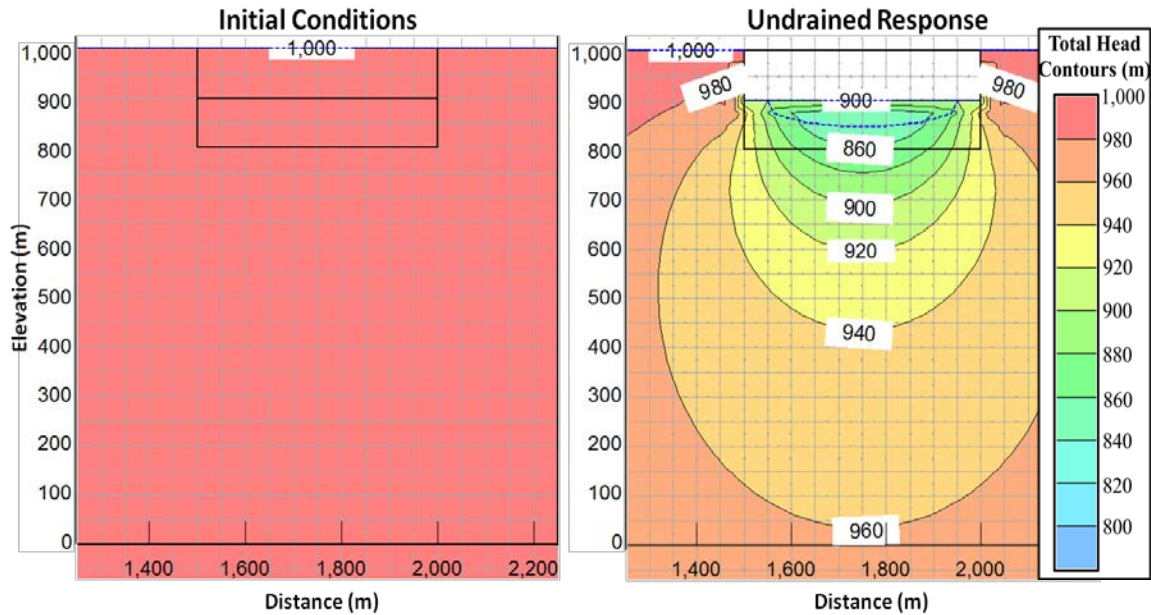


Figure 4.12: Analysis 3.1. Total head contours for the initial conditions and the undrained response.

As the transient response begins, the total head increases over time to a new steady-state as seen in Figure 4.13. The hydraulic velocity vectors in Figure 4.13 show that during the transient response, from around 0 to 150 meters depth below the center of the excavation (elevations 900 to 750 meters), a groundwater stagnation zone develops as flow comes downward from the pit floor and upward flow comes from the sides of the mine. The steady-state results indicate that this groundwater stagnation zone disappears during the transient response. Figure 4.14, a comparison of the transient seepage response and the transient coupled response at a time of 90 days, shows that the total head for the transient seepage analysis is higher than the total head for the transient coupled response. Figure 4.14 also displays that there is no groundwater stagnation zone for the transient seepage response results.

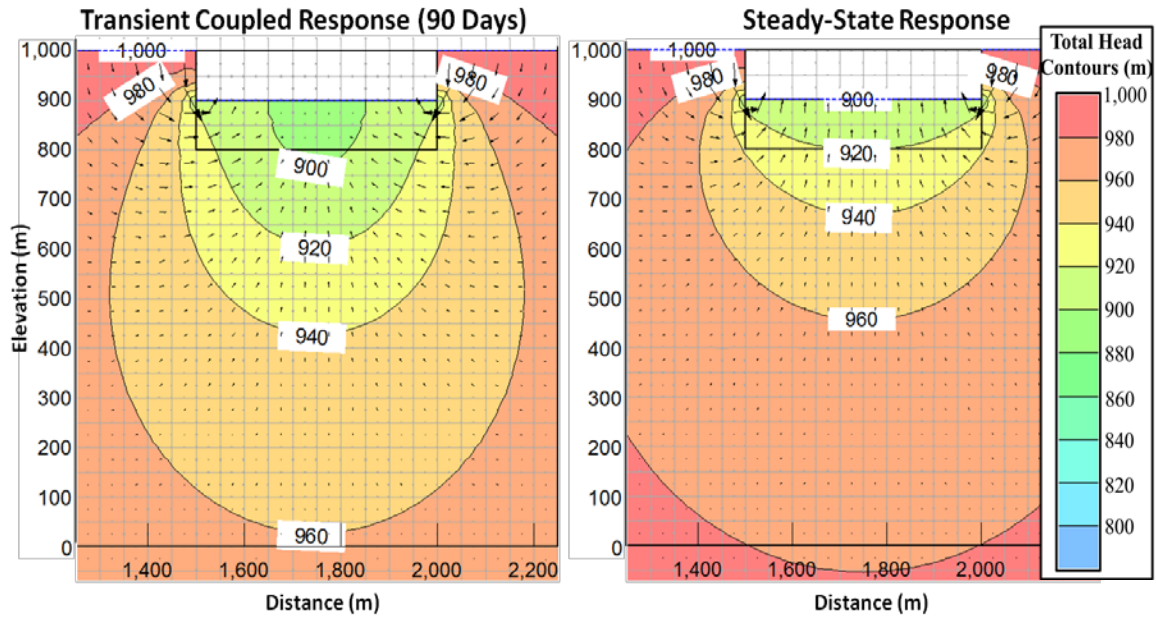


Figure 4.13: Analysis 3.1. Total head contours and hydraulic velocity vectors for the transient coupled response and the steady-state response.

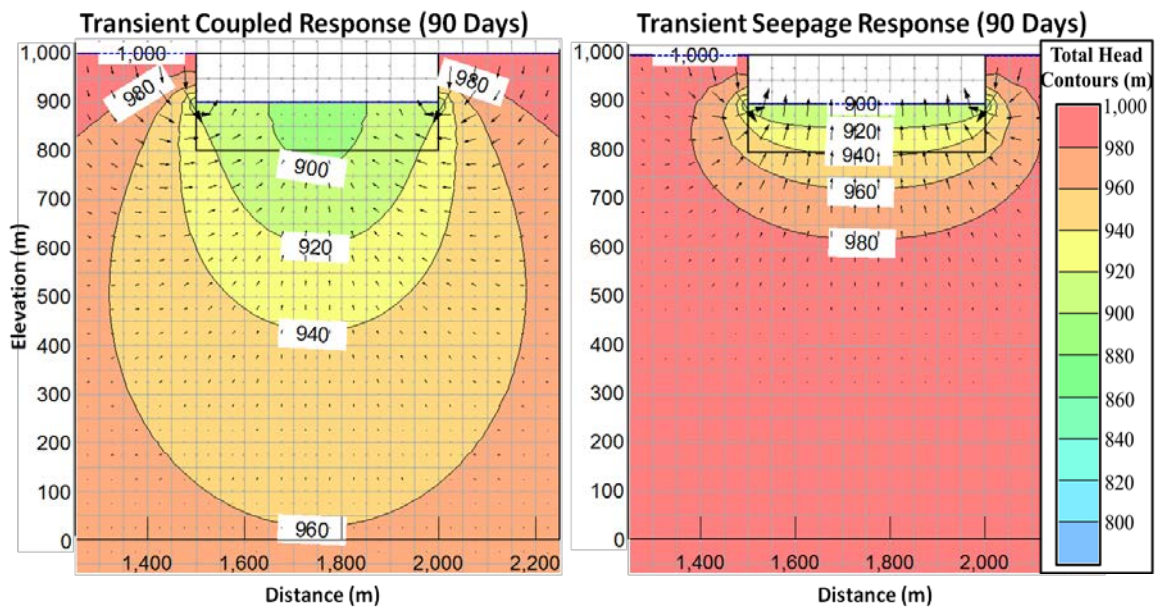


Figure 4.14: Analysis 3.1. Total head contours and hydraulic velocity vectors for the transient coupled response as compared to the transient seepage response.

Results from Analysis 3.1 show the effects of a single excavation in terms of contours, and the results from the next analysis, Analysis 3.2, show the effects of a single

excavation of materials with different diffusion coefficients in terms of graphs. The set of parameter values used in this particular analysis, Analysis 3.2, is given in Table 4.5.

Parameter	E (kPa)	ν	m_v (1/kPa)	k (m/s)	c_v (m ² /s)	γ_w (kN/m ³)	γ_s (kN/m ³)	Load Response Ratio
Value	10^6	1/3	10^{-6}	10^{-7} - 10^{-9}	10^{-2} - 10^{-4}	10	20	1.0

Table 4.5: Parameters for Analysis 3.2.

Figures 4.15, 4.16, and 4.17, display the pore water pressure distributions of the transient coupled response, the transient seepage response, and the steady-state response for a material with diffusion coefficients of 10^{-2} m²/s, 10^{-3} m²/s and 10^{-4} m²/s, respectively. Only the top 500 meters of the profile are shown.

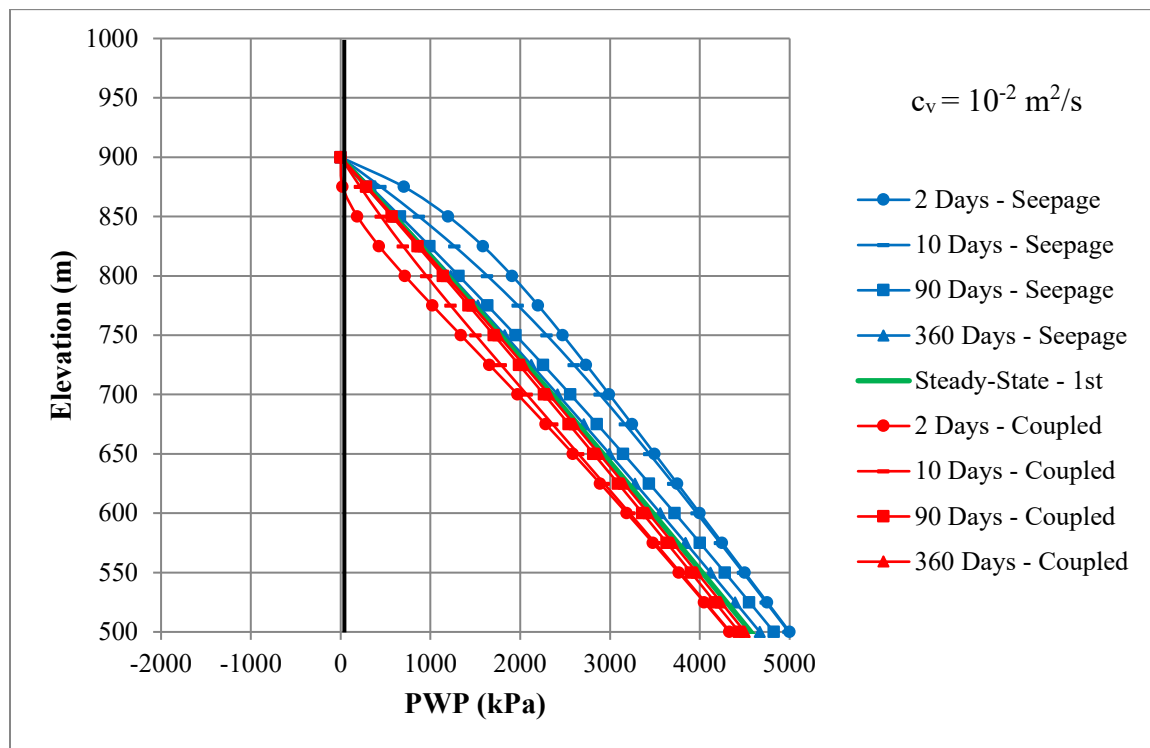


Figure 4.15: Analysis 3.2. Pore water pressure (PWP) distributions for both the transient seepage and transient coupled response for one excavation.

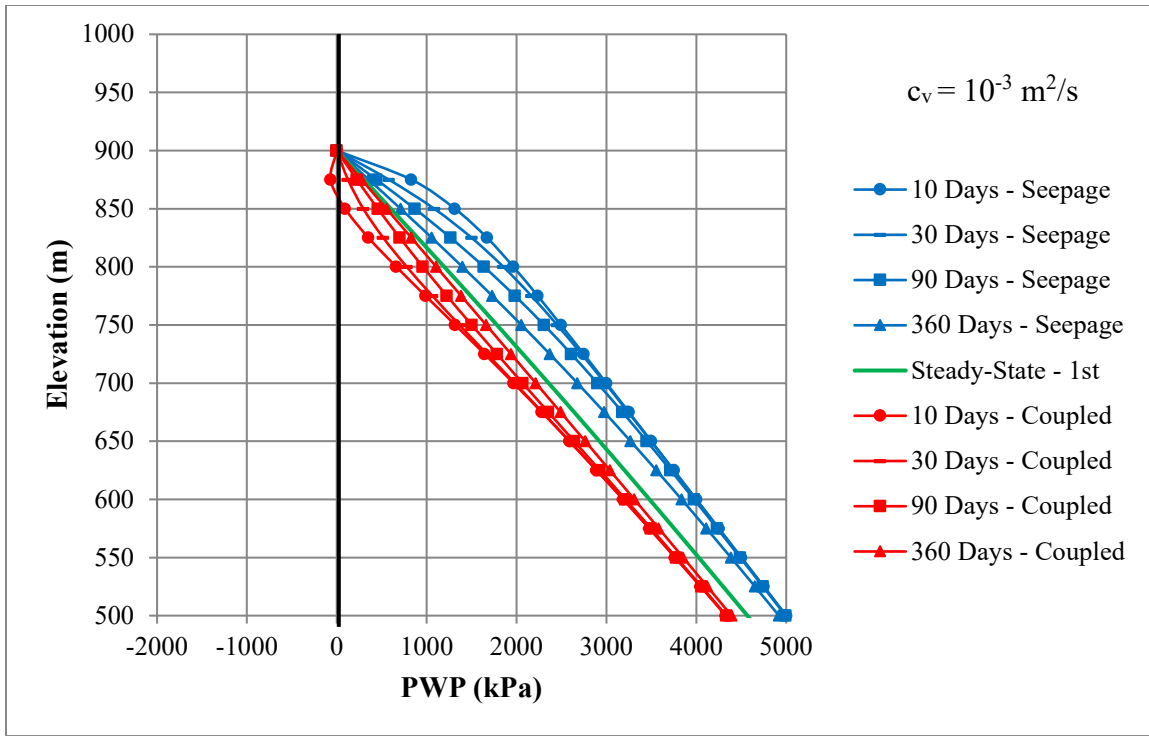


Figure 4.16: Analysis 3.2. Pore water pressure (PWP) distributions for both the transient seepage and transient coupled response for one excavation and a lower diffusion coefficient.

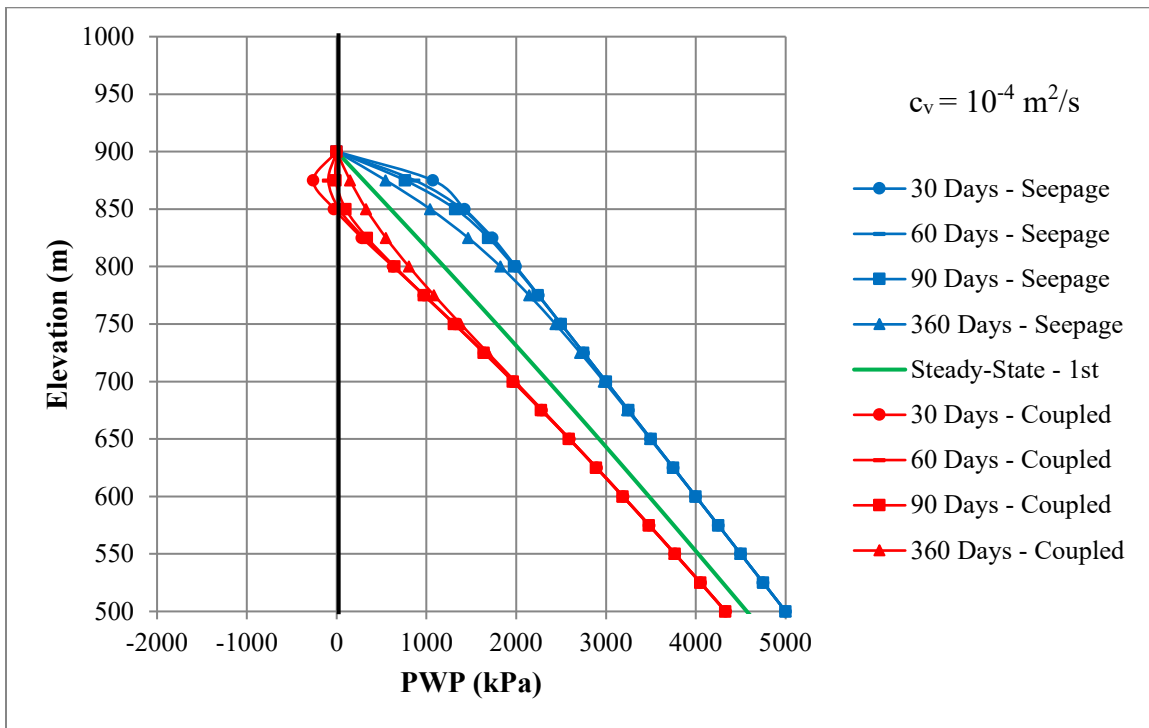


Figure 4.17: Analysis 3.2. Pore water pressure (PWP) distributions for both the transient seepage and transient coupled response for one excavation and a low diffusion coefficient.

The distributions of total head for the transient seepage, the transient coupled, and the steady-state analyses are shown in Figures 4.18, 4.19, and 4.20. These results show that the difference between the total heads of the transient seepage response and the total heads of the transient coupled response becomes larger as the diffusion coefficient decreases in magnitude. The total heads of the transient seepage response are always higher than the total heads of the transient coupled response for any given time or depth.

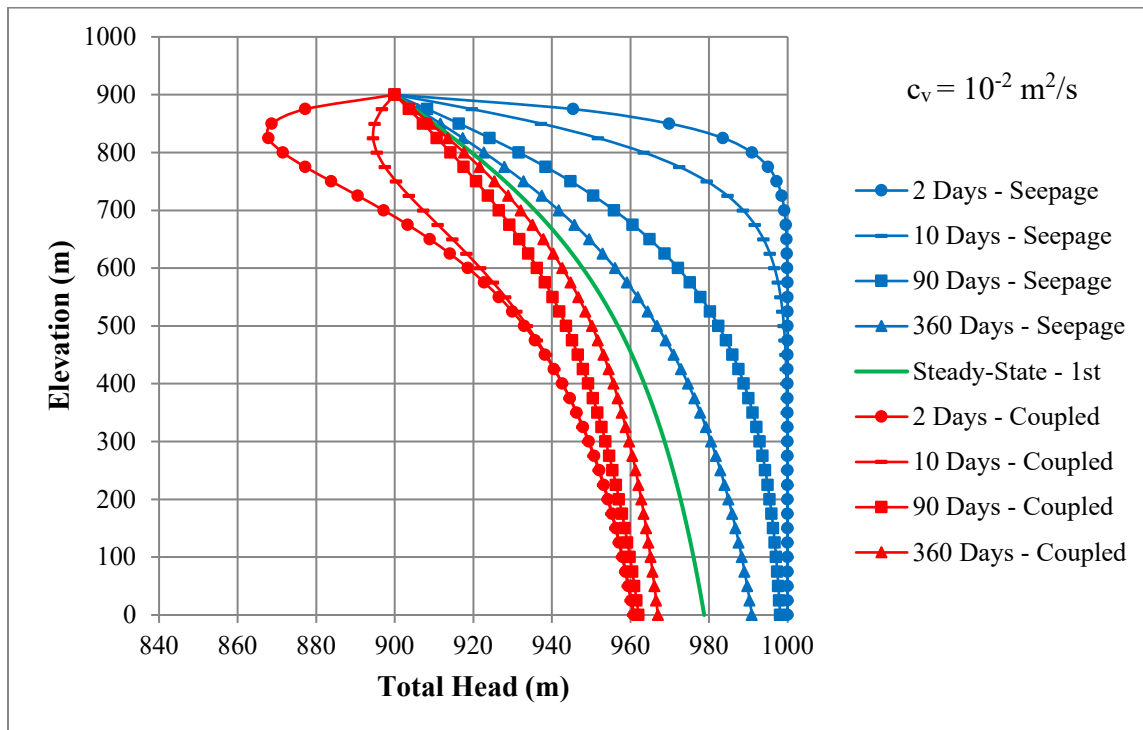


Figure 4.18: Analysis 3.2. Total head distributions for the transient seepage and transient coupled response for one excavation.

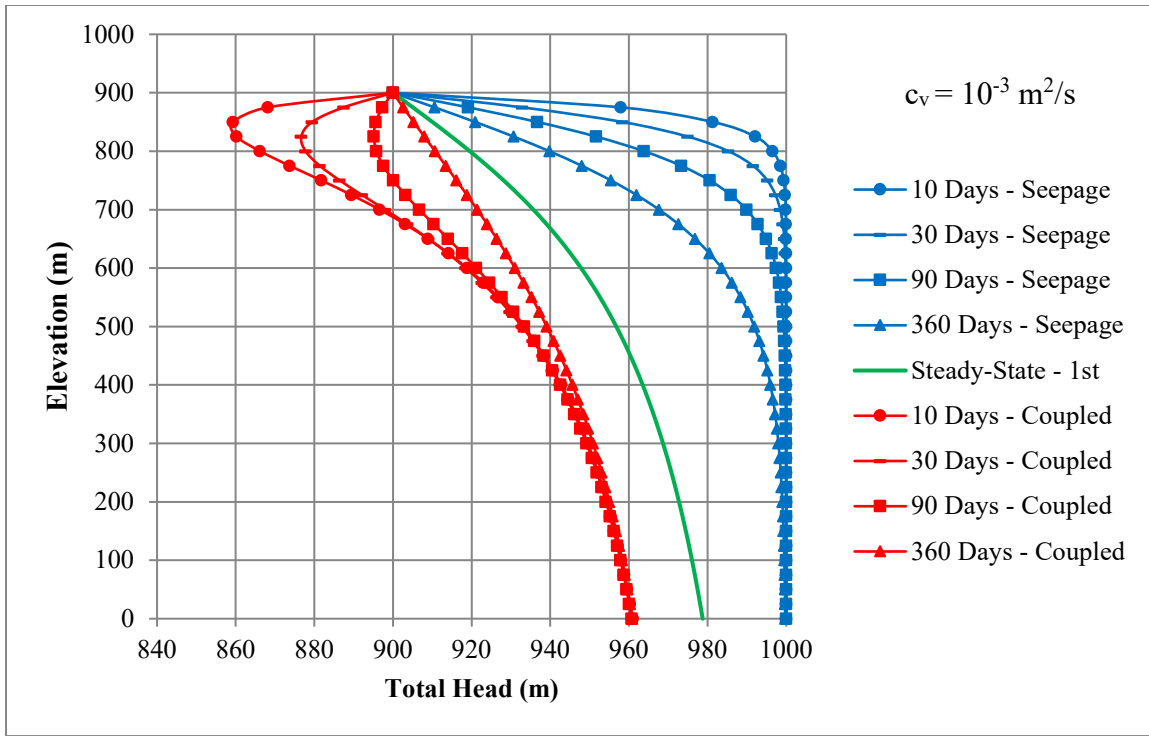


Figure 4.19: Analysis 3.2. Total head distributions for the transient seepage and transient coupled response for one excavation and a lower diffusion coefficient.

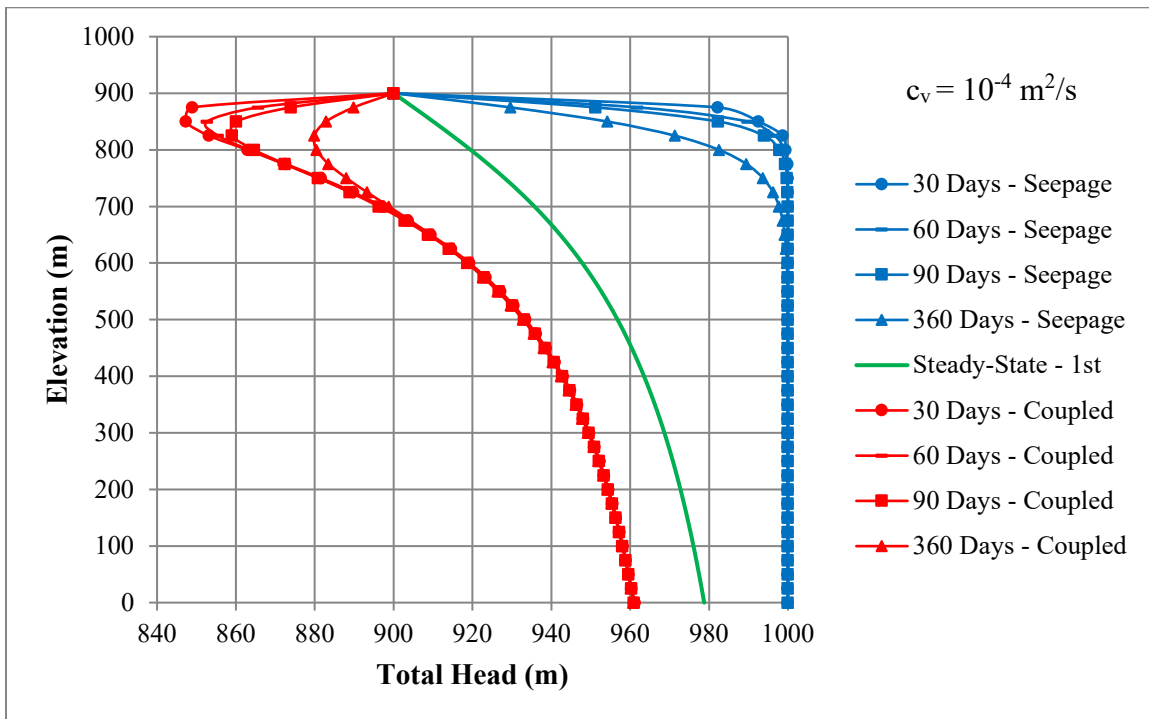


Figure 4.20: Analysis 3.2. Total head distributions for the transient seepage and transient coupled responses for one excavation and a low diffusion coefficient.

As total heads change, the hydraulic gradients change as well. The results in figures 4.21, 4.22, and 4.23 show that, generally, the hydraulic gradients decrease in the top 50 meters of the profile below the excavation and at depths below 50 meters, the hydraulic gradients increase slightly. Comparing the transient seepage response results to the transient coupled response results indicates that for a time period ranging from a few weeks to a few months, depending upon the diffusion coefficient, the hydraulic gradients for the coupled response are negative, indicating that water is flowing in a downward direction from the pit bottom. After this period, the hydraulic gradients for the transient coupled response become positive again, indicating upward flow from the sides of the mine. These results also show that with a lower diffusion coefficient the gradients are higher for longer periods of time. In addition, the results indicate that below a depth of 100 meters, the hydraulic gradients do not change much at all.

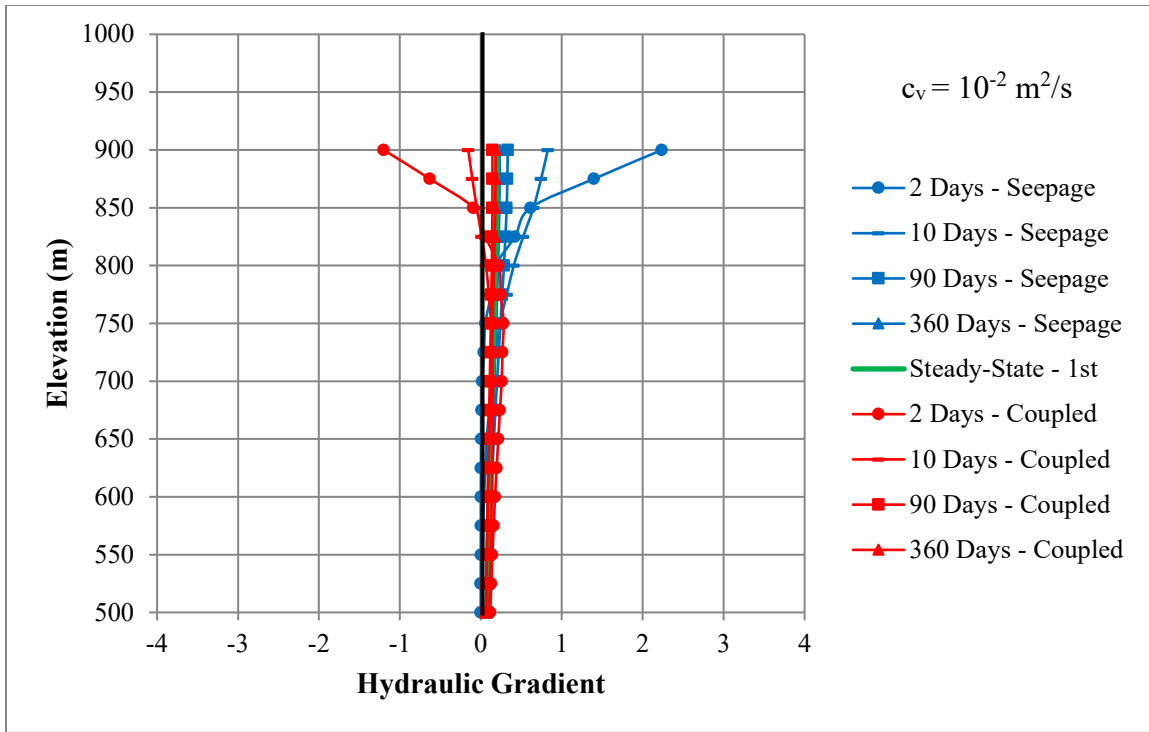


Figure 4.21: Analysis 3.2. Hydraulic gradients for the transient seepage and transient coupled response for one excavation.

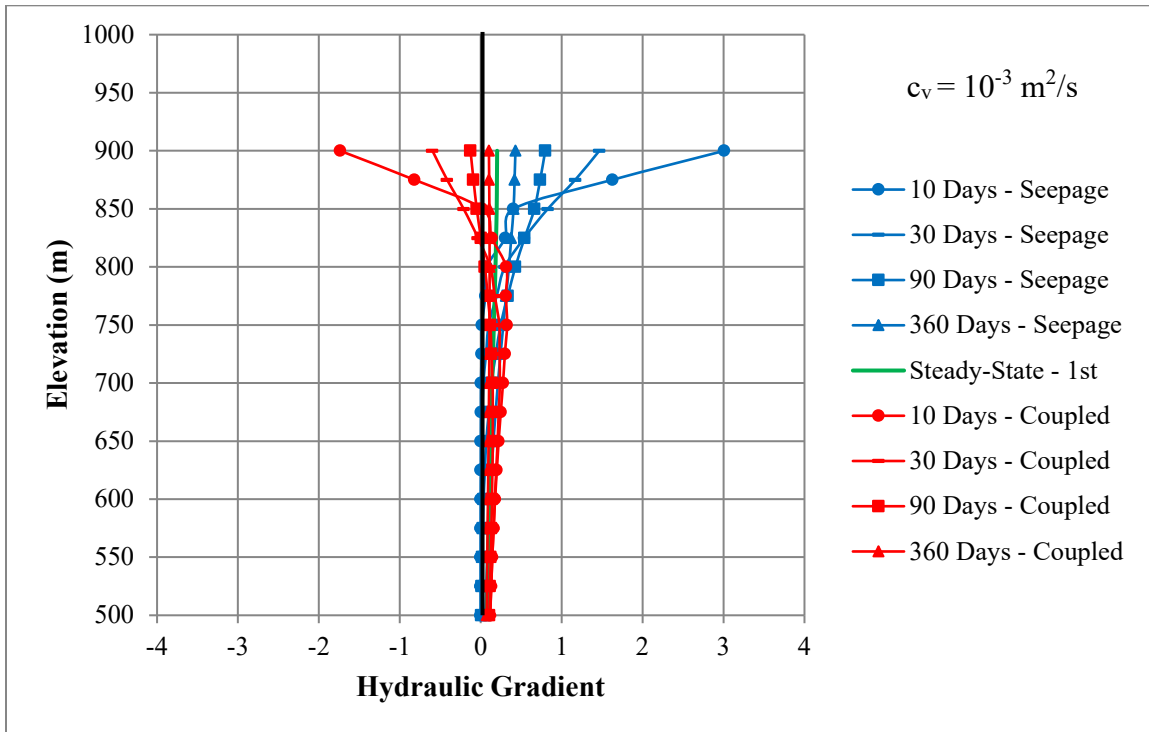


Figure 4.22: Analysis 3.2. Hydraulic gradients for the transient seepage and transient coupled response for one excavation and a material with a lower diffusion coefficient.

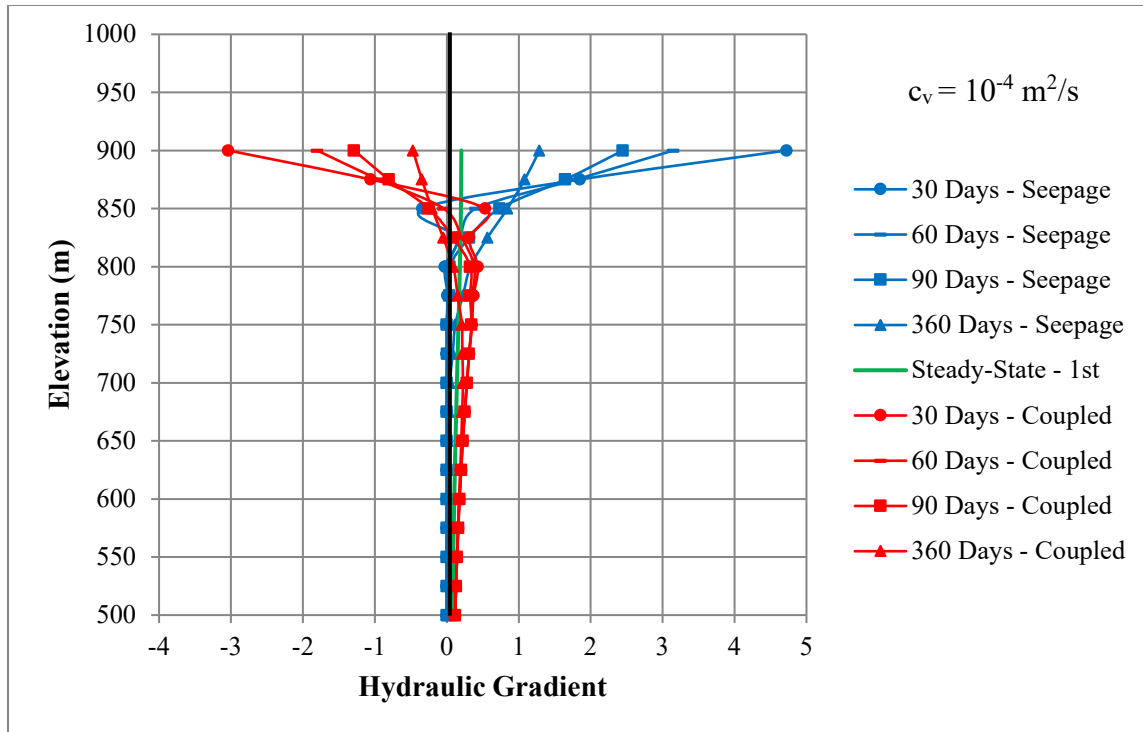


Figure 4.23: Analysis 3.2. Hydraulic gradients for the transient seepage and transient coupled response for one excavation and a material with a low diffusion coefficient.

The change in pore water pressures, total heads, and hydraulic gradients due to the lithostatic unloading also cause a change in the amount of groundwater discharging into the pit. Figure 4.24 depicts the discharge results for both a transient seepage analysis and a transient coupled analysis for two different diffusion coefficients. It is evident from the transient coupled results that groundwater discharge is flowing from the surface of the bottom of the excavation into the geologic material for a period of about 90 days. The transient seepage results show that a large amount of groundwater discharges into the pit and this discharge rate rapidly falls off to a lower level after 90 days. The discharge values are higher for the material with a lower diffusion coefficient.

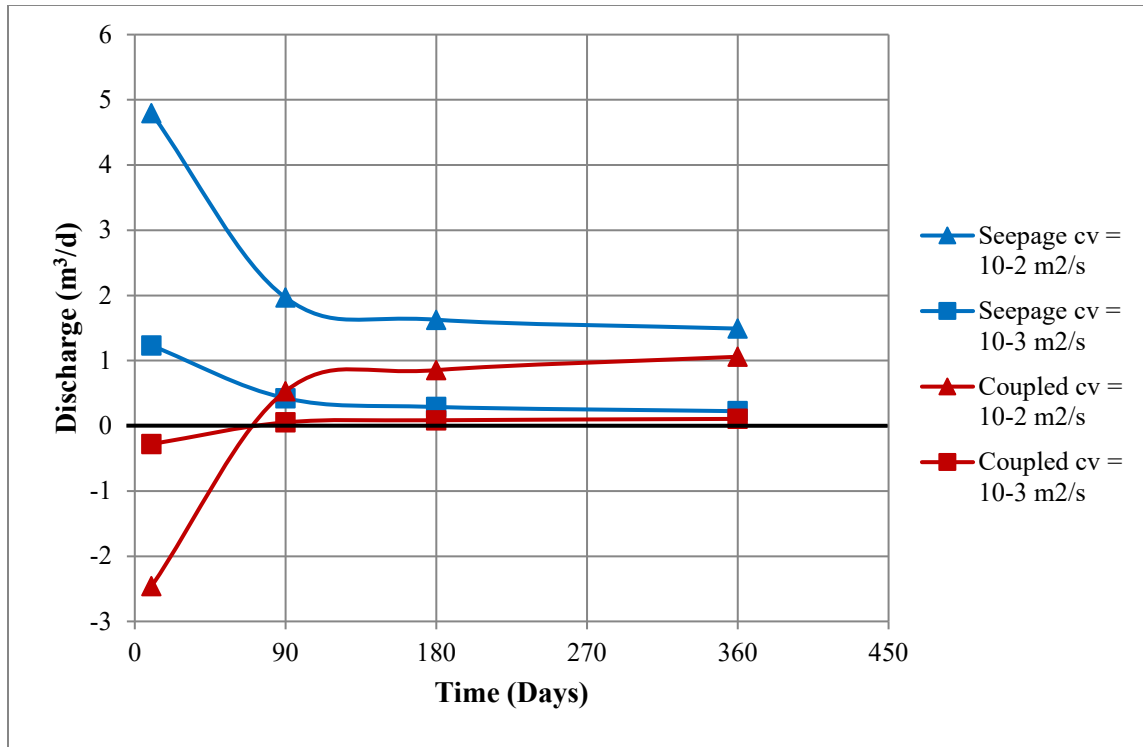


Figure 4.24: Analysis 3.2. Groundwater discharge over time, along the 500 meter long surface of the pit bottom. Positive discharge indicates groundwater flow into the pit. Negative discharge indicates groundwater flow into the material.

The previous analyses, Analysis 3.1 and Analysis 3.2, were performed with the assumption that the hydraulic conductivity, k , of the geologic material stays constant during swelling after the lithostatic unloading. Results from Analysis 3.3, where the hydraulic conductivity increases over time from $10^{-8} \text{ m}^2/\text{s}$ to $10^{-7} \text{ m}^2/\text{s}$ due to swelling, are presented here for comparison to the previous analyses. Table 4.6 shows the parameter values used for Analysis 3.3.

Parameter	E (kPa)	ν	m_v (1/kPa)	k (m/s)	c_v (m ² /s)	γ_w (kN/m ³)	γ_s (kN/m ³)	Load Response Ratio
Value	10^6	1/3	10^{-6}	10^{-7} - 10^{-8}	10^{-2} - 10^{-3}	10	20	1.0

Table 4.6: Parameter values for Analysis 3.3.

Figures 4.25 and 4.26 show the pore water pressures, and total heads, respectively, from Analysis 3.3. These results indicate that the increase in hydraulic

conductivity due to the swelling results in faster dissipation of excess negative pore water pressures than the for the other analyses with constant hydraulic conductivity. In addition, the increase in hydraulic conductivity results in both lower steady-state distributions of pore water pressures and total heads. It is clear from Figure 4.25 that while the total heads reach steady-state conditions within a year, the steady-state conditions for the material with a modified hydraulic conductivity is lower than the steady-state conditions for a material with a constant hydraulic conductivity.

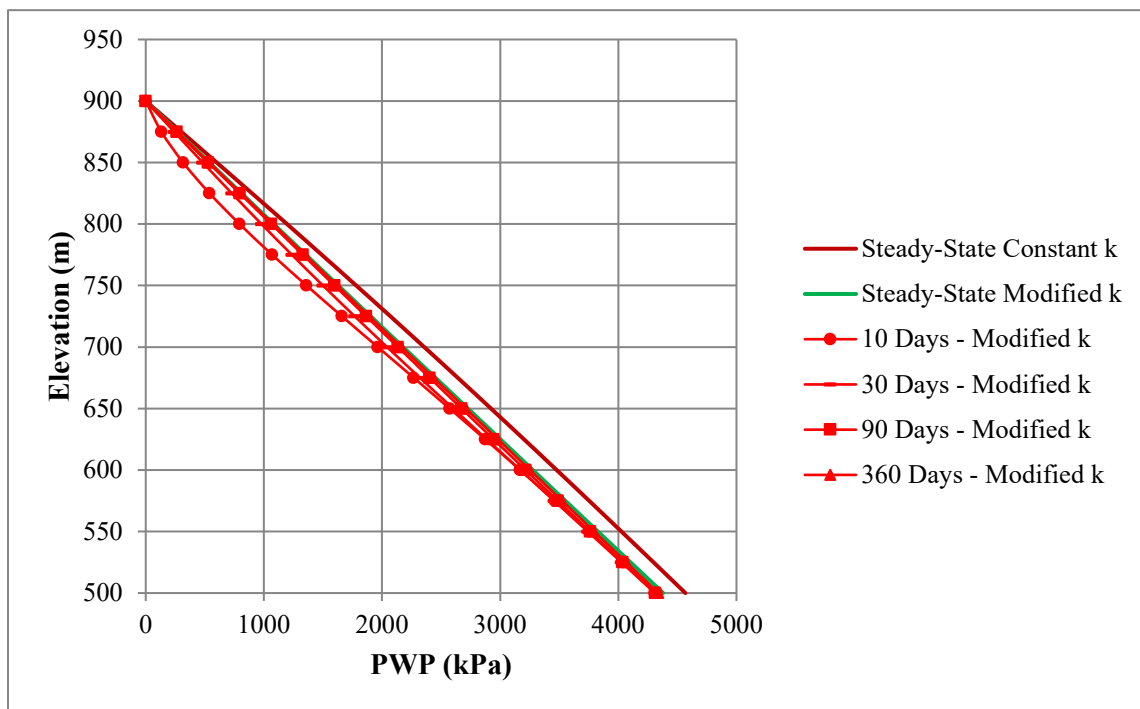


Figure 4.25: Analysis 3.3. Pore water pressures (PWP) for the steady-state response of an analysis with a constant k of 10^{-8} m/s, and PWP's for the transient coupled and steady-state response of an analysis with a modified k that increases by a factor of 10 from 10^{-8} m/s to 10^{-7} m/s.

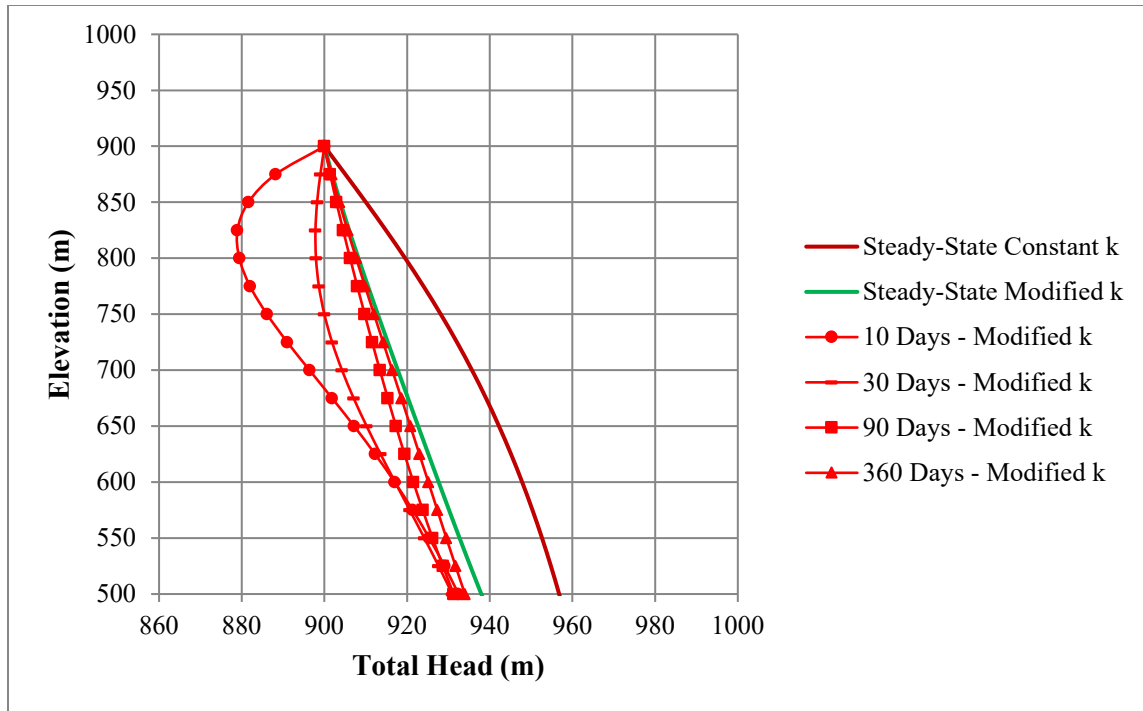


Figure 4.26: Analysis 3.3. Total head for the steady-state response of an analysis with a constant k of 10^{-8} m^2/s , and for the transient coupled and steady-state response of an analysis with a modified k that increases by a factor of 10 from 10^{-8} m^2/s to 10^{-7} m^2/s .

Additional pore water pressure, total head, and hydraulic gradient results from the 2-D confined flow rectangular excavation analyses are included in Appendix B for reference. The additional results include full sequences of pore water pressures and total head contour charts for three different diffusion coefficients (10^{-2} , 10^{-3} , and 10^{-4} m^2/s) and graphs depicting the results of a 2nd excavation.

4.4 Results from the 2-D Unconfined Trapezoid-Shaped Excavation Analyses

The 2-D unconfined trapezoid-shaped excavation analyses are the analyses that most closely represent the geometry of an actual open-pit mine, and model unconfined groundwater flow. The pore water pressure, total head, hydraulic gradient and discharge results of these analyses are shown in a series of contour cross sections and graphs. In addition to these analyses, a series of total and effective stress path analyses were

performed in order to determine the stability of the mine slope during the lithostatic unloading process. The set of parameter values used in the first analysis (Analysis 4.1), which shows the pore water pressure and total head contour results, is shown in Table 4.7. The contour cross section results are organized in terms of the undrained response, the transient coupled response, the transient seepage response, and the steady-state response. The hydromechanical effect of the undrained response on pore water pressure contours is shown in Figure 4.27.

Parameter	E (kPa)	ν	m_v (1/kPa)	k (m/s)	c_v (m ² /s)	γ_w (kN/m ³)	γ_s (kN/m ³)	Load Response Ratio
Value	10 ⁶	1/3	10 ⁻⁶	10 ⁻⁸	10 ⁻³	10	20	1.0

Table 4.7: Table of the ranges of parameter values used in Analysis 4.1.

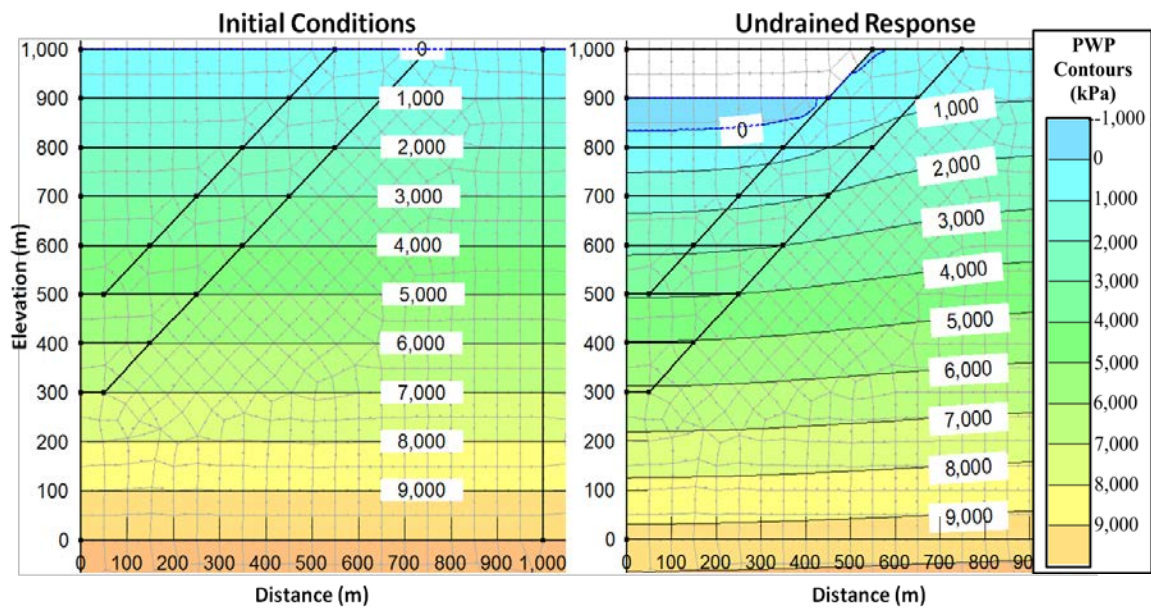


Figure 4.27: Analysis 4.1. Pore water pressure (PWP) contours for initial conditions and undrained response.

Figure 4.27 shows that the decrease in pore water pressures is greatest at the center of the excavation and the least on the outside of the excavation. During the

transient response the excess negative pore water pressures dissipate and so the pore water pressures increase over time to a new steady-state as shown in Figure 4.28.

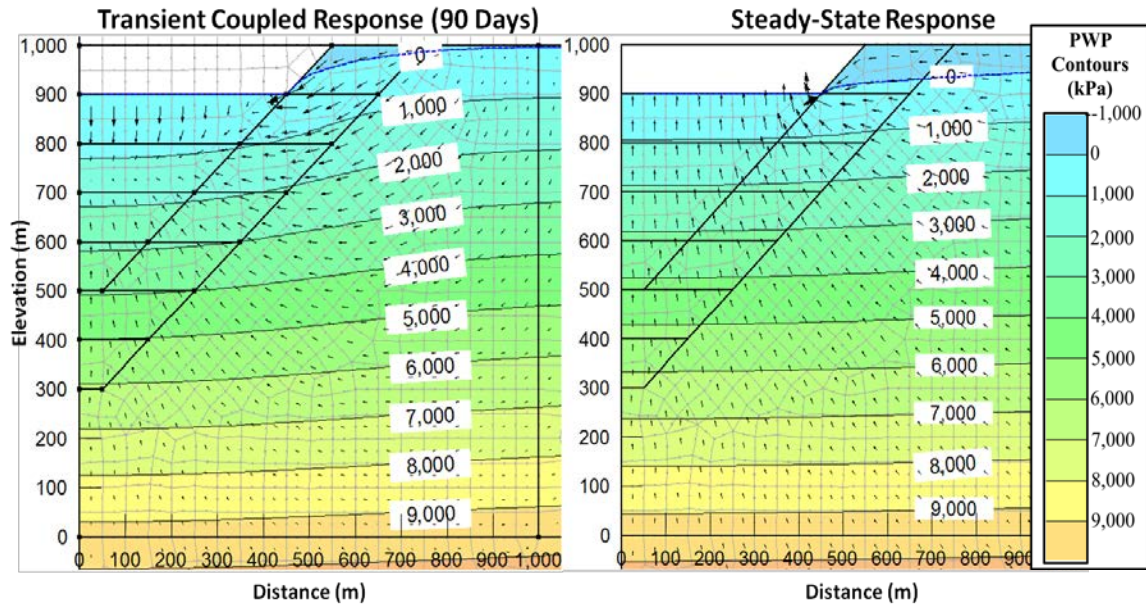


Figure 4.28: Analysis 4.1. Pore water pressure (PWP) contours and hydraulic velocity vectors for the transient and steady-state responses.

Initially, the total head within the entire profile is constant at 1,000 meters so there is no flow of water. The undrained response results in the generation of lower total head, and an increase in the hydraulic gradient, as shown in Figure 4.29. Figure 4.30 shows that during the transient coupled response the total head increases throughout the domain due to groundwater inflow as indicated by the hydraulic velocity vectors and increases to a new steady-state. Note the groundwater stagnation zone that develops under the excavation at about 100 to 150 meters depth during the transient response. It disappears over time as the excess negative pore water pressures dissipate and total head increases to a new steady-state. Figure 4.31 shows the differences between the transient coupled response results and the transient seepage response results. Total head for a given elevation is generally higher in the transient seepage results than in the transient

coupled results as the effect of the lithostatic unloading is ignored in the transient seepage analysis.

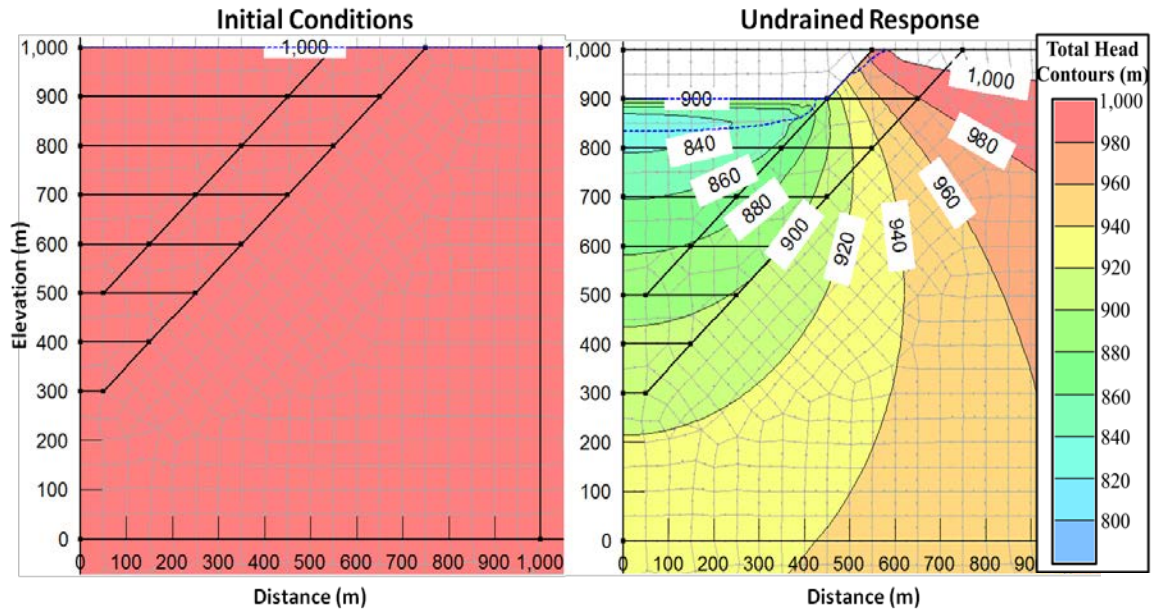


Figure 4.29: Analysis 4.1. Total head contours for the initial conditions and the undrained response.

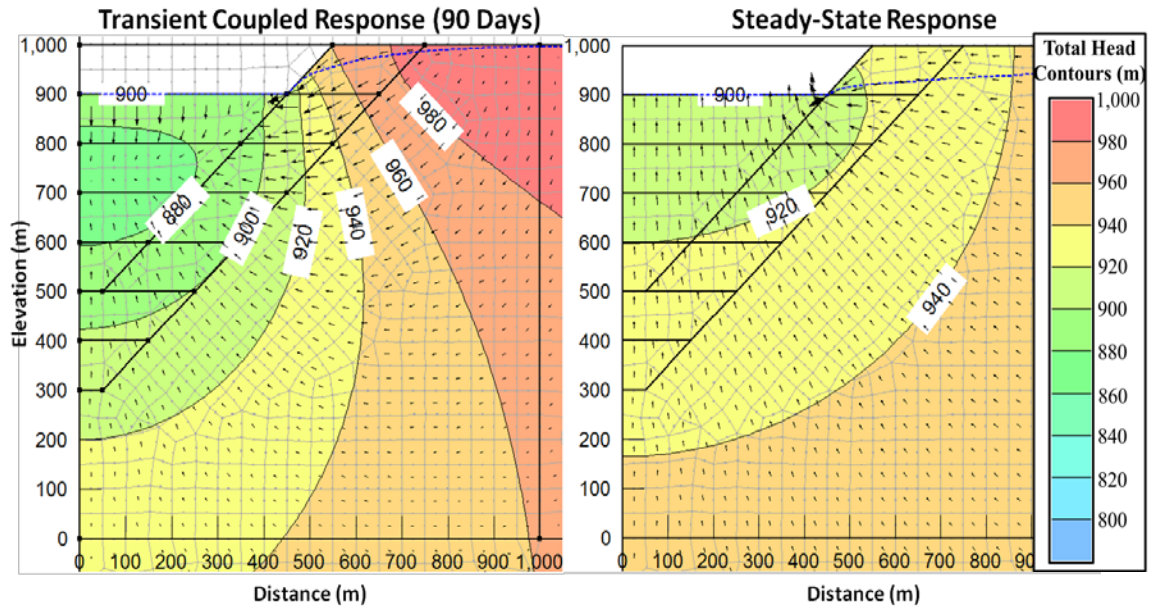


Figure 4.30: Analysis 4.1. Total head contours and hydraulic velocity vectors for the transient coupled response and steady-state response.

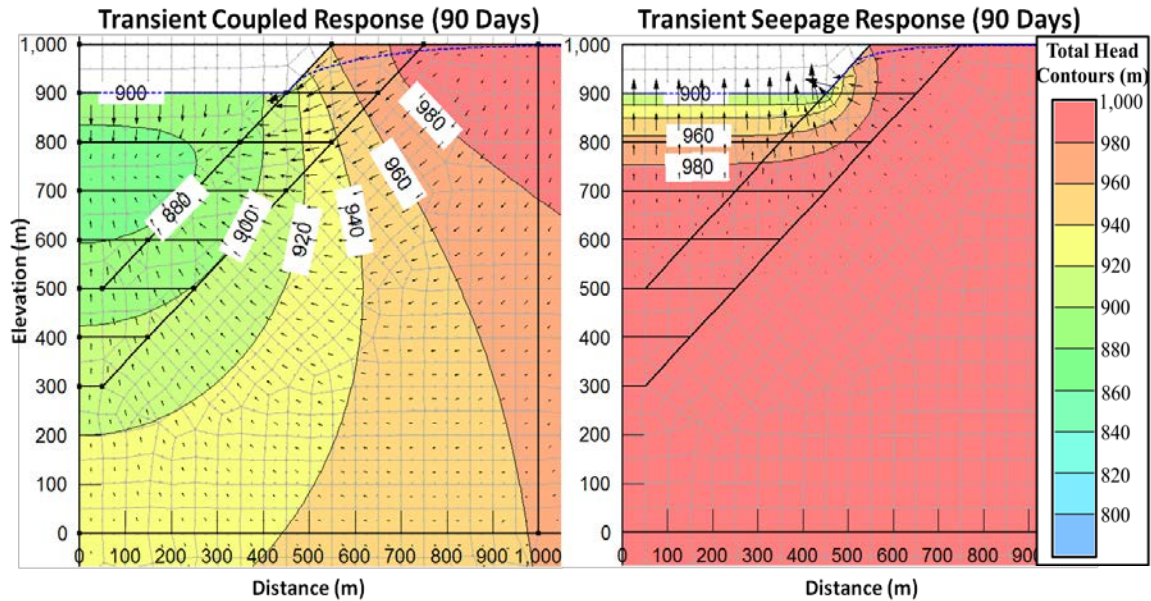


Figure 4.31: Analysis 4.1. Total head contours and hydraulic velocity vectors for the transient coupled response as compared to the transient seepage response at a time of 90 days.

The previous results from Analysis 4.1 modeled the effects of a single excavation. The following results, in the form of graphs, are from Analysis 4.2, where a total of 10 excavations over a period of 2,700 days (approximately 7.5 years) were modeled. Excavations 1-5 are excavated with an interval of 360 days (approximately one year) and excavations 6-10 are excavated with an interval of 180 days (approximately one half of a year). These analyses were run for materials with three different diffusion coefficients: 10^{-2} m²/sec, 10^{-3} m²/sec, and 10^{-4} m²/sec. Pore water pressures were measured at three locations at a depth of 500 meters below the ground surface. Table 4.8 shows the set of parameter values used in Analysis 4.2 and Figure 4.32 shows these three locations with respect to the entire pit and the 10 excavations.

Parameter	E (kPa)	ν	m_v (1/kPa)	k (m/s)	c_v (m ² /s)	γ_w (kN/m ³)	γ_s (kN/m ³)	Load Response Ratio
Value	10^6	1/3	10^{-6}	10^{-7} - 10^{-9}	10^{-2} - 10^{-4}	10	20	1.0

Table 4.8: Table of the ranges of parameter values used in Analysis 4.2.

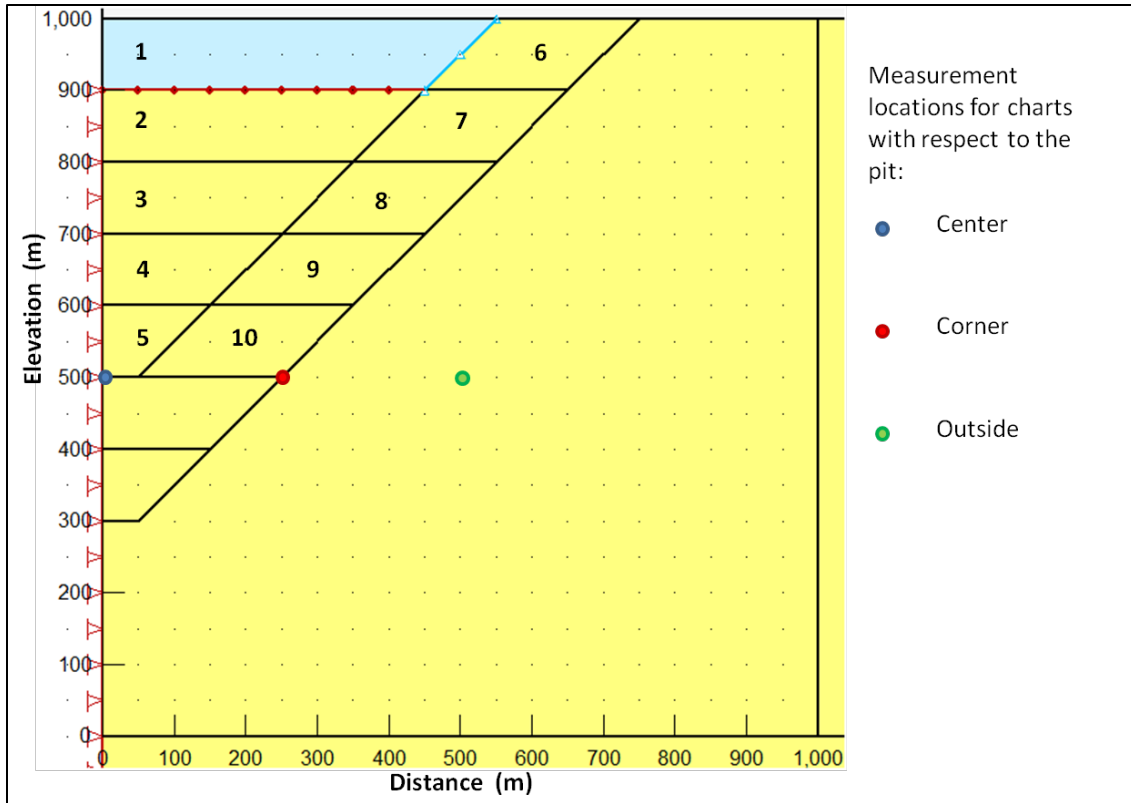


Figure 4.32: Analysis 4.2. Measurement locations for the graphs from Analysis 4.2. The numbers identify the sequence of excavations.

Figure 4.33 shows pore water pressures under the center of the pit and indicates that, in general, the lower the diffusion coefficient the lower the pore water pressure will be at any given time. The pore water pressure results for a material with a diffusion coefficient of $10^{-4} \text{ m}^2/\text{s}$ indicate that the pore water pressures are almost undrained as they increase very little after the first few excavations. Under the center of the pit, the pore water pressure reaches zero after the fifth excavation and so excavations 6-10 have no effect. Figure 4.34 shows the pore water pressures under the corner of the pit and indicates similar results to those in Figure 4.35. At the corner of the pit, however, the effects of excavations 6-10 are visible in the results as the pore water pressure at the corner of the pit does not decrease to zero until the tenth excavation. In general, Figure 4.34 indicates that at the corner, the lower the diffusion coefficient the lower the pore

water pressure is at any given time, though between 1,080 days (3 years) and 1,980 days (5.5 years), this is not the case.

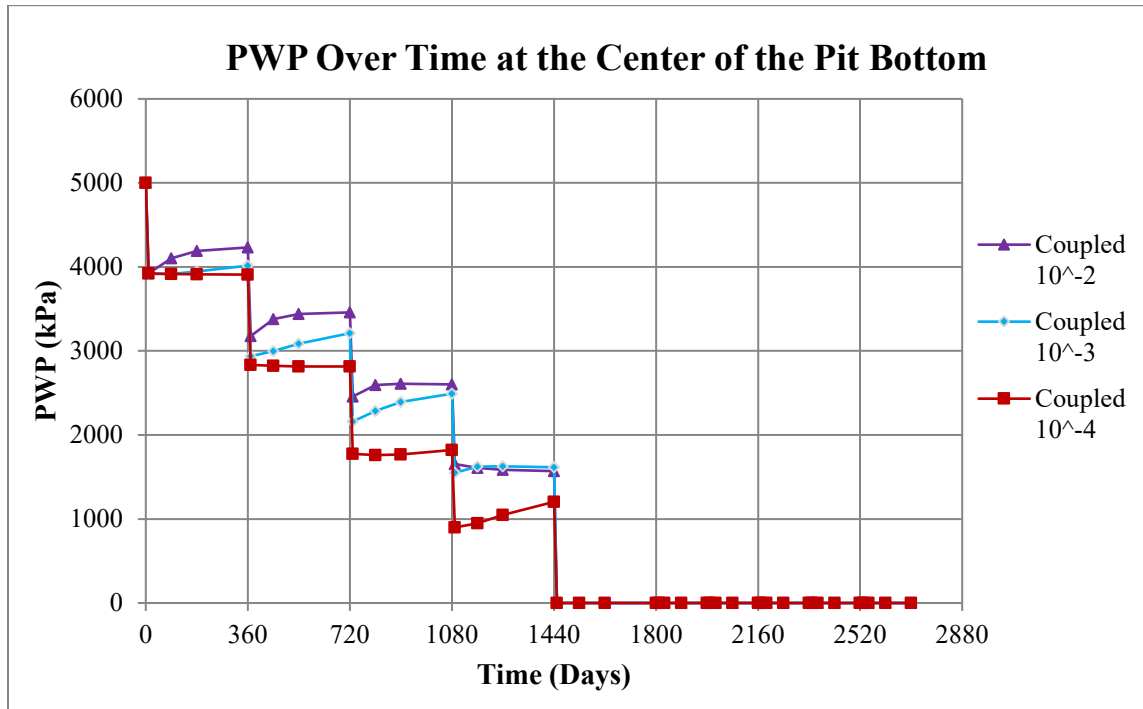


Figure 4.33: Analysis 4.2. Graph displaying pore water pressure (PWP) over time at a point initially 500 meters beneath the center of the ground surface for different diffusion coefficients (in m^2/sec).

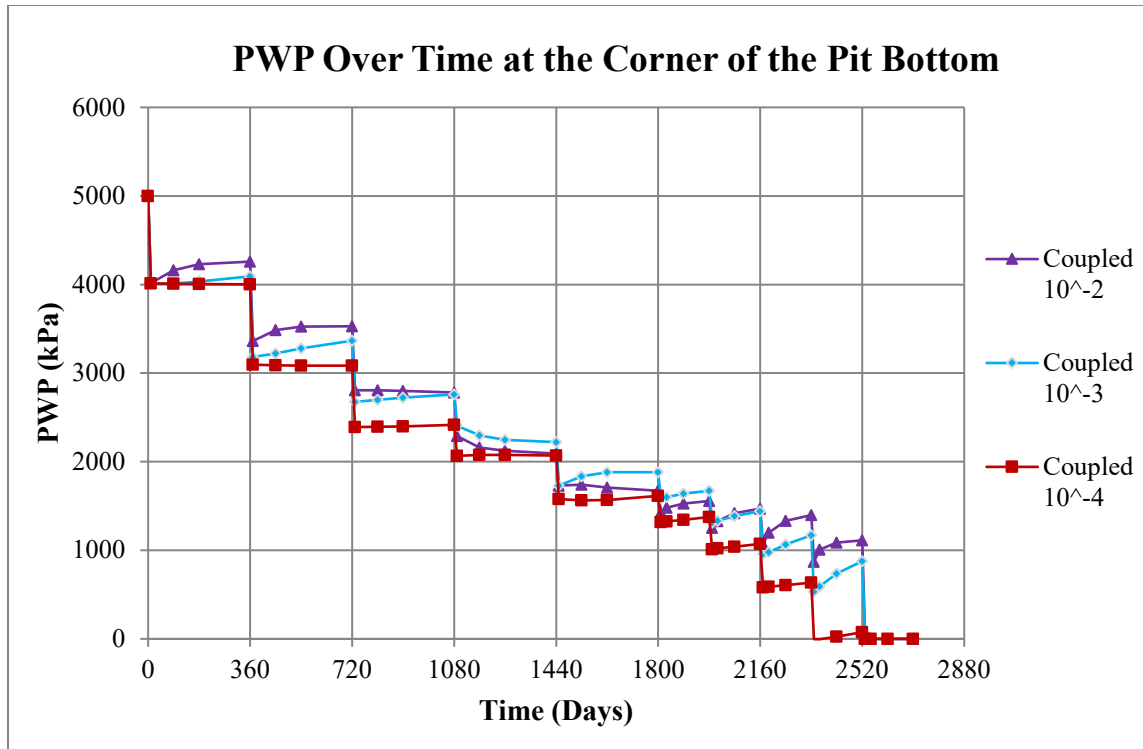


Figure 4.34: Analysis 4.2. Graph displaying pore water pressure (PWP) over time at a position initially 500 meters beneath the corner of the ground surface for different diffusion coefficients (in m^2/sec).

The results from the position beneath the outside of the pit indicate that the pore water pressures generally decrease after each of the excavations 5-10 as opposed to increase, as they did for the points at the center and corner of the pit. Figure 4.35 displays the pore water pressure results from outside of the pit.

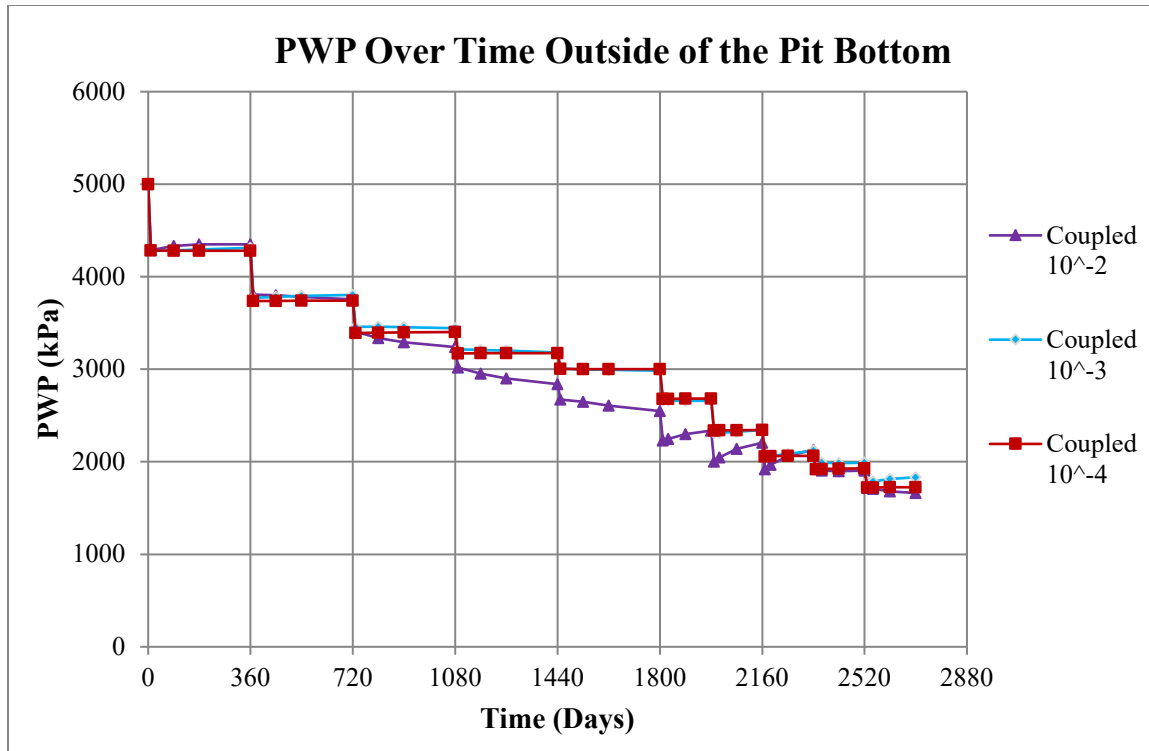


Figure 4.35: Analysis 4.2. Graph displaying pore water pressure (PWP) over time at a point 500 meters beneath the outside of the pit for materials with different diffusion coefficients (in m^2/sec).

As expected, the overall trend of these results shows that pore water pressure decreases over time during the entire lithostatic unloading process, totaling 10 excavations. In addition to the results for just the transient coupled response, it is useful to see these results as compared to the transient seepage response and the steady-state response. Figure 4.36 shows the pore water pressures under the center of the excavation for the transient coupled response, the transient seepage response and the steady-state response for a material with a diffusion coefficient of $10^{-3} \text{ m}^2/\text{s}$. These results show that at any given time, the pore water pressures are higher for the transient seepage response than for the steady-state or coupled response.

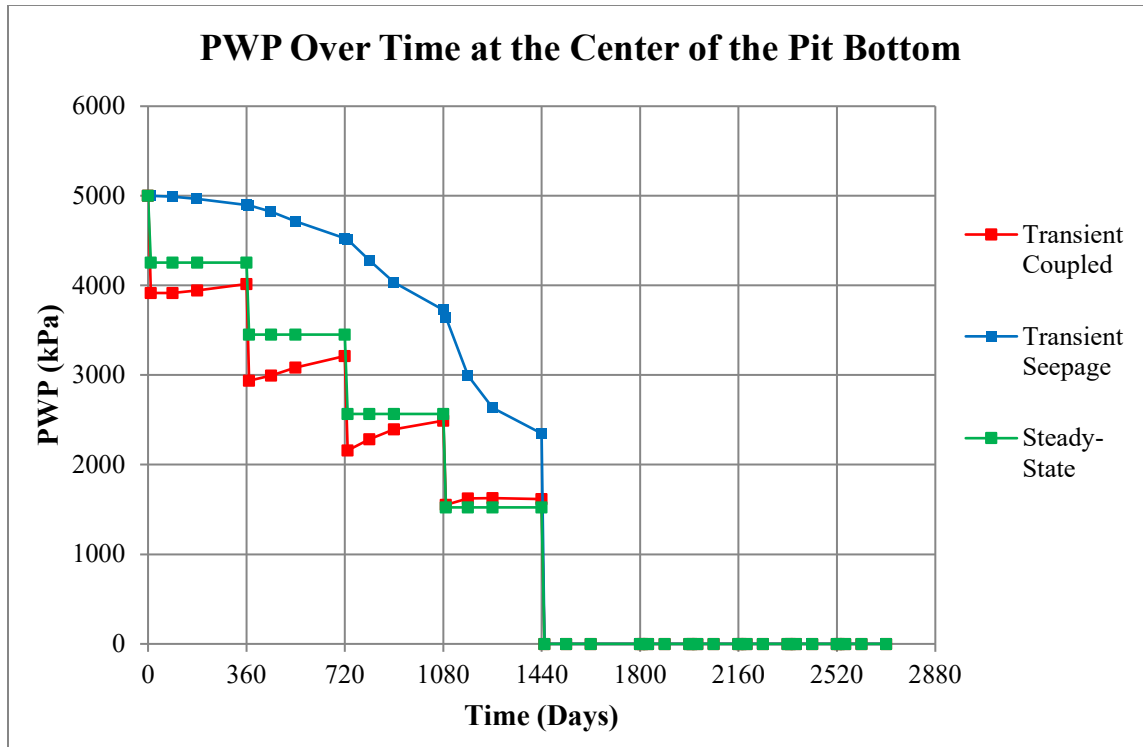


Figure 4.36: Analysis 4.2. Graph displaying pore water pressure (PWP) over time at a point 500 meters beneath the center of the pit.

Similar results to those found under the center of the pit were also found under the corner of the pit and at the point outside of the pit as shown in Figures 4.37 and 4.38, respectively. However, the pore water pressures at the corner of the pit are higher at any given time compared to the center of the pit and the pore water pressures at the outside of the pit are higher at any given time step compared to pore water pressures under the corner of the pit.

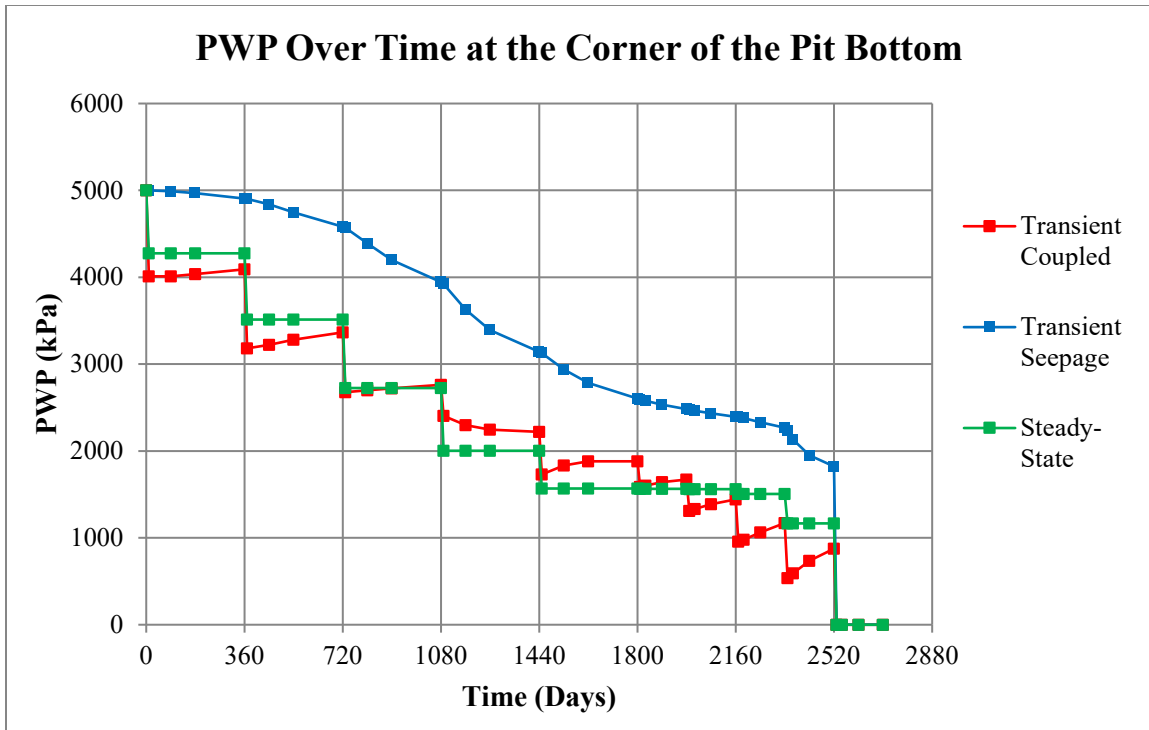


Figure 4.37: Analysis 4.2. Graph displaying pore water pressure (PWP) over time at a point 500 meters beneath the corner of the pit.

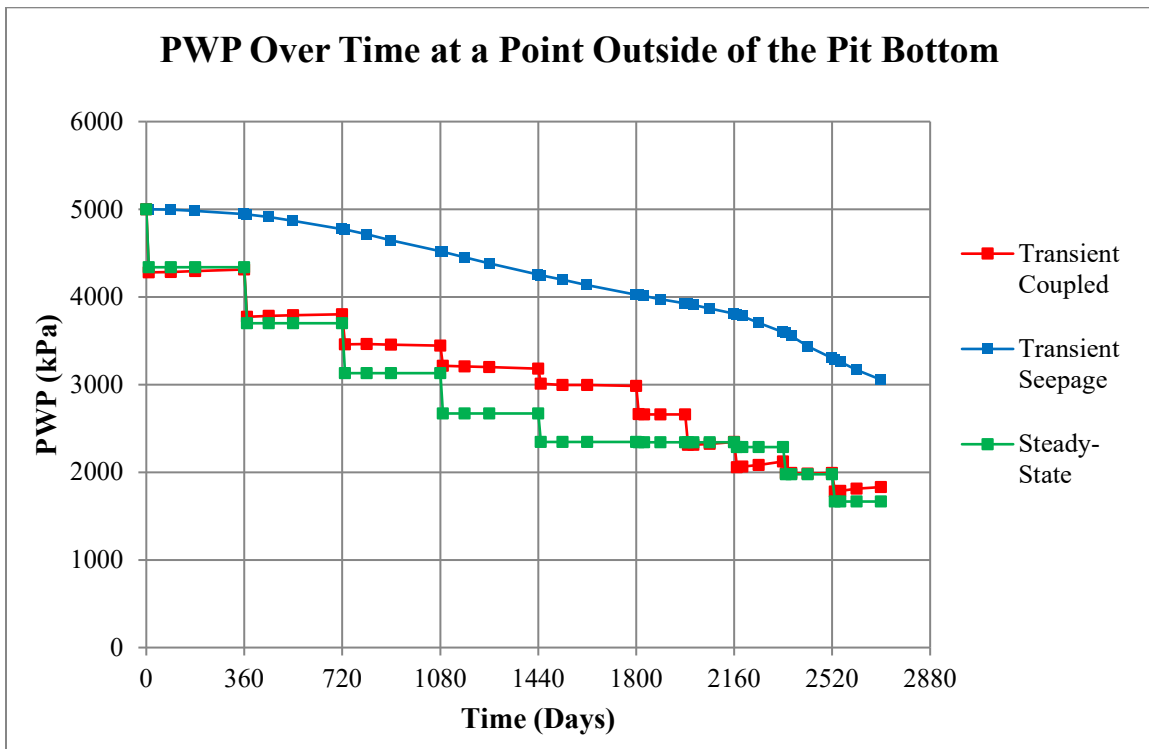


Figure 4.38: Analysis 4.2. Graph displaying pore water pressure (PWP) over time at 500 meters depth at a point outside of the pit.

The hydraulic gradients for the 10 excavations from Analysis 4.2 are shown in Figures 4.39, 4.40, and 4.41. The results are for points beneath the center of the pit, the corner of the pit, and at a point outside of the pit that is within the slope. These hydraulic gradient measurements were taken at a depth of approximately 530 meters due to numerical noise at the surface of the pit. These results show that the lower the diffusion coefficient, the higher the hydraulic gradients are at any given time. Also, the results indicate that the hydraulic gradients are generally lower at the corner of the pit and outside of the pit than at the center of the pit.

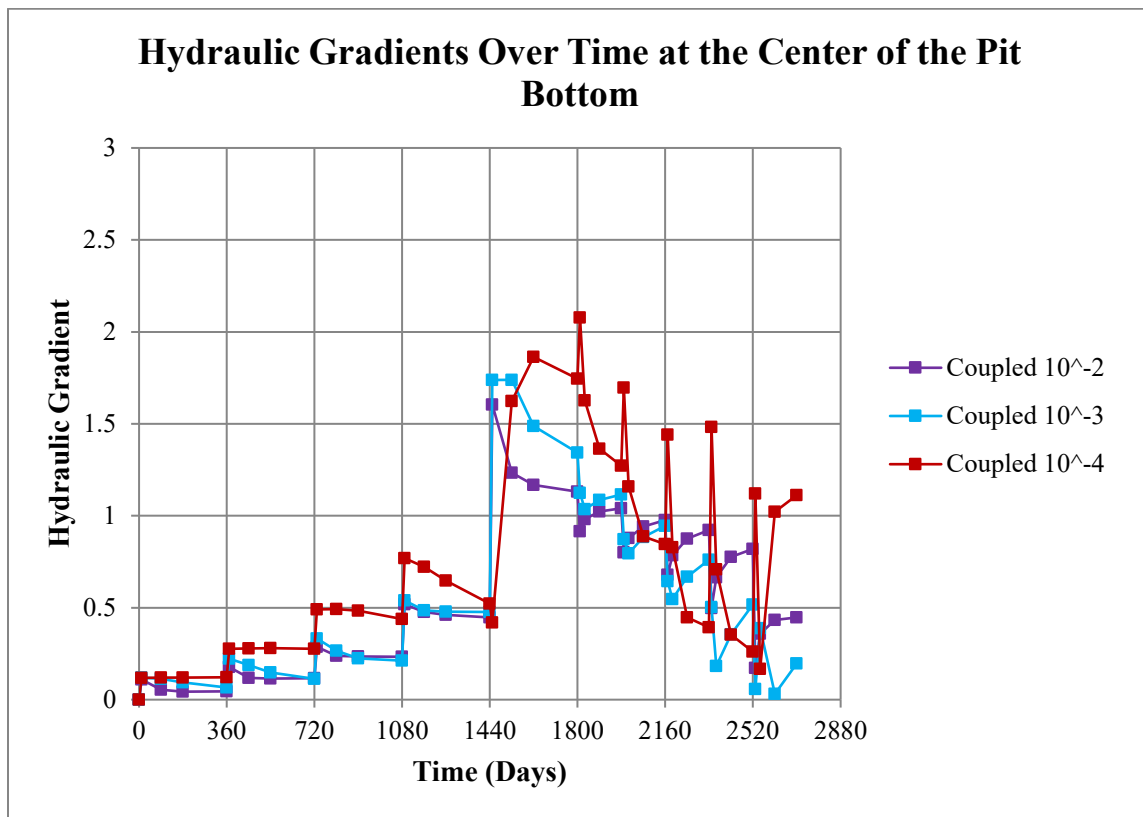


Figure 4.39: Analysis 4.2. Graph displaying hydraulic gradients over time at a point initially 530 meters beneath the center of the ground surface for three different diffusion coefficients (in m^2/sec).

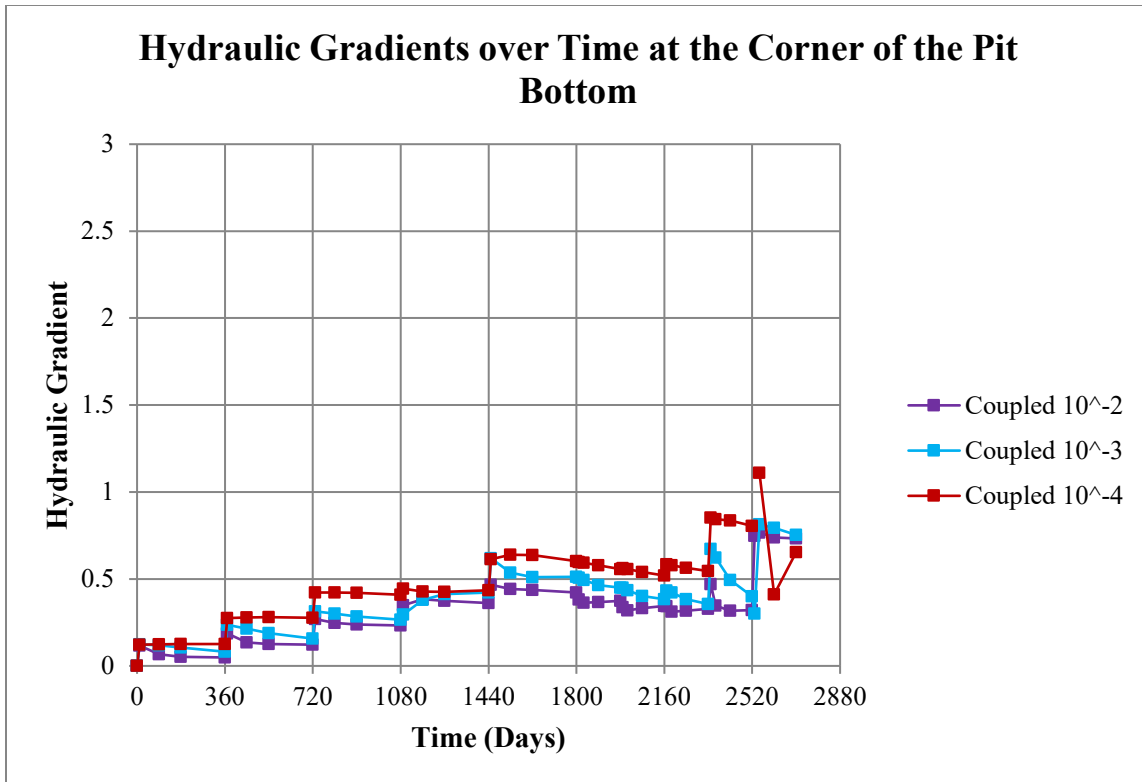


Figure 4.40: Analysis 4.2. Graph displaying hydraulic gradients over time at a point initially 530 meters beneath the corner of pit for three different diffusion coefficients (in m^2/sec).

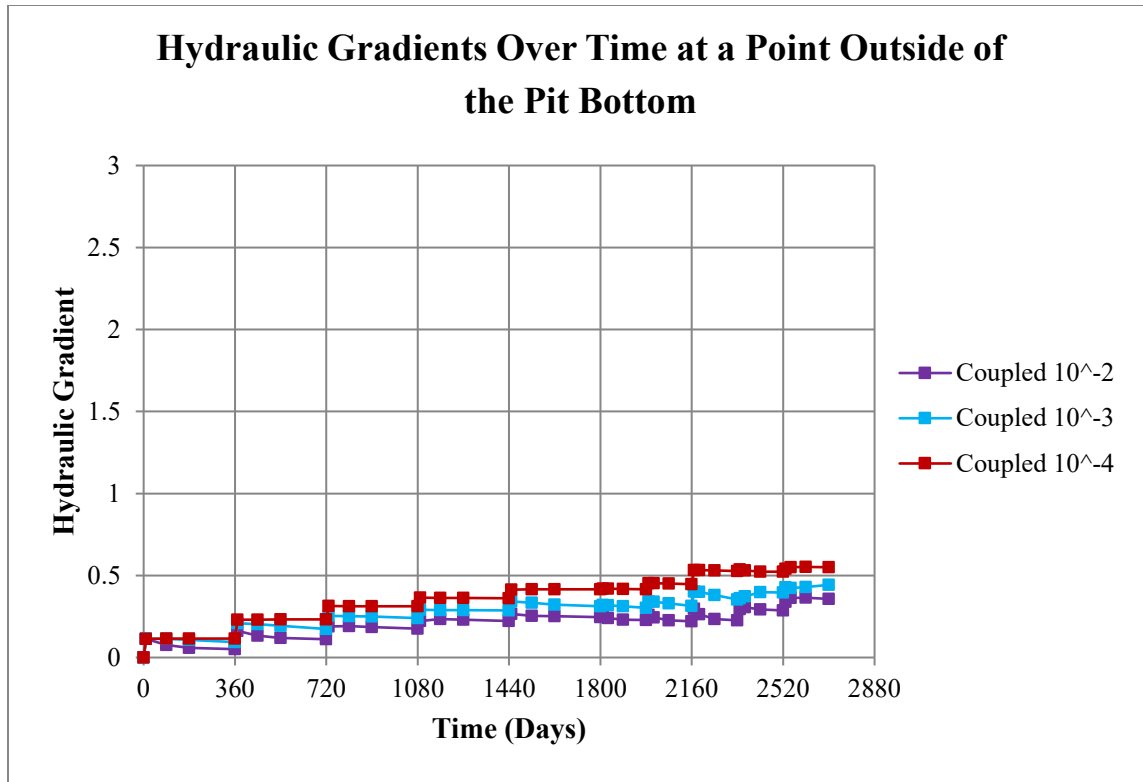


Figure 4.41: Analysis 4.2. Graph displaying hydraulic gradients over time at a point initially 530 meters beneath a point outside of the pit for three different diffusion coefficients (in m^2/sec).

The discharge results from the 2-D trapezoid excavation analyses are quite similar to those of the 2-D rectangular excavation analyses. Figure 4.42 depicts the discharge results for both a transient seepage analysis and a transient coupled analysis for two different diffusion coefficients. It is evident from the transient coupled results that groundwater discharge is actually flowing from the surface of the pit bottom into the geologic material for a period lasting approximately 90 days for both diffusion coefficients. This result is in agreement with previous results that indicated that a groundwater stagnation zone forms right beneath the bottom of the pit. The transient seepage results show that a large amount of groundwater is discharging into the pit after the excavation and this discharge rate rapidly falls off to a lower level during the first 90

days after the excavation. In addition, these results indicate that the discharge values are higher for the material with a lower diffusion coefficient.

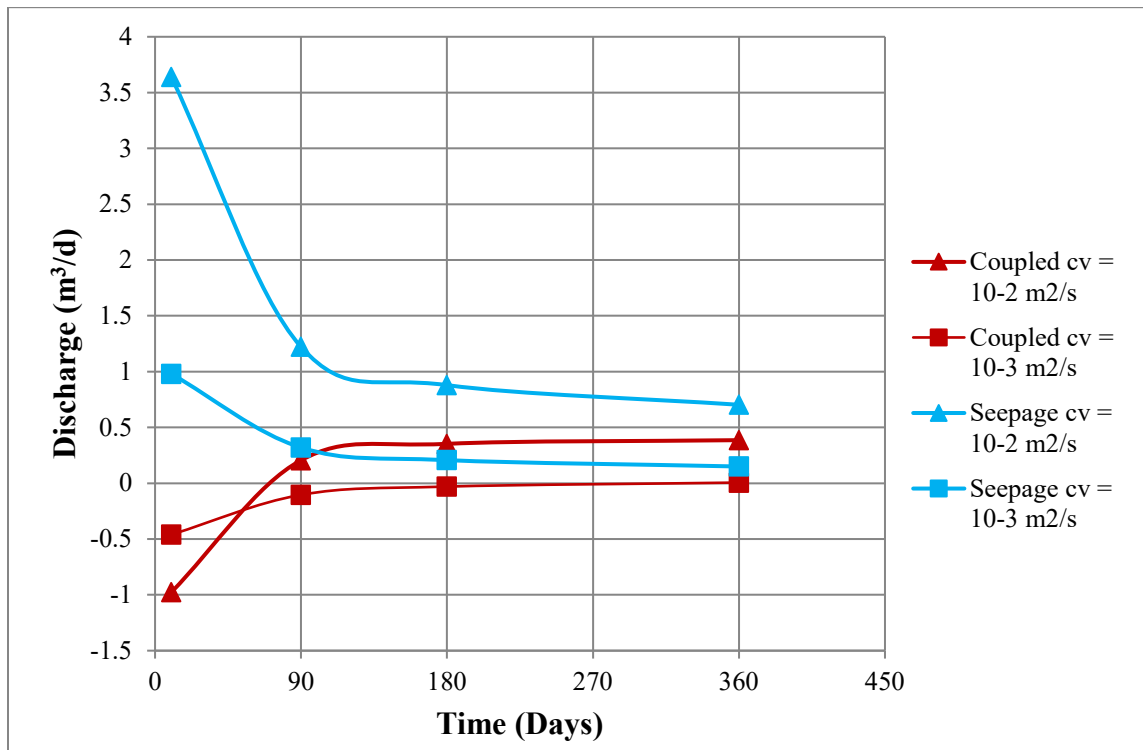


Figure 4.42: Analysis 4.2. Groundwater discharge through the 250 meter long surface of the pit bottom over time.

In addition to the preceding analyses, stress path analyses (Analysis 4.3) were also performed for the unconfined 2-D trapezoid excavations. The stress path analysis results are presented in the form of p-q charts, which depict the peak points of stress-strain curves. The line through these peak points is known as the K_f line where the f stands for failure. If the p-q stress paths cross the K_f line then the soil/rock is in a state of failure. Analyses for both unsaturated and saturated profiles were performed in order to determine the stability of the slope during the lithostatic unloading process of 10 excavations. Figure 4.43 shows the three measurement locations for the total and effective stresses within the slope during the lithostatic unloading process. The set of parameter values used in this particular analysis is displayed in Table 4.9.

Parameter	E (kPa)	ν	m_v (1/kPa)	k (m/s)	c_v (m ² /s)	γ_w (kN/m ³)	γ_s (kN/m ³)	Load Response Ratio
Value	10^6	1/3	10^{-6}	10^{-8}	10^{-3}	10	20	1.0

Table 4.9: Table of the ranges of parameter values used in Analysis 4.3.

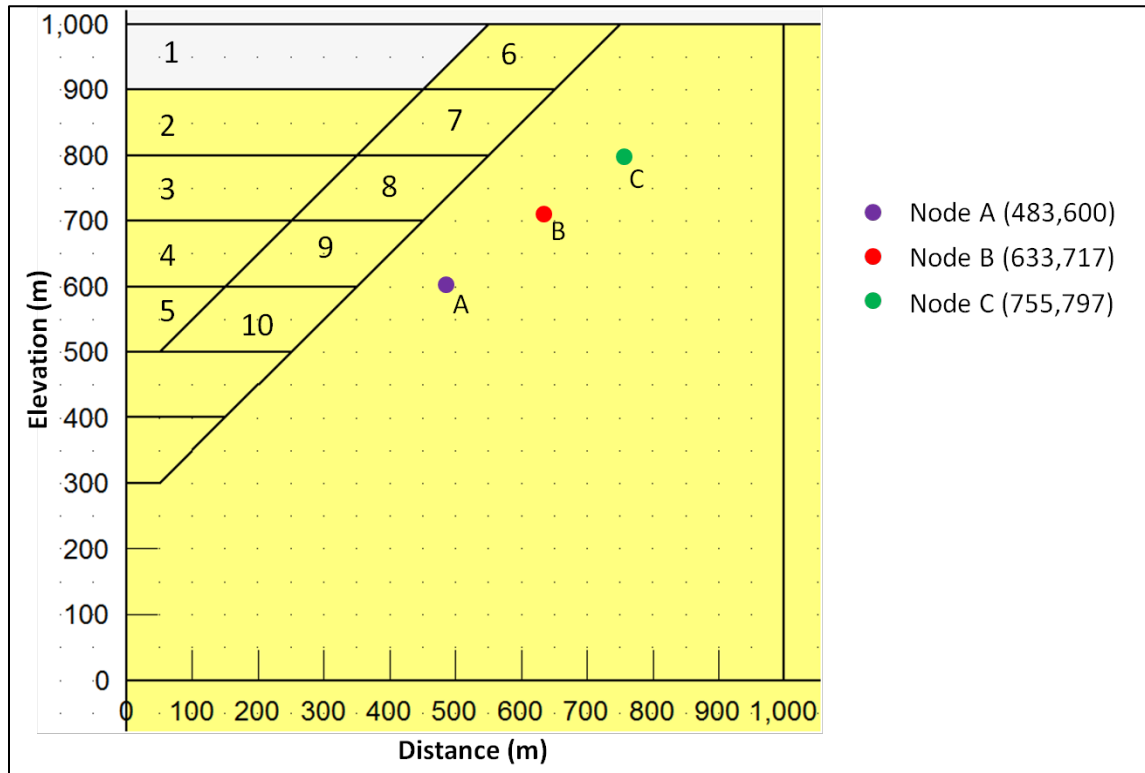


Figure 4.43: Analysis 4.3. Measurement locations for total and effective stresses within the slope during the lithostatic unloading process (10 numbered excavations).

The results of the total stress path analysis for the unsaturated case is given in Figure 4.44. It can be seen from these results that the total stress paths for each of the three measurement locations within the slope do not cross the K_f line.

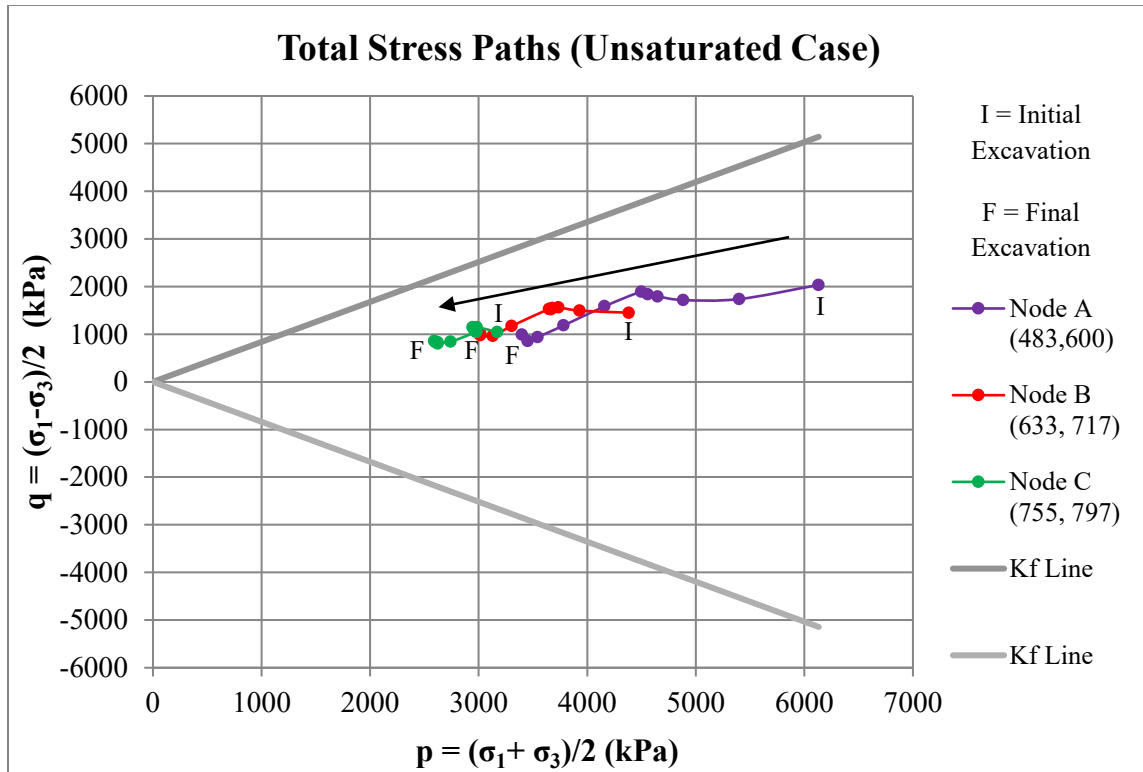


Figure 4.44: Analysis 4.3. The total stress paths for Nodes A, B, and C. The black arrow indicates the general trend from the initial excavation to the final excavation for each of the three stress paths.

The results from the analyses with saturated profiles are in terms of effective stress as pore pressures change during the lithostatic unloading process. Figure 4.45 displays the transient seepage (uncoupled) and the transient coupled effective stress paths for Node A. The figure shows that the uncoupled effective stress path tends to get closer to the Kf line than the coupled effective stress path, yet both do not cross the Kf line.

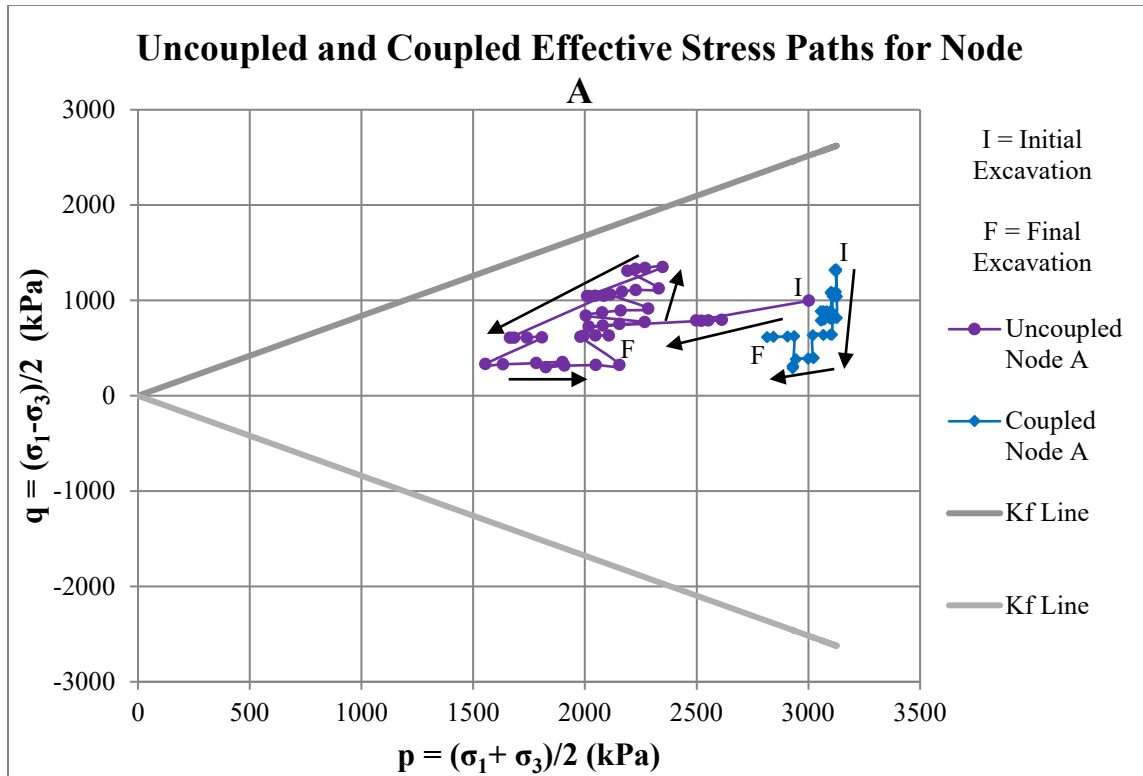


Figure 4.45: Analysis 4.3. The uncoupled and coupled effective stress paths for Node A. The black arrows depict the general trend of the stress paths. The Kf lines are for a material with an internal angle of friction of 40°.

Figure 4.46 shows the uncoupled and coupled effective stress paths for Node B.

As with the results from Node A, the uncoupled effective stress path gets closer to the K_f line than does the coupled effective stress path, yet both do not cross it.

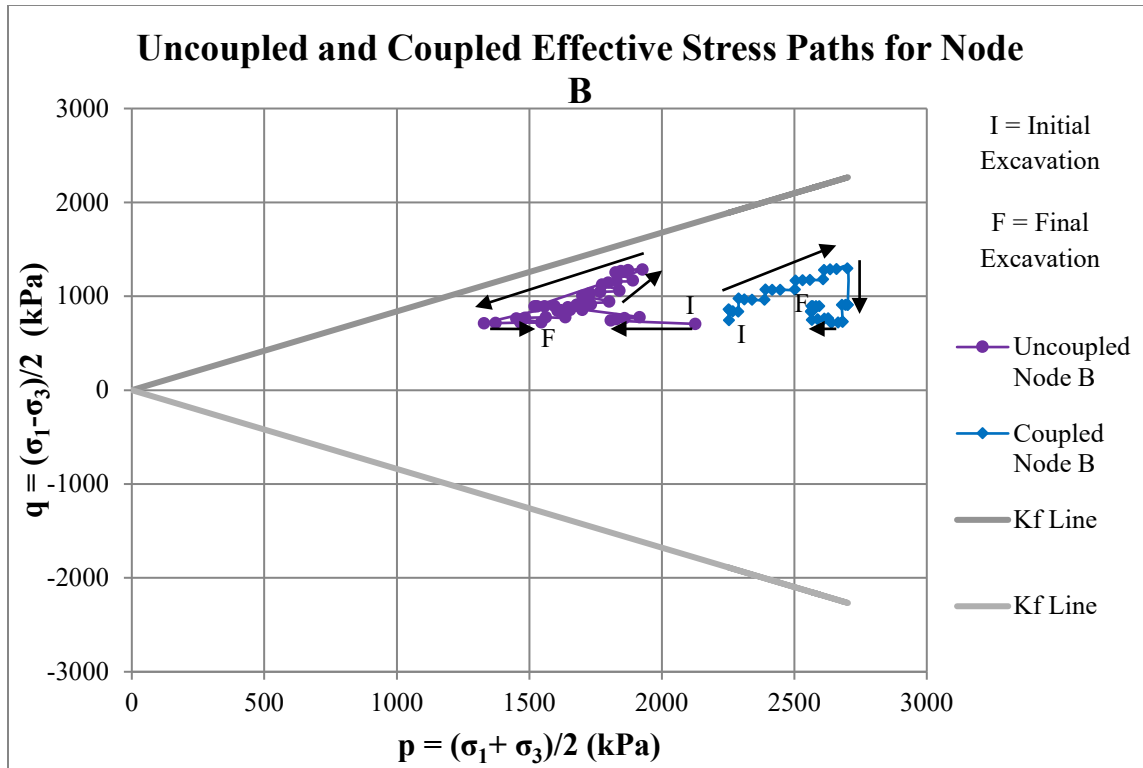


Figure 4.46: Analysis 4.3. The uncoupled and coupled effective stress paths for Node B. The black arrows depict the general trend of the stress paths. The K_f lines are for a material with an internal angle of friction of 40° .

Figure 4.47 displays the uncoupled and coupled effective stress paths for Node C. The results from Figure 4.47 show that the uncoupled effective stress path gets close to the K_f line while the coupled effective stress path does not.

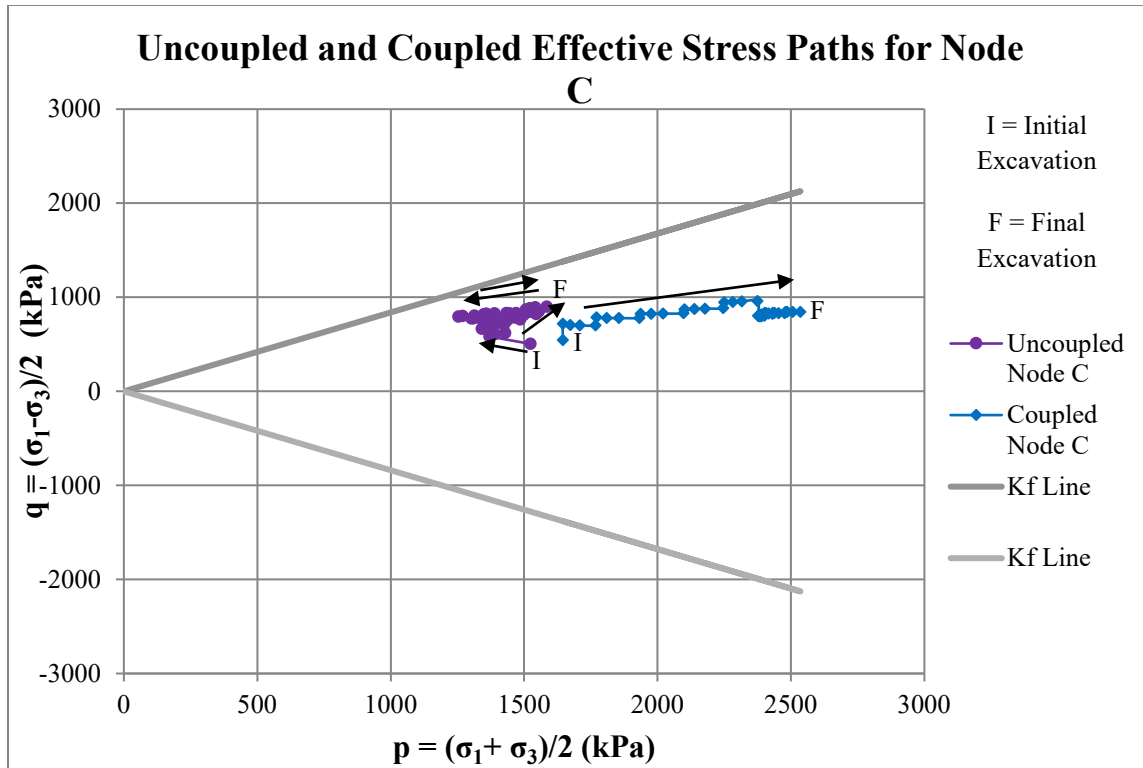


Figure 4.47: Analysis 4.3. The uncoupled and coupled effective stress paths for Node C. The black arrows depict the general trends of the stress paths. The Kf lines are for a material with an internal angle of friction of 40°.

Additional unconfined trapezoid-shaped excavation results in the form of pore water pressure and total head contour charts are included in Appendix C.

Chapter 5: Discussion

The results of this thesis indicate that open-pit mine groundwater models that ignore the effects of lithostatic unloading may be incomplete and/or inaccurate. The magnitude of this inaccuracy depends upon the geometry of the excavation, the hydraulic and mechanical parameters of the geologic material comprising the mine, and the excavation rate of the mining operation.

The geometry of the excavation affects the magnitude of the hydromechanical coupling effect. The results of the normalized octahedral stress distributions from Analysis 1.1 show that the choice of the excavation geometry in a mine groundwater model is important in determining the magnitude of the hydromechanical effects. The use of a 1-D excavation model will result in a large decrement of octahedral stress throughout the profile and the use of a more realistic circular/axisymmetric excavation model will result in a smaller decrement that decreases with depth. As the decrement in pore water pressure is directly dependent on the decrement in octahedral stress during the undrained response, the effect of the hydromechanical coupling is directly related to the geometry of the excavation. For the 2-D and circular excavation models the decrement in octahedral stress decreases with depth and distance away from the center of the excavation. These results suggest that the 1-D analyses overestimate the effect of the lithostatic unloading below 50 meters beneath the excavation. Overall, the octahedral stress distribution results show that the 2-D trapezoid-shaped and axisymmetric analyses give the most realistic octahedral stress distributions and therefore the most realistic undrained response results.

Regarding the transient effects of hydromechanical coupling, the results from all of the analyses generally demonstrate that materials with a diffusion coefficient equal to or lower than $10^{-3} \text{ m}^2/\text{s}$ will have pore water pressures around the excavation that are below hydrostatic for periods of time greater than one year. The lower the diffusion coefficient, the longer the pore water pressures will remain below hydrostatic. If, for example, the excavation rate were increased from one per year to one per half of a year then this would cause the pore water pressures to be lowered even more. This result

indicates that the excavation rate, in addition to the diffusion coefficient, affects how long the pore water pressures remain below hydrostatic during the operation of the mine. The lowered pore water pressures indicated by these analyses could increase the strength of the mine walls and so slope stability analyses should incorporate these lowered pore water pressures. In addition, Analysis 3.3 indicates that a material with a high diffusion coefficient, possibly greater than $10^{-3} \text{ m}^2/\text{s}$, may have sufficient swelling that causes the hydraulic conductivity of the material to increase over time and yield a lower steady-state distribution than if there were no swelling and no change in hydraulic conductivity. Therefore, if a mine is excavated in a material with a high diffusion coefficient, that does not necessarily mean that hydromechanical coupling can be ignored. Overall, these results suggest that an accurate measurement of a mine's diffusion coefficient is the most important parameter measurement for a groundwater model that incorporates the effects of hydromechanical coupling. Also, the choice of whether to use undrained or drained parameters in slope stability analyses will be affected by the magnitude of the hydromechanical coupling effect, which is in turn a function of the diffusion coefficient and the excavation rate.

The results from the 2-D rectangular-strip excavation analyses and the 2-D trapezoid-shaped excavation analyses of subchapters 4.3 and 4.4, respectively, show that an uncoupled analysis (transient seepage analysis), overestimates the pore water pressures and heads in a mine at any given time because it neglects the hydromechanical coupling effect of the lithostatic unloading. The difference in pore water pressures between the transient seepage analysis and the coupled analysis for the 2-D trapezoid-shaped excavations can be as much as 100% higher, and so at times this difference in

pore water pressures can be as large as a few thousand kPa. The difference becomes larger for a lower diffusion coefficient, again indicating that obtaining an accurate measurement for the diffusion coefficient should be a high priority for a particular mine's groundwater model.

Overall, a coupled analysis will provide the most complete results for a groundwater model and/or slope stability analysis, as it takes the hydromechanical coupling effect of the unloading into account. Though, if the diffusion coefficient of the mine material is high, a steady-state analysis may also be accurate and useful, as the high diffusion coefficient results show that pore water pressures, heads, etc., reach steady-state conditions quickly after each excavation and these results are not much different from the coupled results.

The 2-D results indicate that the hydraulic gradients are mostly affected in the top 100-200 meters of the profile below the center of the excavation, which is expected given that the pore water pressures and heads are also mostly affected in the top 100-200 meters. In addition, the hydraulic gradients are highest below the center of the excavation and lowest outside of the excavation, within the slope of the pit. Immediately after an excavation the hydraulic gradients increase rapidly to a peak and then drop off steadily until steady-state conditions are reached. As with the pore water pressures and heads, the transient seepage analyses overestimate the hydraulic gradients as they do not take the effect of the lithostatic unloading into account. In addition, the lower the diffusion coefficient, the higher the hydraulic gradients are at any given time. Again, these results show that a coupled analysis is the most complete analysis.

The final finding of interest from this study is that of the groundwater stagnation zone that forms after some of the larger excavations. The 2-D rectangular-strip excavation and 2-D trapezoid-shaped excavation analyses indicate that groundwater flows from the pit into a zone of low total head immediately after the excavation. As time passes, the groundwater stagnation zone declines in size until it dissipates completely and groundwater flow goes directly into the pit. The groundwater stagnation zone can be thought of as an interplay between the groundwater flow from the high elevations outside the mine and the flow coming from the pit to relieve the decreased pore water pressures and total head caused by the lithostatic unloading. Overtime, the groundwater flow from the high elevations overcomes the effect of the lithostatic unloading, the stagnation zone dissipates and groundwater flow goes into the pit. Though, the lower the diffusion coefficient is the longer the groundwater stagnation zone will last beneath the pit. The groundwater stagnation zone only appears in the transient coupled analyses with 2-D geometries, suggesting that, again, a coupled analysis is the most complete.

In summary, the transient seepage (uncoupled) analysis overestimates the pore water pressures, heads, hydraulic gradients, and groundwater discharge in a mine. It should only be used if the most conservative results are required by a mine.

Chapter 6: Conclusions and Future Research

The three major conclusions of this thesis are: (1) the hydromechanical effects of the lithostatic unloading should not be ignored in groundwater models developed for open-pit mines, (2) the overall hydromechanical effect of the lithostatic unloading over

time is mainly a function of the magnitude of the diffusion coefficient of the materials comprising the mine and the excavation rate, and (3) the transient seepage (uncoupled) analyses greatly overestimate the pore water pressures, heads, hydraulic gradients and discharges in a mine.

The simplified methodology for a groundwater model that takes hydromechanical coupling into account should have an accurate excavation geometry for the model. A 2-D trapezoid-shaped excavation or a 2-D axisymmetric excavation would, in general, be the most accurate choice of geometry. The results from Subchapter 4.1 show that a 1-D coupled analysis, while simple, overestimates the octahedral stresses and therefore the excess negative pore water pressures generated during the undrained response. In addition, the 1-D coupled analysis does not show the formation of a groundwater stagnation zone.

A hydromechanical groundwater model for a mine requires an accurate measurement of the diffusion coefficient of the geologic material comprising the mine. The diffusion coefficient and the excavation rate will determine how long the hydromechanical effects last between excavations. Also, the magnitude of the diffusion coefficient will determine whether the material will experience heave/swelling and changing hydraulic conductivity or a large decrease in pore water pressures below hydrostatic values.

As discussed in Chapter 5, a hydromechanical model for a mine should avoid relying solely on transient seepage (uncoupled) analyses as these will greatly overestimate pore water pressures, heads, and gradients in the slopes of the pit. If pore water pressures are predicted to be low by a coupled hydromechanical model, mine walls

could be excavated with higher slope angles, resulting in more economical excavations. However, if the most conservative safety standards for a slope are desired, the transient seepage analysis can be used. Overall, if the diffusion coefficient of the material comprising the mine is low, a coupled analysis would be the most accurate, on the other hand, if the diffusion coefficient is high, a steady-state analysis would be ideal. Though, as discussed in Chapter 5, if the material has a high diffusion coefficient the hydraulic conductivity may change over time due to swelling (see results from Analysis 3.3 in Chapter 4), so it is still important to take swelling effects into account for the groundwater model of a mine.

The limitations of this thesis include the simplifying assumptions made for the analyses. While a simplified methodology provides a clear, conceptual insight into the potential hydromechanical effects on pore water pressure and total head distributions in a mine, it can be made more accurate by relaxing the assumptions. Further research into the effect of the lithostatic unloading and a complete groundwater model for an open-pit mine should involve relaxing each of the assumptions of this thesis. Anisotropy and heterogeneity should be incorporated. Unsaturated flow and flow through fractures should also be incorporated into a model. Nonlinear mechanical behavior, such as viscoelastic behavior, should be investigated. Infiltration, evaporation and runoff should also be incorporated into future analyses. In addition, axisymmetric analyses should be undertaken as many open pit mines have a circular geometry.

For use in a specific open-pit mine, the numerical models presented in this thesis need to be validated by data from the mine itself. These numerical analyses were

undertaken to show the possible hydromechanical effects of lithostatic unloading for mines, in general, and are not intended to represent any individual open-pit mine.

References Cited

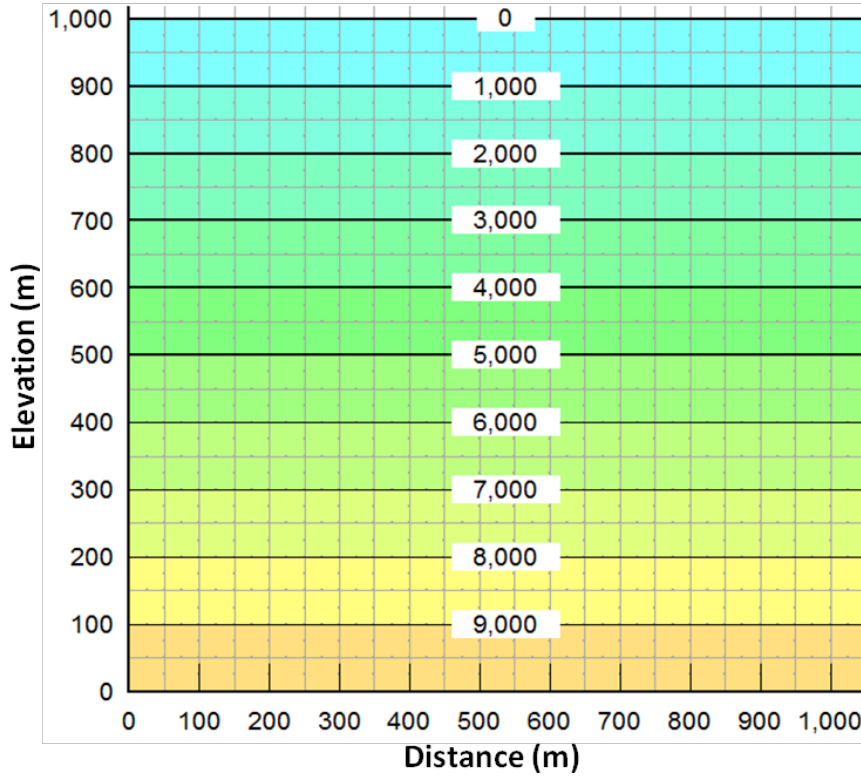
- Batu, Vedat. *Aquifer hydraulics: a comprehensive guide to hydrogeologic data analysis*. Vol. 1. John Wiley & Sons, 1998.
- Bear, Jacob. *Dynamics of fluids in porous media*. Dover publications, 1988.
- Bell, M. Lee, and Amos Nur. "Strength changes due to reservoir-induced pore pressure and stresses and application to Lake Oroville." *Journal of geophysical research* 83.B9 (1978): 4469-4483.
- Biot, Maurice A. "General theory of three-dimensional consolidation." *Journal of applied physics* 12.2 (1941): 155-164.
- Detournay, E. and Cheng, A.H.-D., "Fundamentals of Poroelasticity," Chapter 5 in *Comprehensive Rock Engineering: Principles, Practice and Projects, Vol. II, Analysis and Design Method*, ed. C. Fairhurst, Pergamon Press, pp. 113-171, 1993.
- Domenico, P. A., and M. D. Mifflin. "Water from low-permeability sediments and land subsidence." *Water Resources Research* 1.4 (1965): 563-576.
- Hazzard, J., Damjanac, B., Detournay, C., & Lorig, L. "Developing rules of thumb for groundwater modeling in large open pit mine design." *Pan-Am CGS Geotechnical Conference Proceedings*. 2011.
- Hodge, Robert AL, and R. Allan Freeze. "Groundwater flow systems and slope stability." *Canadian Geotechnical Journal* 14.4 (1977): 466-476.
- Lambe, T. W., and Whitman, R. V. *Soil Mechanics*. 553 p. John Wiley & Sons, 1969.
- Li, Victor C. "Estimation of in-situ hydraulic diffusivity of rock masses." *Pure and Applied Geophysics* 122.2-4 (1984): 545-559.
- Lutton, R. J., and Banks, D. C., 1970, Study of clay shale slopes along the Panama Canal: report I, East Culebra and West Culebra slides and the model slope: U.S. Army Eng. Waterways Experiment Station Tech. Rept. S-70-9, 385 p.
- Mercer, JW, and C.R. Faust. "Ground-Water Modeling: Numerical Models." *Ground Water* (1980): Vol. 18, No. 4.
- Neuzil, C. E., and D. W. Pollock. "Erosional unloading and fluid pressures in hydraulically 'tight' rocks." *The Journal of Geology* (1983): 179-193.
- Neuzil, C. E. "Groundwater flow in low-permeability environments." *Water Resources Research* 22.8 (1986): 1163-1195.

- Neuzil, C. E. "Hydromechanical coupling in geologic processes." *Hydrogeology Journal* 11.1 (2003): 41-83.
- Rice, James R., and Michael P. Cleary. "Some basic stress diffusion solutions for fluid-saturated elastic porous media with compressible constituents." *Reviews of Geophysics* 14.2 (1976): 227-241.
- Roeloffs, Evelyn. "Poroelastic techniques in the study of earthquake-related hydrologic phenomena." *Advances in geophysics* 37 (1996): 135-195.
- Rutqvist, Jonny, and Ove, Stephansson. "The role of hydromechanical coupling in fractured rock engineering." *Hydrogeology Journal* 11.1 (2003): 7-40.
- Sullivan, T. D. "Hydromechanical coupling and pit slope movements." In *Slope Stability 2007, Proceedings of 2007 international symposium on rock slope stability in open pit mining and civil engineering, September, Perth, Australia* (2007): 3-43. Australian Centre for Geomechanics.
- Stacey, T. R., Xianbin, Y., Armstrong, R., and Keyter, G.J. "New slope stability considerations for deep open pit mines." *Journal of the South African Institute of Mining and Metallurgy* 103.6 (2003): 373-389.
- Terzaghi, Karl, Ralph B. Peck, and Gholamreza, Mesri. *Soil mechanics in engineering practice*. John Wiley & Sons, 1996.
- Van der Kamp, G., and J. E. Gale. "Theory of earth tide and barometric effects in porous formations with compressible grains." *Water Resources Research* 19.2 (1983): 538-544.
- Wang, Herbert. *Theory of linear poroelasticity with applications to geomechanics and hydrogeology*. Princeton University Press, 2000.

Appendix A: Additional 1-D Confined Flow Results

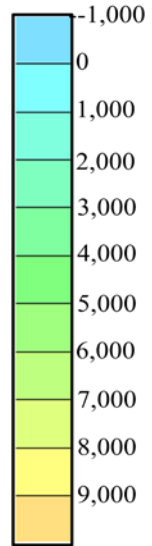
Pages 85-102: Pore water pressure and total head contour charts for each of the three diffusion coefficients (10^{-2} , 10^{-3} and 10^{-4} m²/s).

Initial Conditions

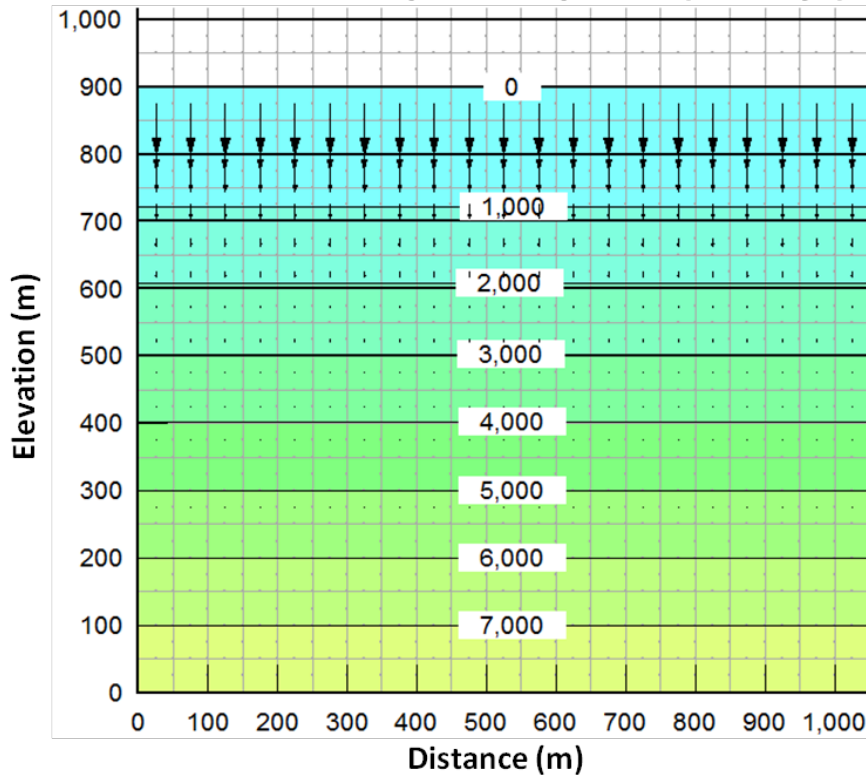


$c_v = 10^{-2} \text{ m}^2/\text{s}$

**PWP
Contours
(kPa)**

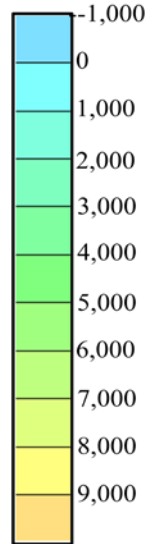


Transient Coupled Response (10 Days)

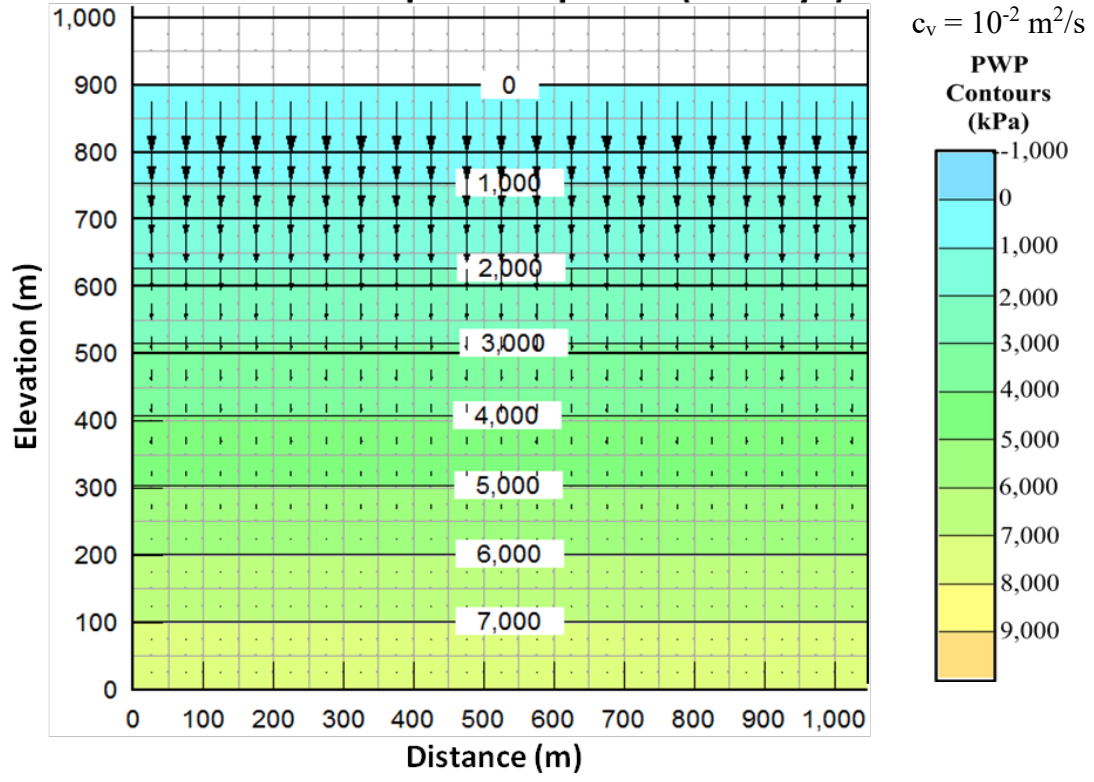


$c_v = 10^{-2} \text{ m}^2/\text{s}$

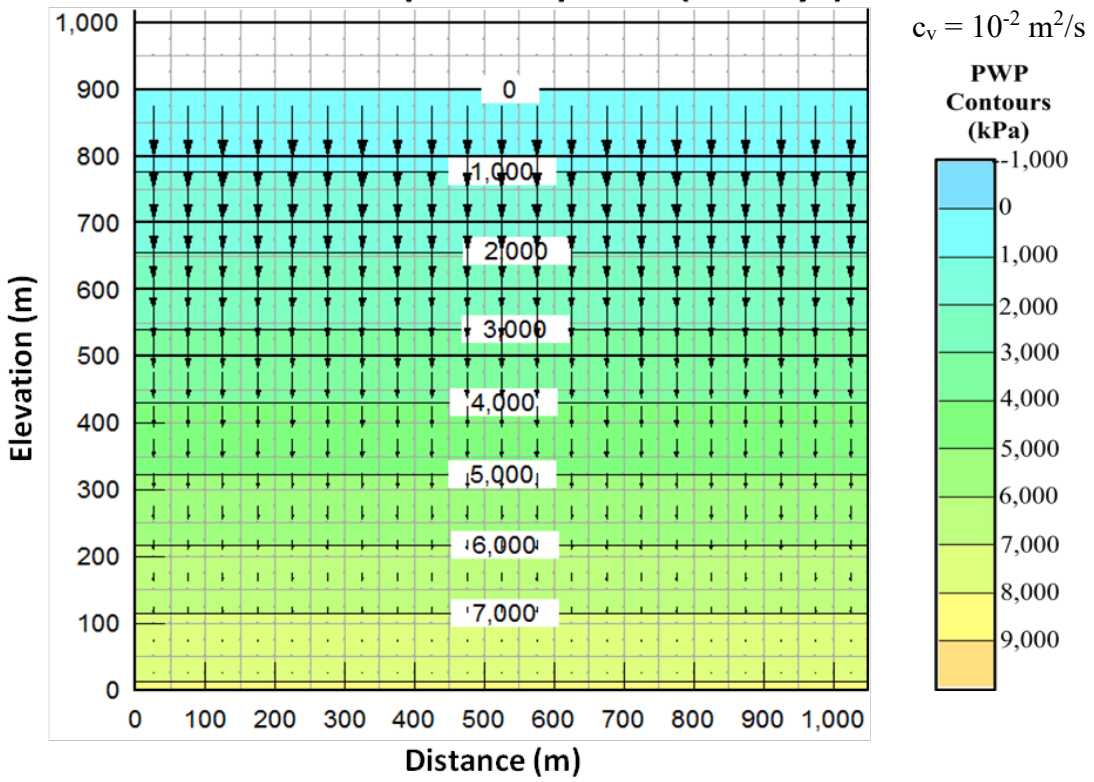
**PWP
Contours
(kPa)**



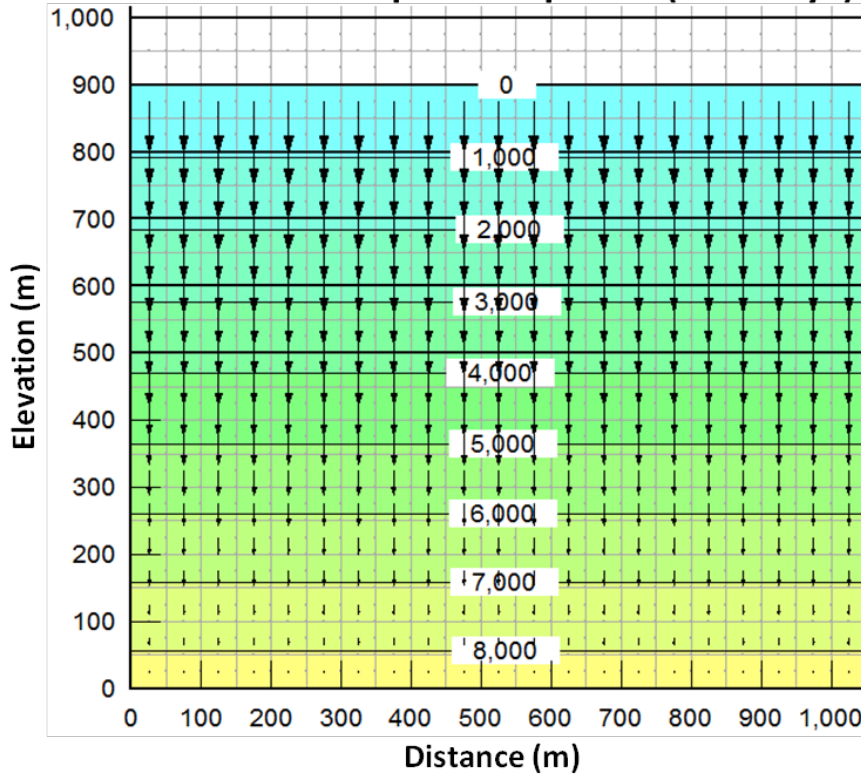
Transient Coupled Response (30 Days)



Transient Coupled Response (90 Days)

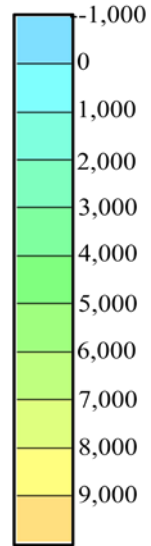


Transient Coupled Response (360 Days)

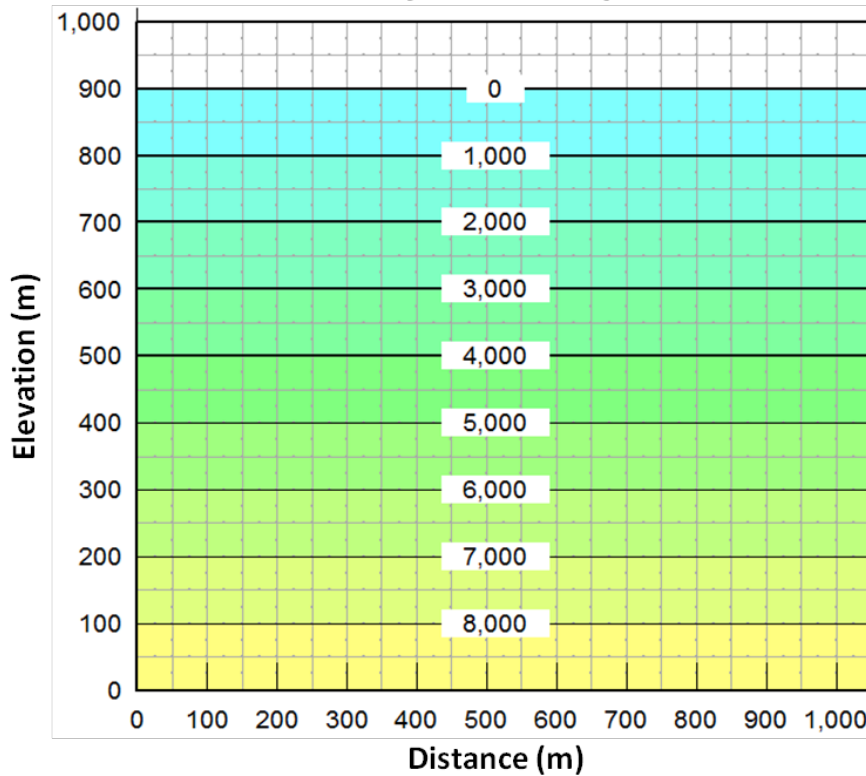


$c_v = 10^{-2} \text{ m}^2/\text{s}$

**PWP
Contours
(kPa)**

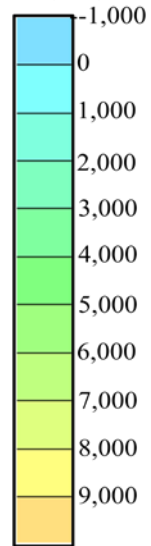


Steady-State Response

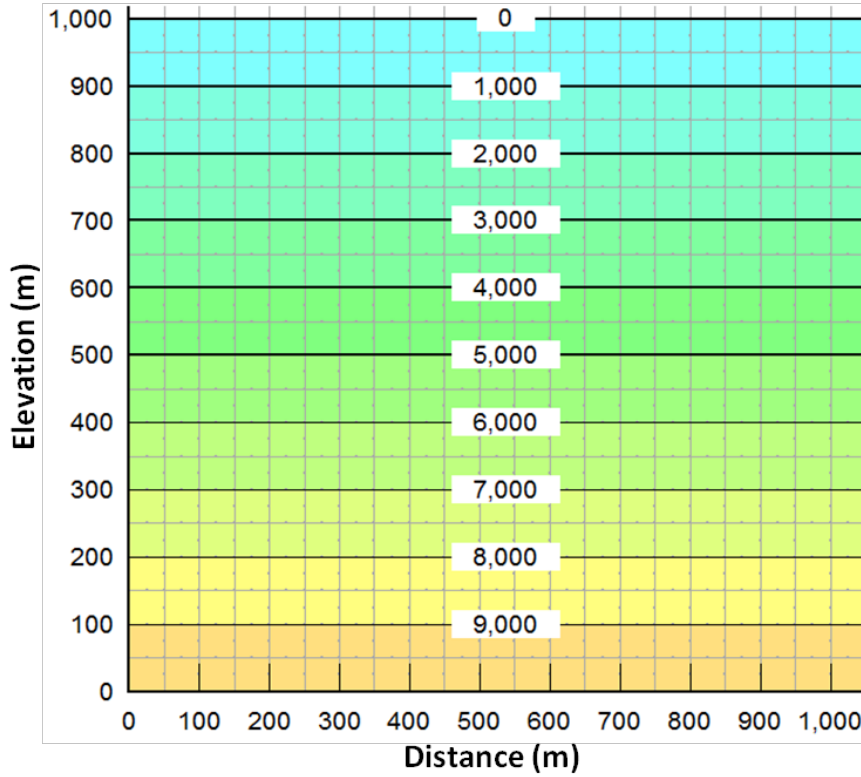


$c_v = 10^{-2} \text{ m}^2/\text{s}$

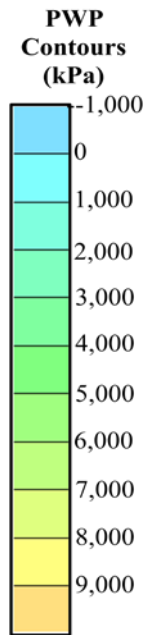
**PWP
Contours
(kPa)**



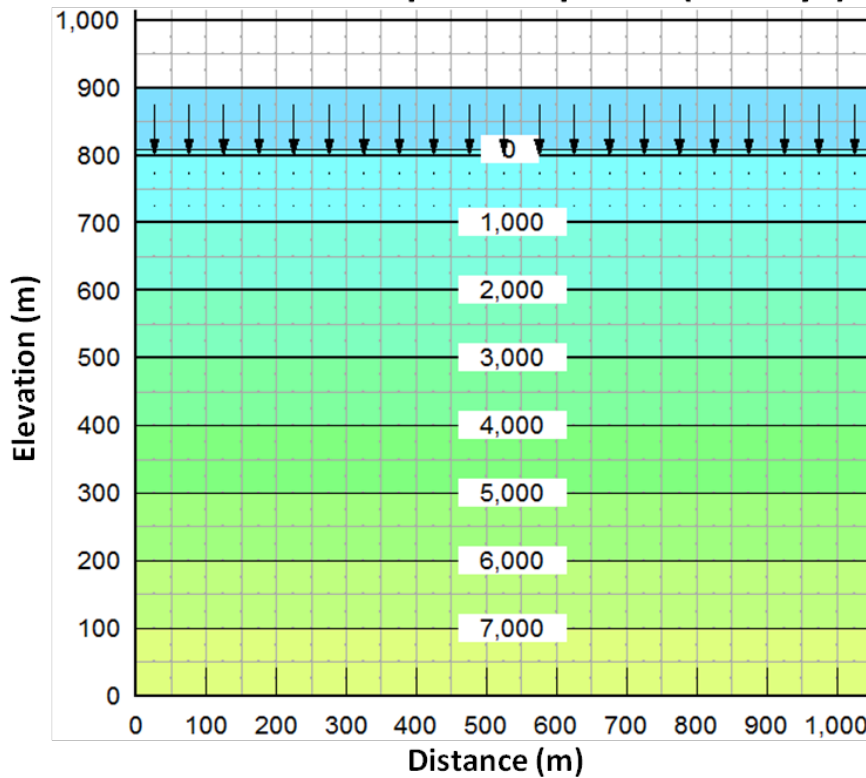
Initial Conditions



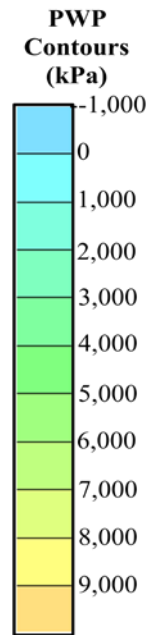
$c_v = 10^{-3} \text{ m}^2/\text{s}$



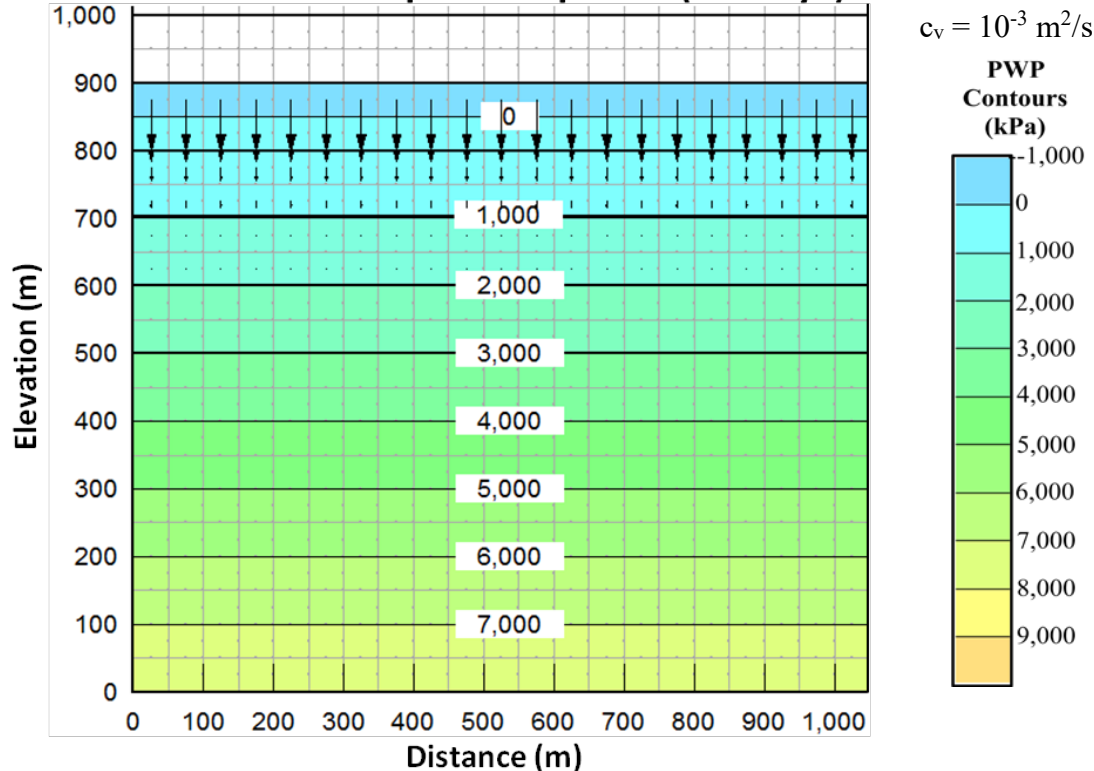
Transient Coupled Response (10 Days)



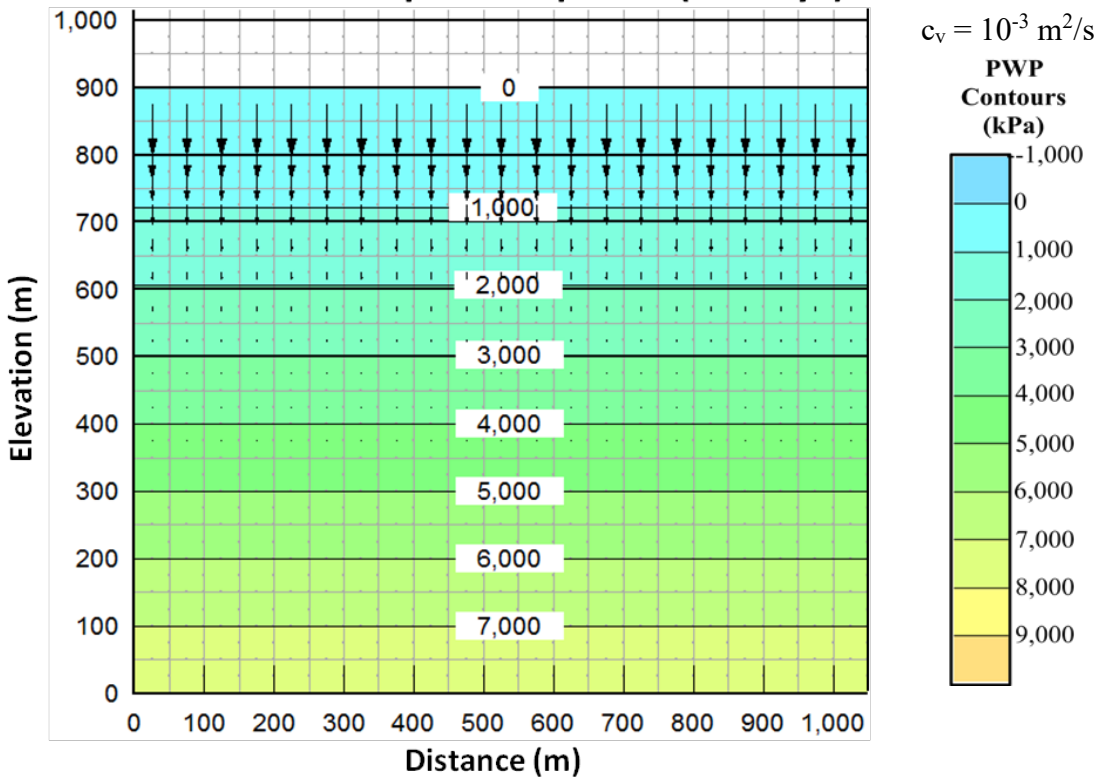
$c_v = 10^{-3} \text{ m}^2/\text{s}$



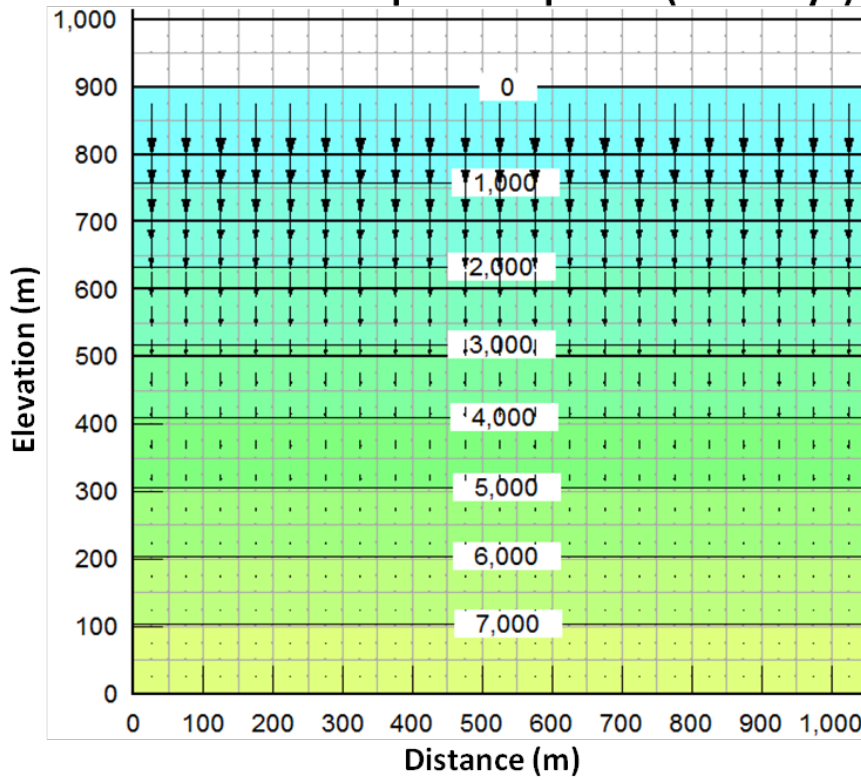
Transient Coupled Response (30 Days)



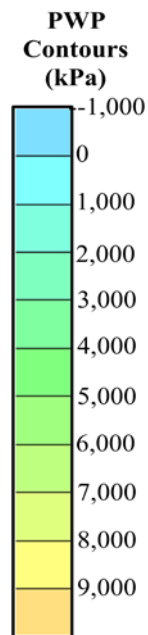
Transient Coupled Response (90 Days)



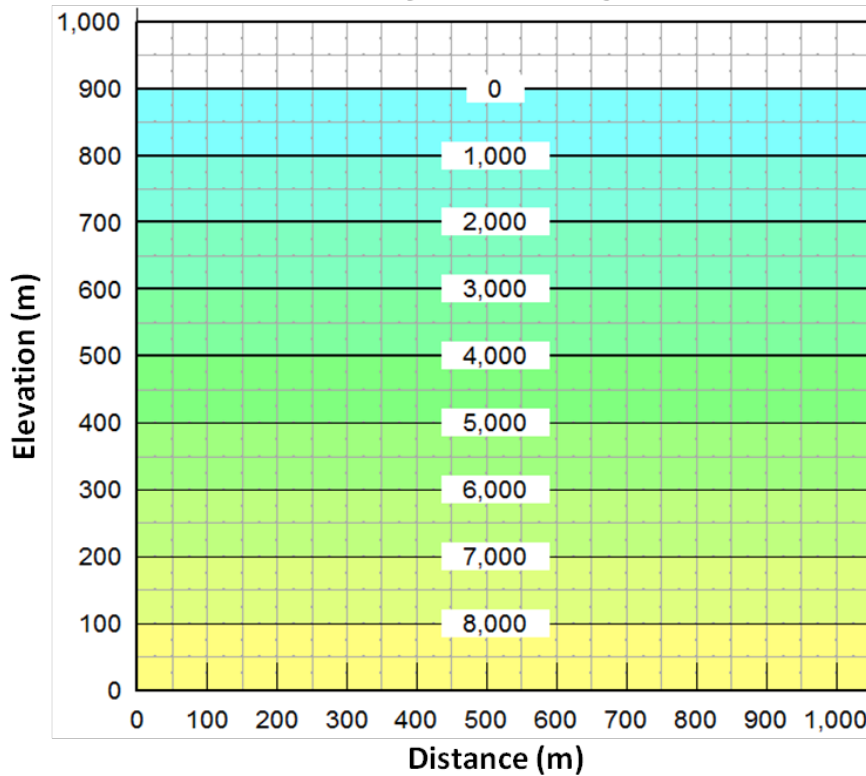
Transient Coupled Response (360 Days)



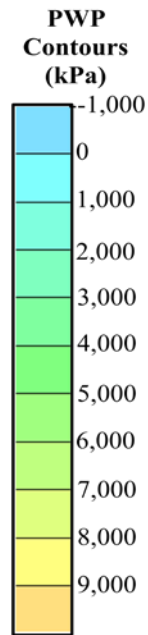
$c_v = 10^{-3} \text{ m}^2/\text{s}$



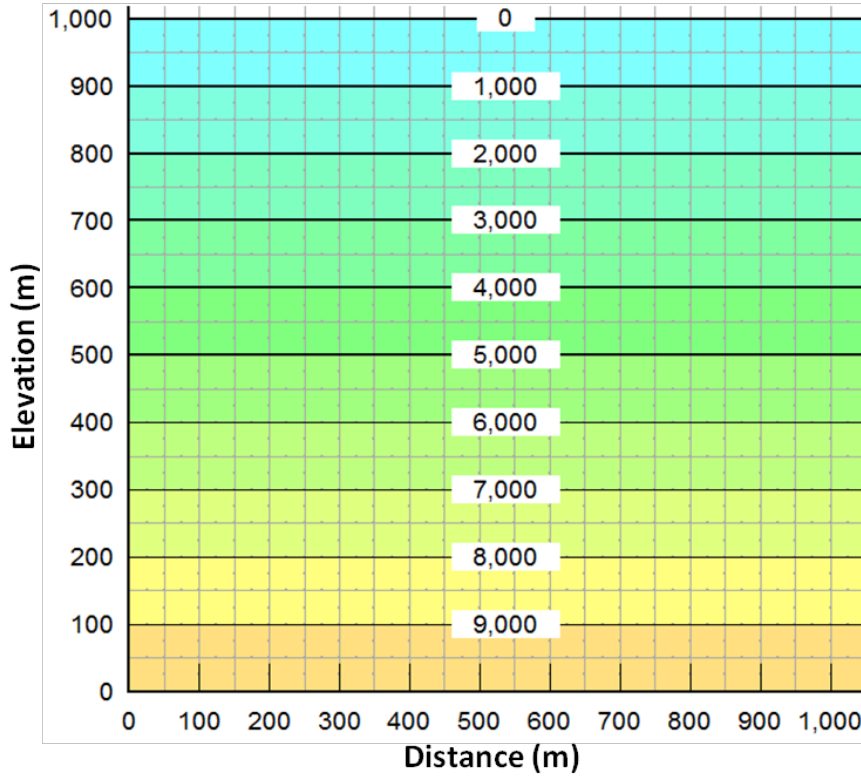
Steady-State Response



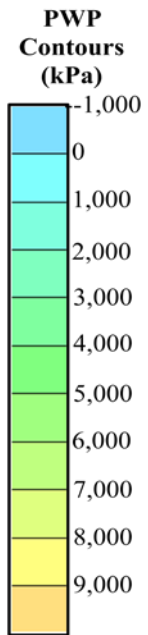
$c_v = 10^{-3} \text{ m}^2/\text{s}$



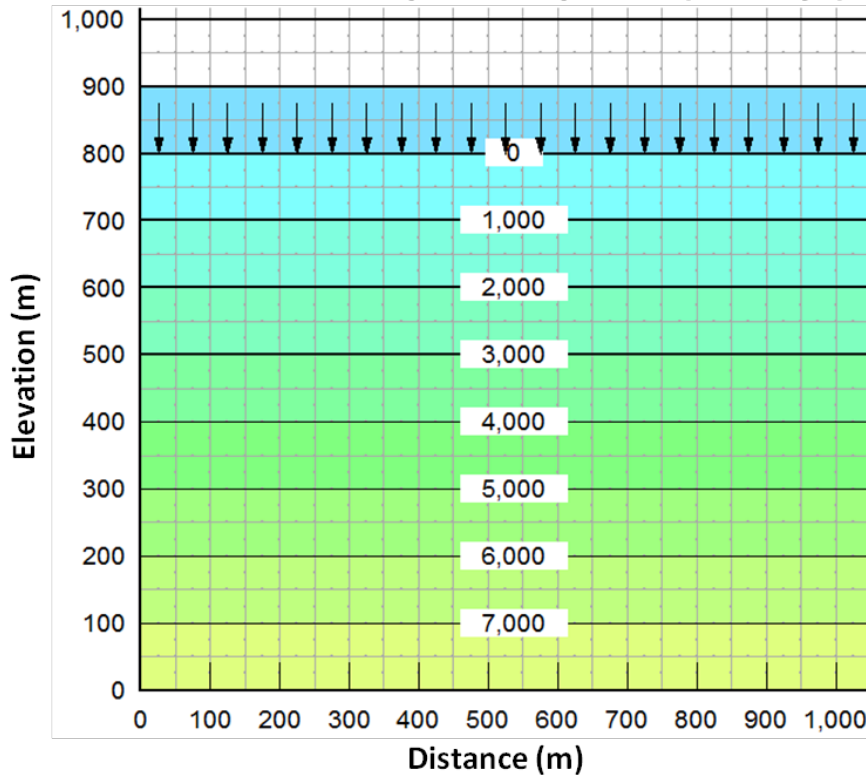
Initial Conditions



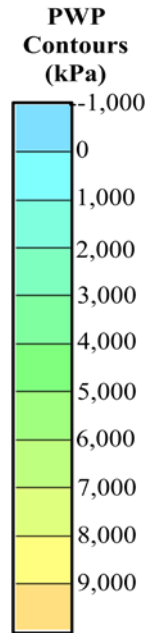
$$c_v = 10^{-4} \text{ m}^2/\text{s}$$



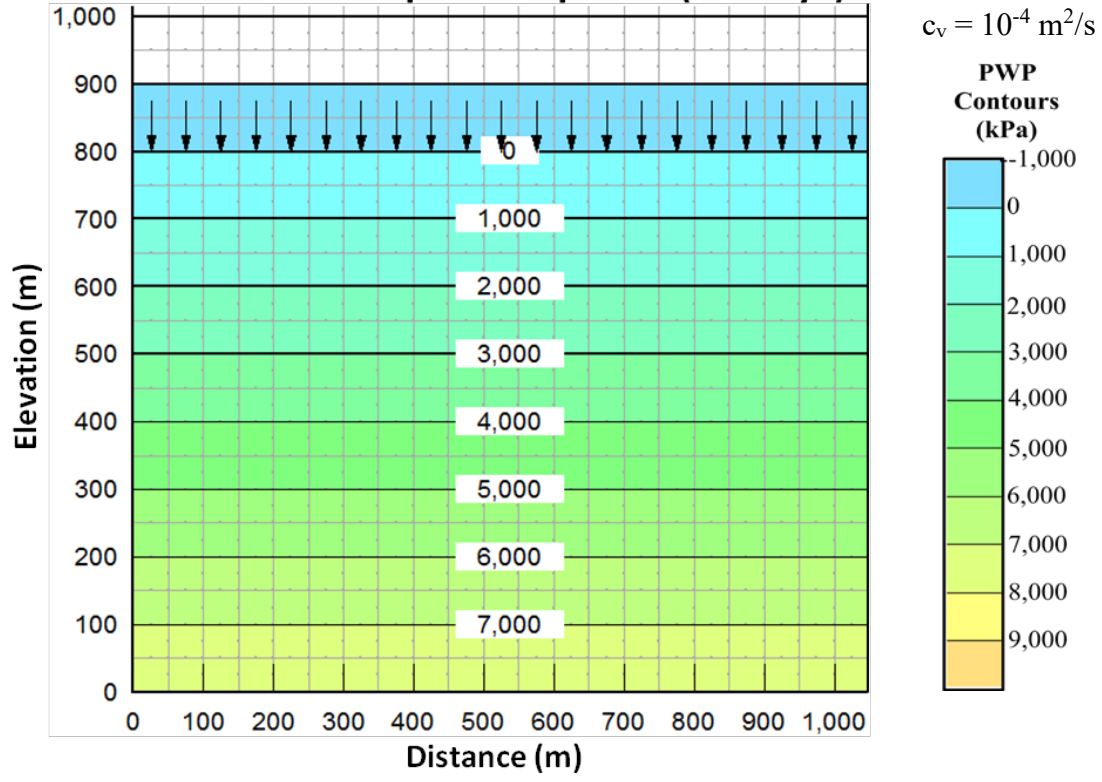
Transient Coupled Response (10 Days)



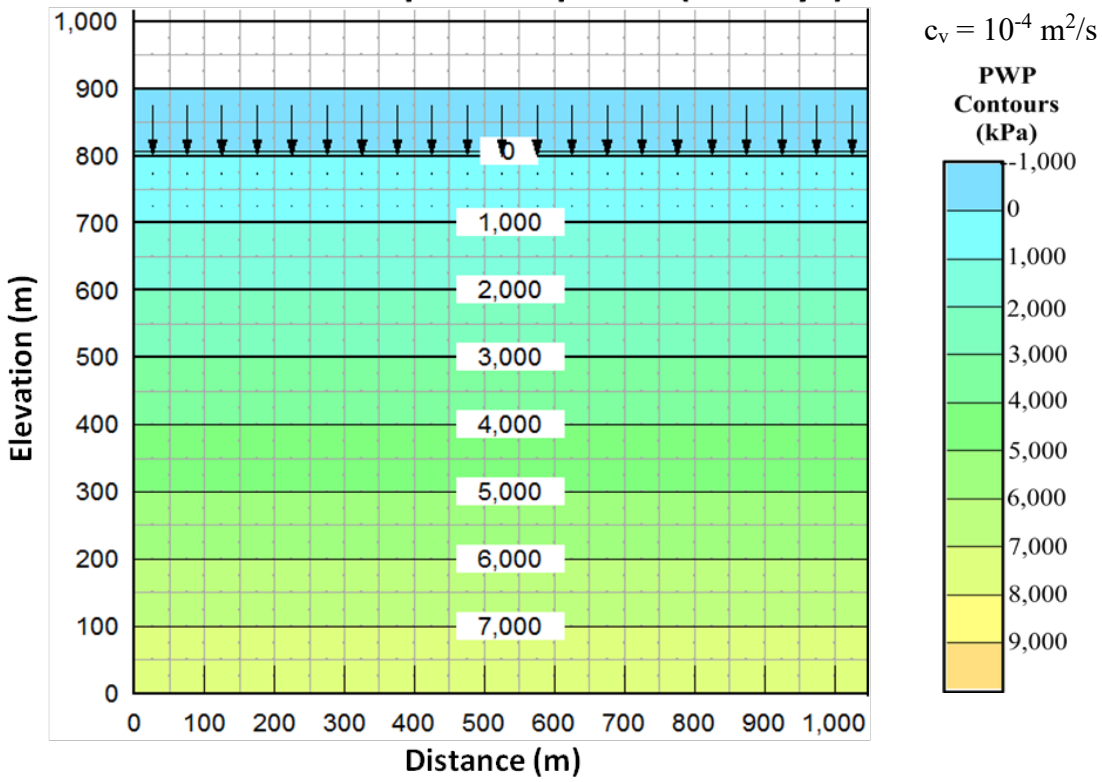
$$c_v = 10^{-4} \text{ m}^2/\text{s}$$



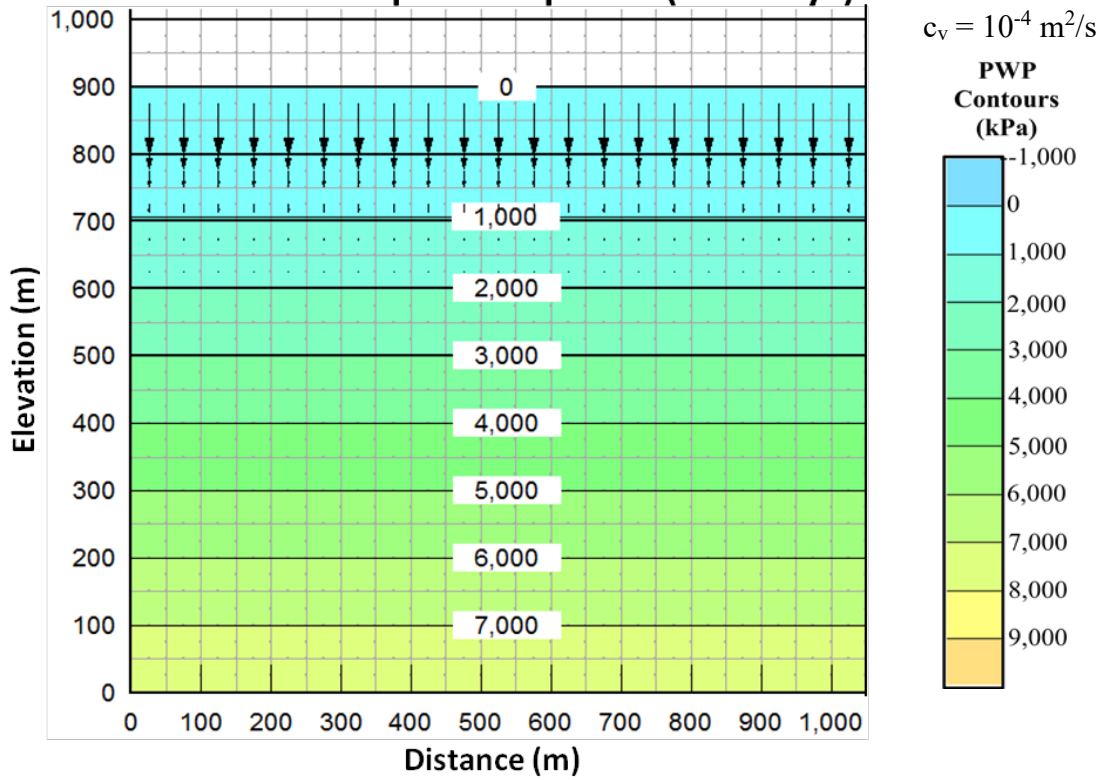
Transient Coupled Response (30 Days)



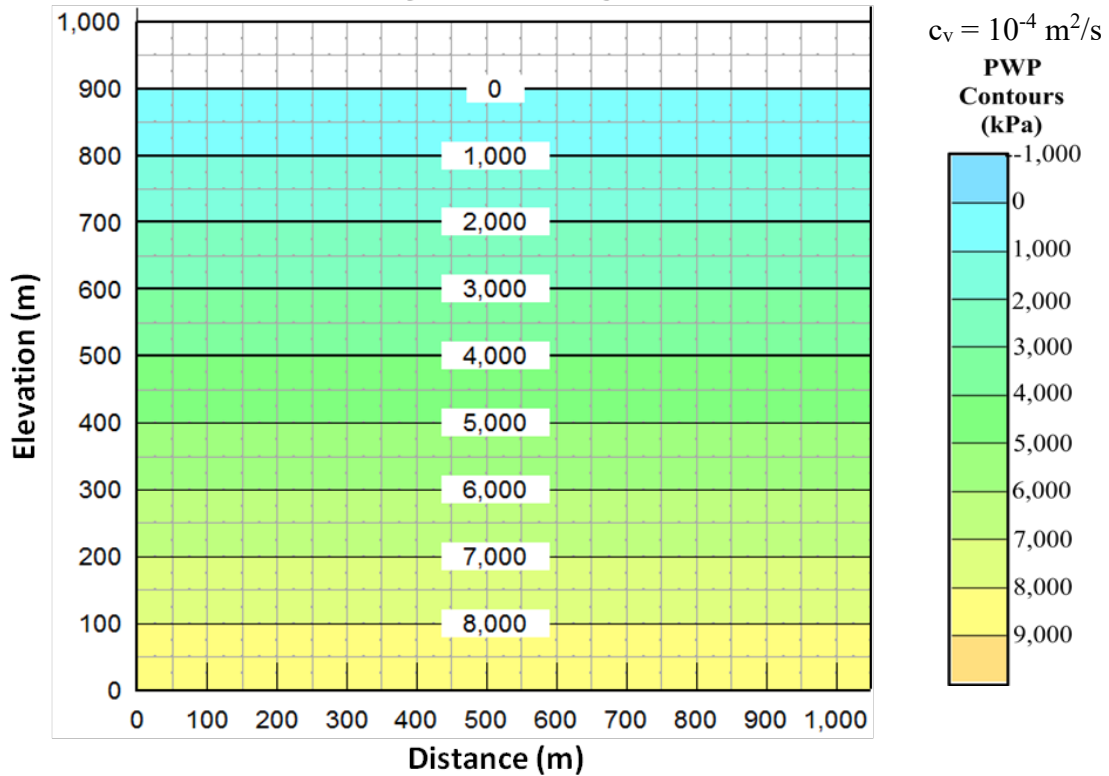
Transient Coupled Response (90 Days)

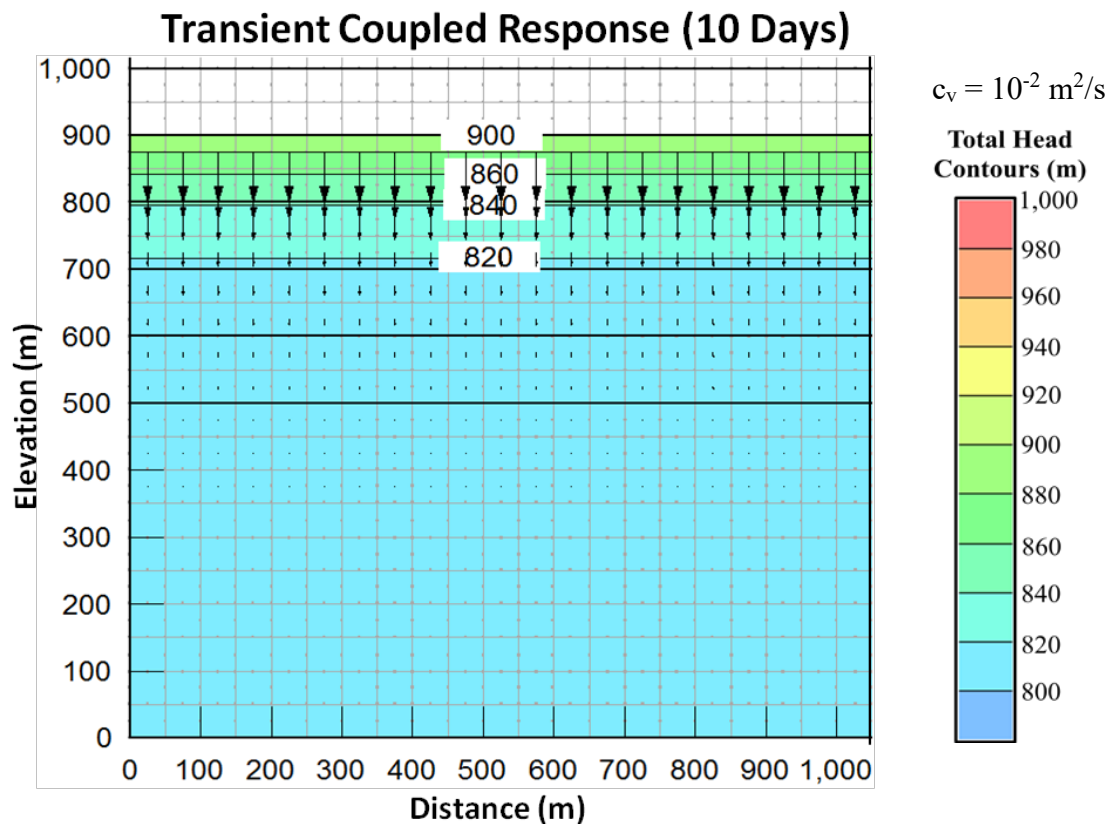
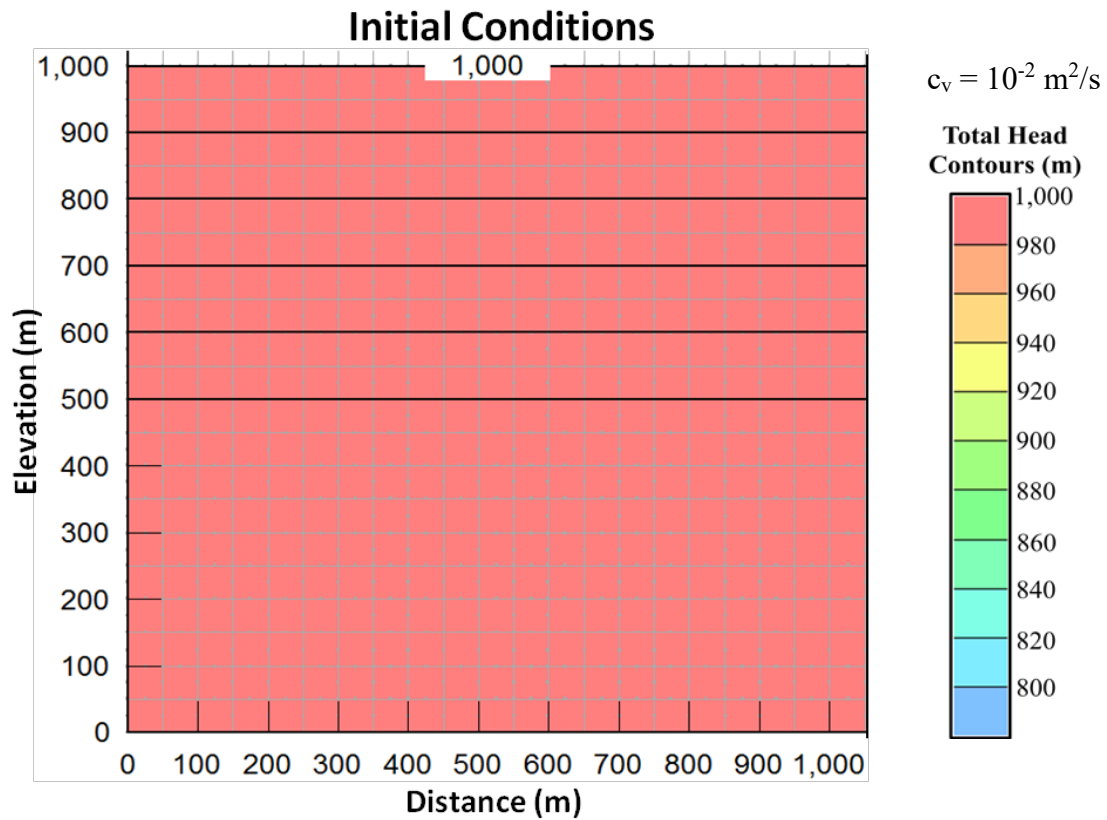


Transient Coupled Response (360 Days)

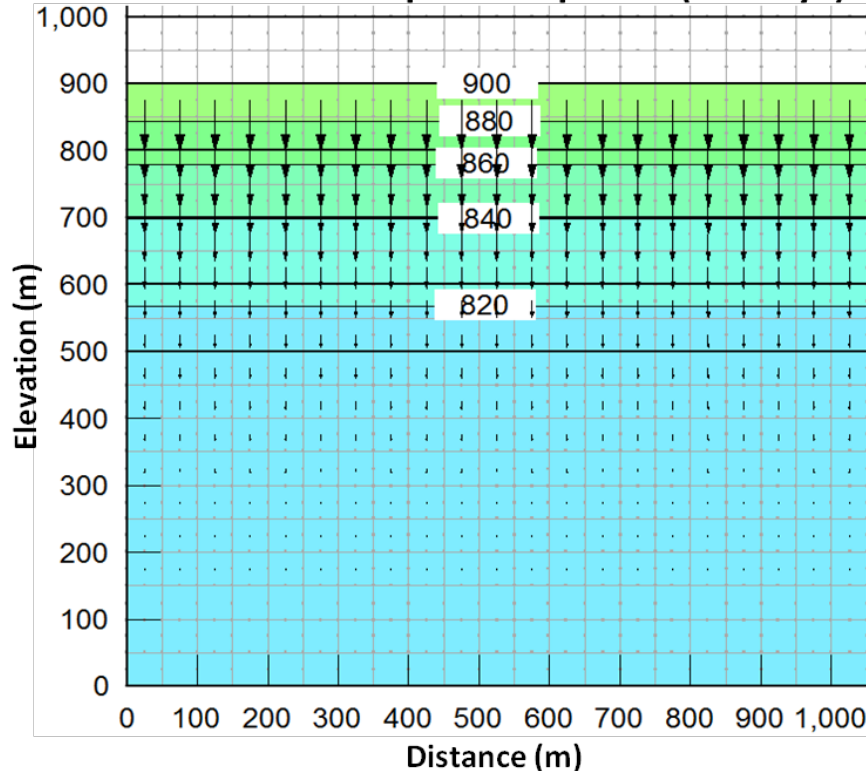


Steady-State Response



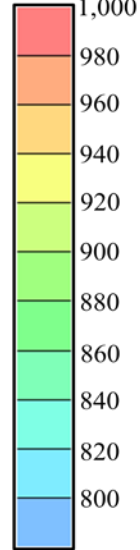


Transient Coupled Response (30 Days)

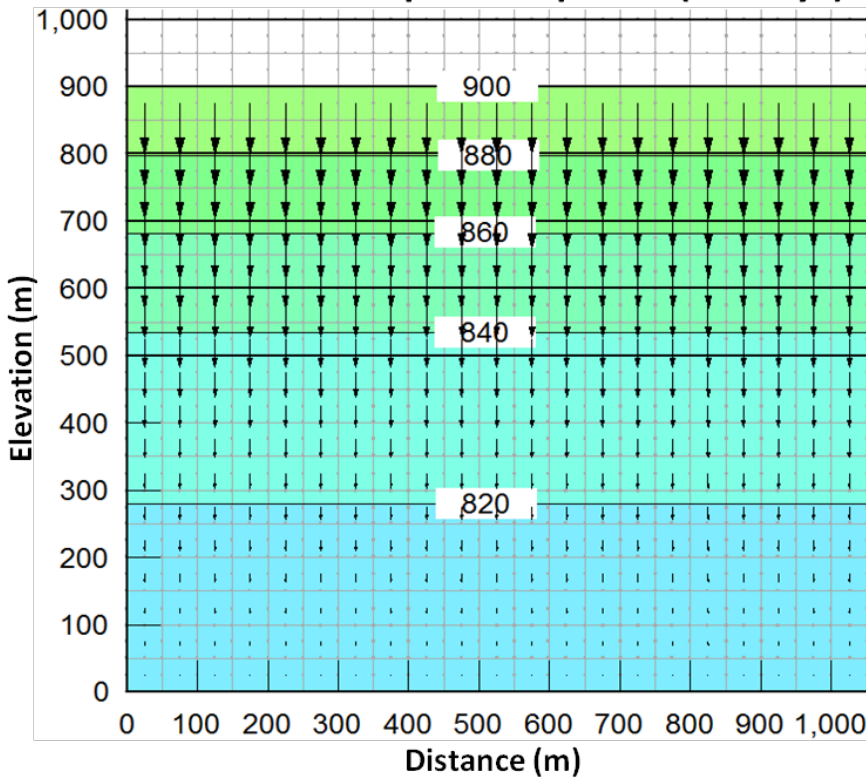


$c_v = 10^{-2} \text{ m}^2/\text{s}$

Total Head Contours (m)

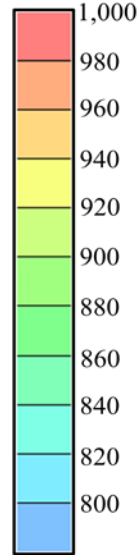


Transient Coupled Response (90 Days)

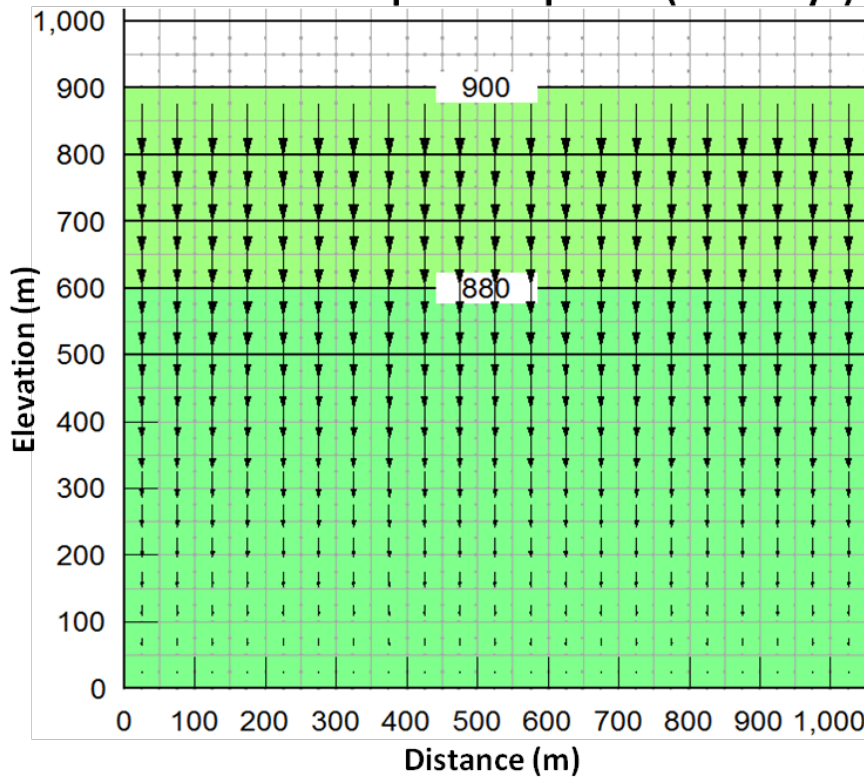


$c_v = 10^{-2} \text{ m}^2/\text{s}$

Total Head Contours (m)

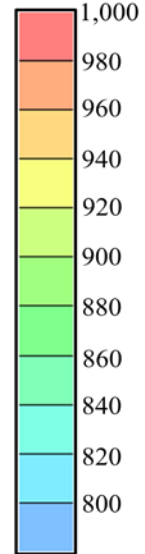


Transient Coupled Response (360 Days)

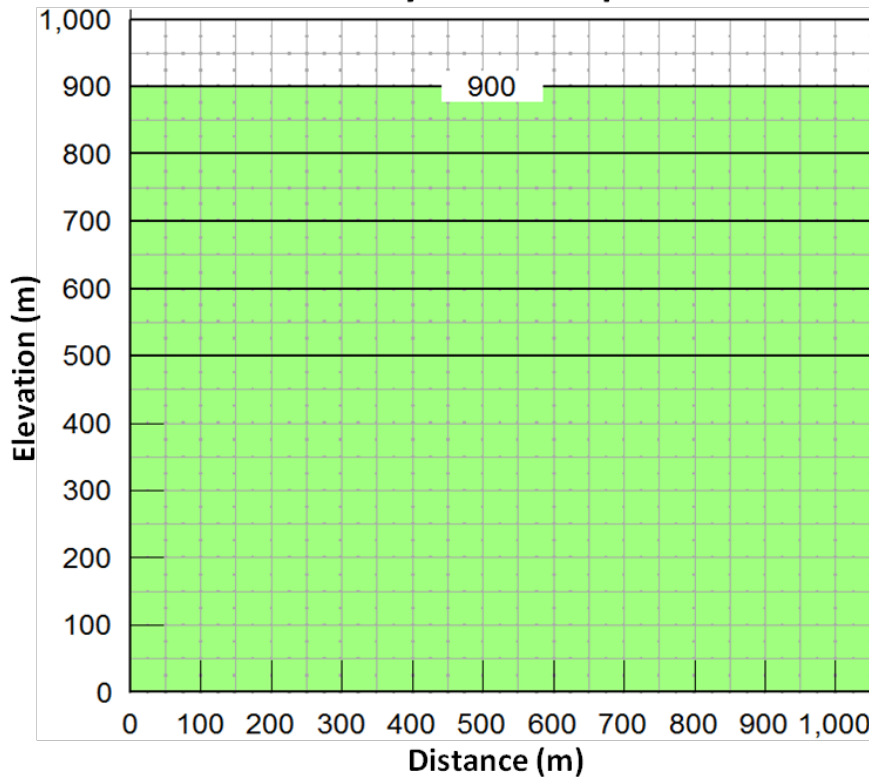


$$c_v = 10^{-2} \text{ m}^2/\text{s}$$

Total Head Contours (m)

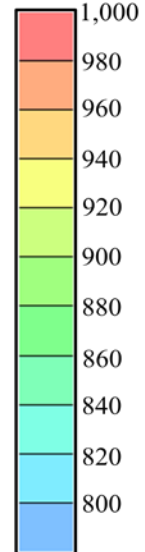


Steady-State Response

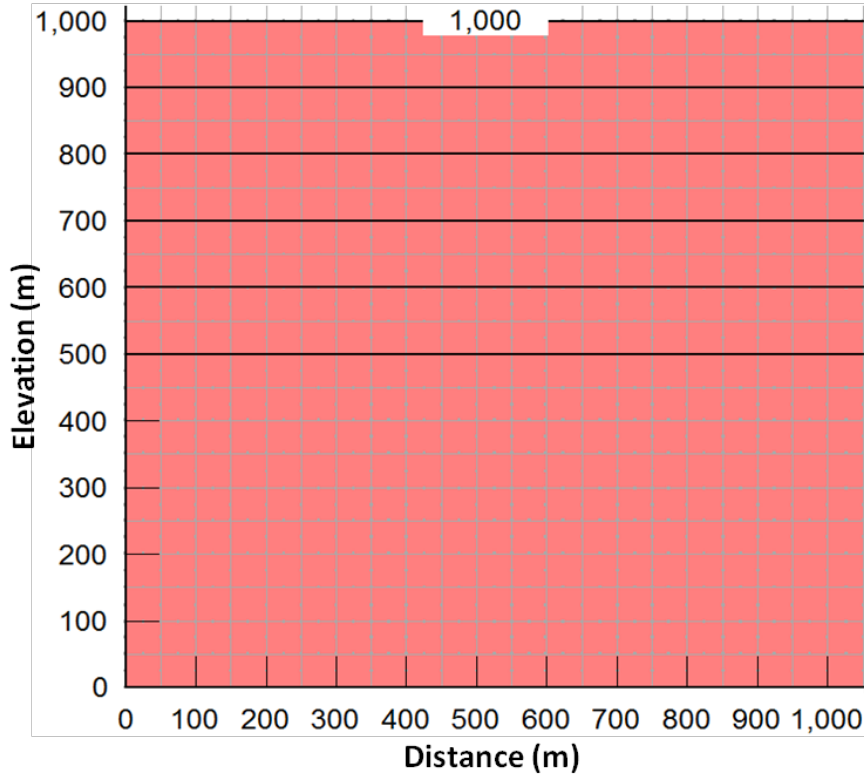


$$c_v = 10^{-2} \text{ m}^2/\text{s}$$

Total Head Contours (m)

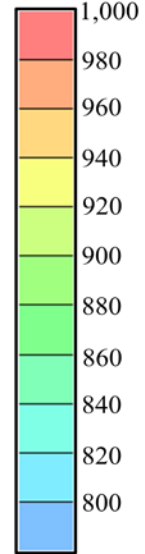


Initial Conditions

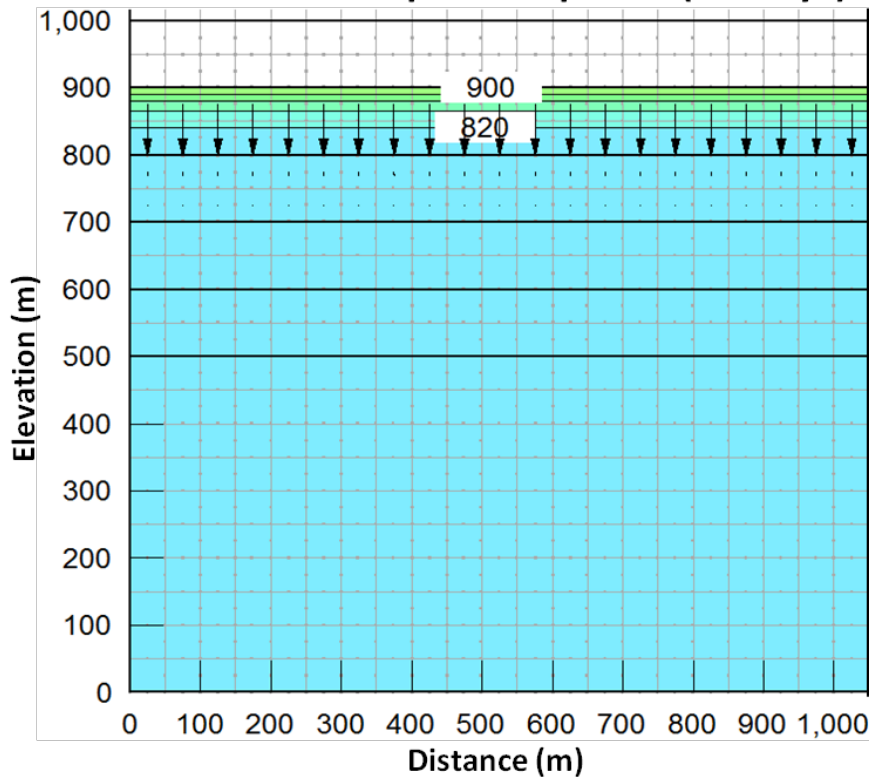


$c_v = 10^{-3} \text{ m}^2/\text{s}$

Total Head Contours (m)

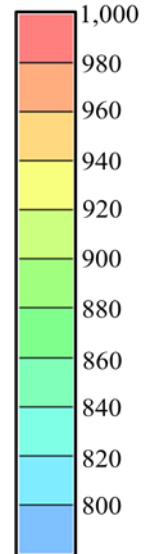


Transient Coupled Response (10 Days)

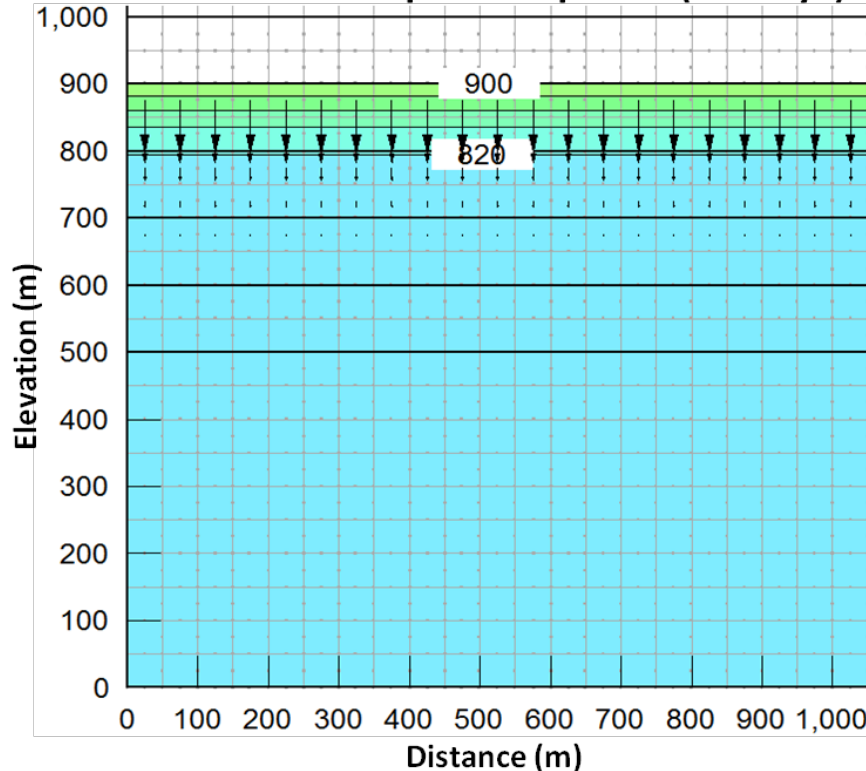


$c_v = 10^{-3} \text{ m}^2/\text{s}$

Total Head Contours (m)

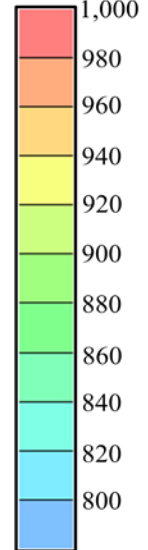


Transient Coupled Response (30 Days)

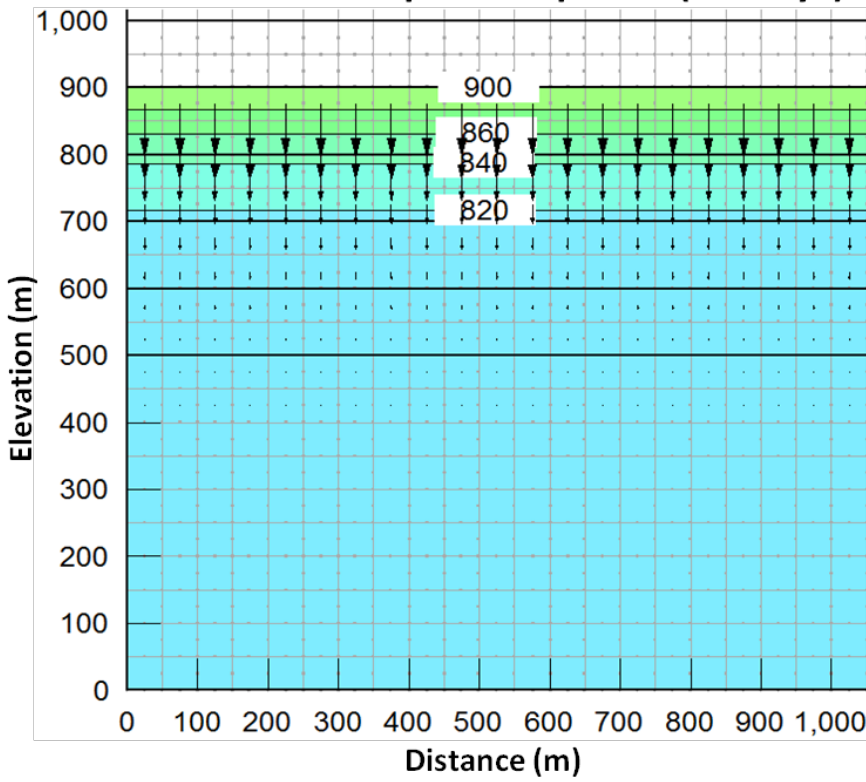


$c_v = 10^{-3} \text{ m}^2/\text{s}$

Total Head Contours (m)

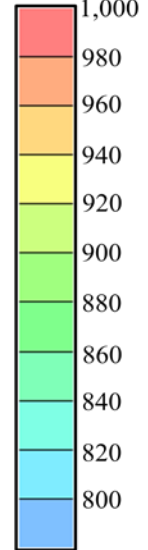


Transient Coupled Response (90 Days)

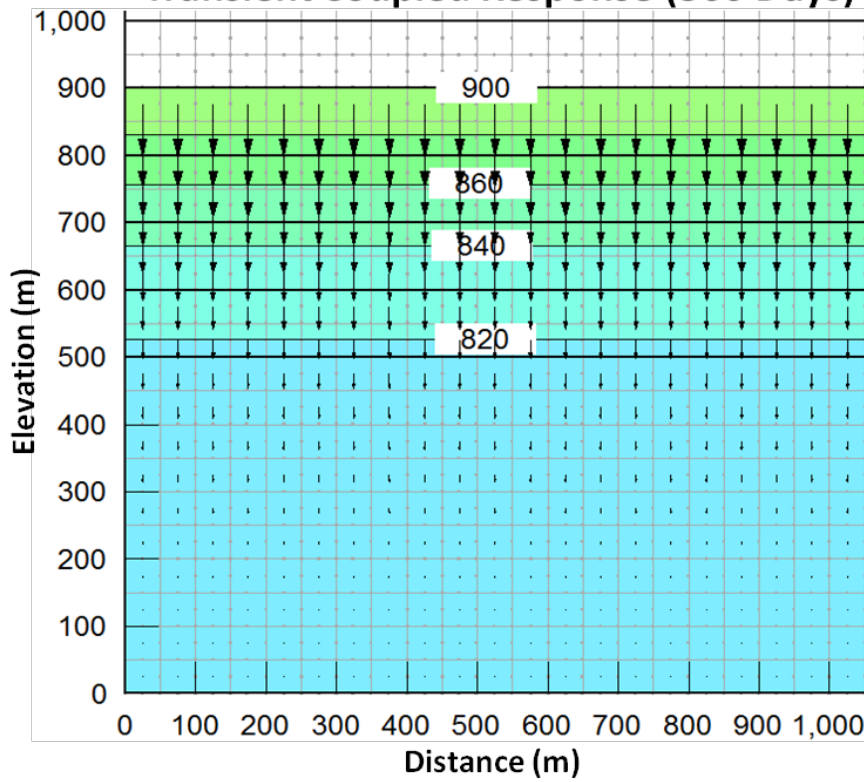


$c_v = 10^{-3} \text{ m}^2/\text{s}$

Total Head Contours (m)

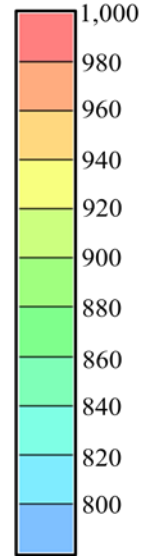


Transient Coupled Response (360 Days)

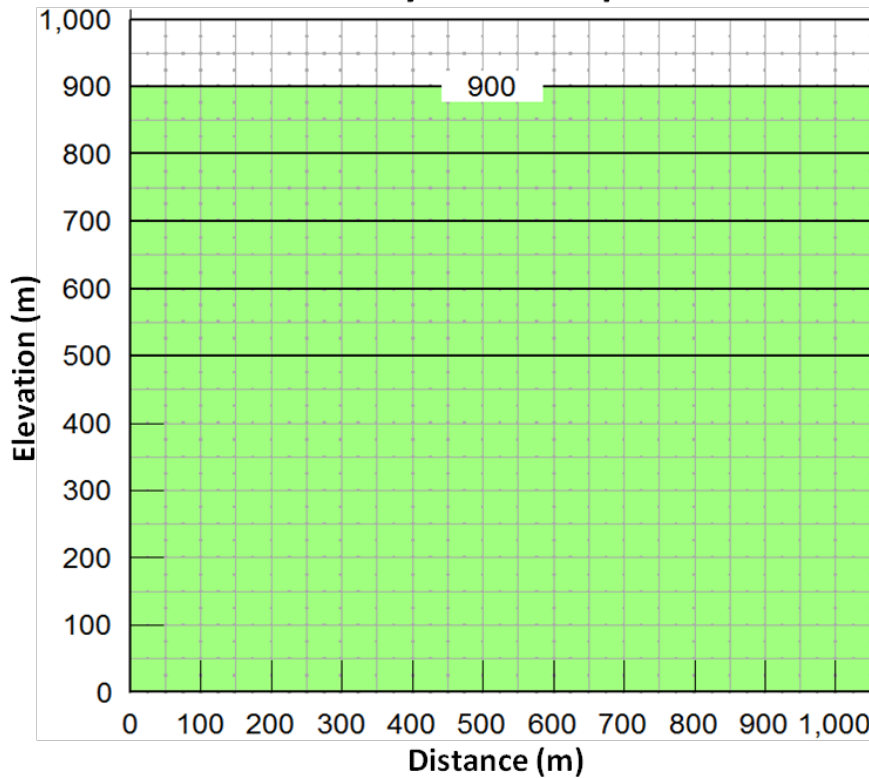


$c_v = 10^{-3} \text{ m}^2/\text{s}$

Total Head Contours (m)

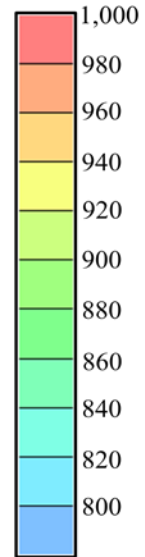


Steady-State Response

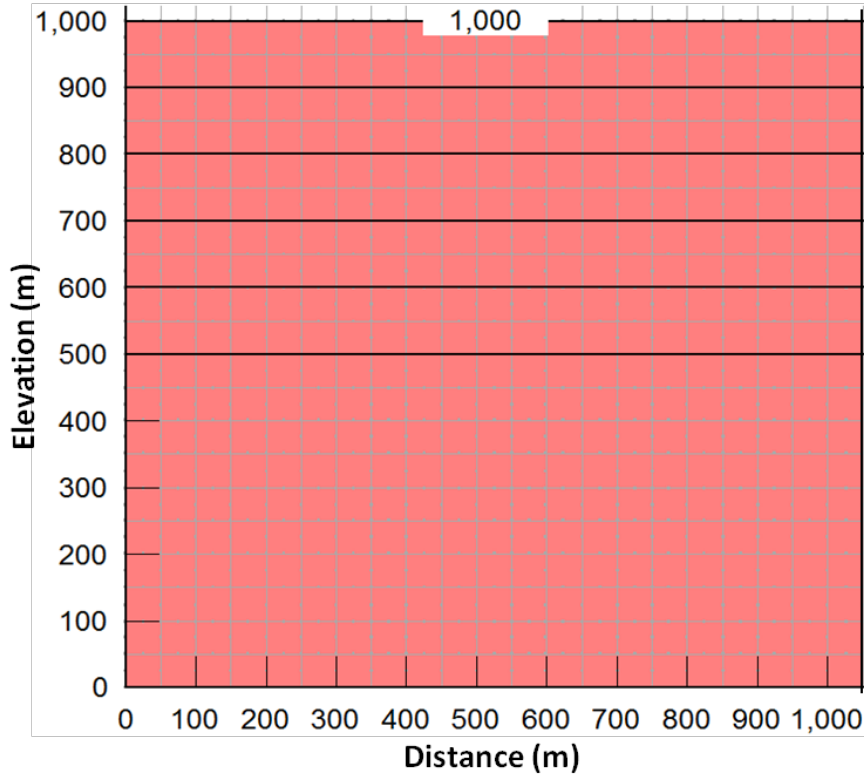


$c_v = 10^{-3} \text{ m}^2/\text{s}$

Total Head Contours (m)

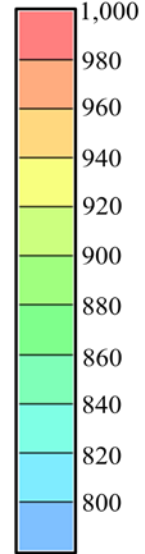


Initial Conditions

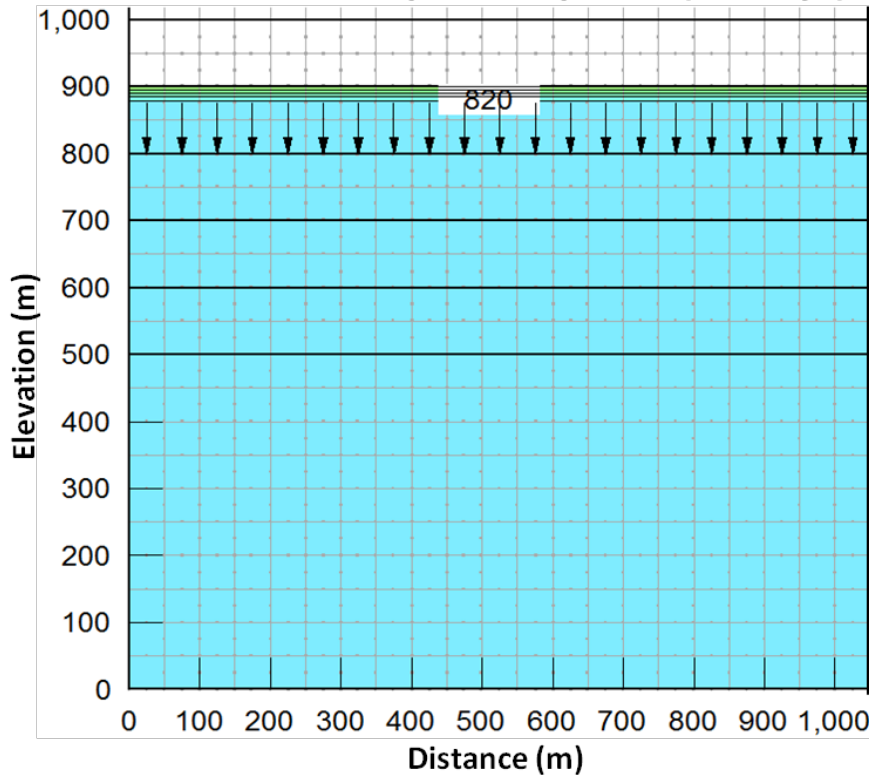


$$c_v = 10^{-4} \text{ m}^2/\text{s}$$

Total Head Contours (m)

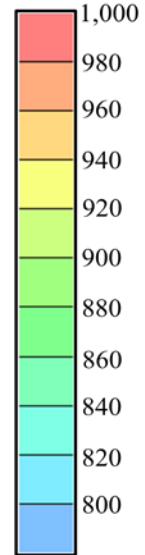


Transient Coupled Response (10 Days)

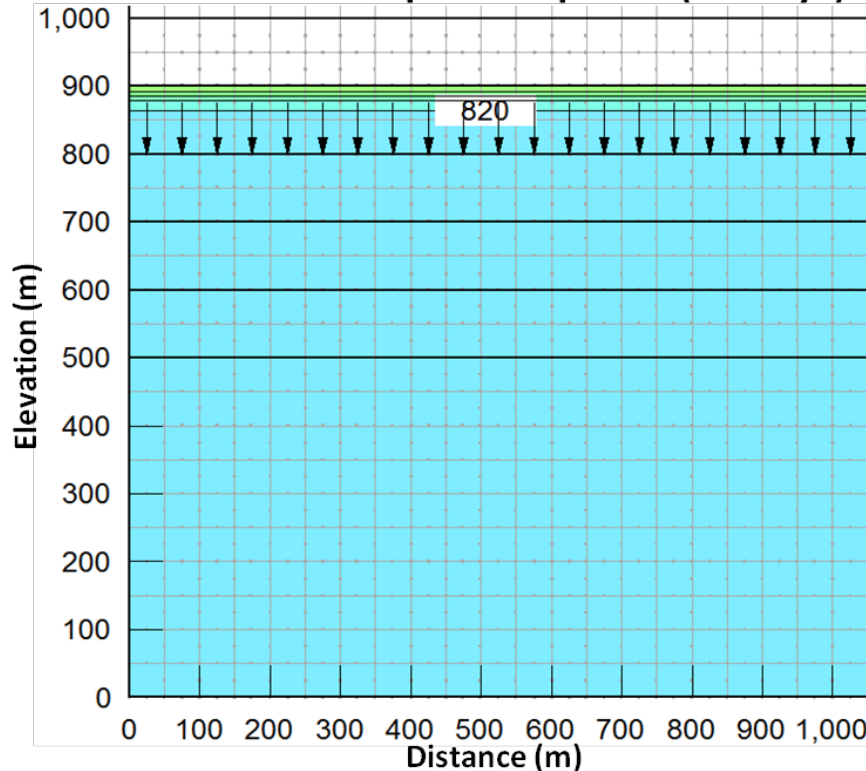


$$c_v = 10^{-4} \text{ m}^2/\text{s}$$

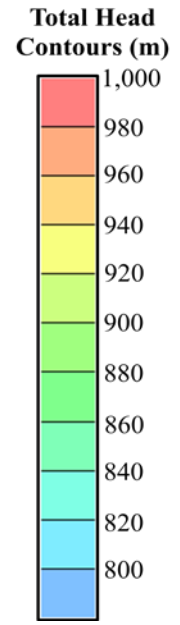
Total Head Contours (m)



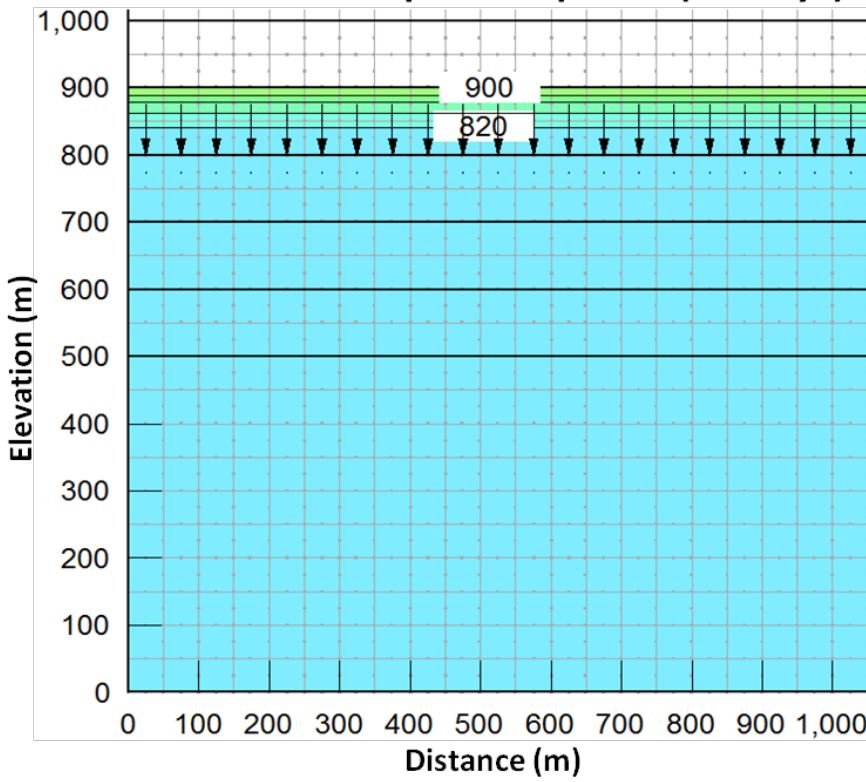
Transient Coupled Response (30 Days)



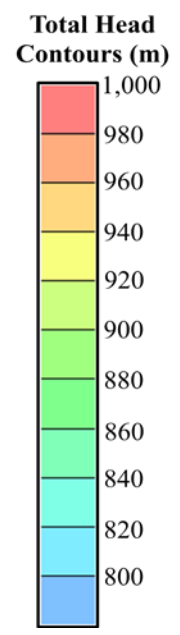
$c_v = 10^{-4} \text{ m}^2/\text{s}$



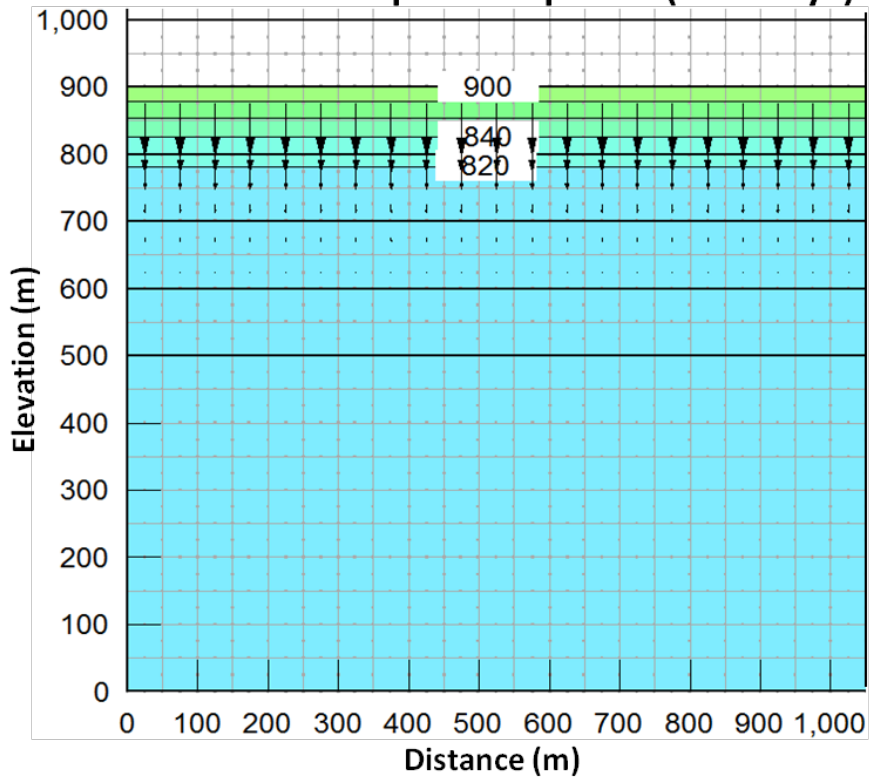
Transient Coupled Response (90 Days)



$c_v = 10^{-4} \text{ m}^2/\text{s}$

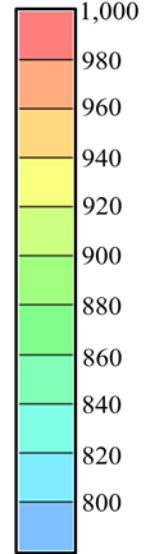


Transient Coupled Response (360 Days)

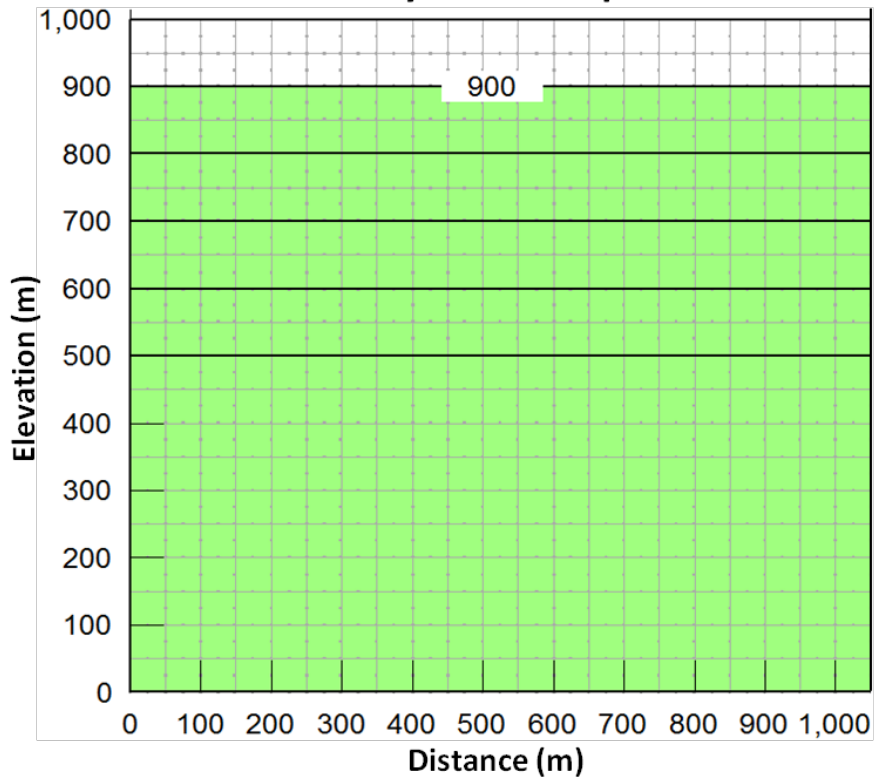


$c_v = 10^{-4} \text{ m}^2/\text{s}$

Total Head Contours (m)

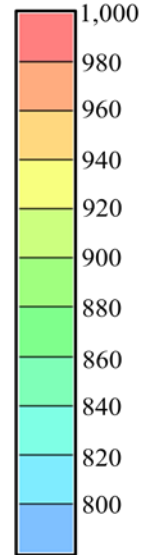


Steady-State Response

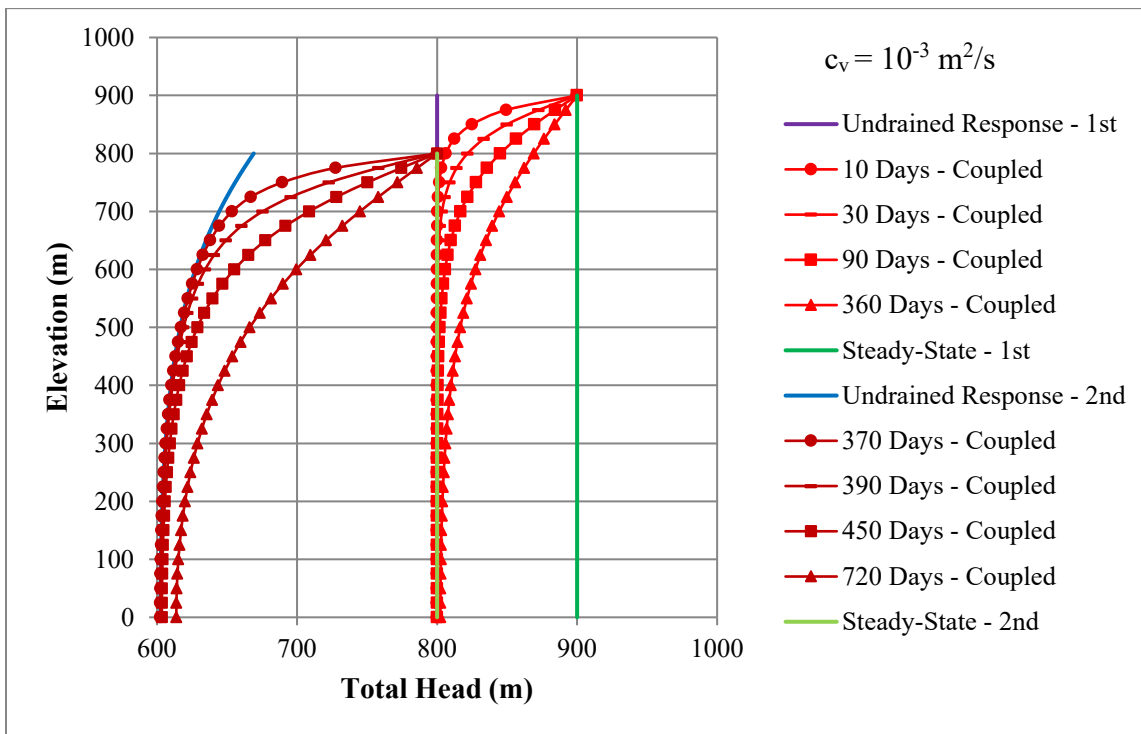
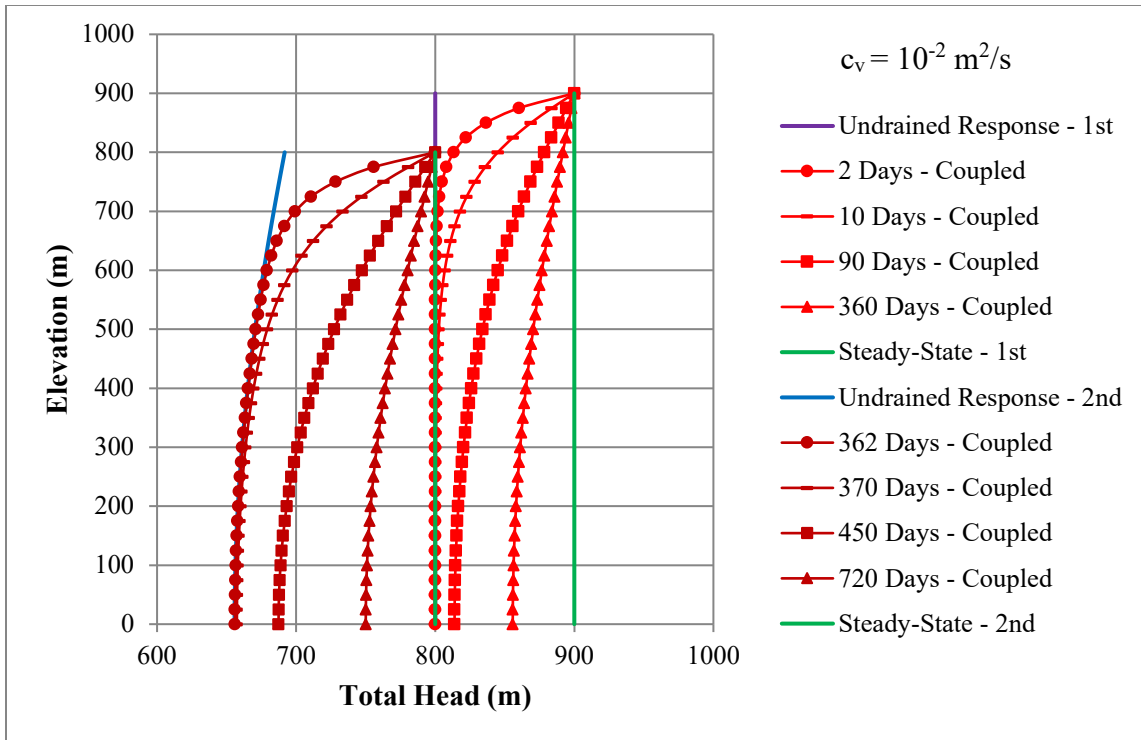


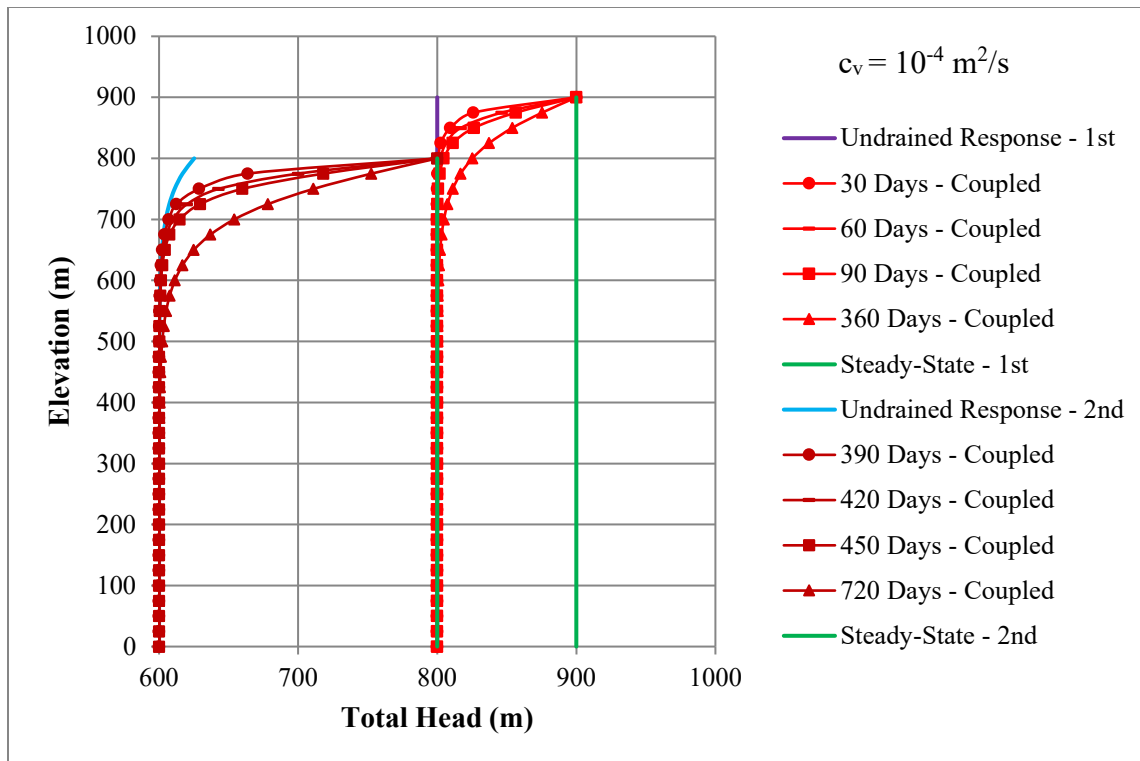
$c_v = 10^{-4} \text{ m}^2/\text{s}$

Total Head Contours (m)



Pages 104-105: Graphs of total heads for each of the three different diffusion coefficients (10^{-2} , 10^{-3} and 10^{-4} m²/s) and two excavations.

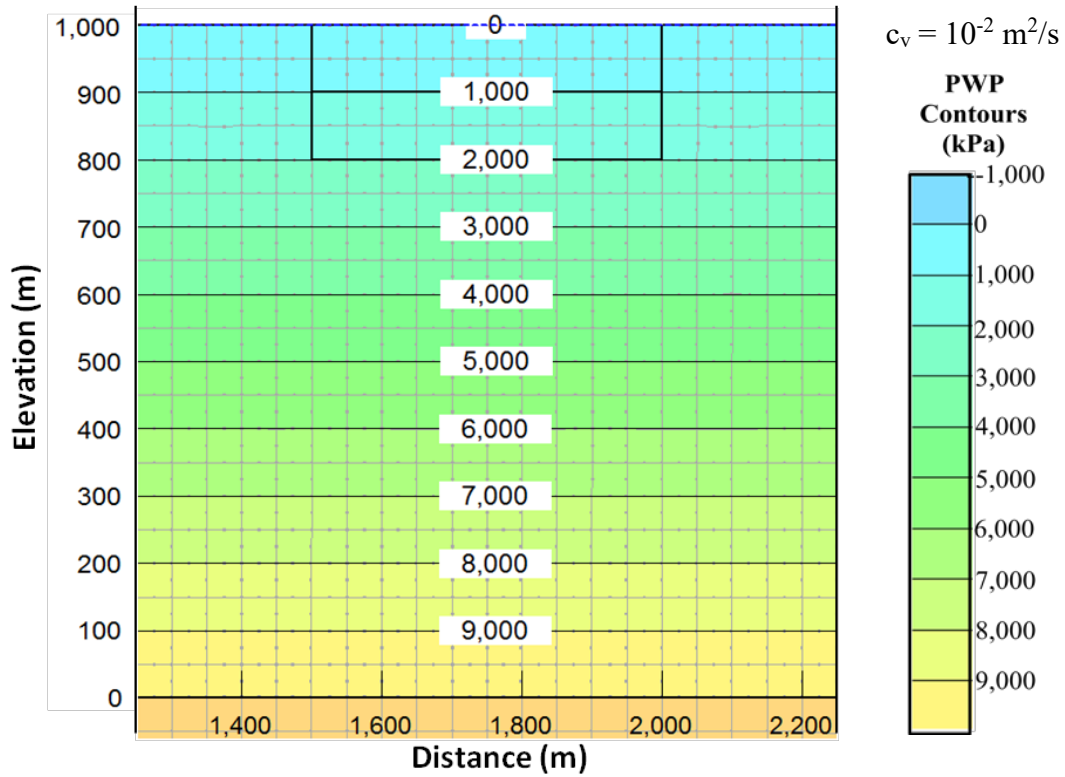




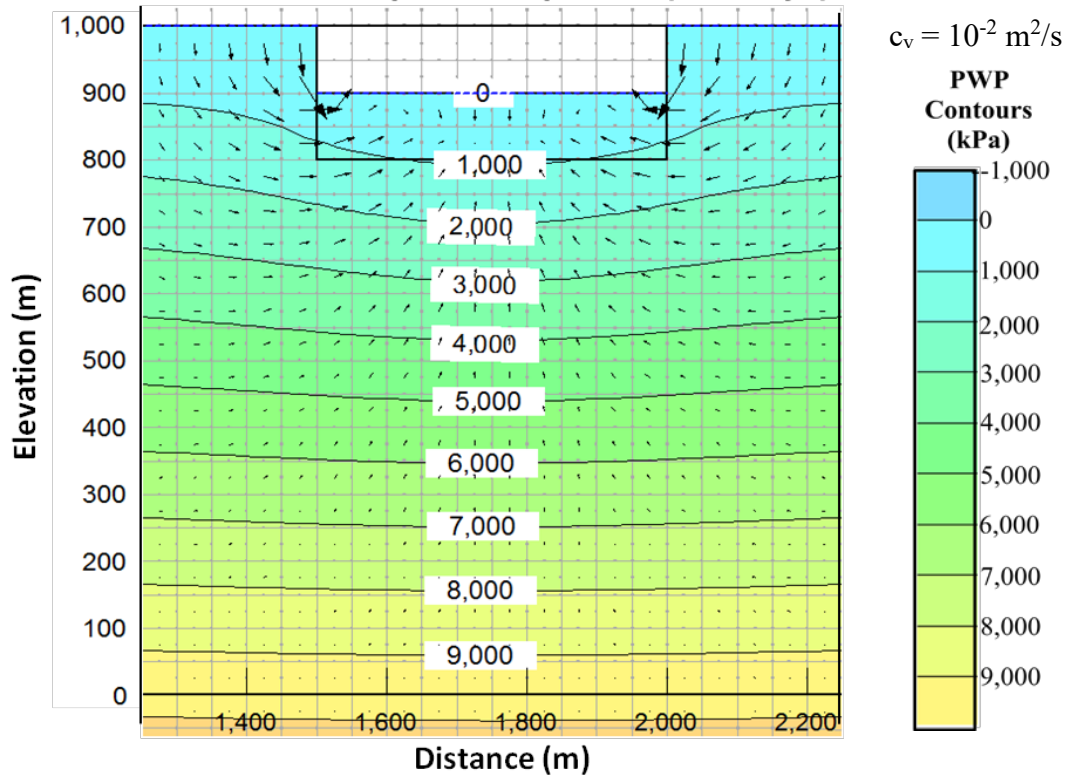
Appendix B: Additional 2-D Confined Flow Results

Pages 108-143: Pore water pressure and total head contour charts for each of the three different diffusion coefficients (10^{-2} , 10^{-3} and 10^{-4} m²/s). Included are comparisons between the transient seepage response and transient coupled response for each diffusion coefficient.

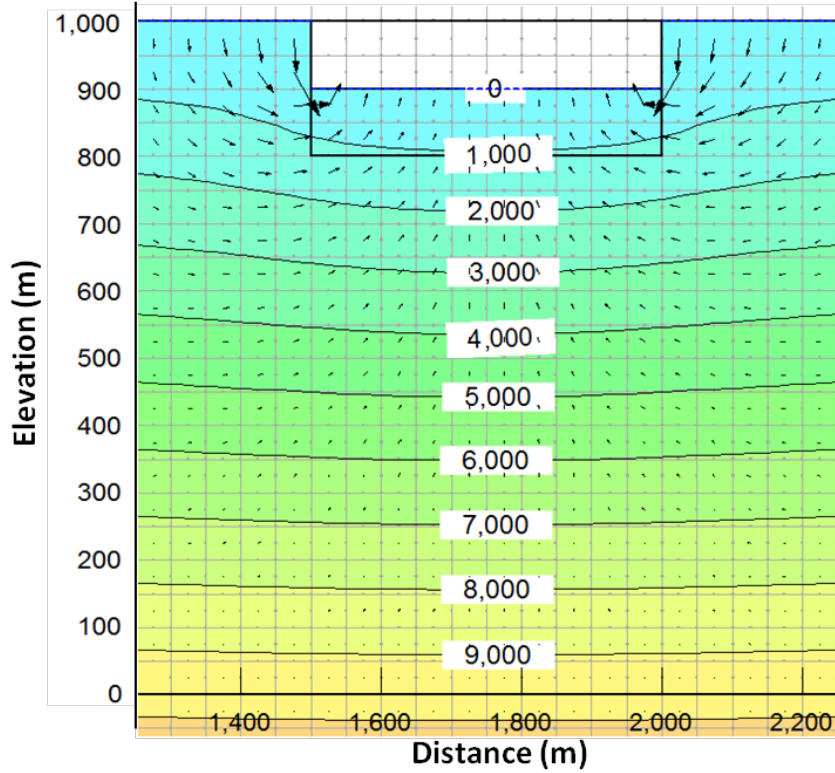
Initial Conditions



Transient Coupled Response (10 Days)

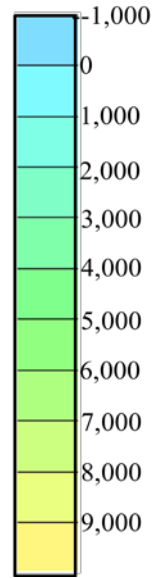


Transient Coupled Response (30 Days)

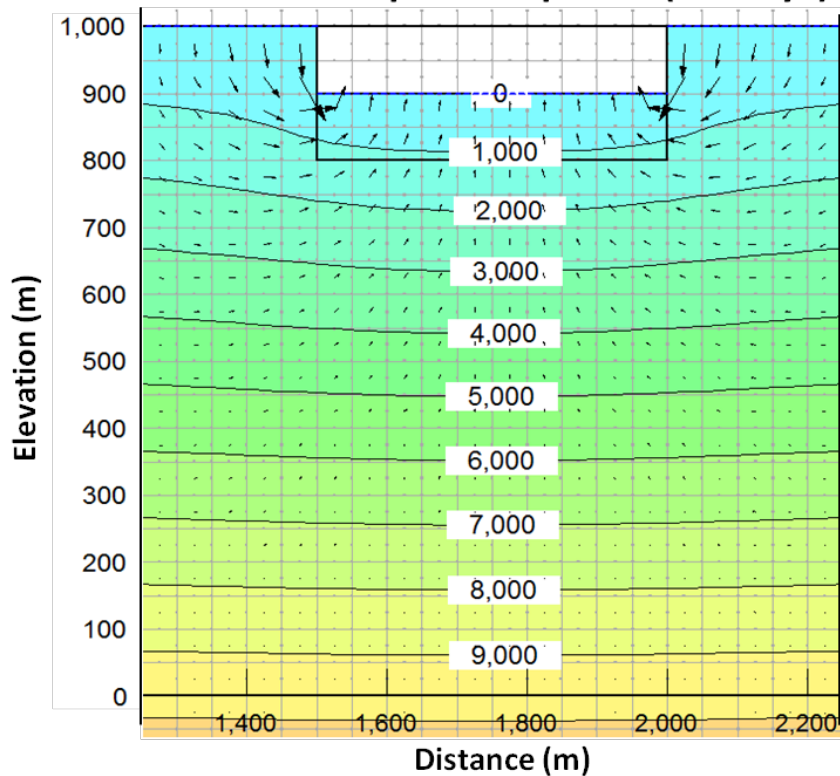


$$c_v = 10^{-2} \text{ m}^2/\text{s}$$

**PWP
Contours
(kPa)**

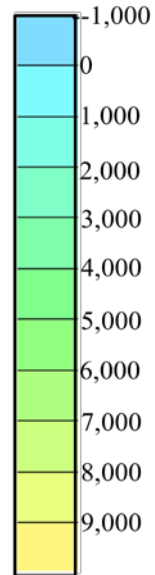


Transient Coupled Response (90 Days)

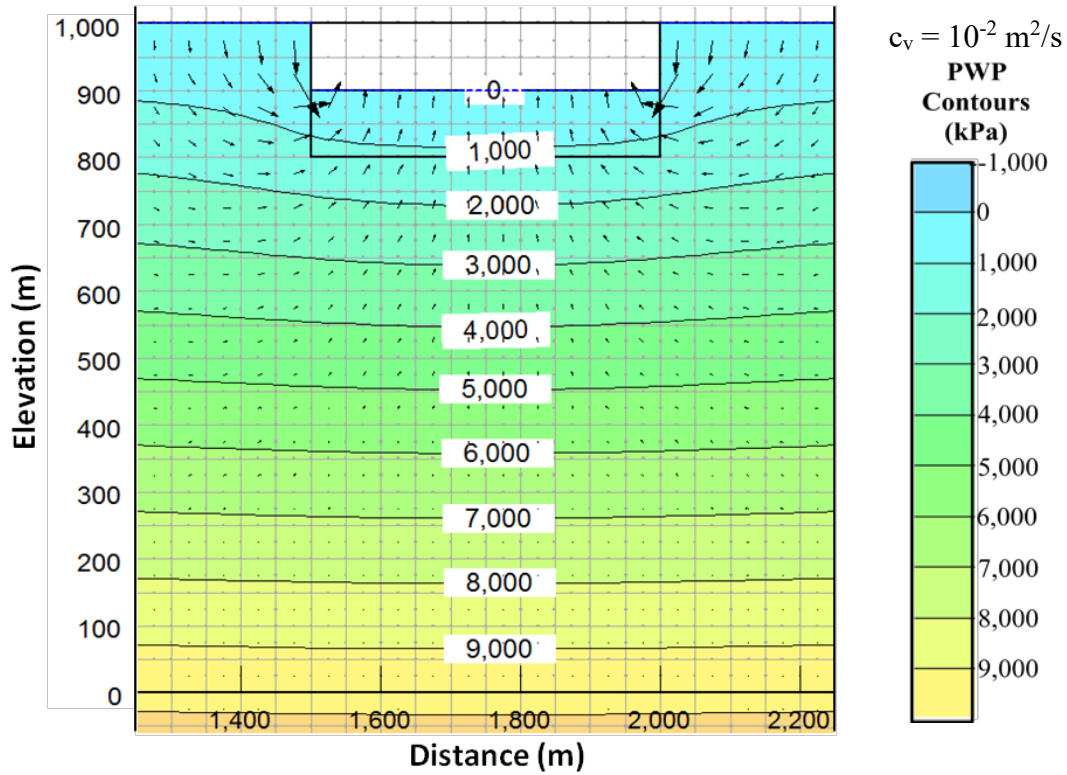


$$c_v = 10^{-2} \text{ m}^2/\text{s}$$

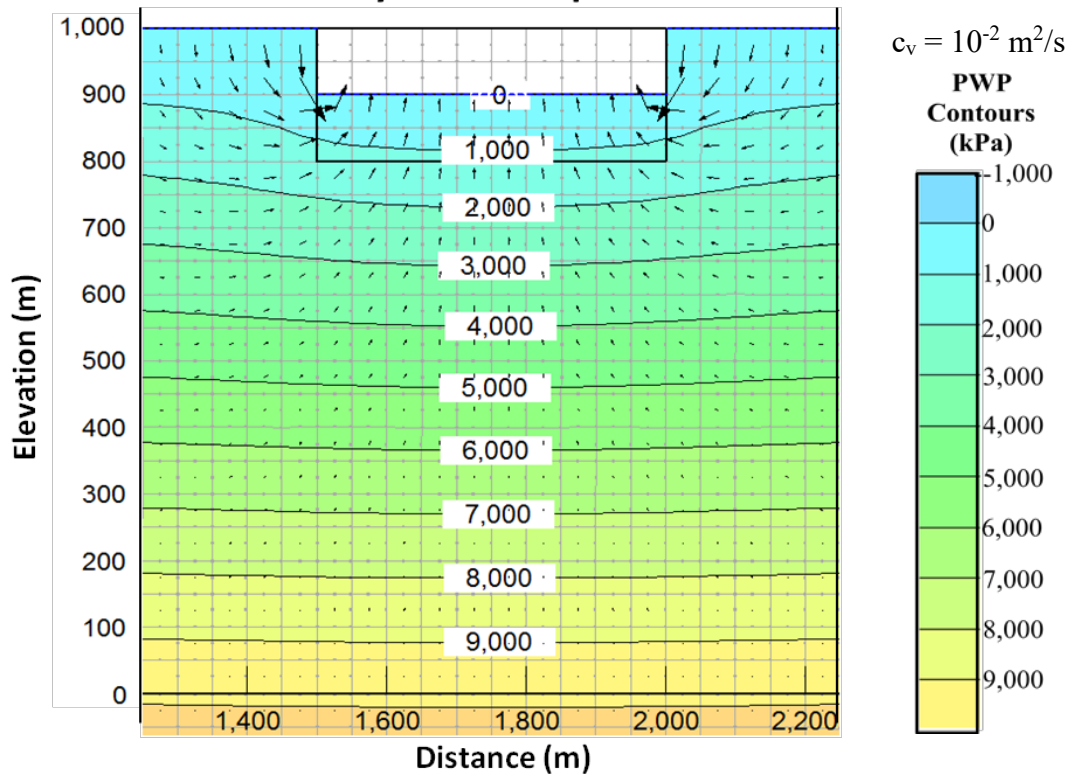
**PWP
Contours
(kPa)**



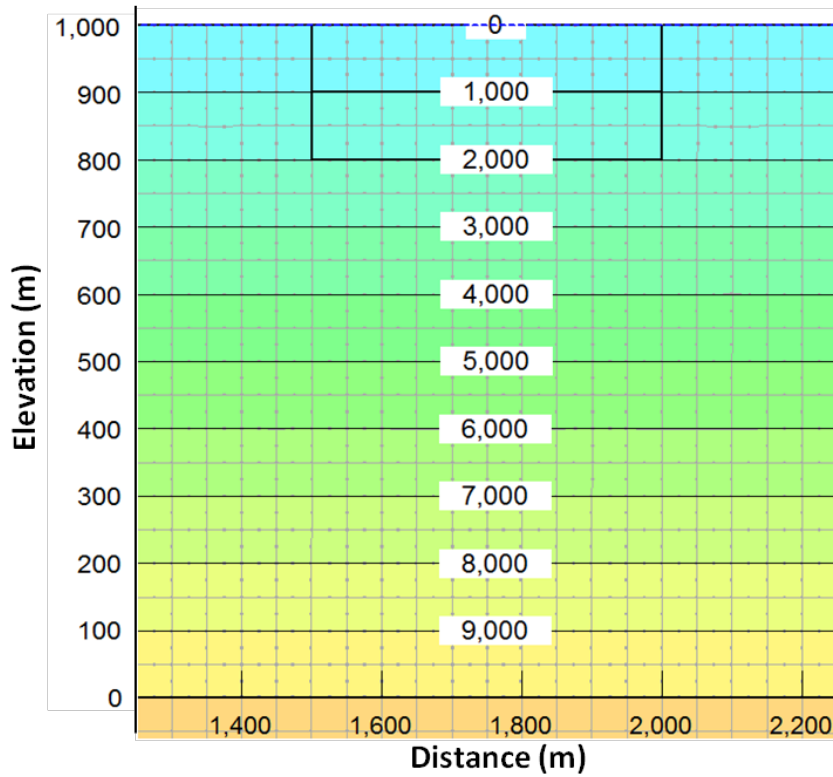
Transient Coupled Response (360 Days)



Steady-State Response

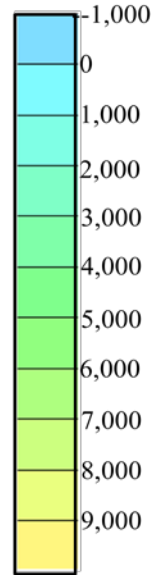


Initial Conditions

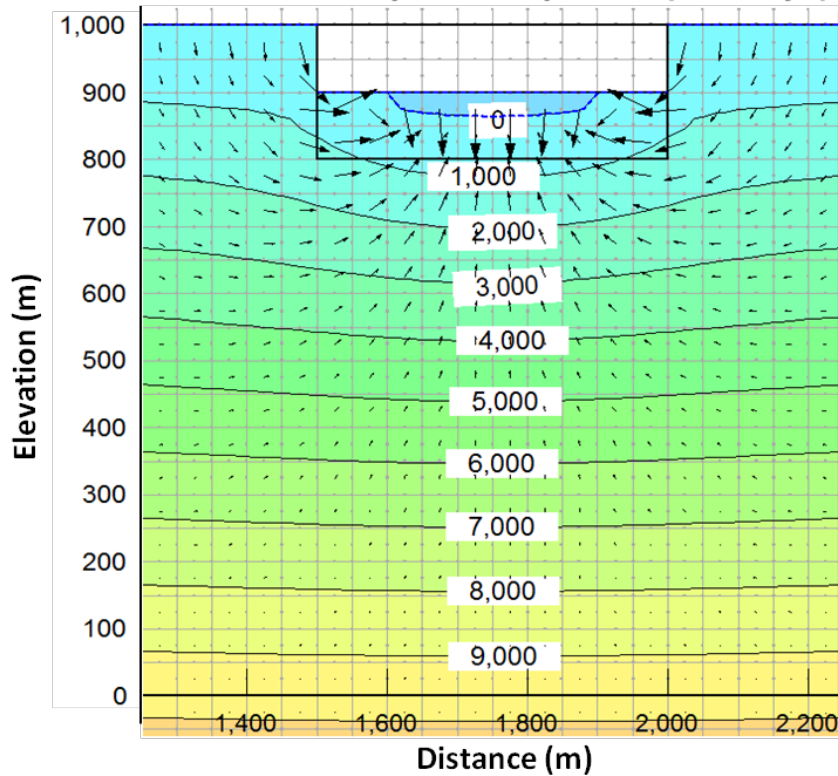


$c_v = 10^{-3} \text{ m}^2/\text{s}$

**PWP
Contours
(kPa)**

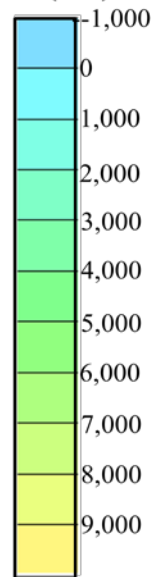


Transient Coupled Response (10 Days)

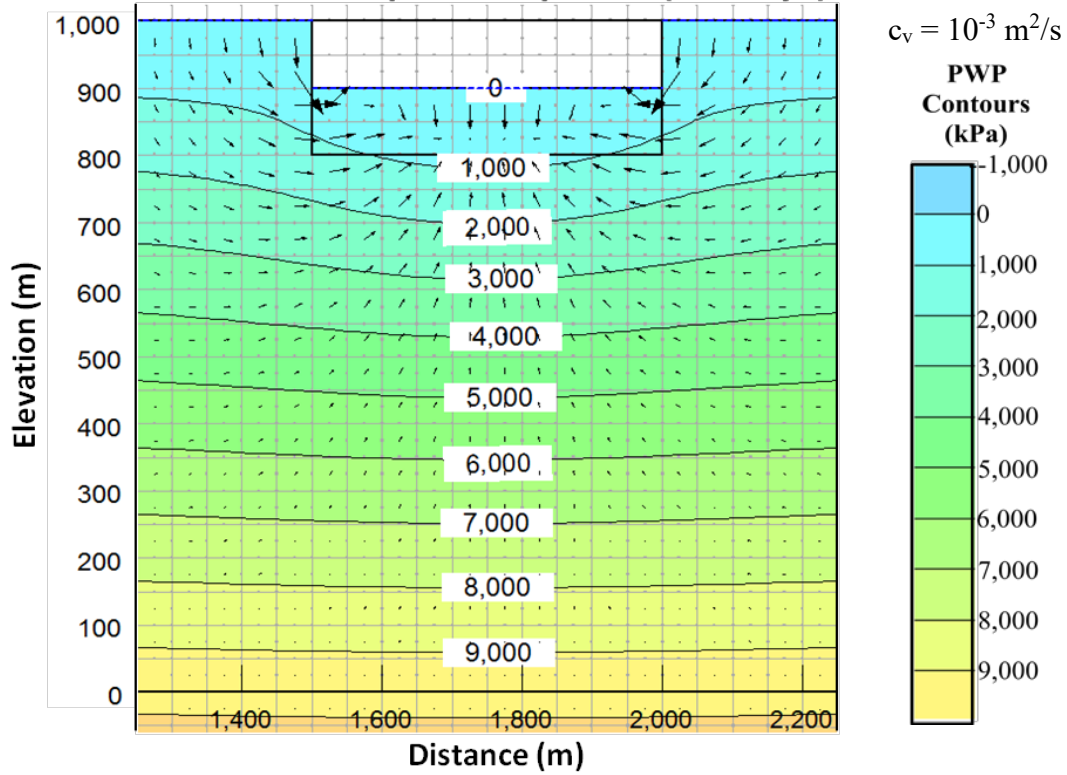


$c_v = 10^{-3} \text{ m}^2/\text{s}$

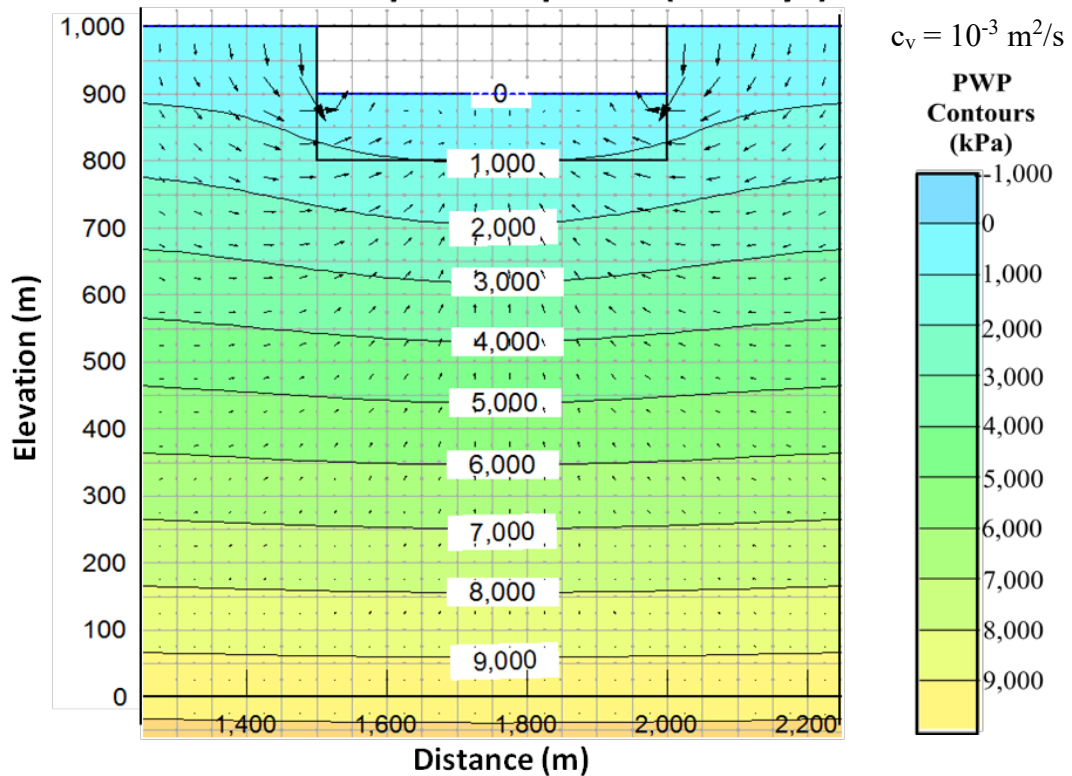
**PWP
Contours
(kPa)**



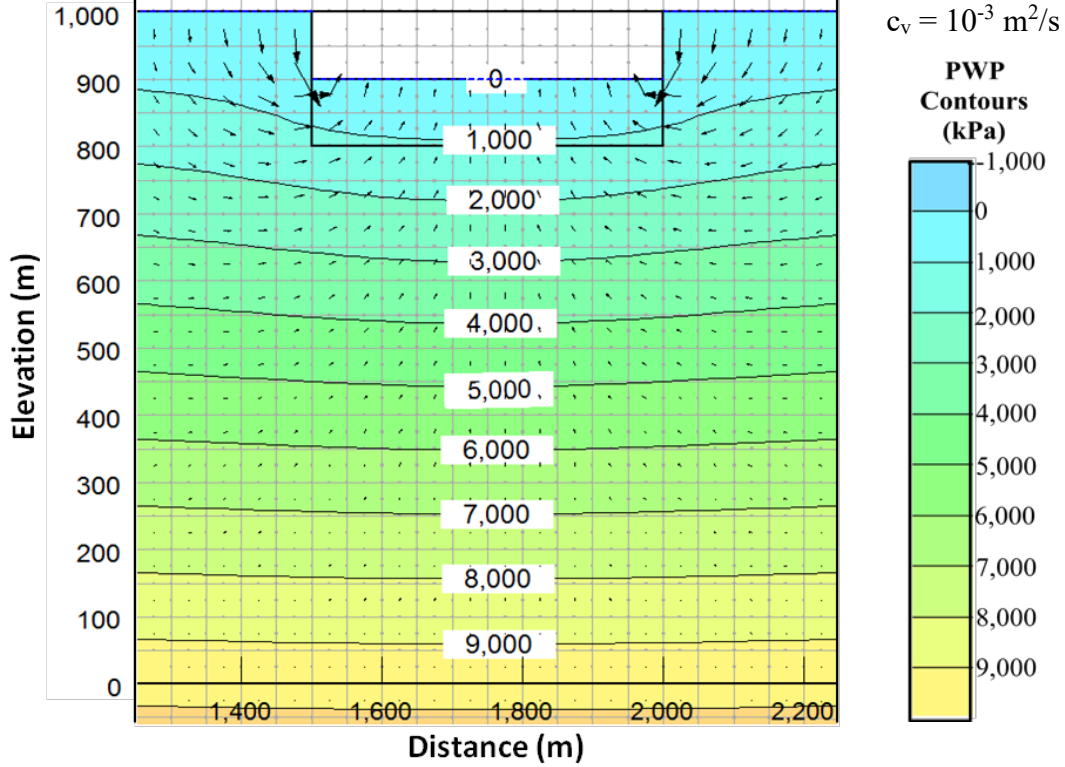
Transient Coupled Response (30 Days)



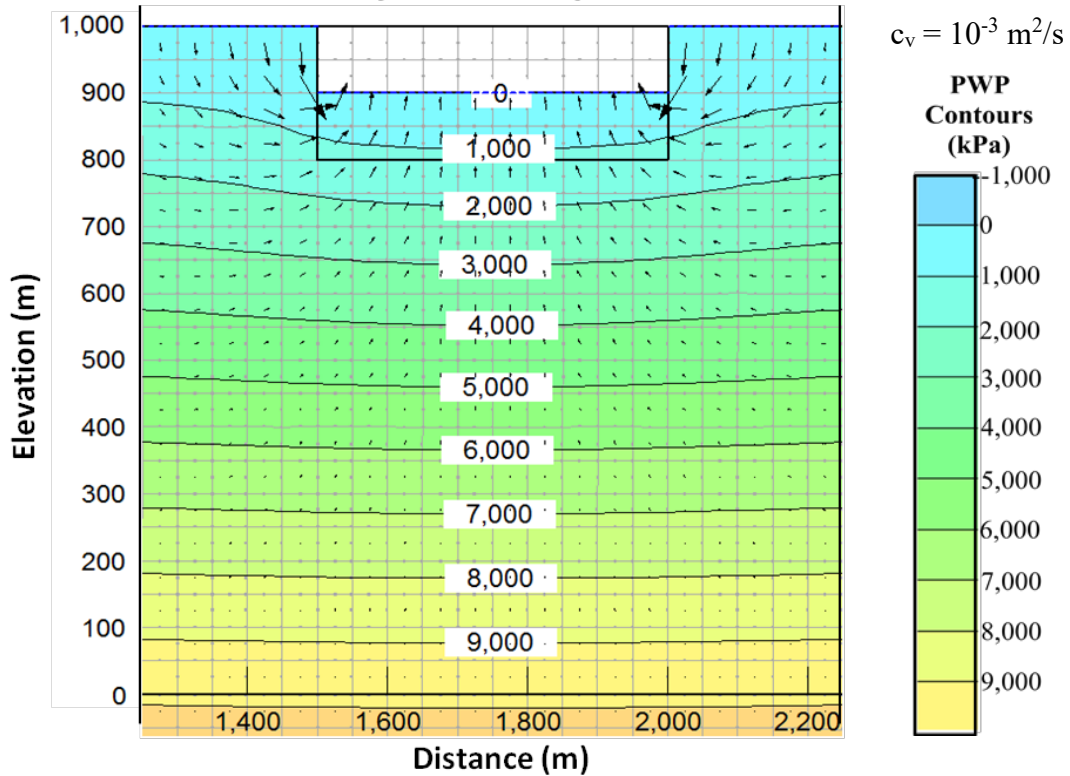
Transient Coupled Response (90 Days)



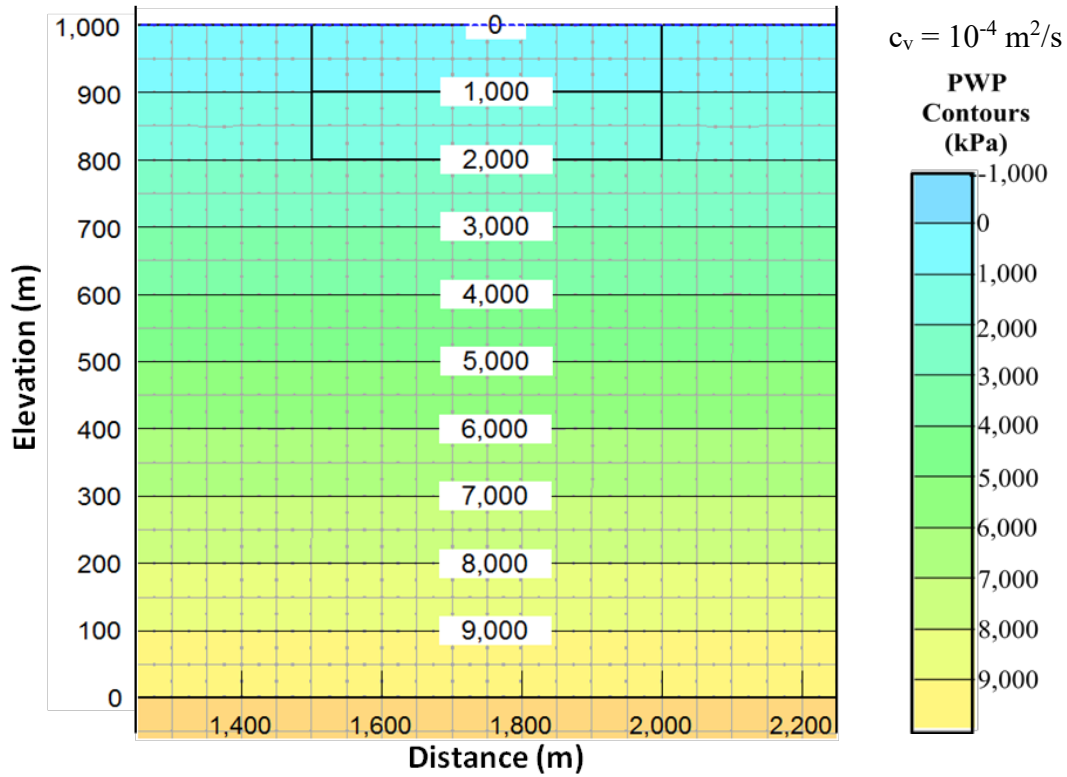
Transient Coupled Response (360 Days)



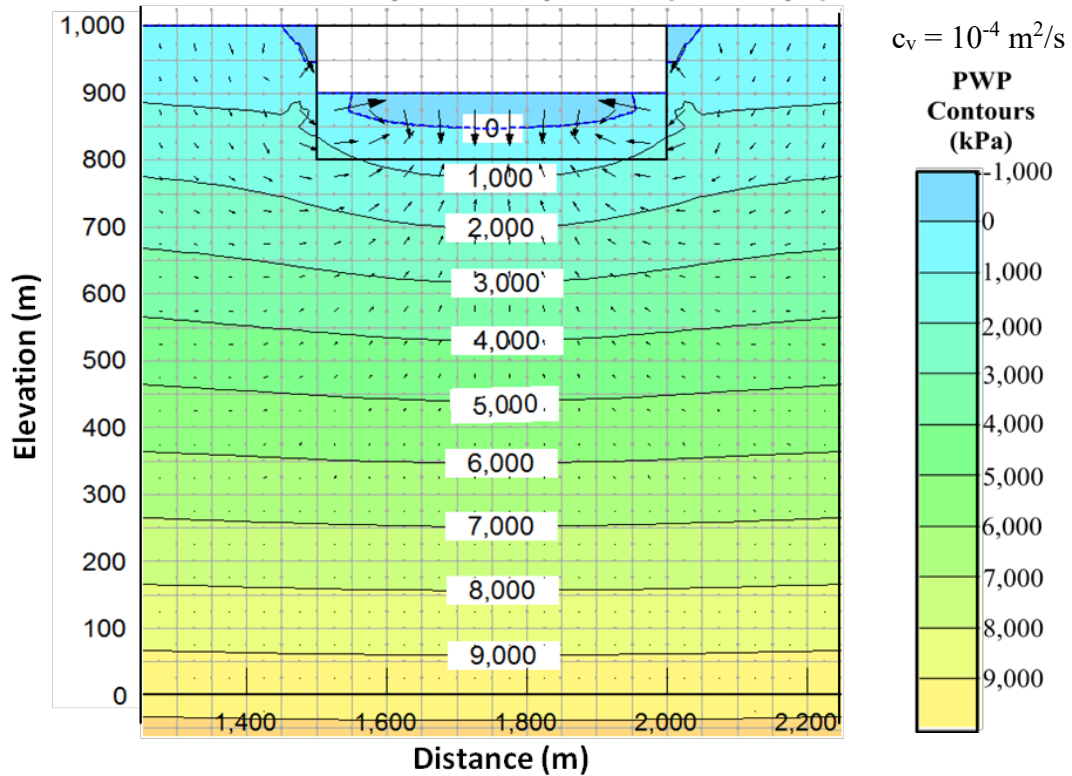
Steady-State Response



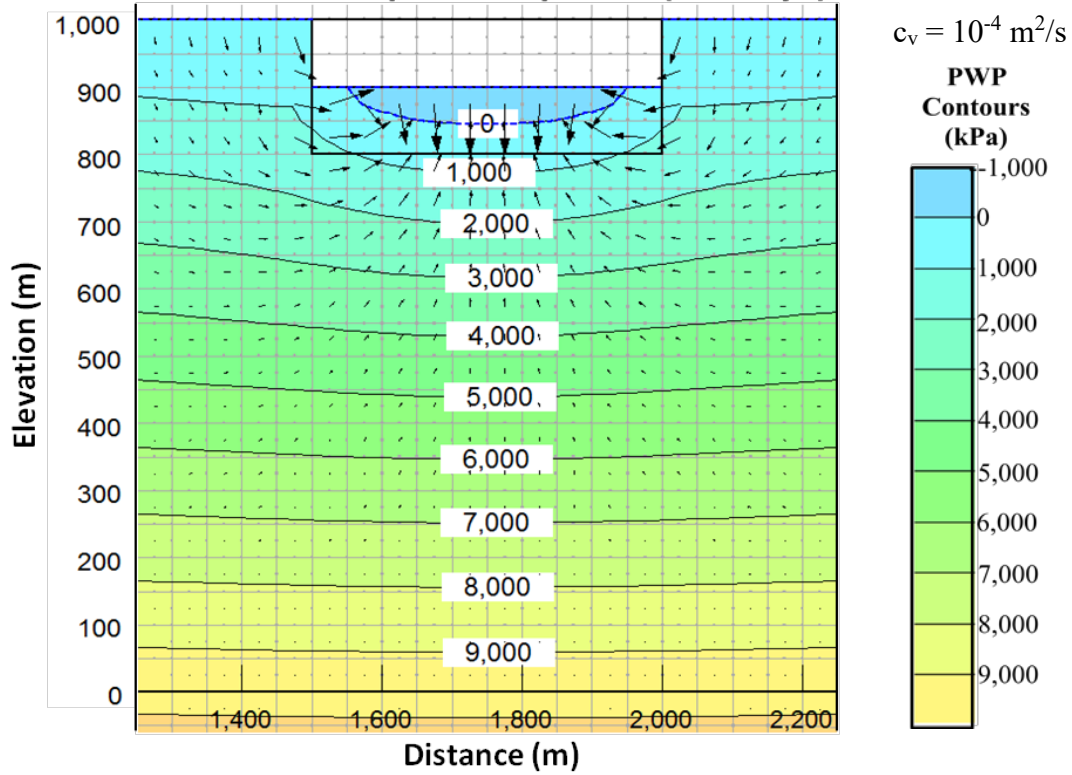
Initial Conditions



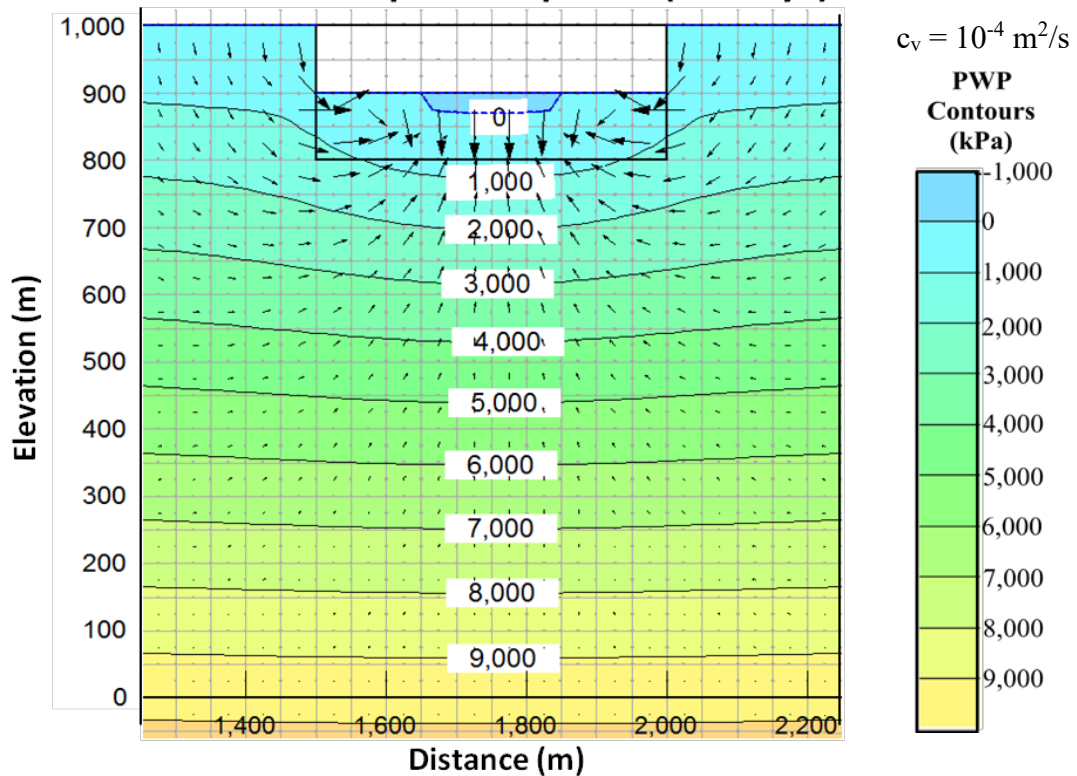
Transient Coupled Response (10 Days)



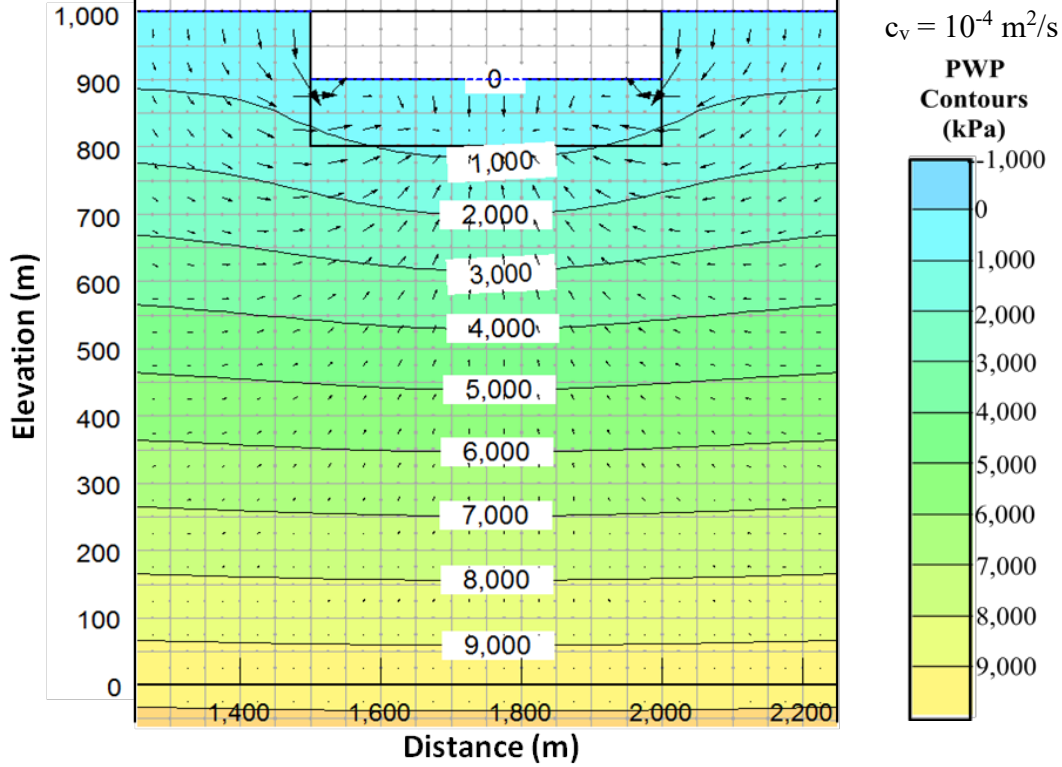
Transient Coupled Response (30 Days)



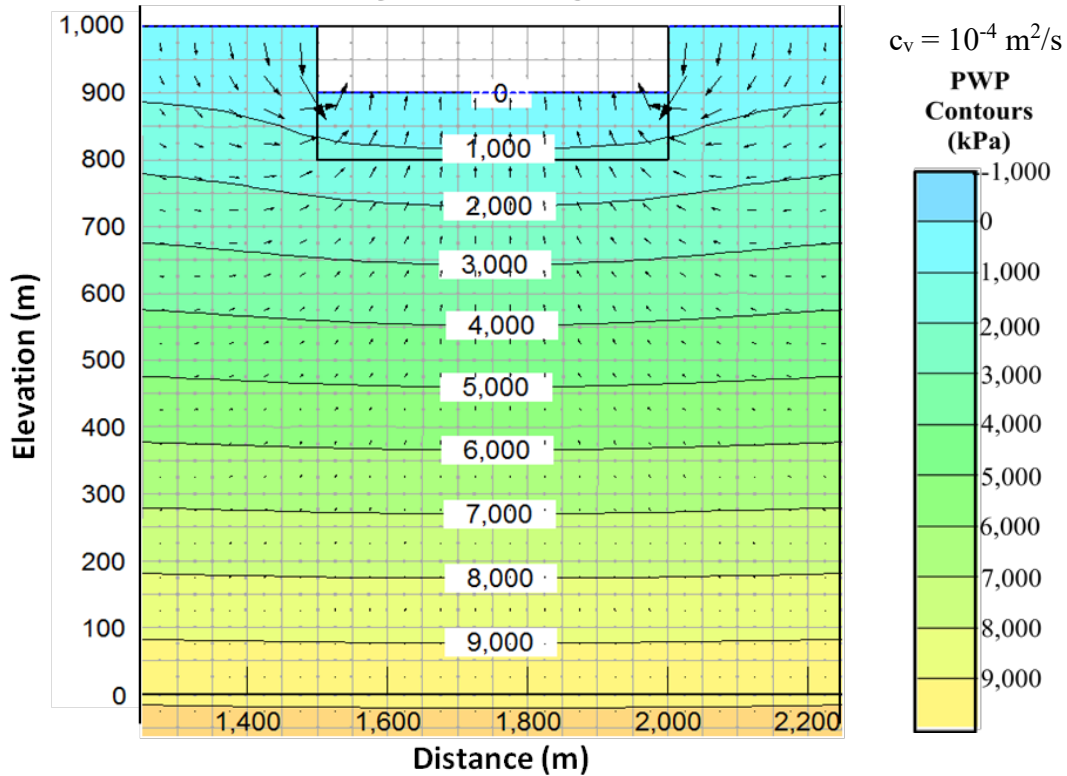
Transient Coupled Response (90 Days)



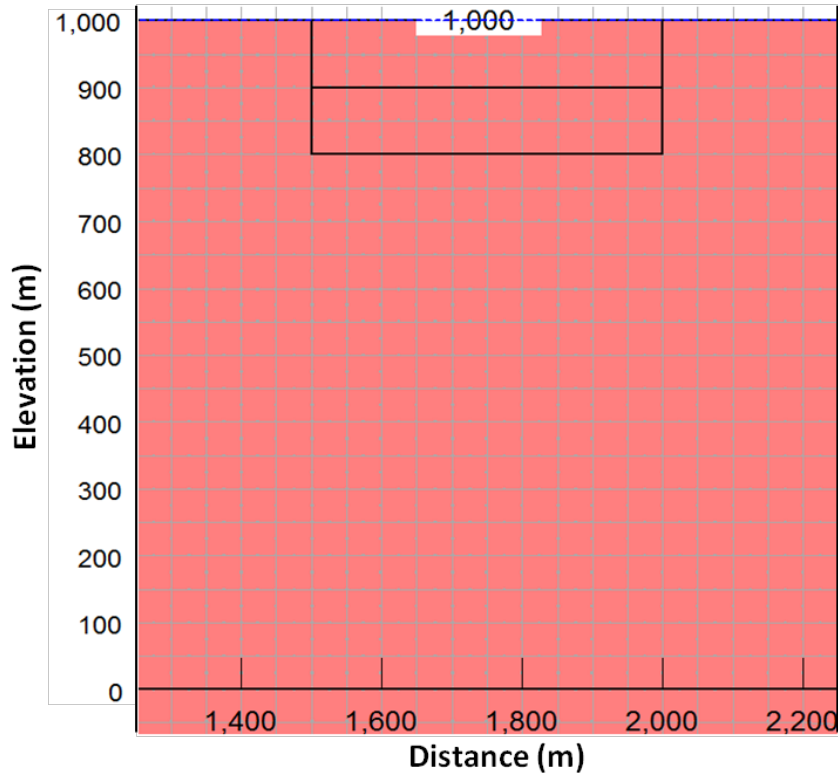
Transient Coupled Response (360 Days)



Steady-State Response

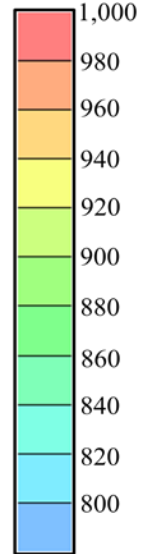


Initial Conditions

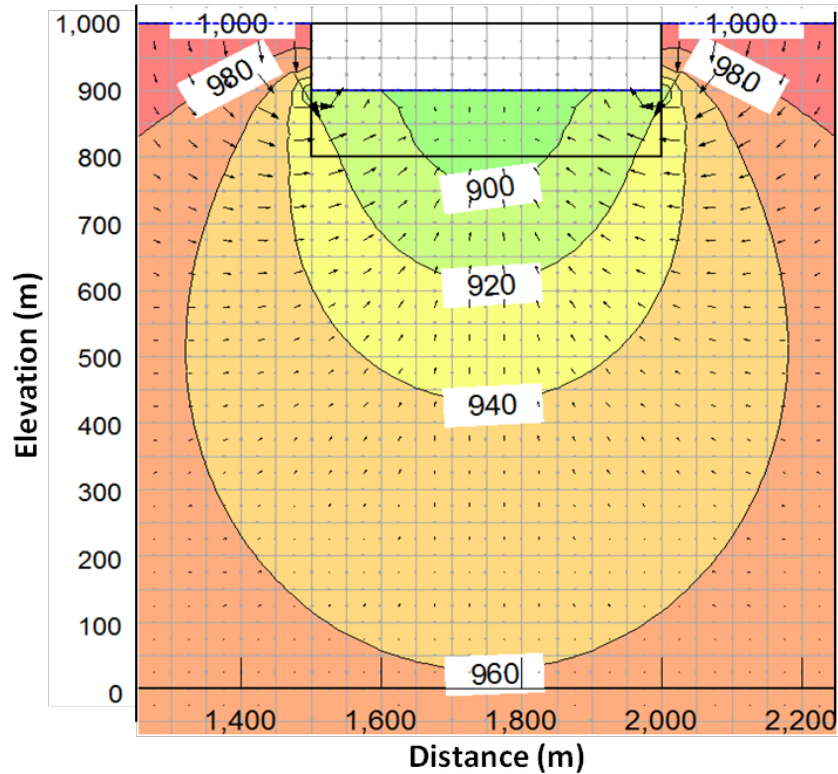


$$c_v = 10^{-2} \text{ m}^2/\text{s}$$

Total Head Contours (m)

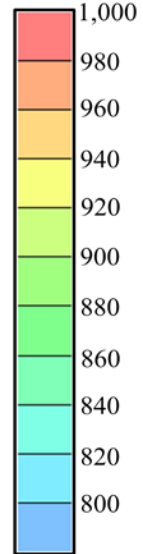


Transient Coupled Response (10 Days)

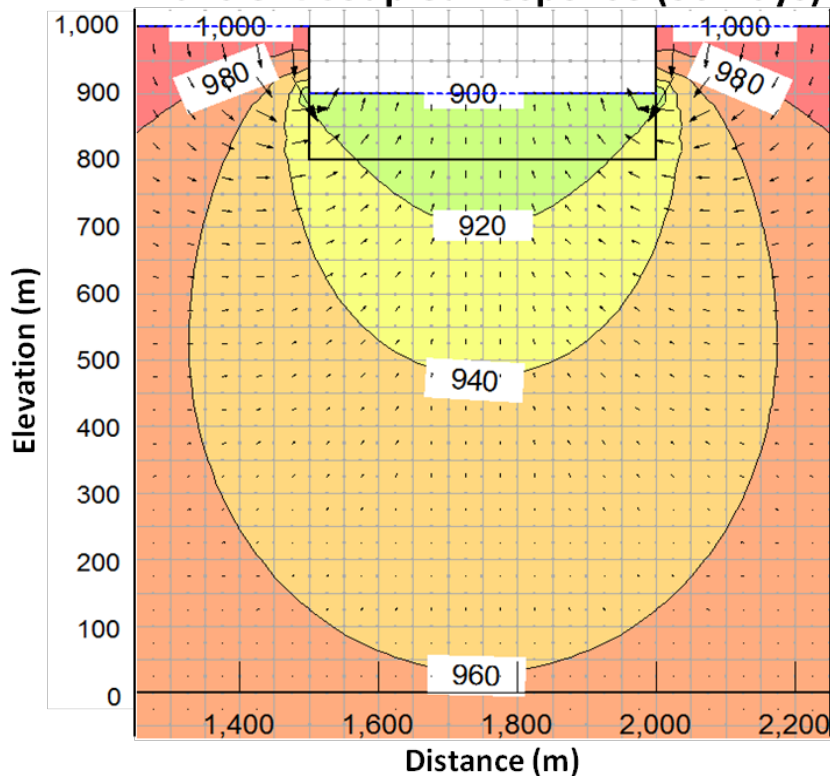


$$c_v = 10^{-2} \text{ m}^2/\text{s}$$

Total Head Contours (m)

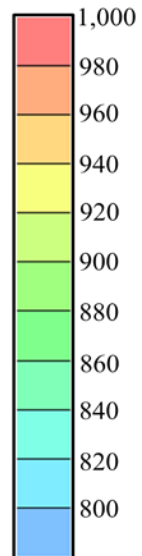


Transient Coupled Response (30 Days)

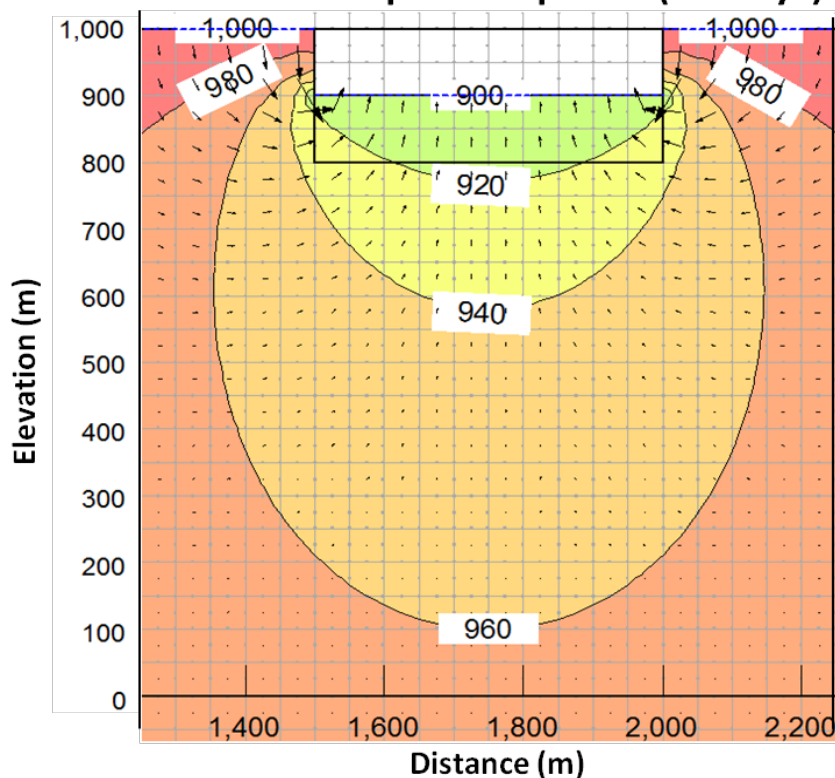


$$c_v = 10^{-2} \text{ m}^2/\text{s}$$

Total Head
Contours (m)

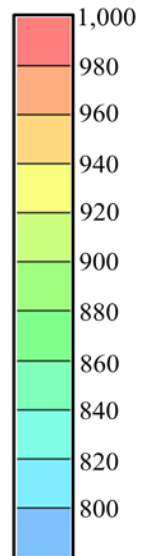


Transient Coupled Response (90 Days)

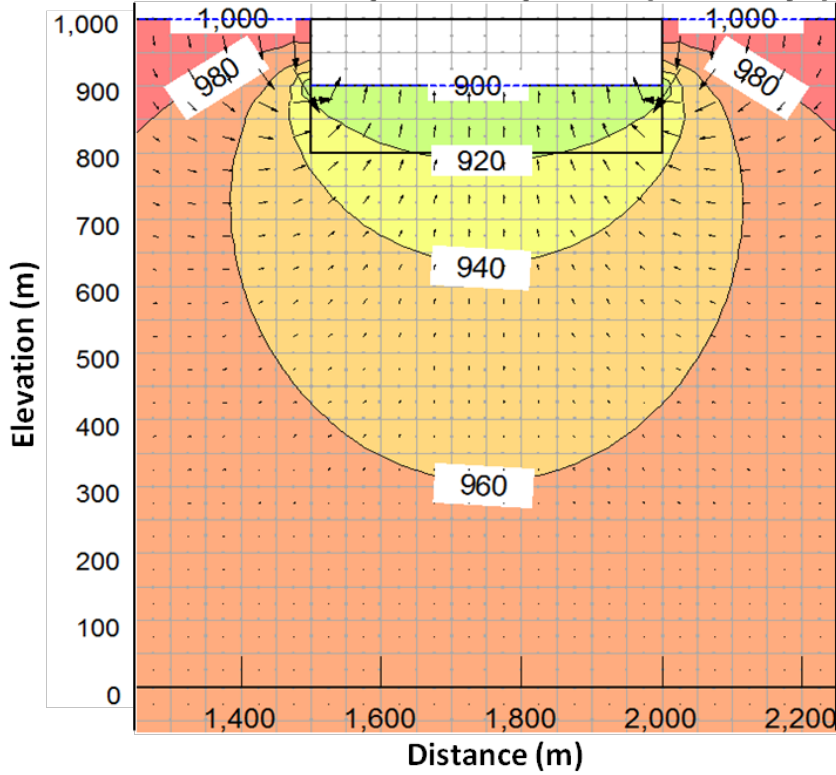


$$c_v = 10^{-2} \text{ m}^2/\text{s}$$

Total Head
Contours (m)

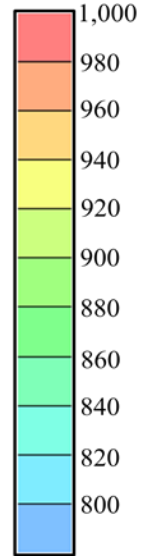


Transient Coupled Response (360 Days)

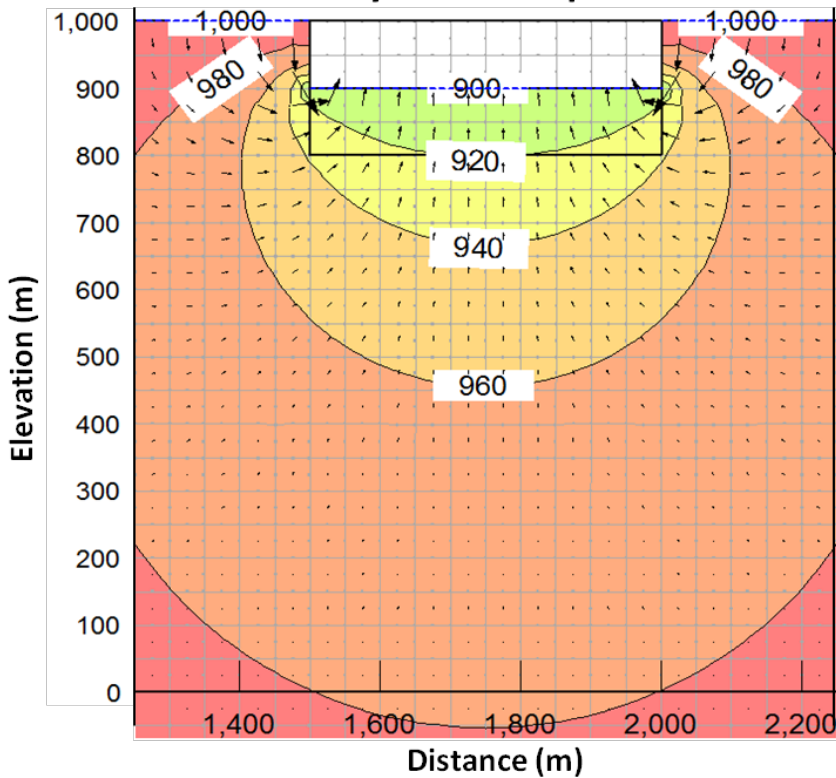


$$c_v = 10^{-2} \text{ m}^2/\text{s}$$

Total Head Contours (m)

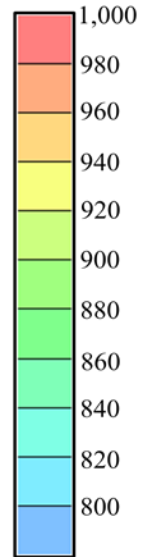


Steady-State Response

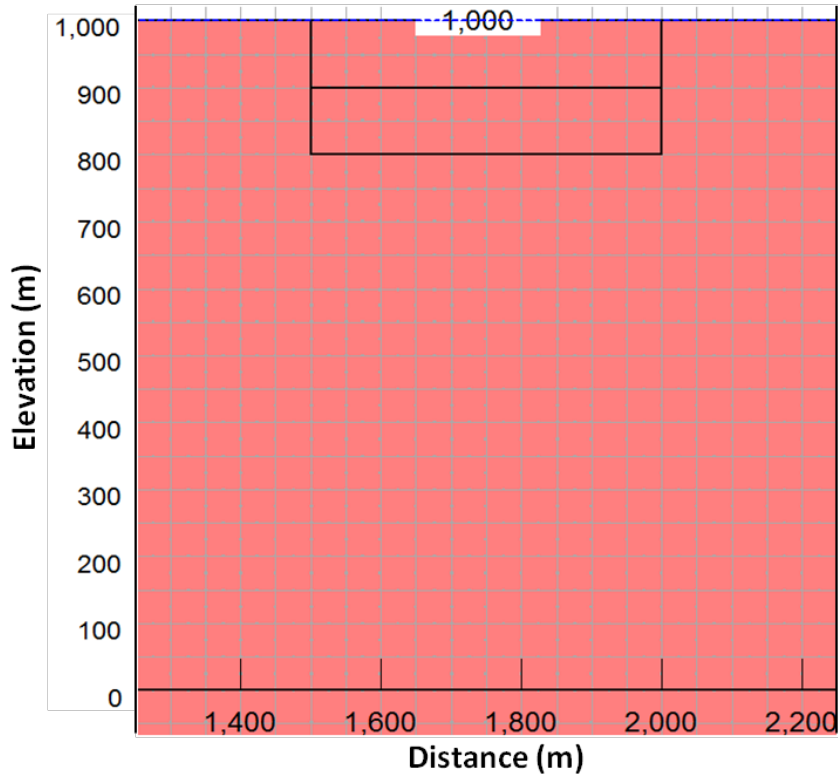


$$c_v = 10^{-2} \text{ m}^2/\text{s}$$

Total Head Contours (m)

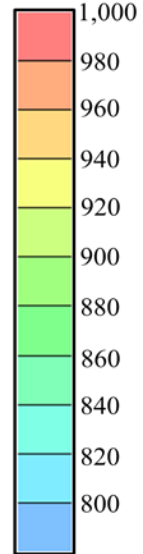


Initial Conditions

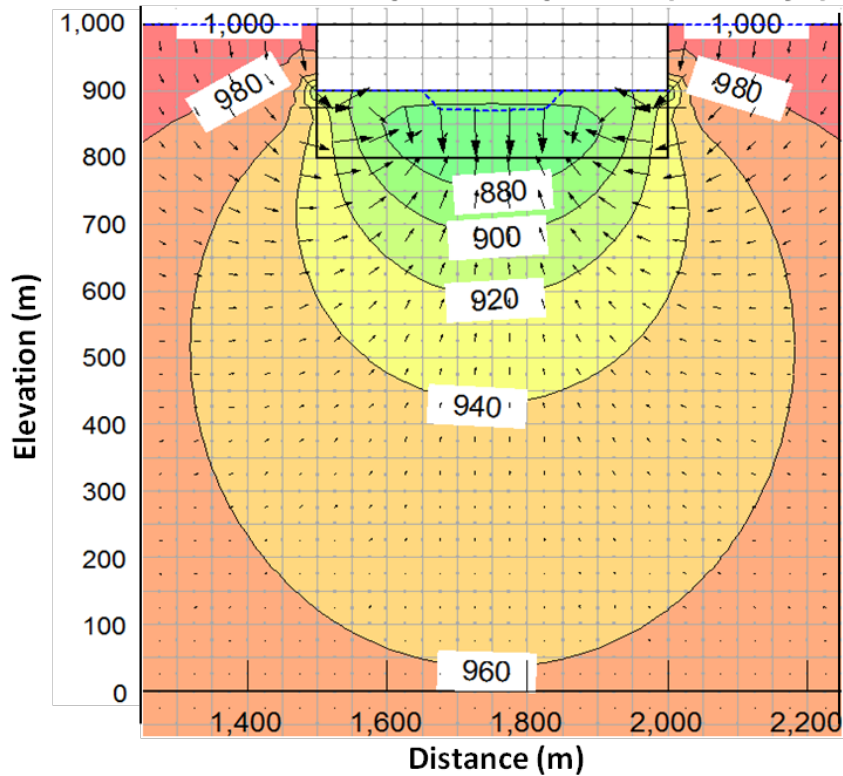


$c_v = 10^{-3} \text{ m}^2/\text{s}$

Total Head Contours (m)

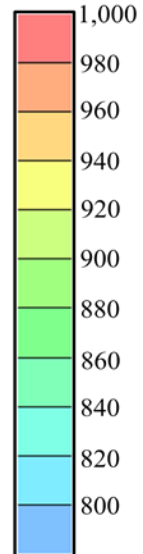


Transient Coupled Response (10 Days)

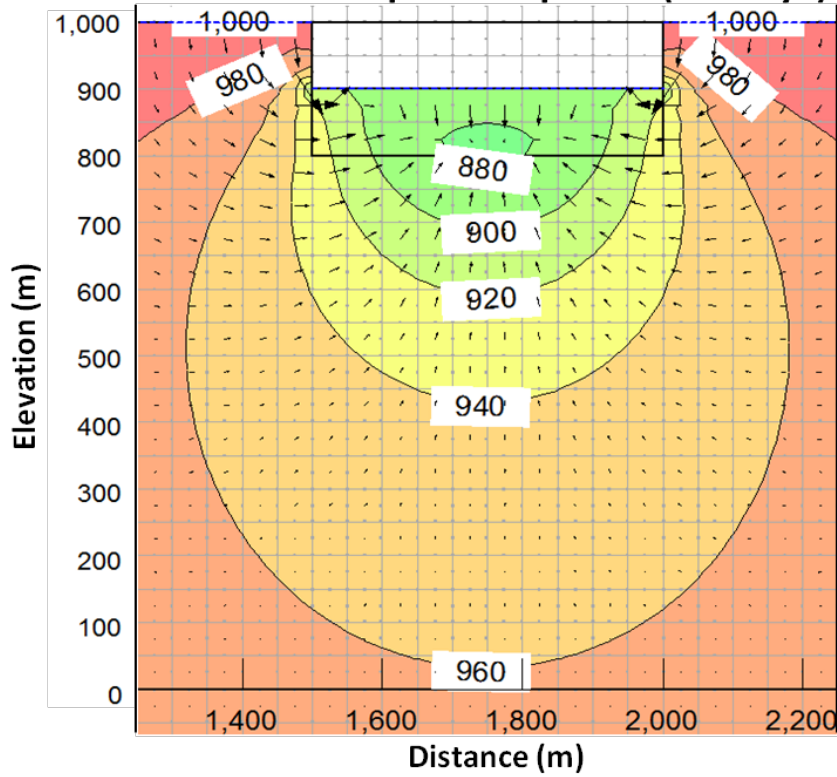


$c_v = 10^{-3} \text{ m}^2/\text{s}$

Total Head Contours (m)

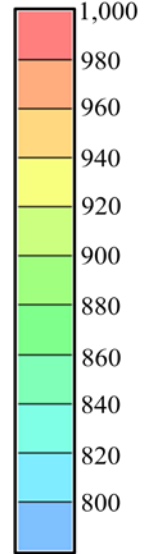


Transient Coupled Response (30 Days)

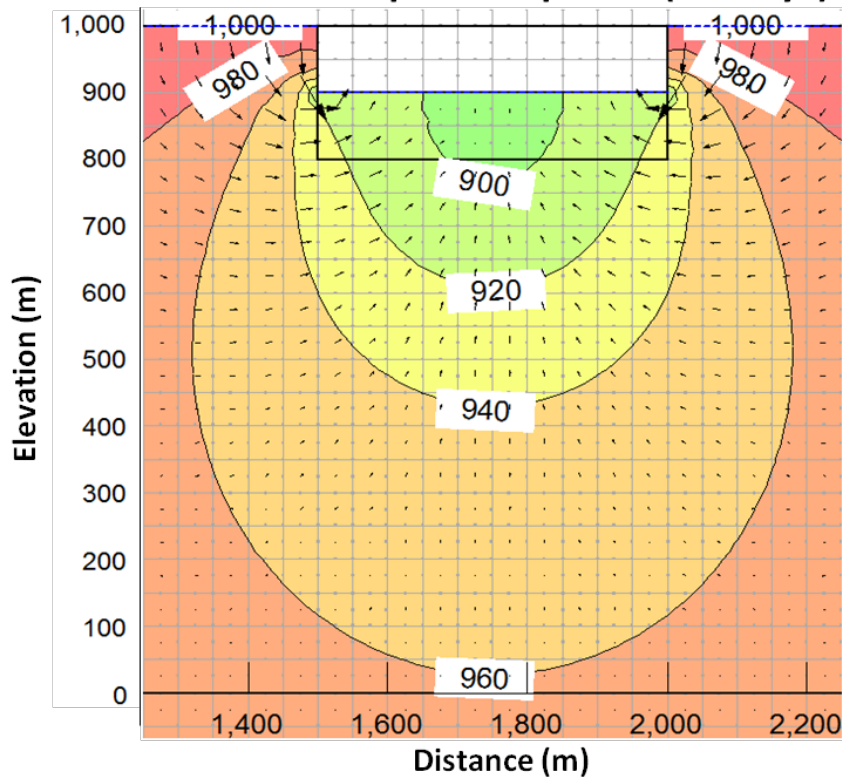


$$c_v = 10^{-3} \text{ m}^2/\text{s}$$

Total Head Contours (m)

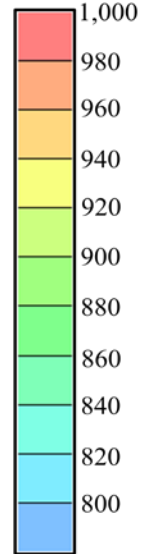


Transient Coupled Response (90 Days)

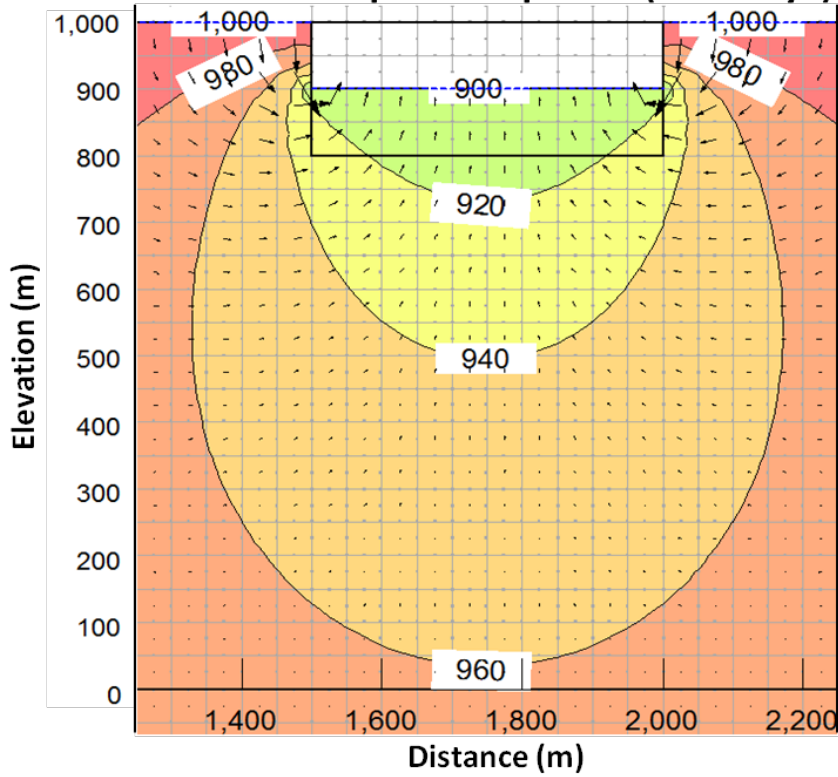


$$c_v = 10^{-3} \text{ m}^2/\text{s}$$

Total Head Contours (m)

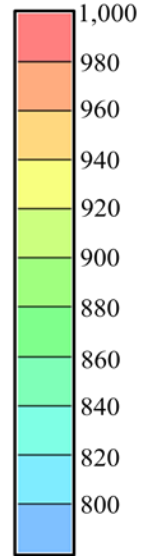


Transient Coupled Response (360 Days)

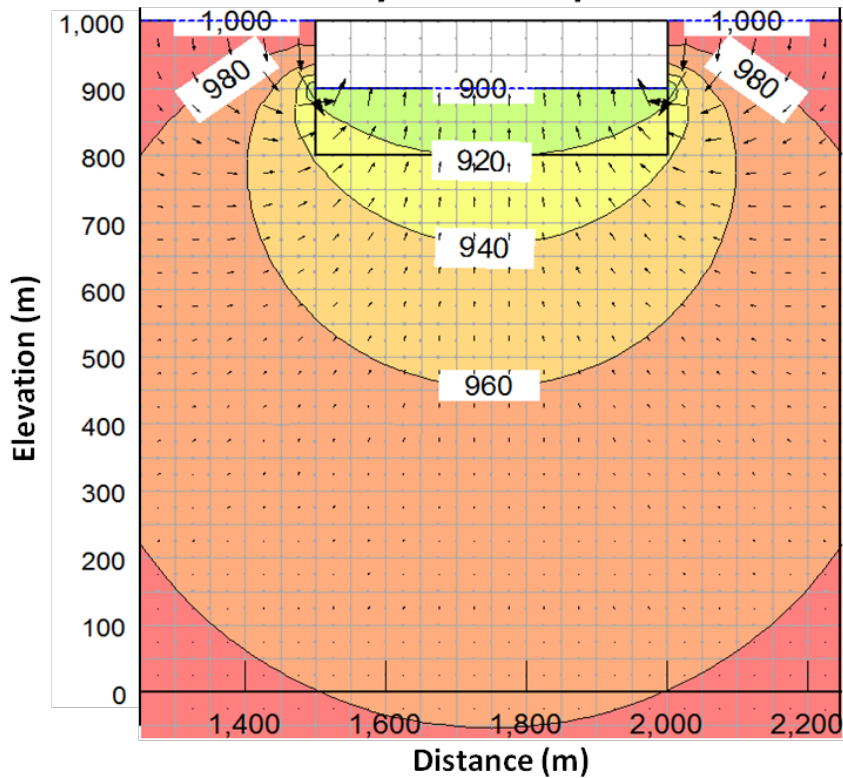


$$c_v = 10^{-3} \text{ m}^2/\text{s}$$

Total Head Contours (m)

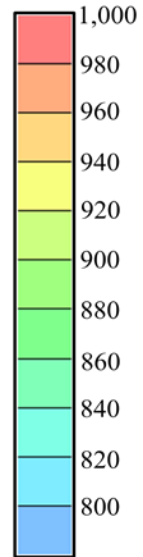


Steady-State Response

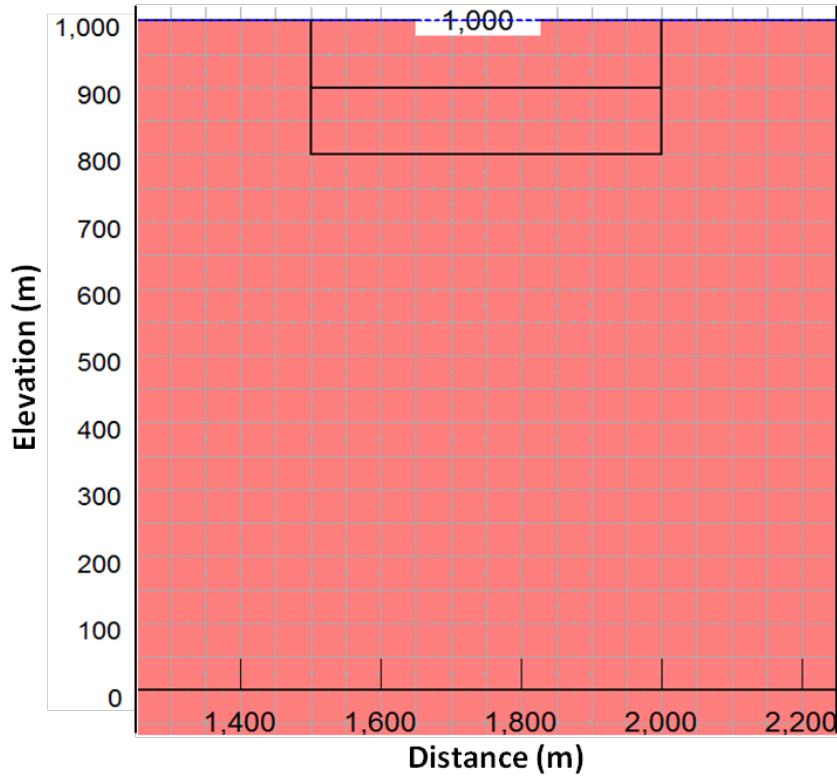


$$c_v = 10^{-3} \text{ m}^2/\text{s}$$

Total Head Contours (m)

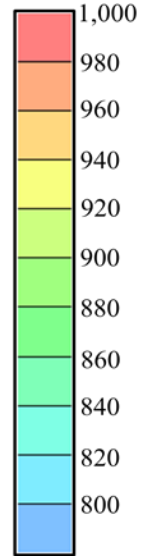


Initial Conditions

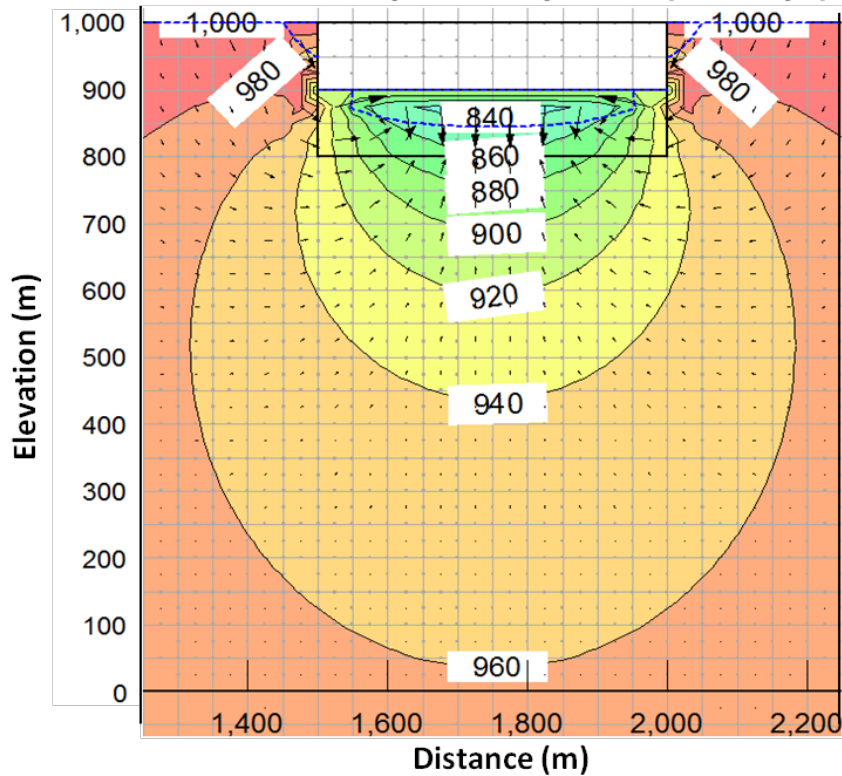


$c_v = 10^{-4} \text{ m}^2/\text{s}$

Total Head Contours (m)

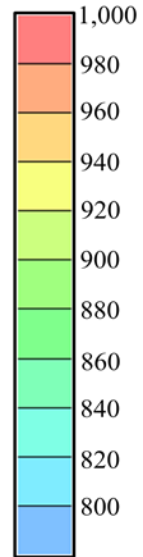


Transient Coupled Response (10 Days)

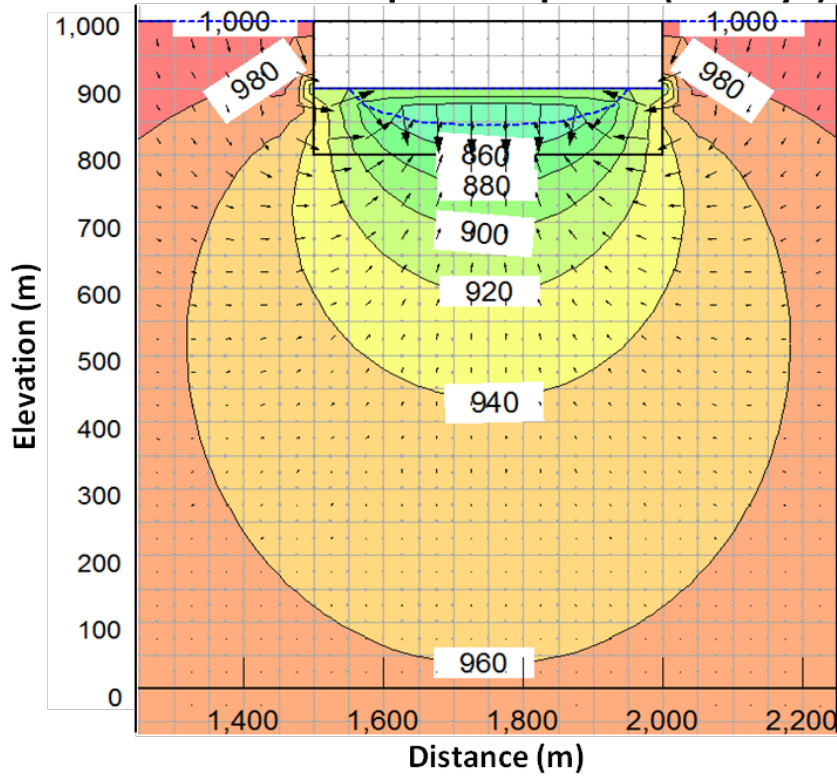


$c_v = 10^{-4} \text{ m}^2/\text{s}$

Total Head Contours (m)

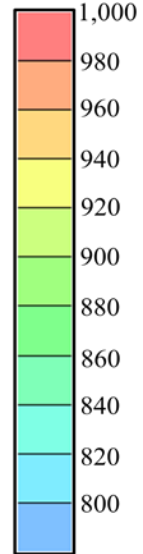


Transient Coupled Response (30 Days)

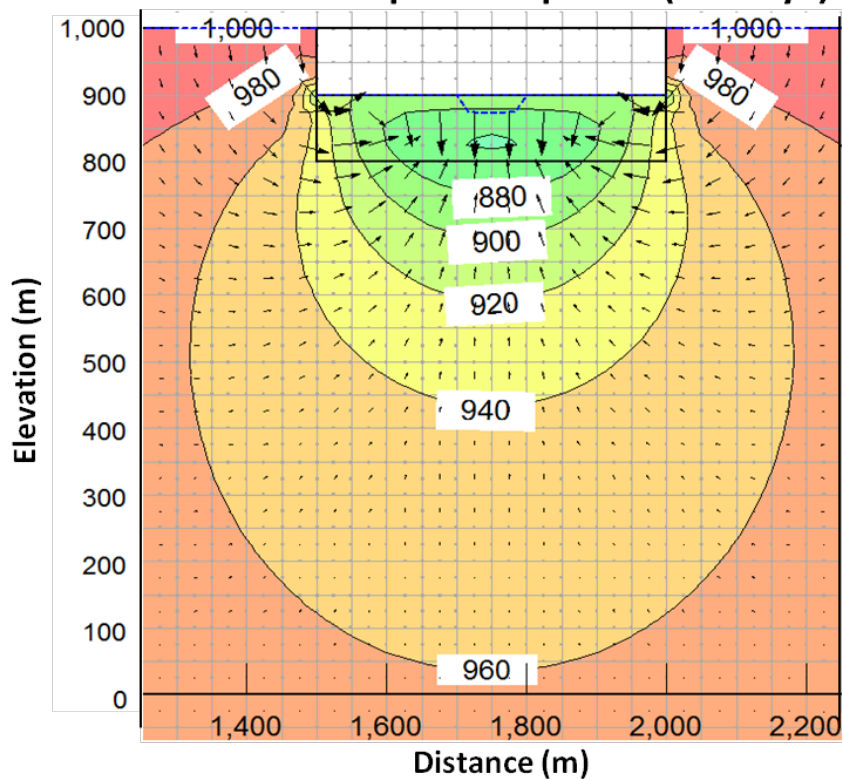


$c_v = 10^{-4} \text{ m}^2/\text{s}$

Total Head Contours (m)

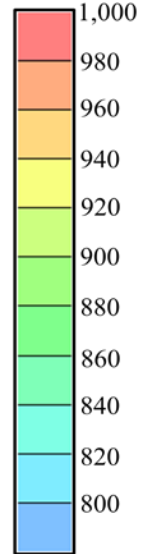


Transient Coupled Response (90 Days)

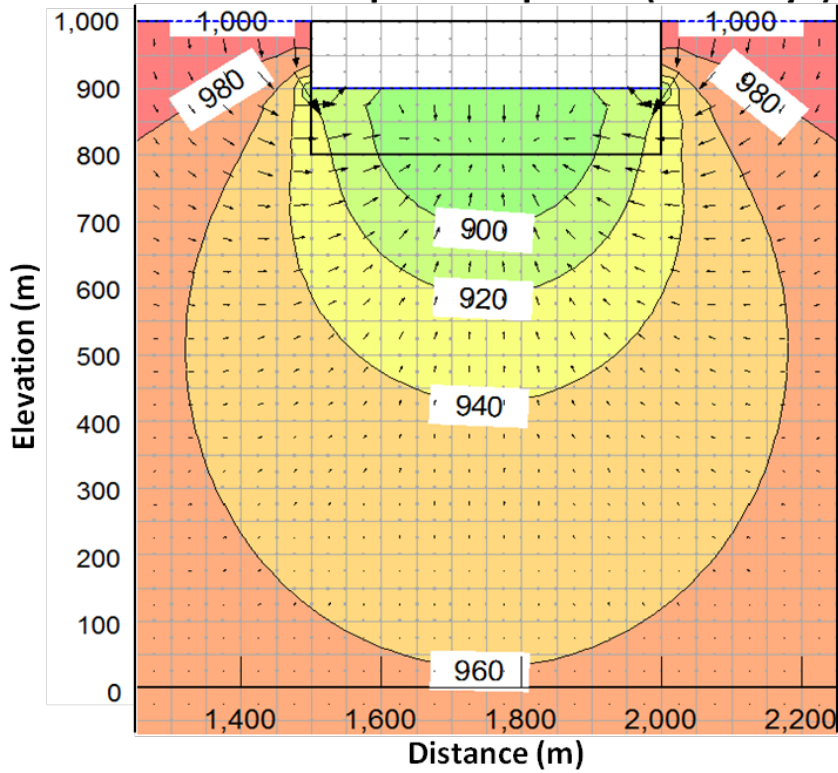


$c_v = 10^{-4} \text{ m}^2/\text{s}$

Total Head Contours (m)

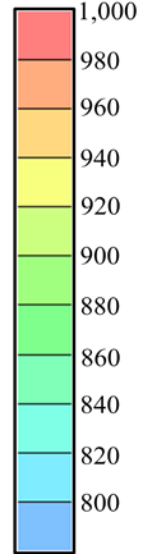


Transient Coupled Response (360 Days)

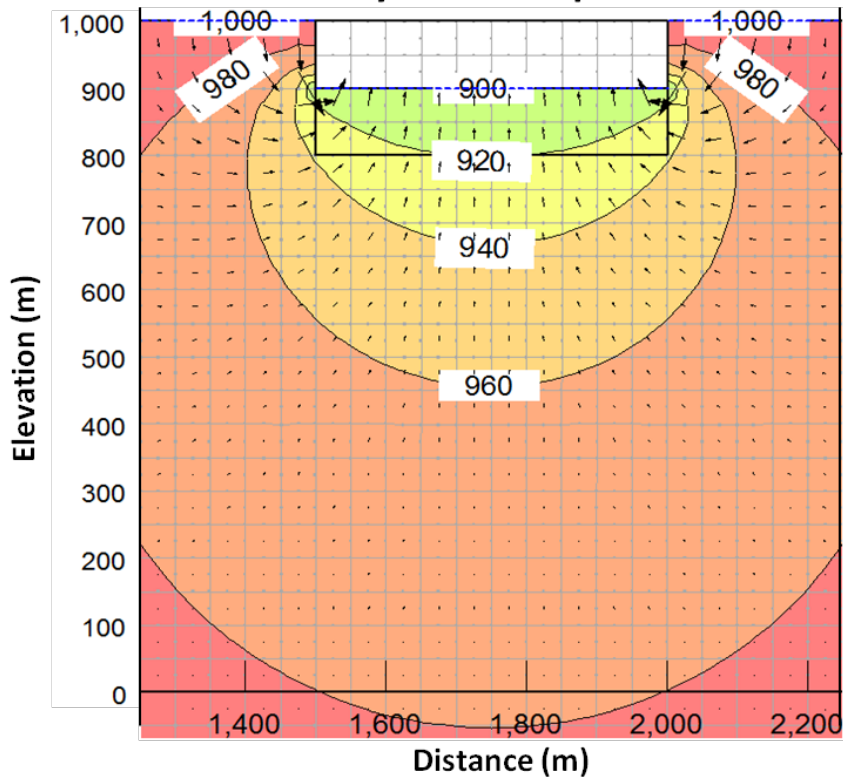


$c_v = 10^{-4} \text{ m}^2/\text{s}$

**Total Head
Contours (m)**

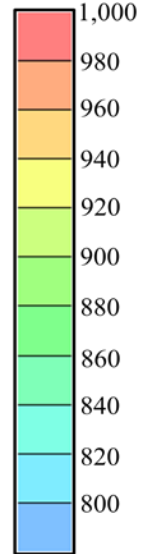


Steady-State Response

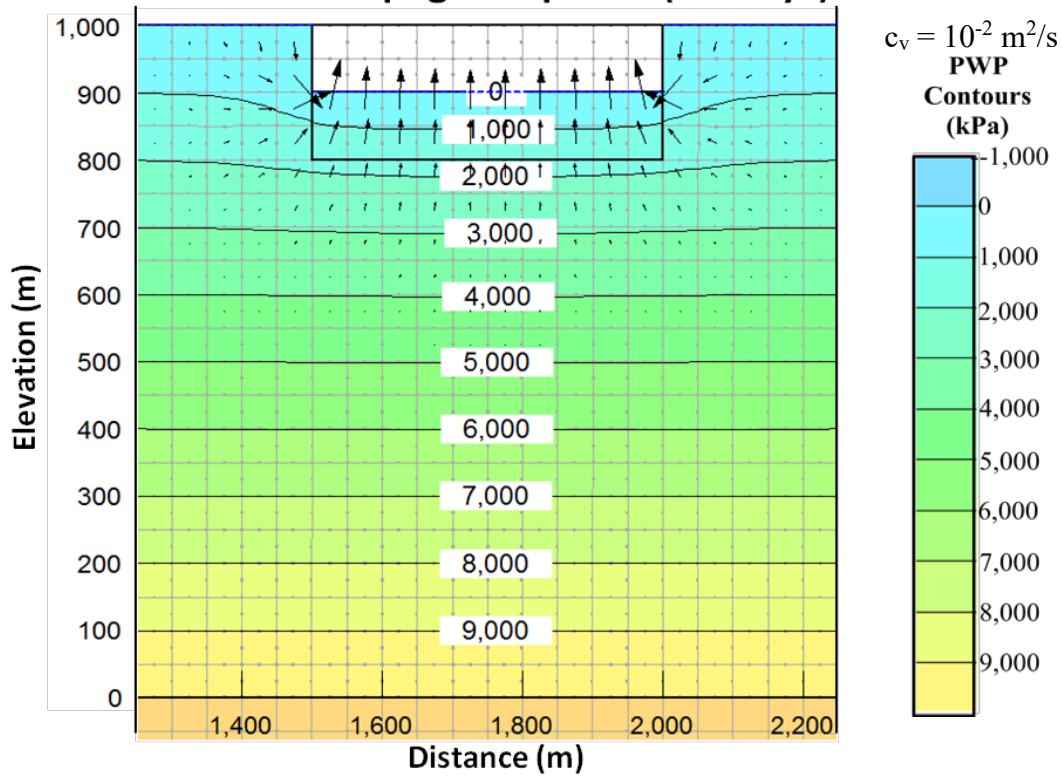


$c_v = 10^{-4} \text{ m}^2/\text{s}$

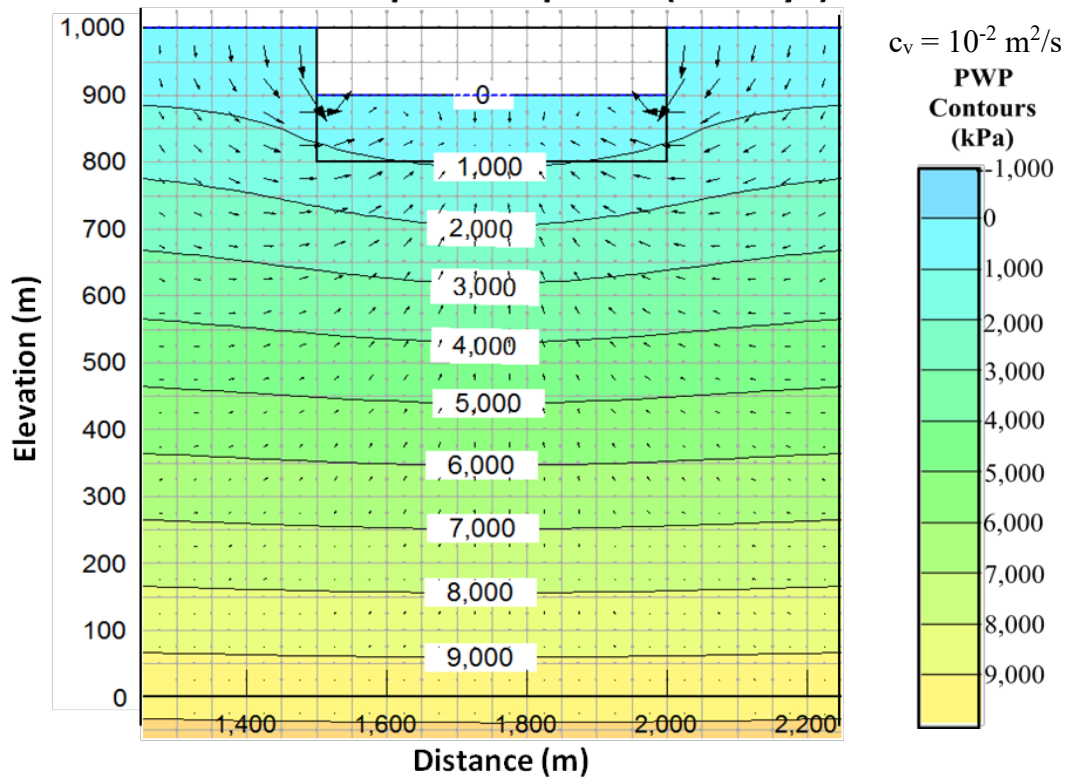
**Total Head
Contours (m)**



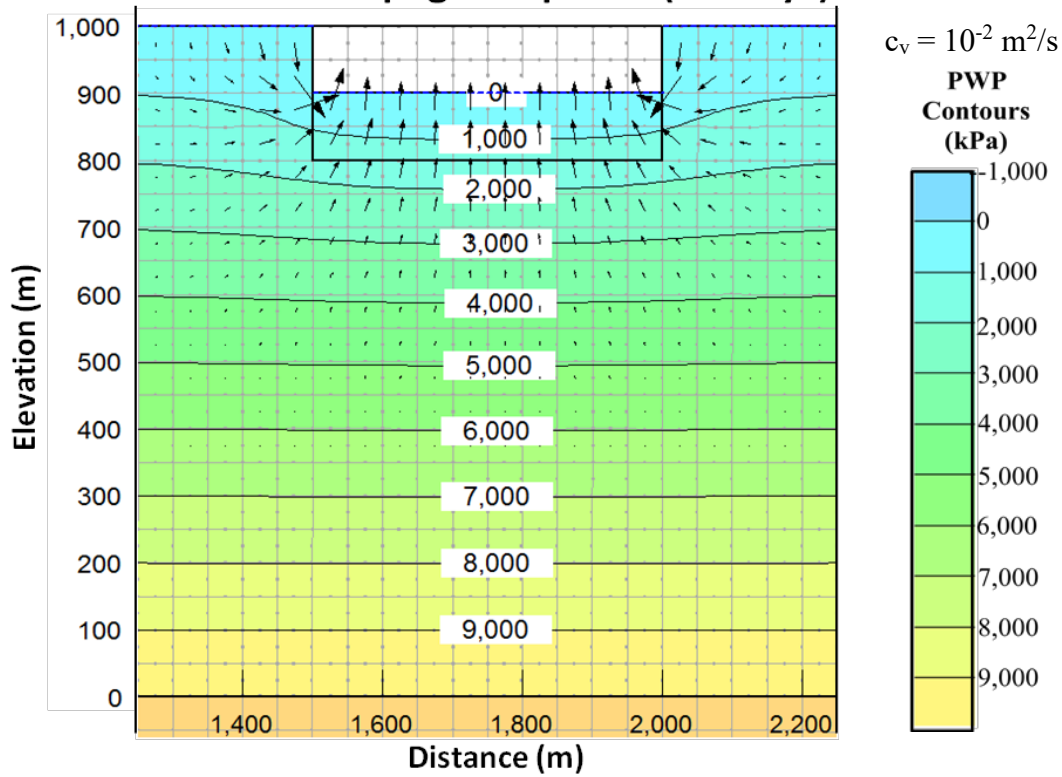
Transient Seepage Response (10 Days)



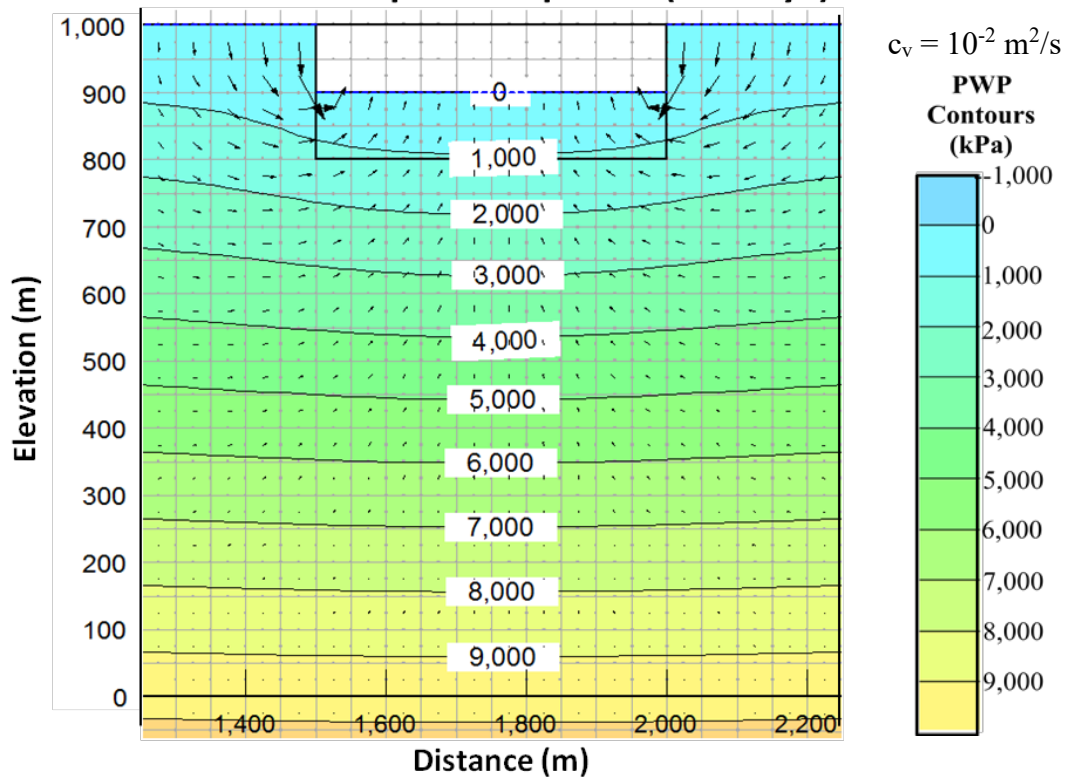
Transient Coupled Response (10 Days)



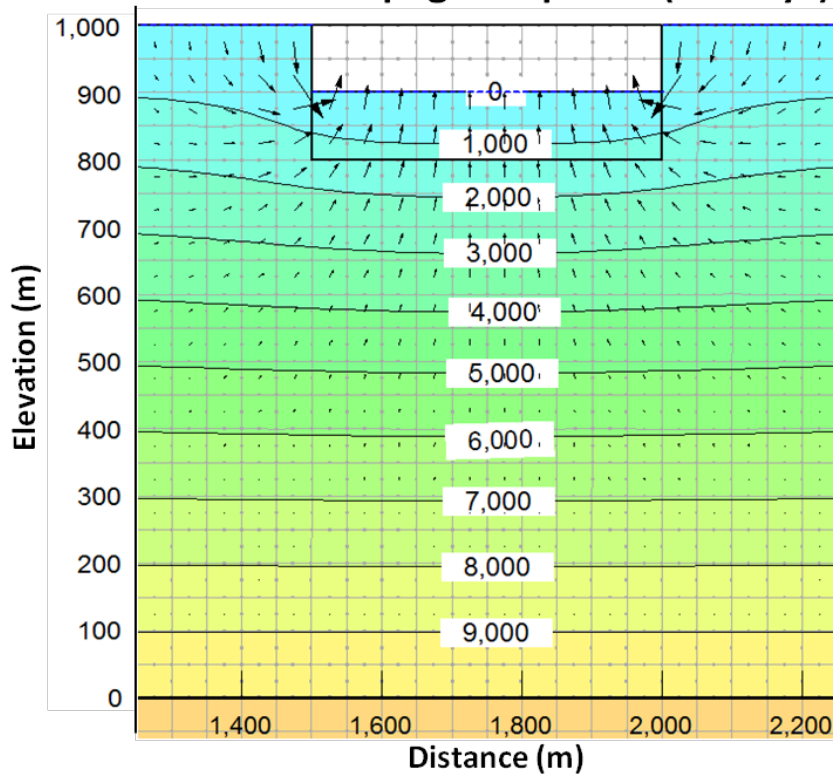
Transient Seepage Response (30 Days)



Transient Coupled Response (30 Days)

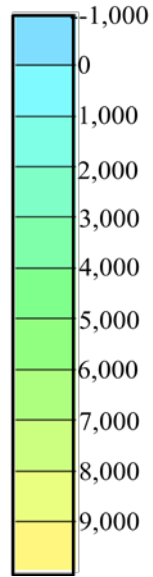


Transient Seepage Response (90 Days)

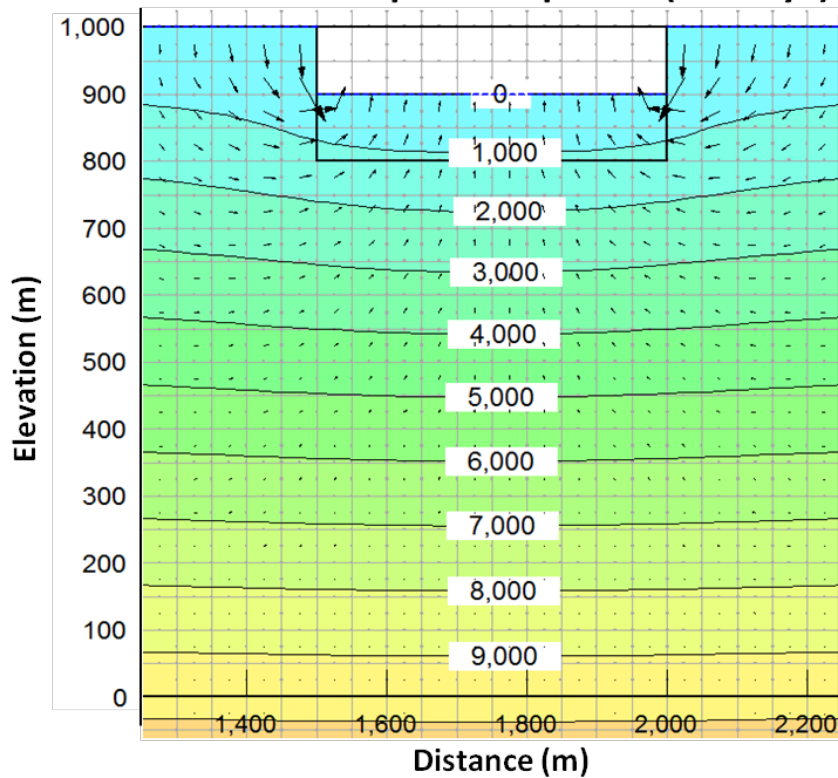


$c_v = 10^{-2} \text{ m}^2/\text{s}$

**PWP
Contours
(kPa)**

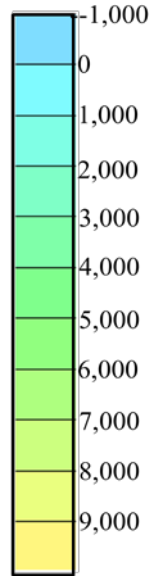


Transient Coupled Response (90 Days)

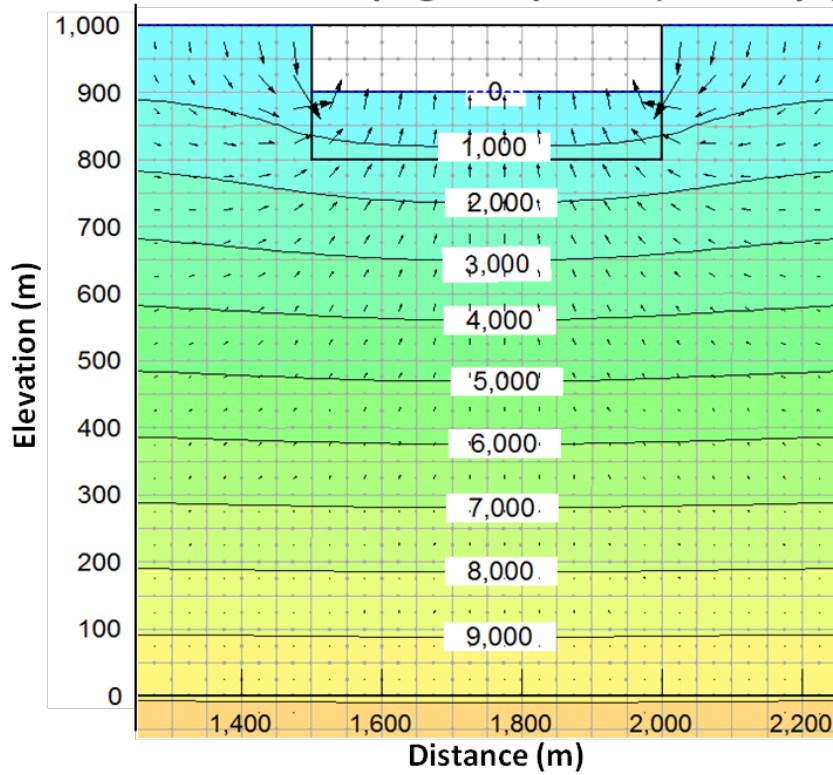


$c_v = 10^{-2} \text{ m}^2/\text{s}$

**PWP
Contours
(kPa)**

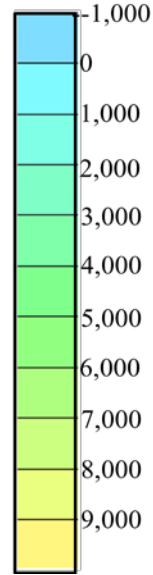


Transient Seepage Response (360 Days)

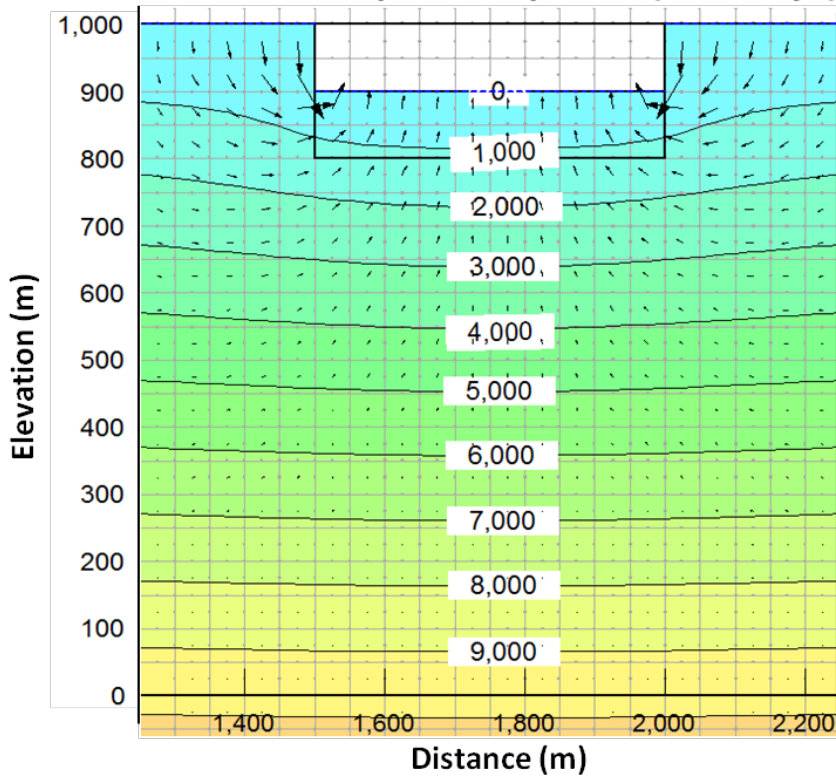


$$c_v = 10^{-2} \text{ m}^2/\text{s}$$

**PWP
Contours
(kPa)**

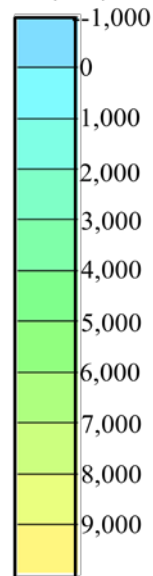


Transient Coupled Response (360 Days)

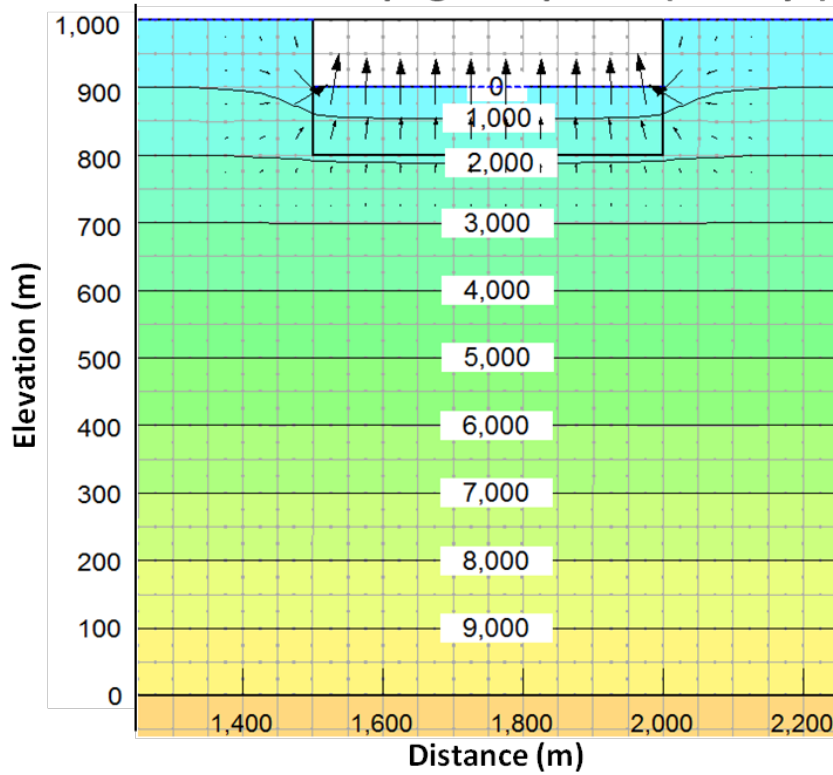


$$c_v = 10^{-2} \text{ m}^2/\text{s}$$

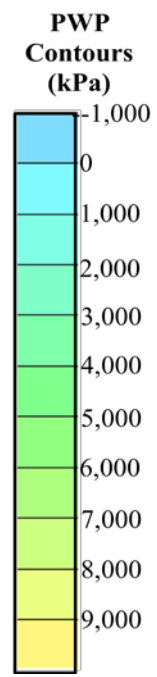
**PWP
Contours
(kPa)**



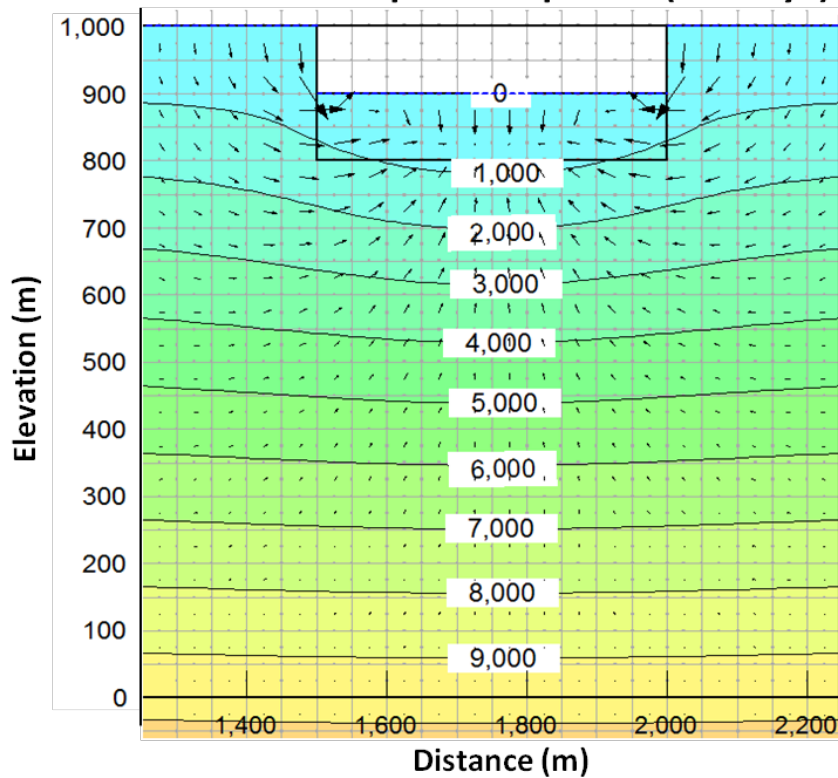
Transient Seepage Response (30 Days)



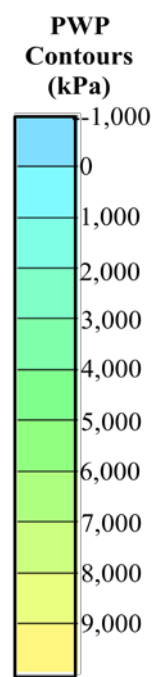
$c_v = 10^{-3} \text{ m}^2/\text{s}$



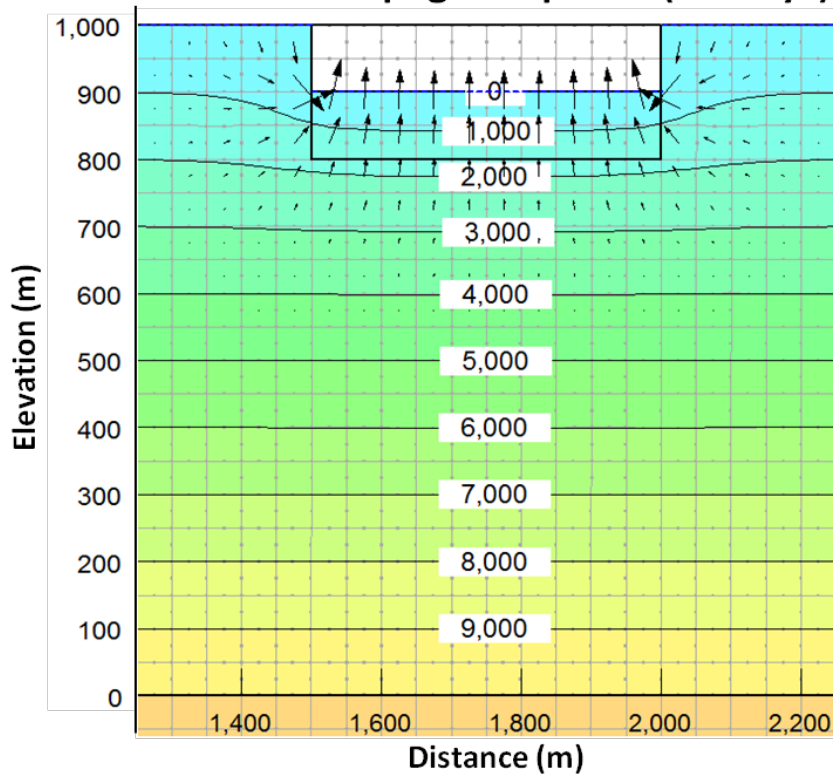
Transient Coupled Response (30 Days)



$c_v = 10^{-3} \text{ m}^2/\text{s}$

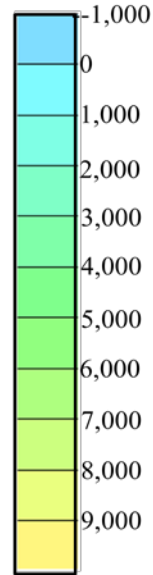


Transient Seepage Response (90 Days)

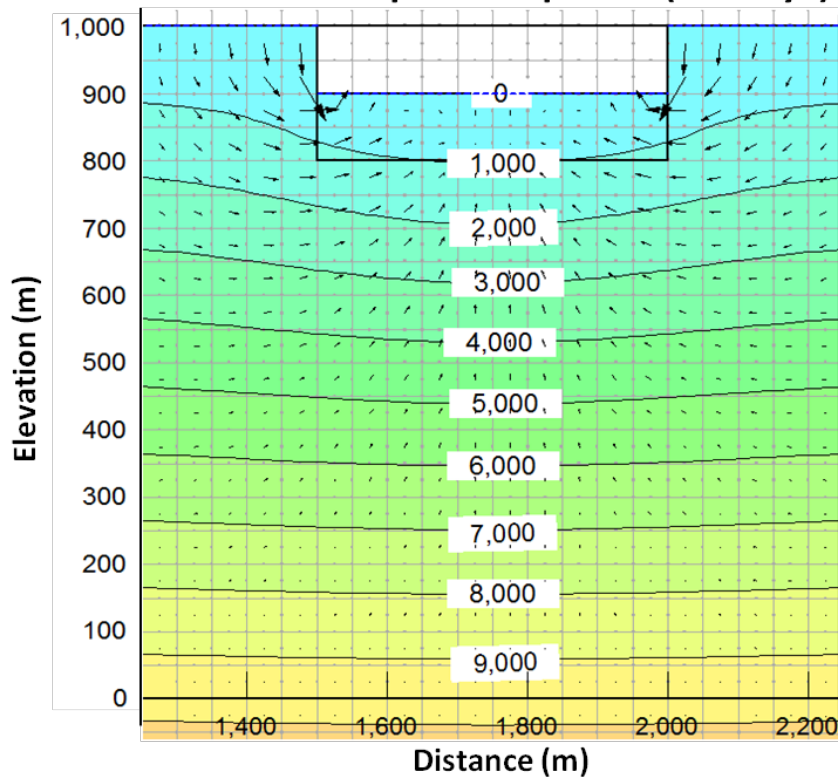


$c_v = 10^{-3} \text{ m}^2/\text{s}$

**PWP
Contours
(kPa)**

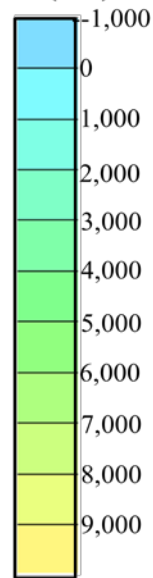


Transient Coupled Response (90 Days)

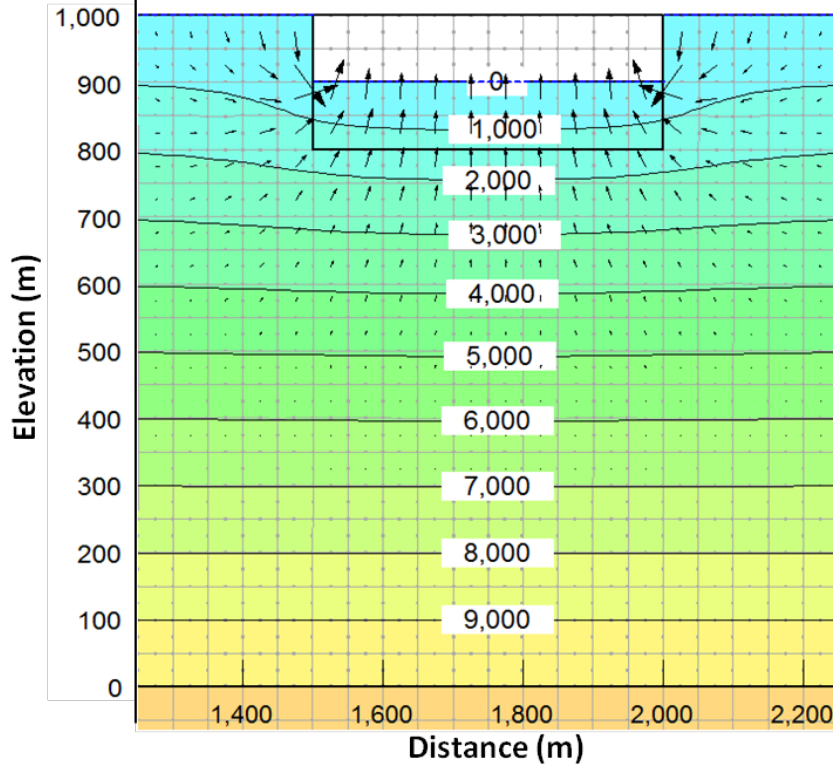


$c_v = 10^{-3} \text{ m}^2/\text{s}$

**PWP
Contours
(kPa)**

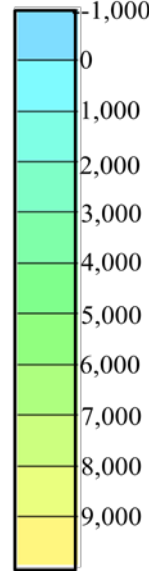


Transient Seepage Response (360 Days)

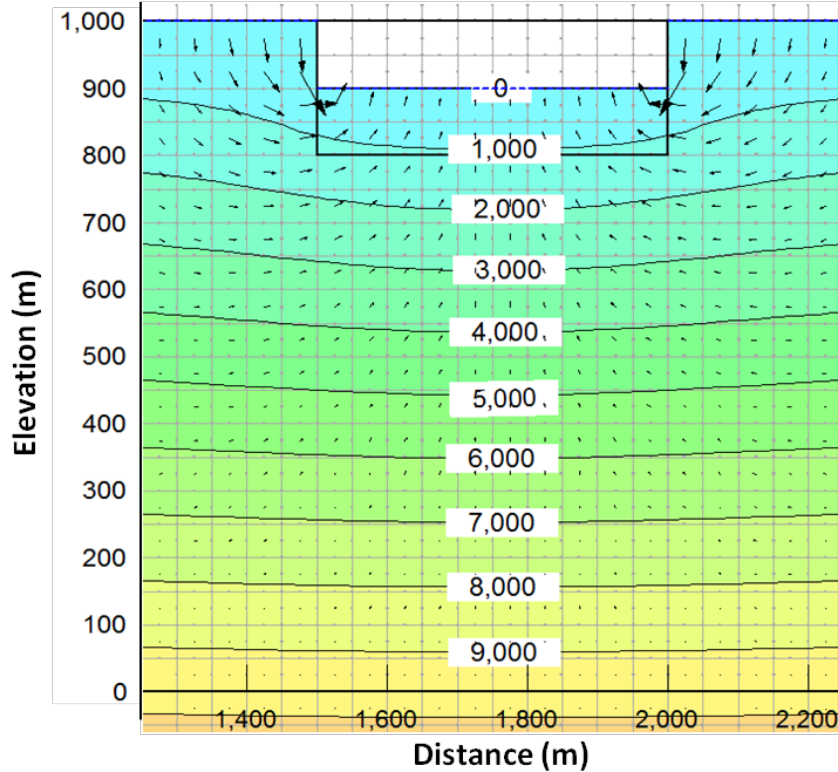


$c_v = 10^{-3} \text{ m}^2/\text{s}$

**PWP
Contours
(kPa)**

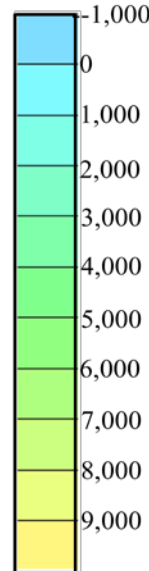


Transient Coupled Response (360 Days)

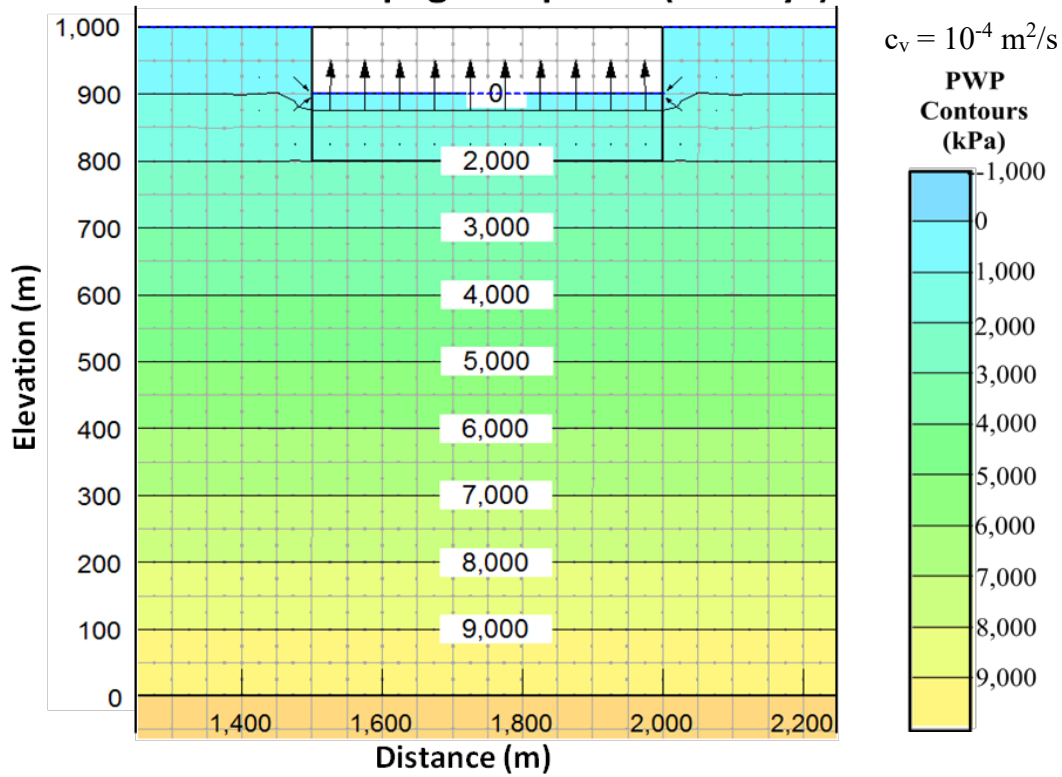


$c_v = 10^{-3} \text{ m}^2/\text{s}$

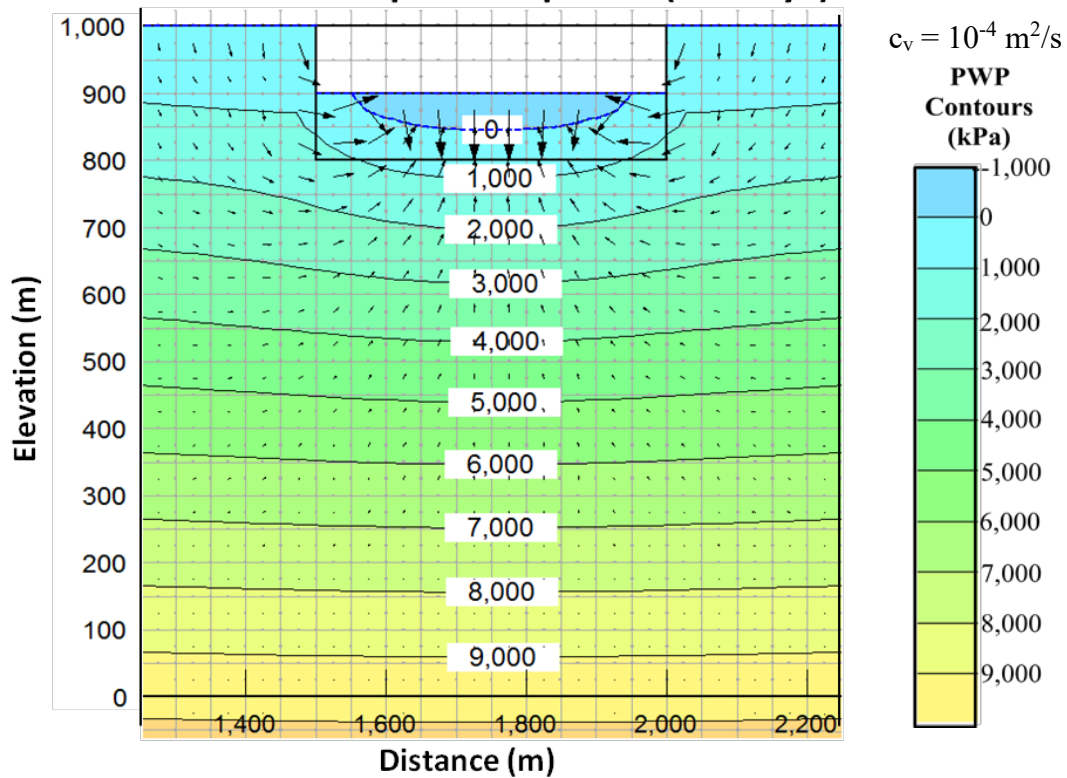
**PWP
Contours
(kPa)**



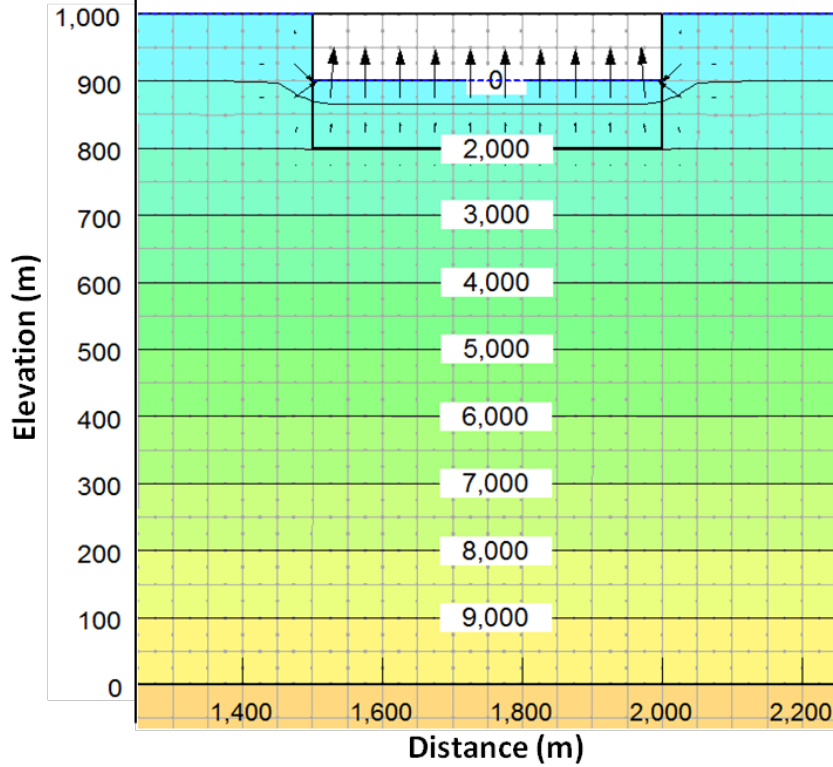
Transient Seepage Response (30 Days)



Transient Coupled Response (30 Days)

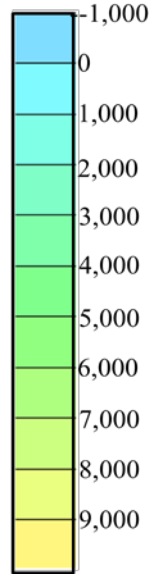


Transient Seepage Response (90 Days)

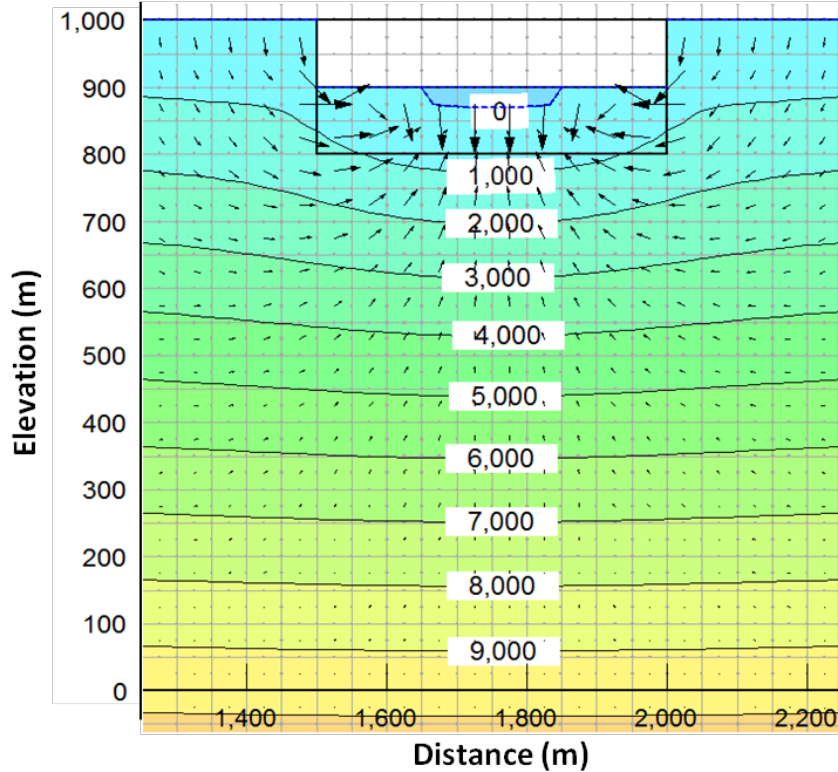


$c_v = 10^{-4} \text{ m}^2/\text{s}$

**PWP
Contours
(kPa)**

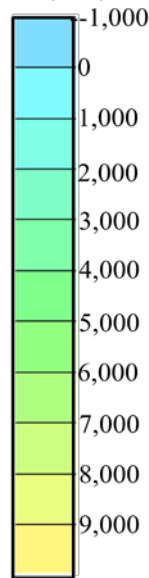


Transient Coupled Response (90 Days)

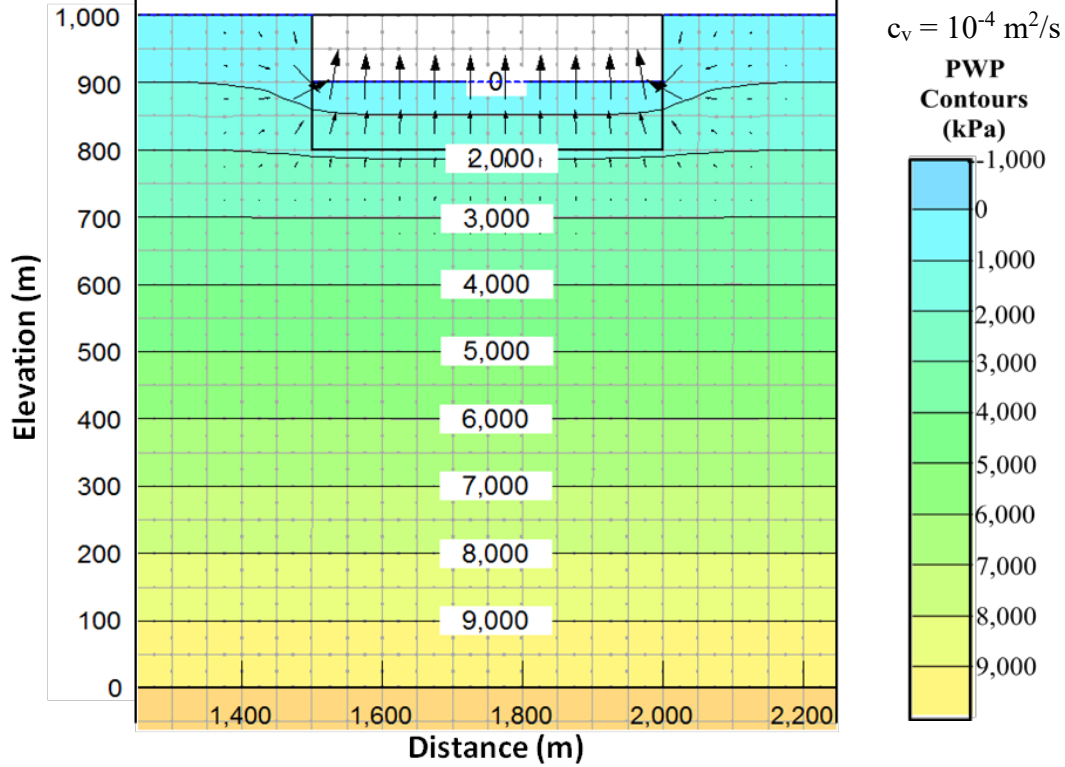


$c_v = 10^{-4} \text{ m}^2/\text{s}$

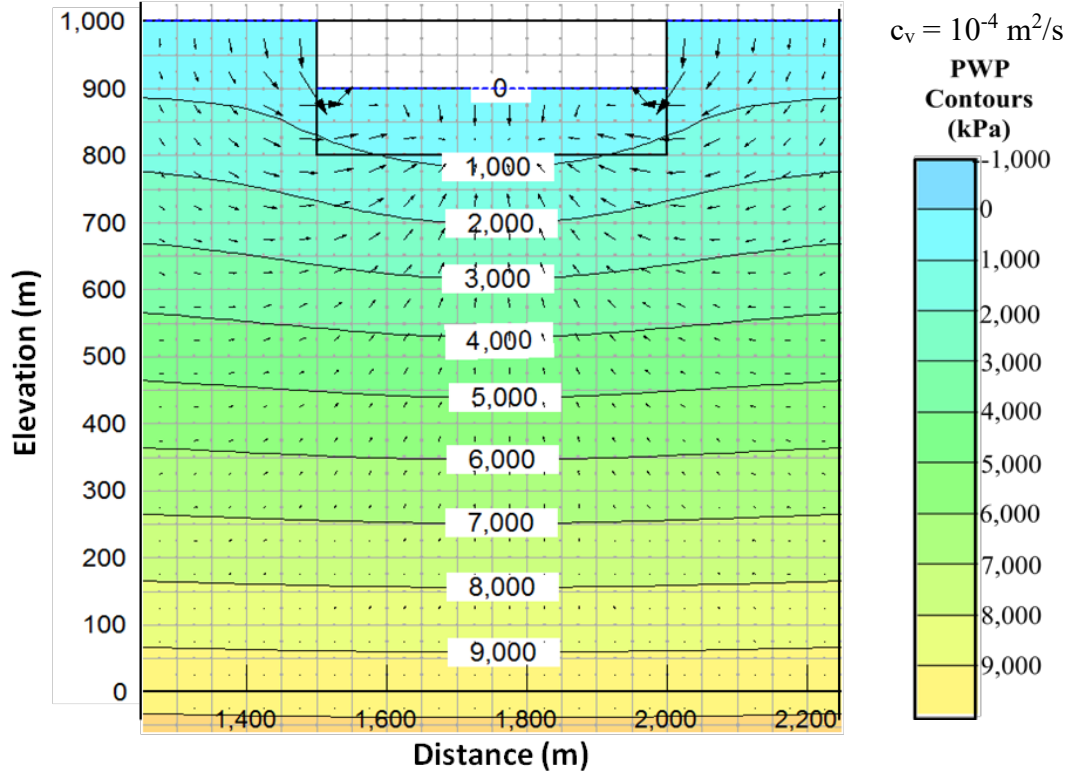
**PWP
Contours
(kPa)**



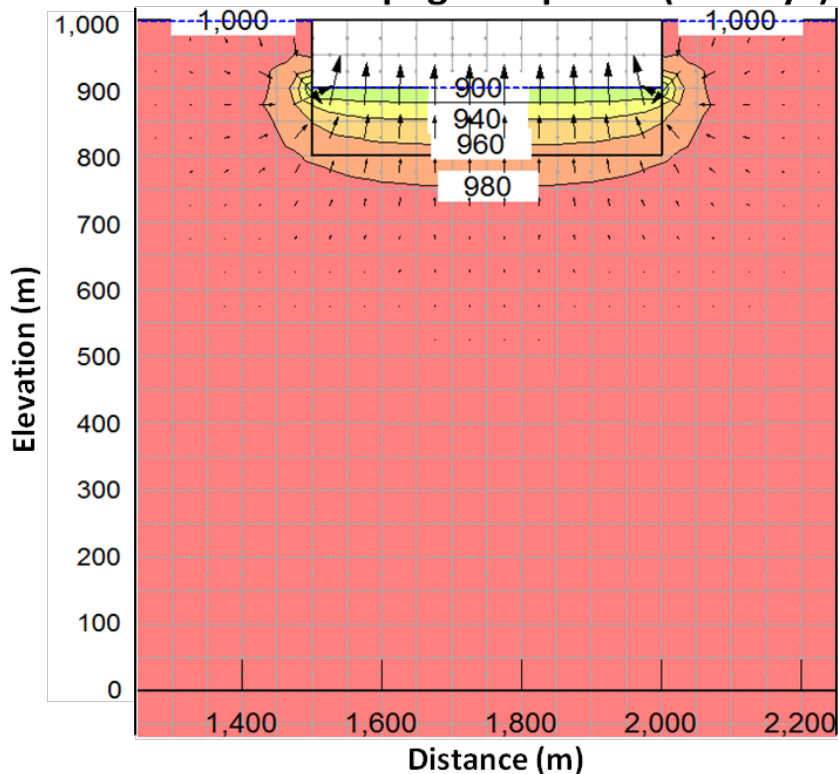
Transient Seepage Response (360 Days)



Transient Coupled Response (360 Days)

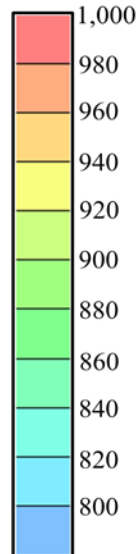


Transient Seepage Response (10 Days)

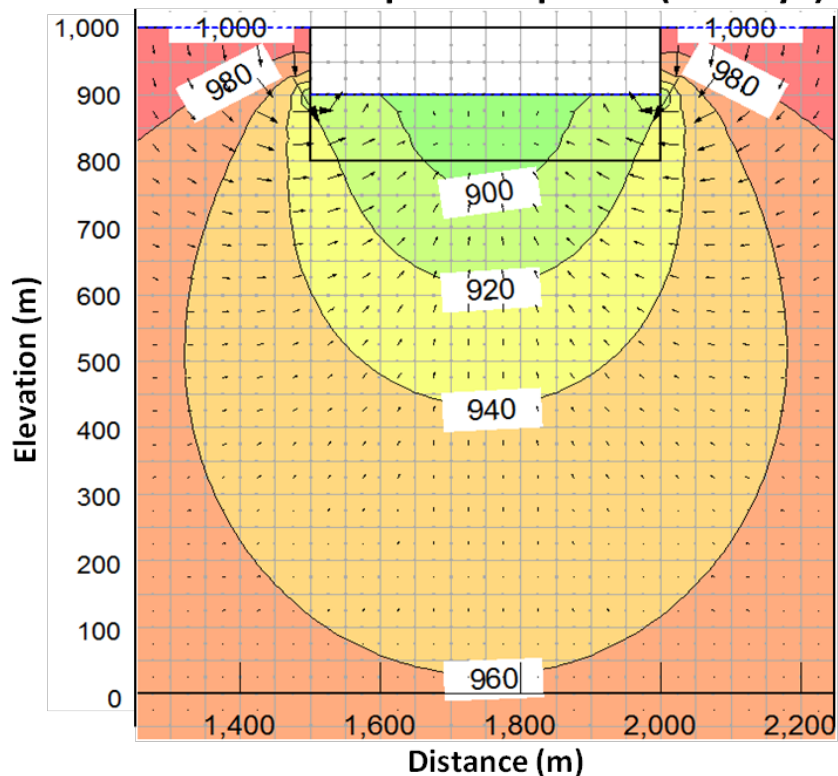


$c_v = 10^{-2} \text{ m}^2/\text{s}$

Total Head Contours (m)

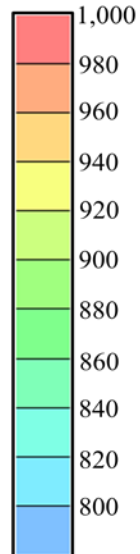


Transient Coupled Response (10 Days)

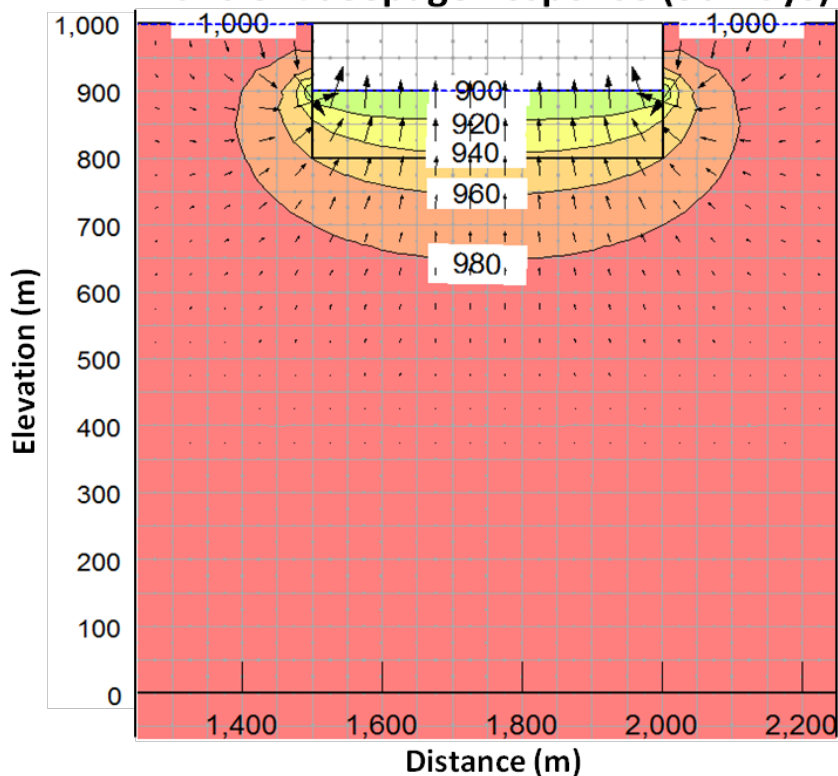


$c_v = 10^{-2} \text{ m}^2/\text{s}$

Total Head Contours (m)

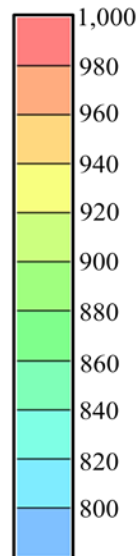


Transient Seepage Response (30 Days)

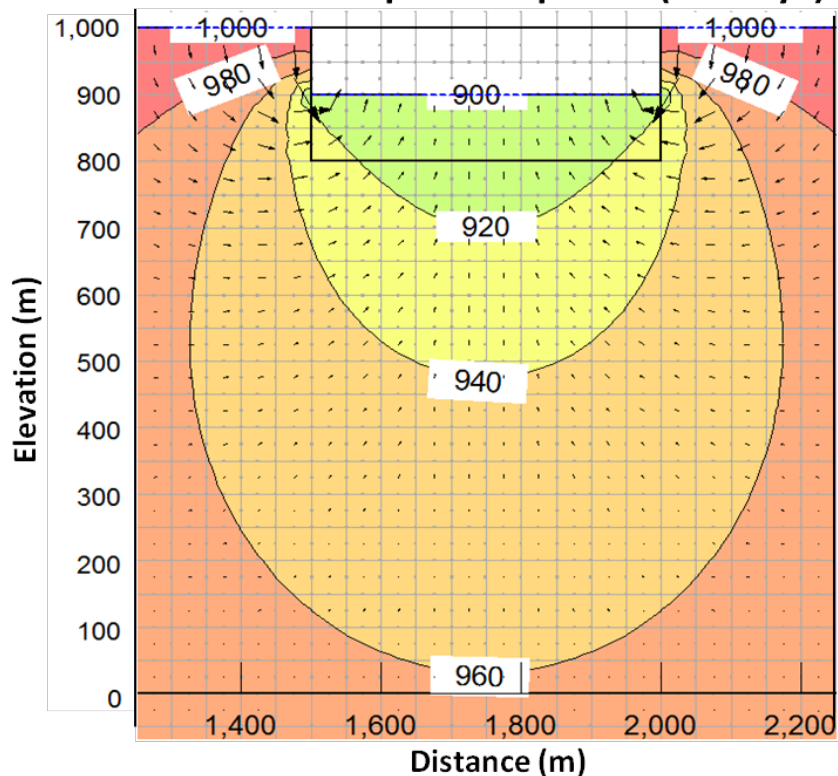


$c_v = 10^{-2} \text{ m}^2/\text{s}$

Total Head Contours (m)

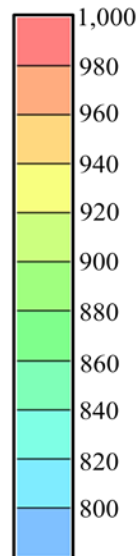


Transient Coupled Response (30 Days)

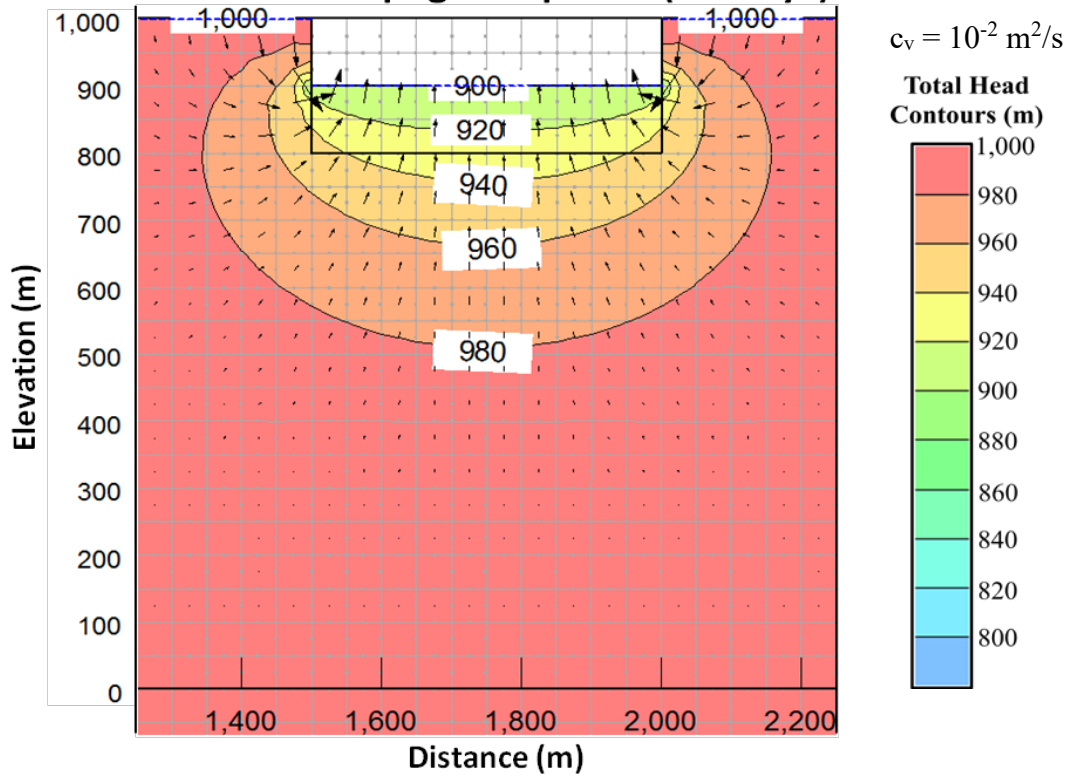


$c_v = 10^{-2} \text{ m}^2/\text{s}$

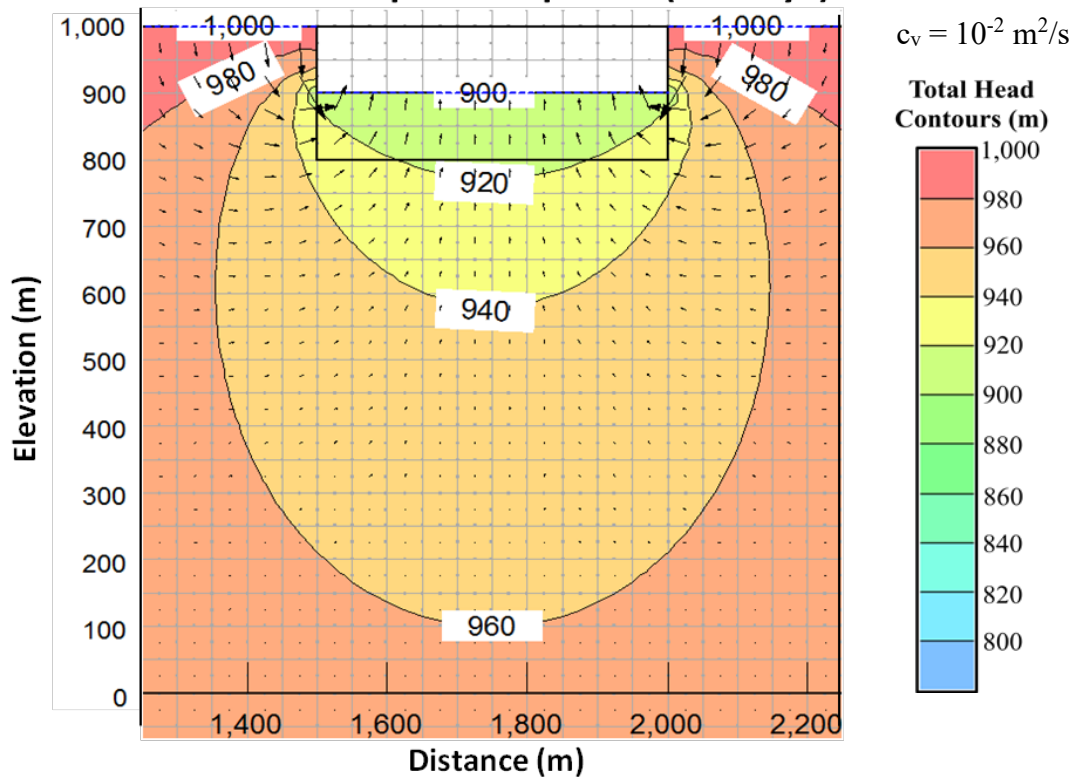
Total Head Contours (m)



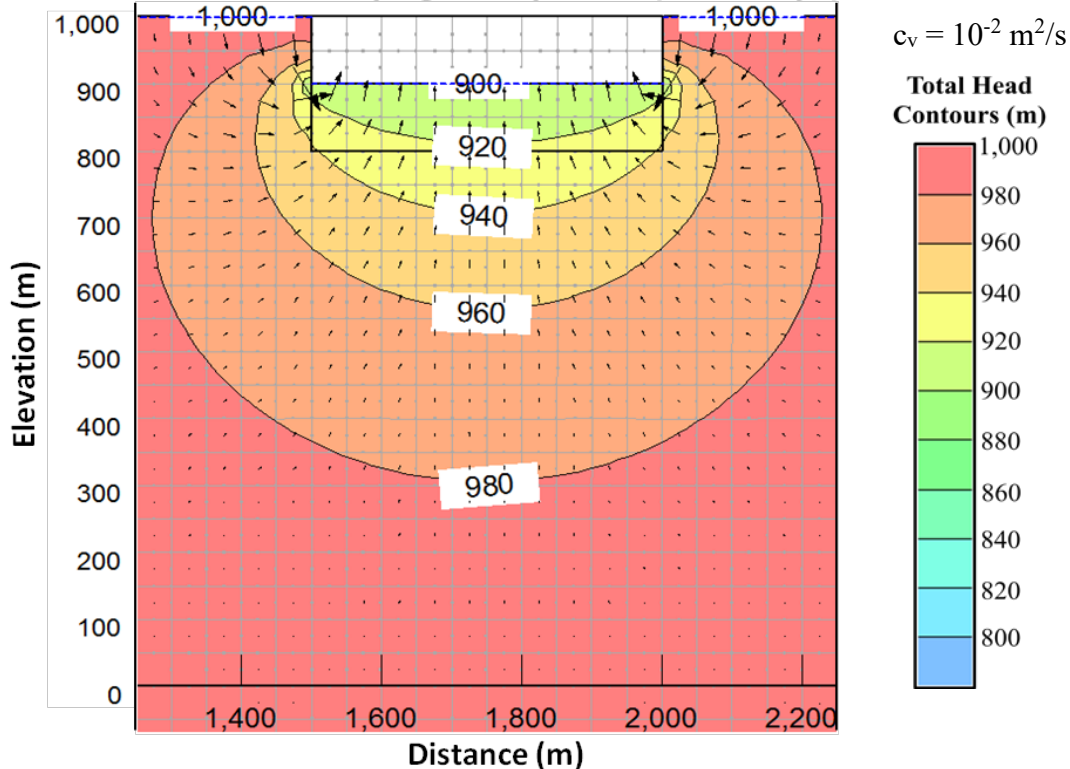
Transient Seepage Response (90 Days)



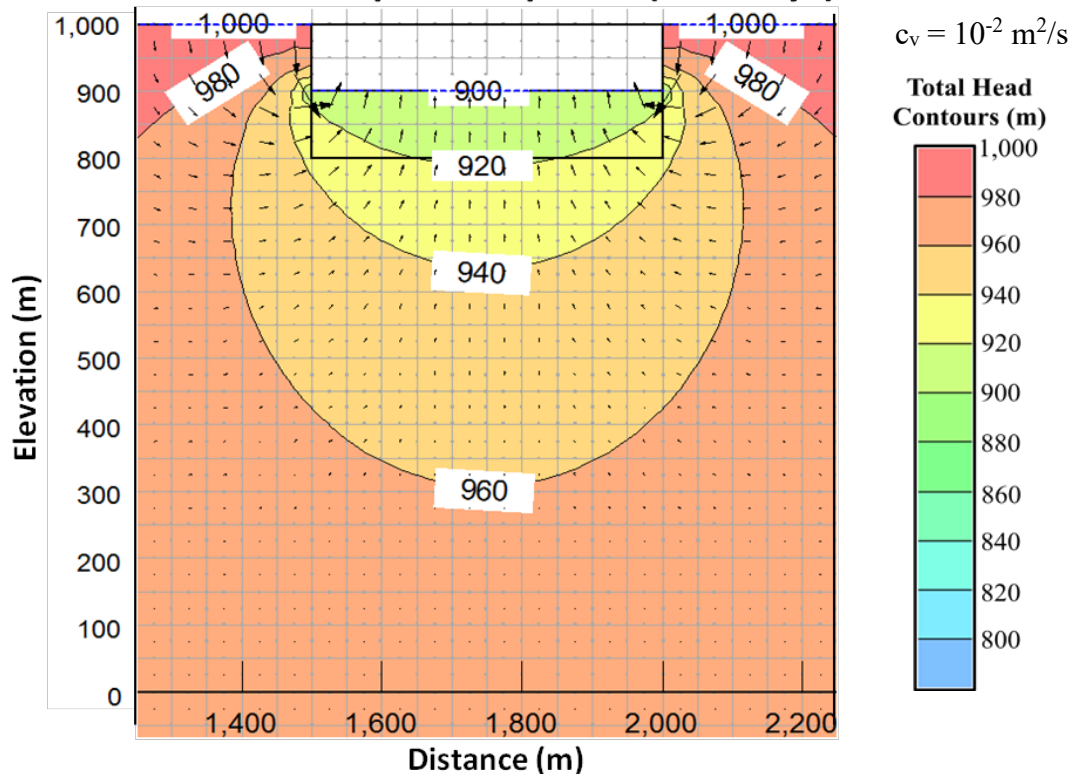
Transient Coupled Response (90 Days)



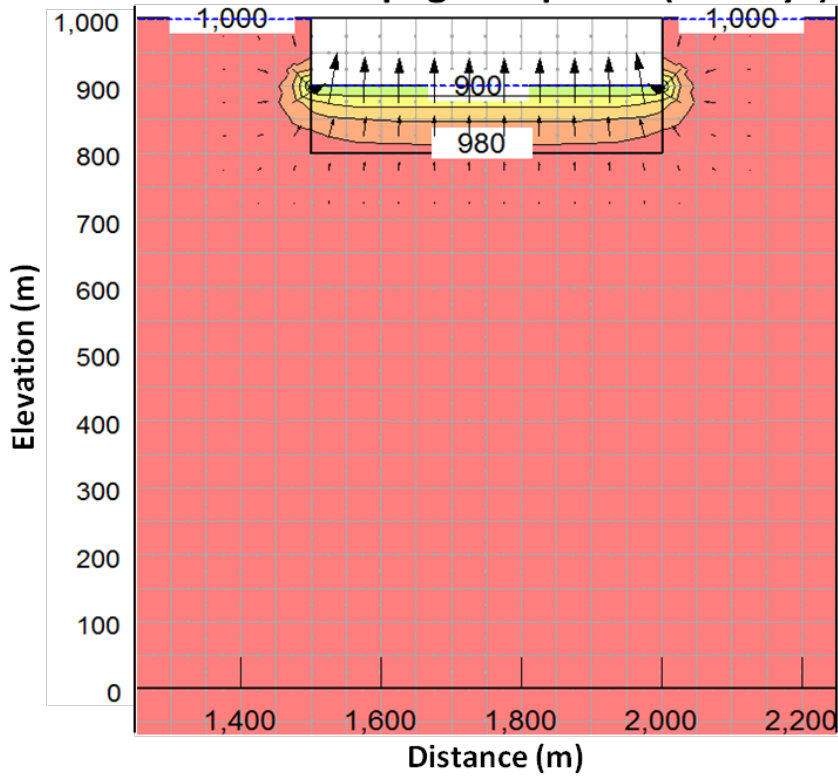
Transient Seepage Response (360 Days)



Transient Coupled Response (360 Days)

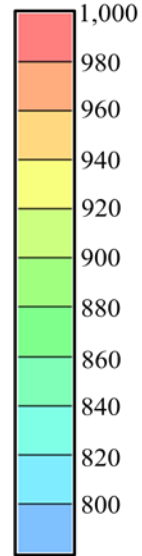


Transient Seepage Response (30 Days)

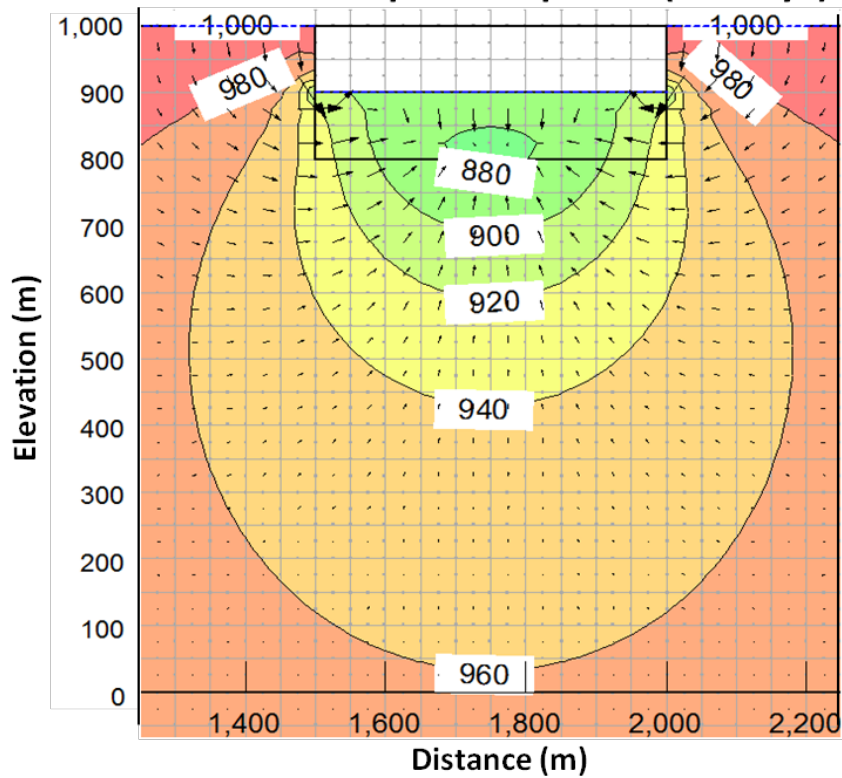


$$c_v = 10^{-3} \text{ m}^2/\text{s}$$

Total Head Contours (m)

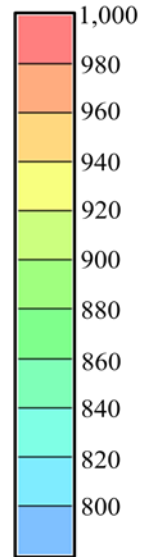


Transient Coupled Response (30 Days)

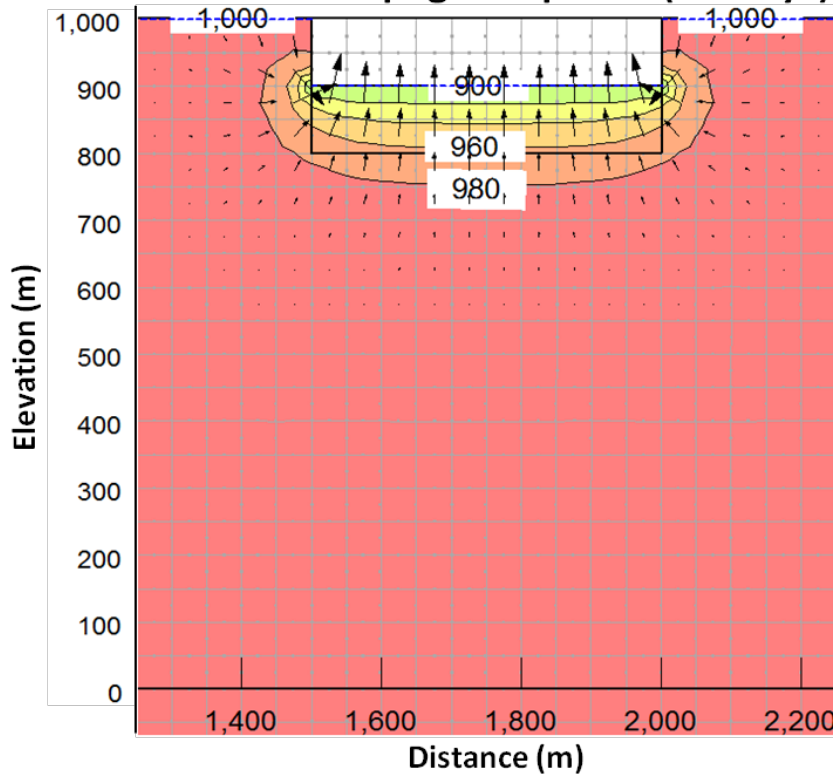


$$c_v = 10^{-3} \text{ m}^2/\text{s}$$

Total Head Contours (m)

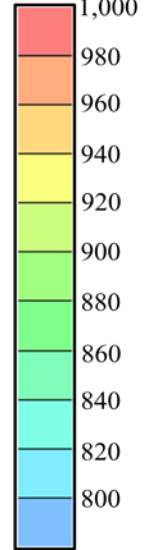


Transient Seepage Response (90 Days)

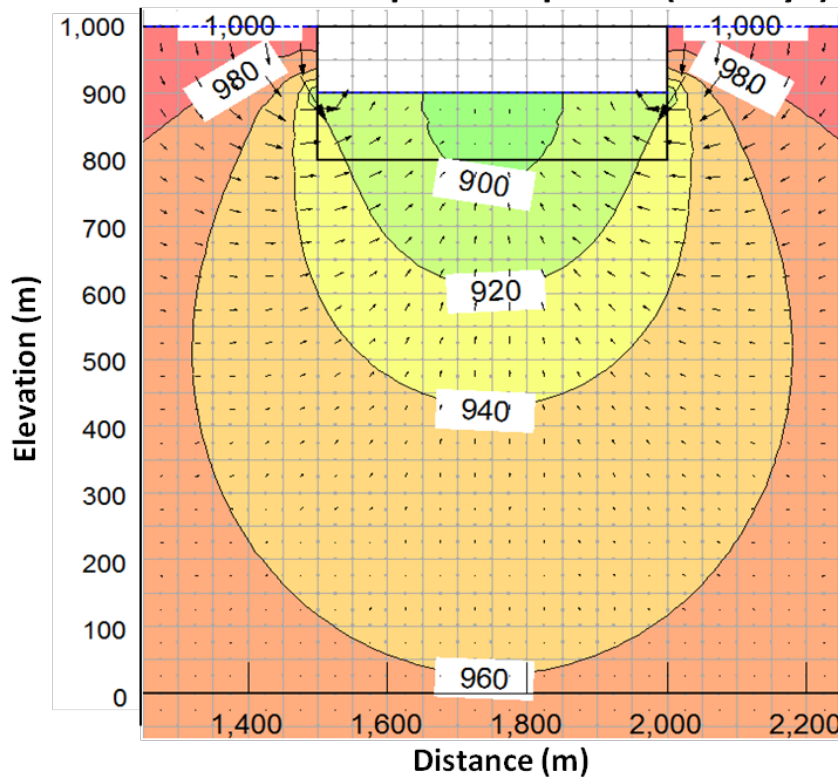


$c_v = 10^{-3} \text{ m}^2/\text{s}$

Total Head Contours (m)

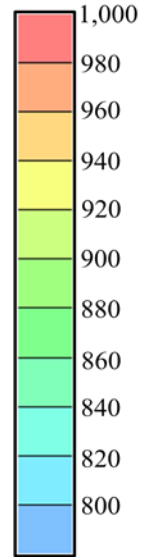


Transient Coupled Response (90 Days)

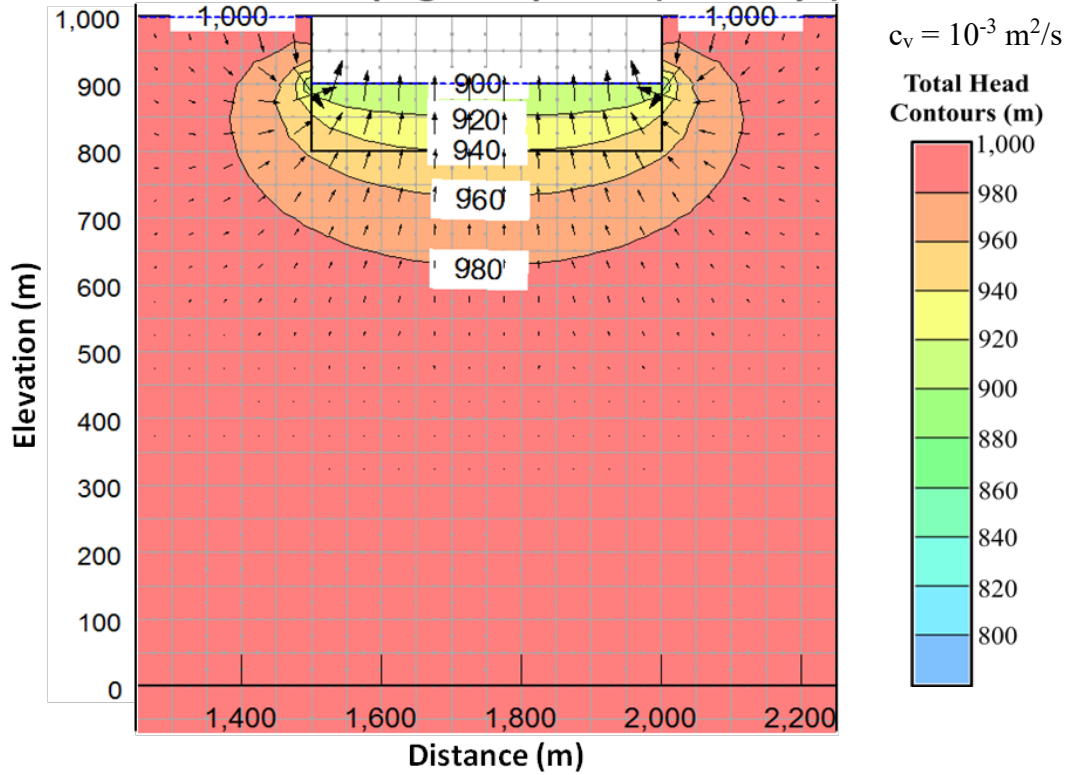


$c_v = 10^{-3} \text{ m}^2/\text{s}$

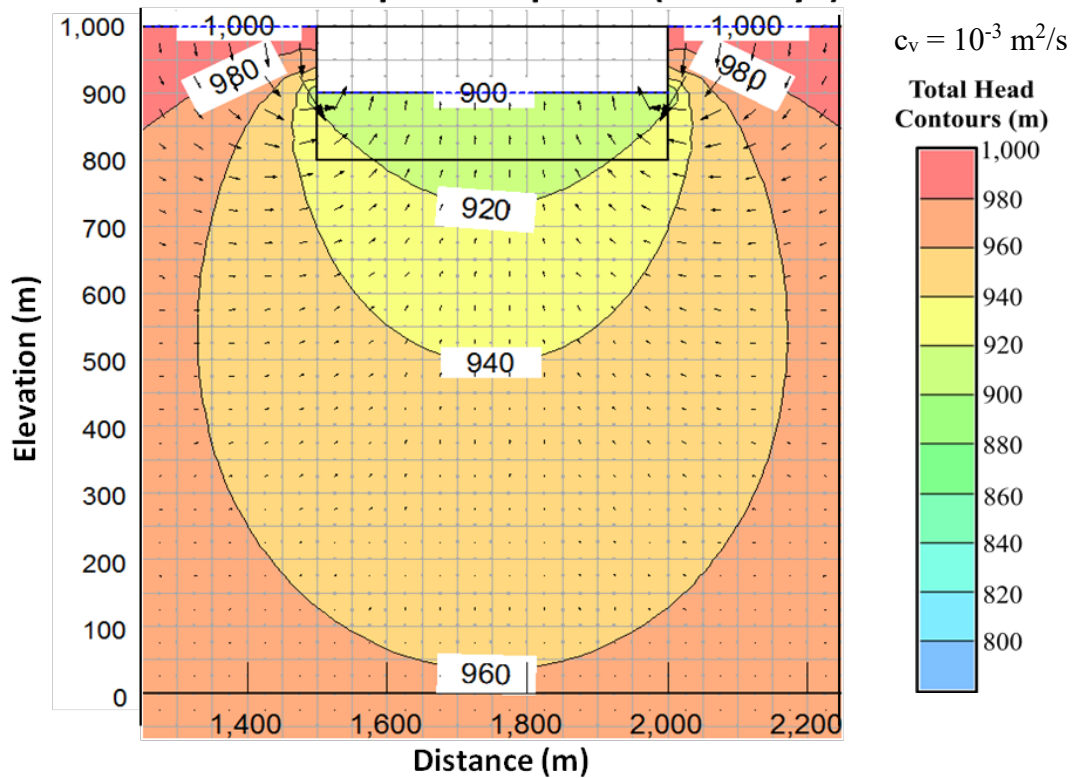
Total Head Contours (m)



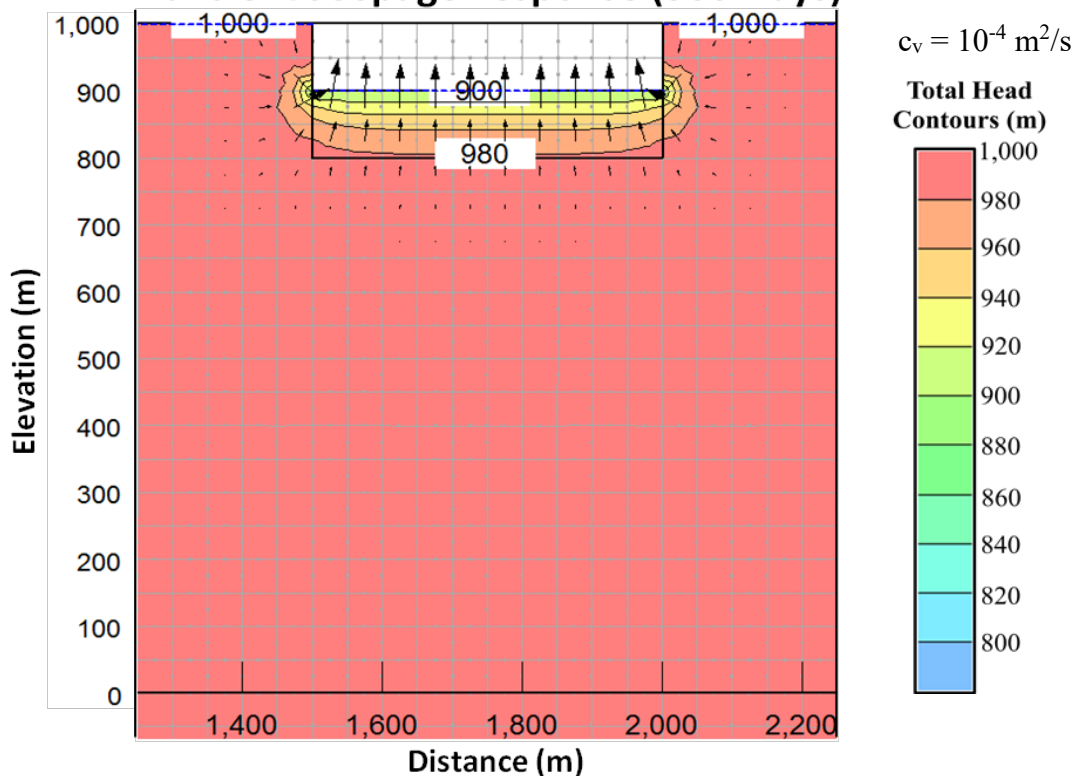
Transient Seepage Response (360 Days)



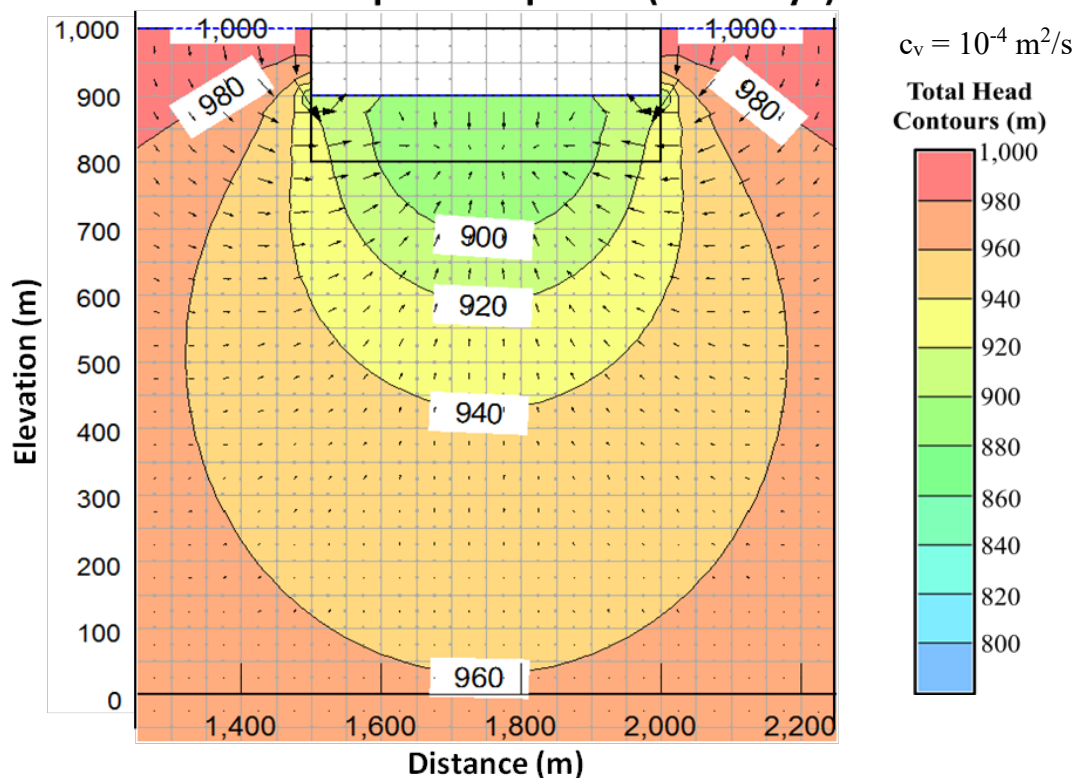
Transient Coupled Response (360 Days)



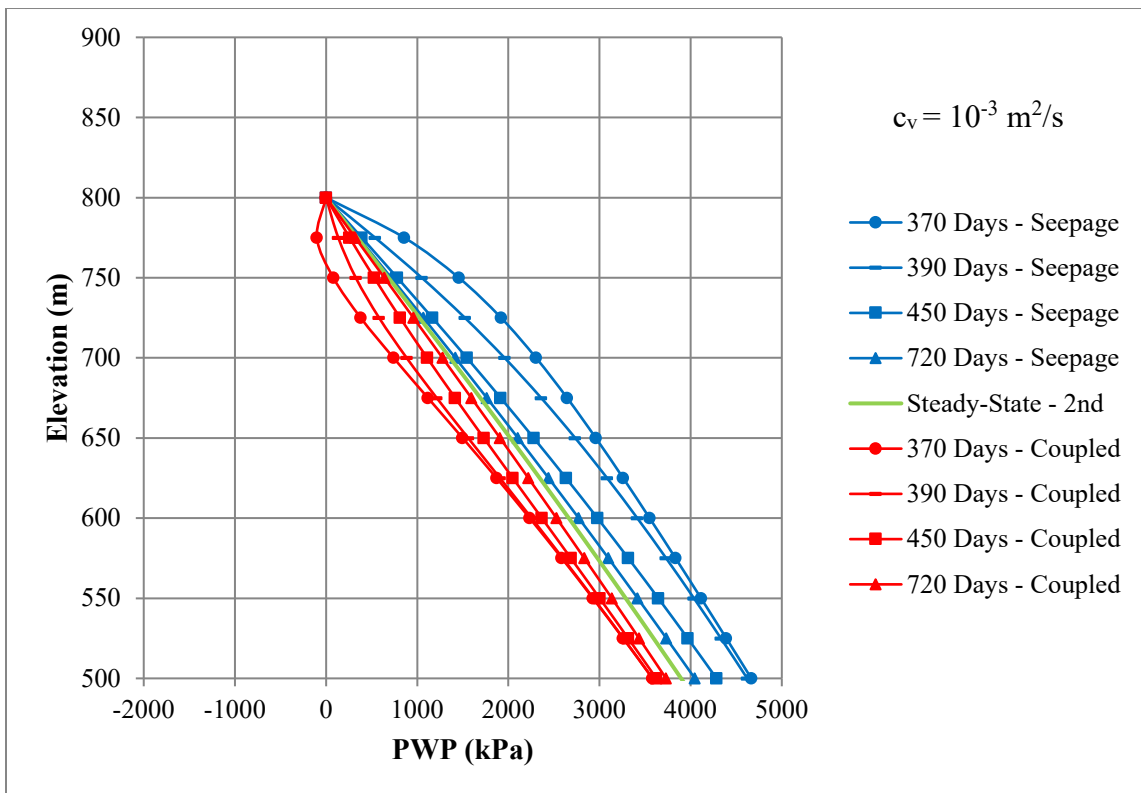
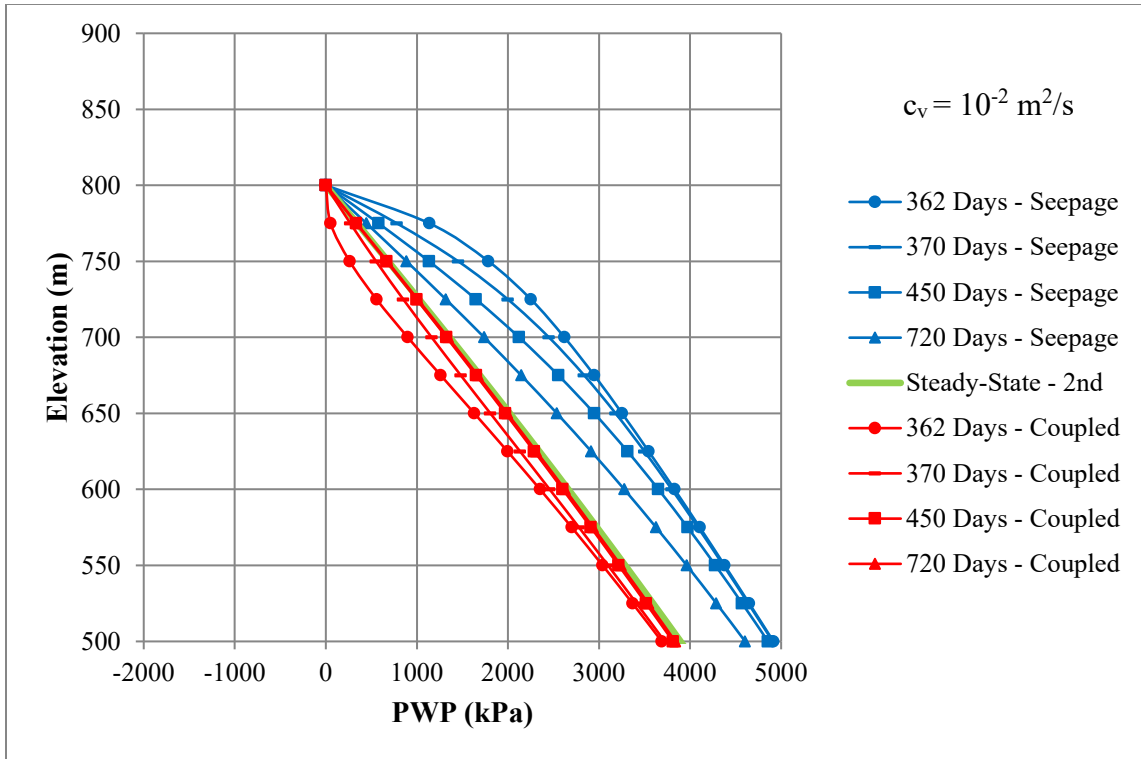
Transient Seepage Response (360 Days)

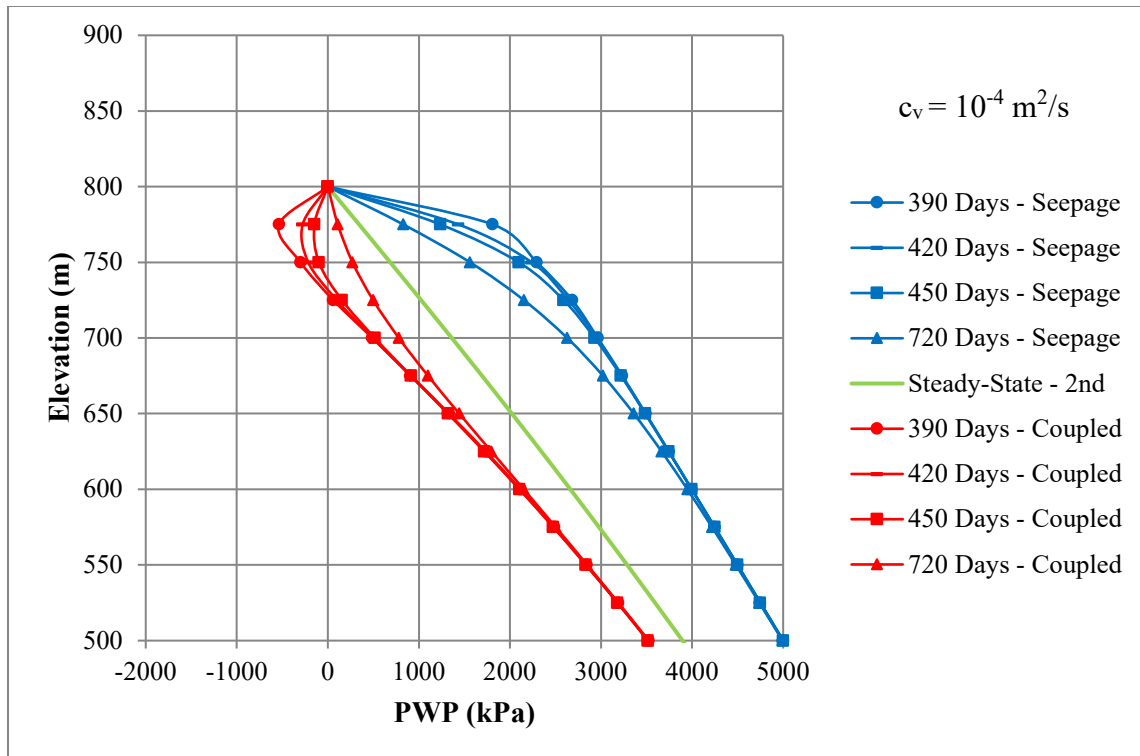


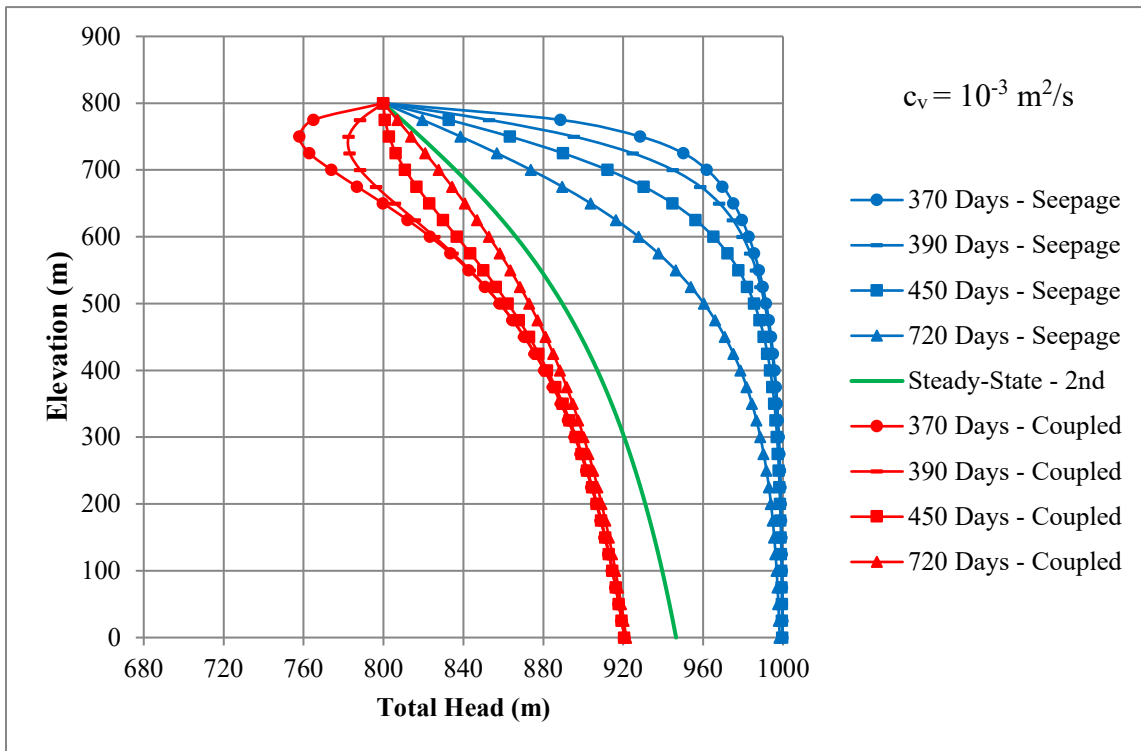
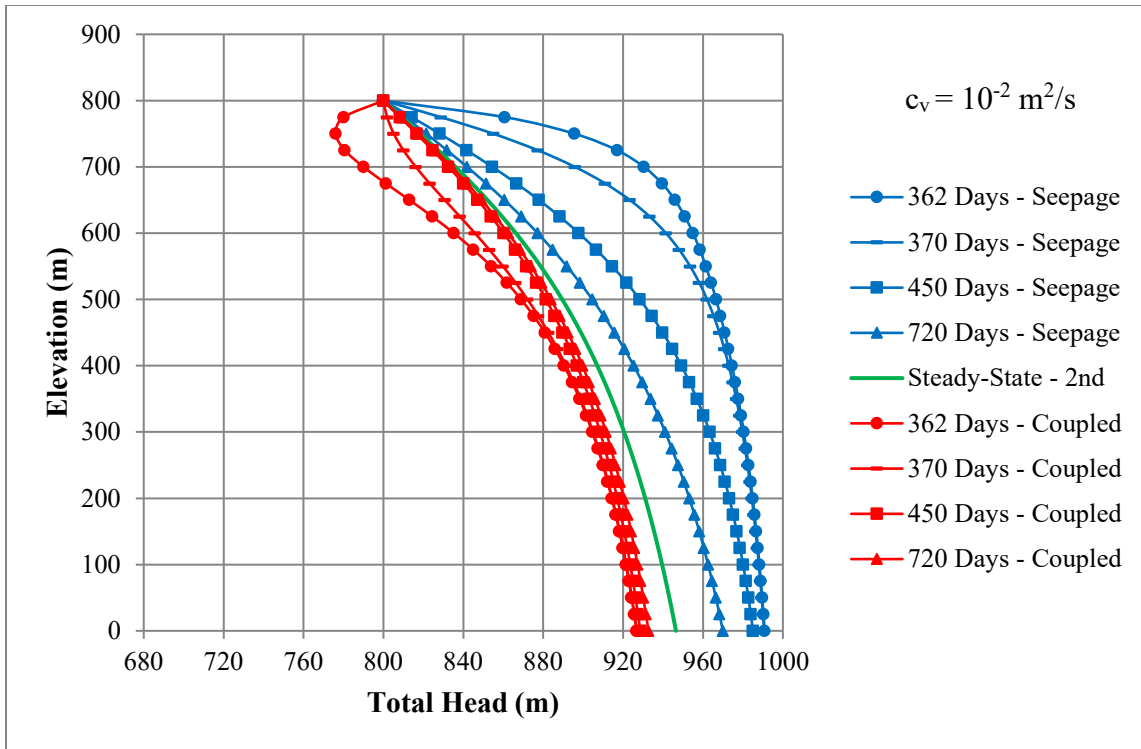
Transient Coupled Response (360 Days)

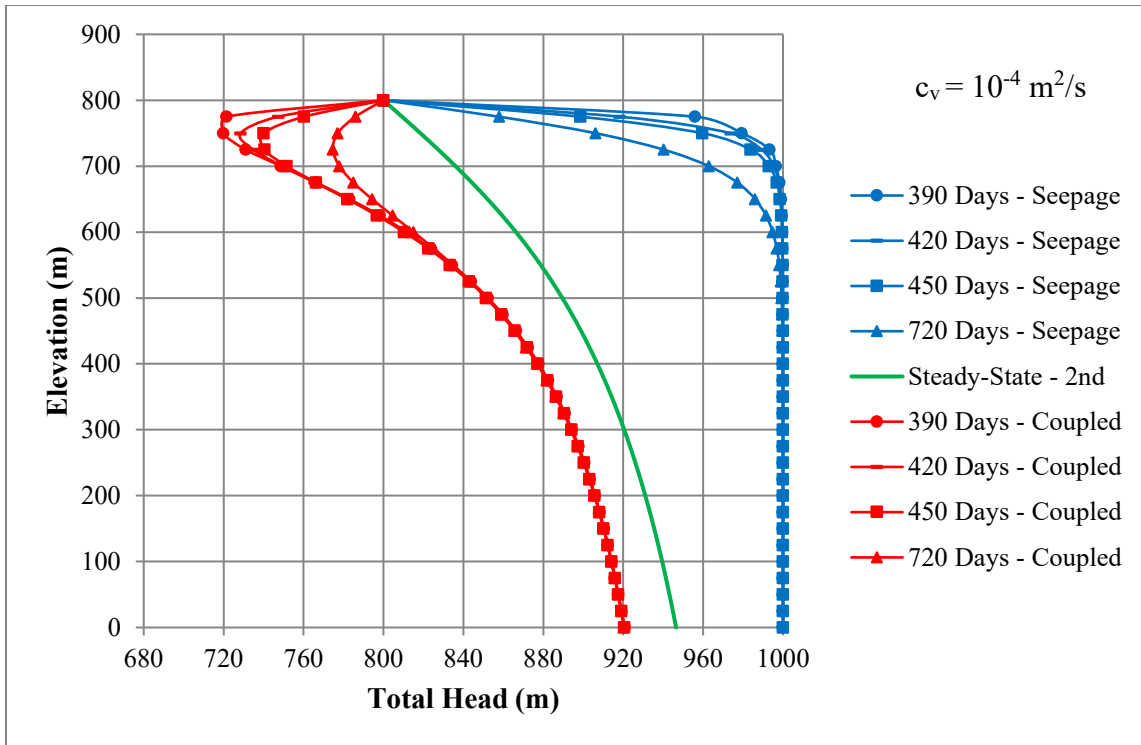


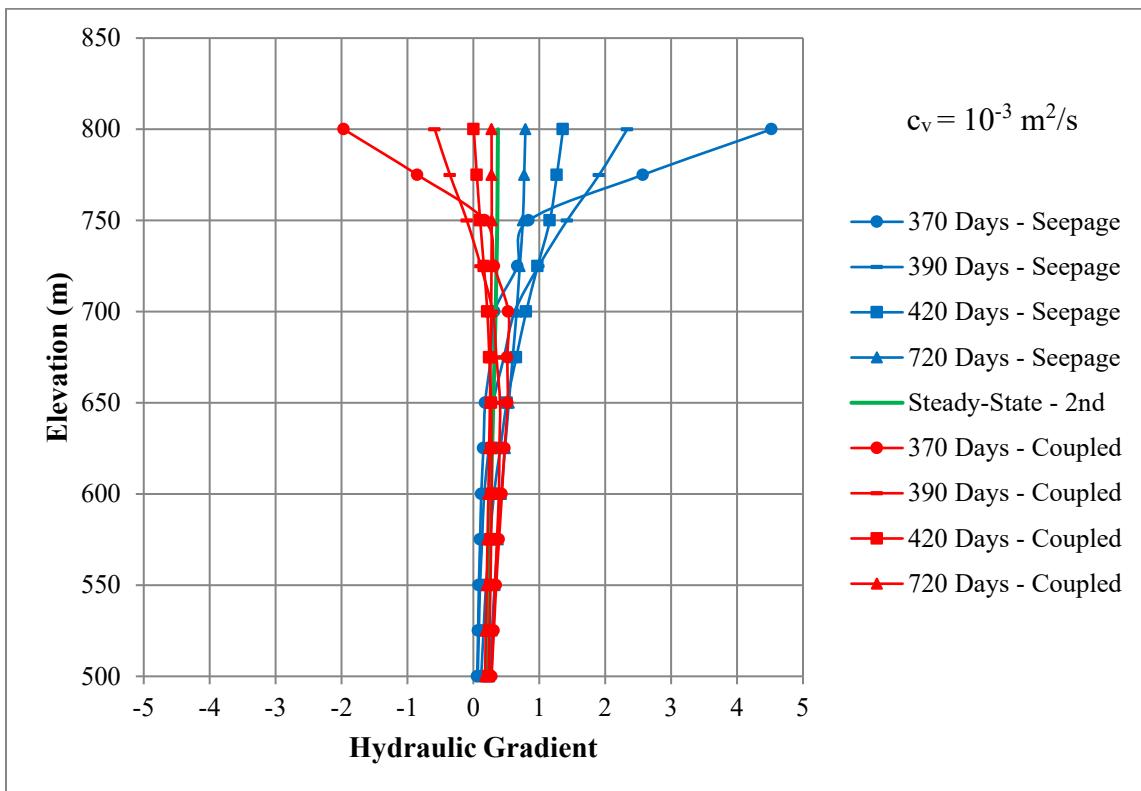
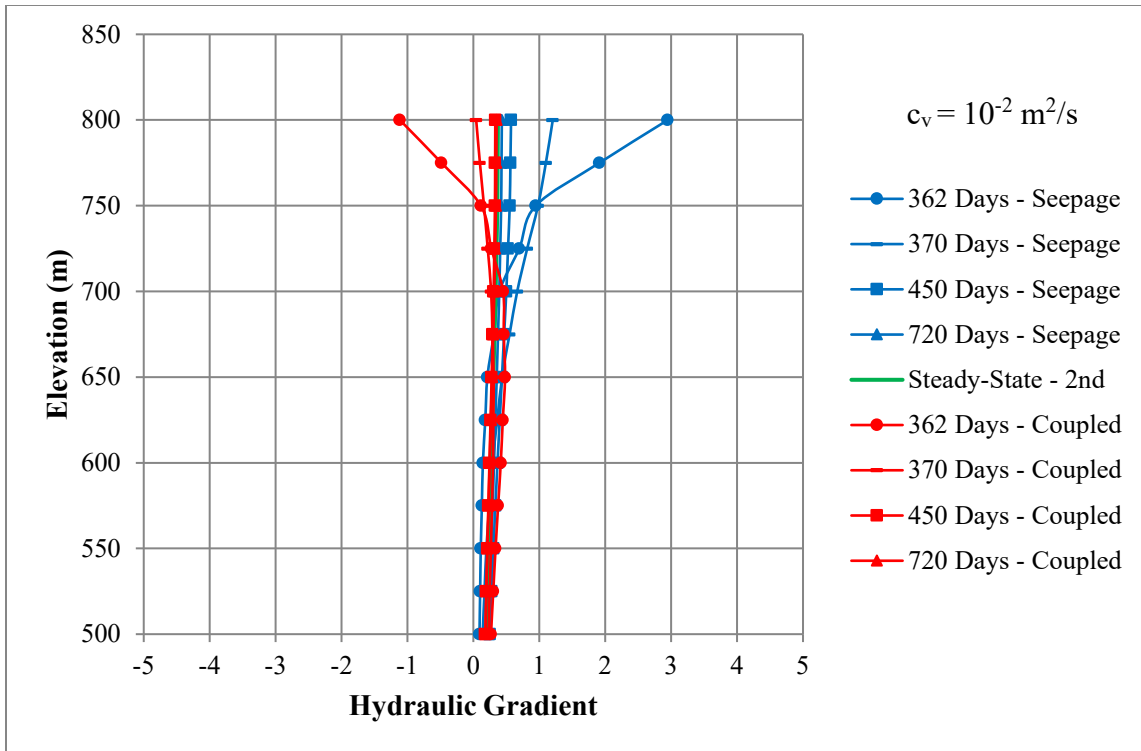
Pages 145-150: Graphs of pore water pressure, total head, and hydraulic gradients for the 2nd excavation and for each of the three diffusion coefficients (10^{-2} , 10^{-3} and 10^{-4} m²/s).

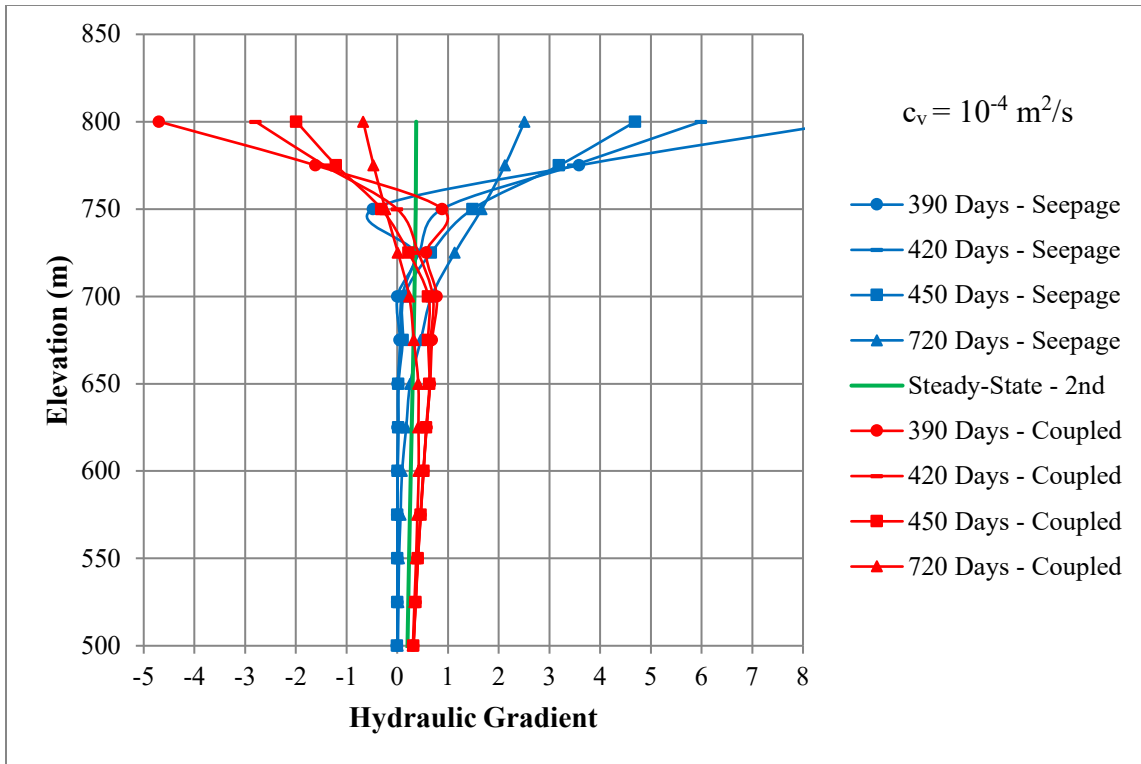








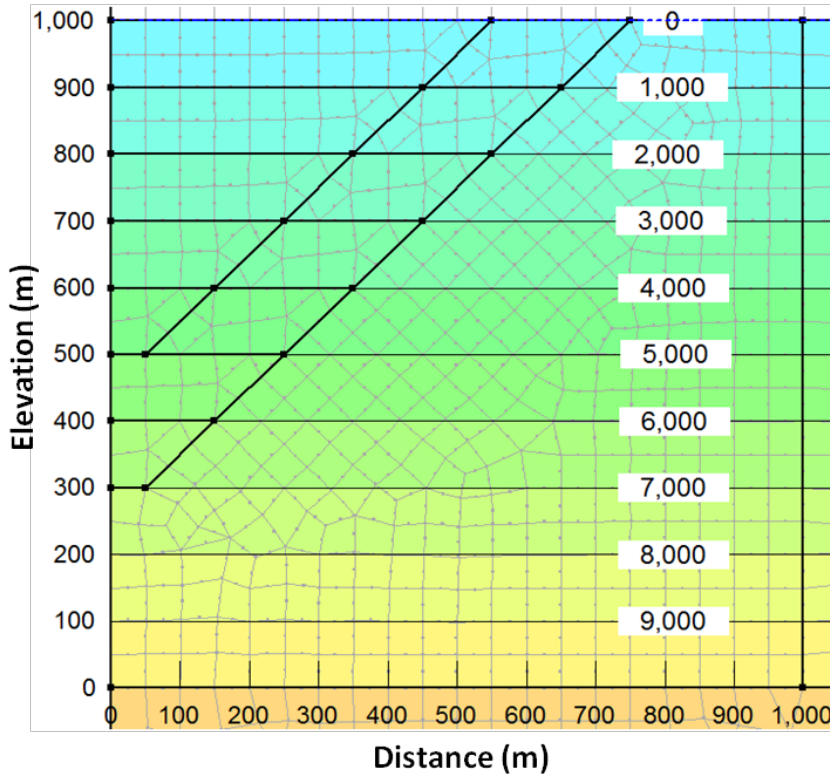




Appendix C: Additional 2-D Unconfined Flow Results

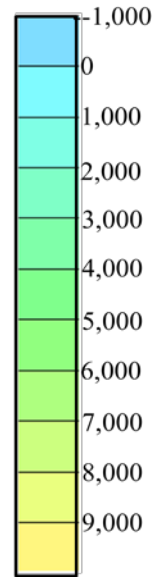
Pages 153-188: Pore water pressure and total head contour charts for each of the three diffusion coefficients (10^{-2} , 10^{-3} and 10^{-4} m²/s). Included are comparisons between the transient seepage response and transient coupled response for each diffusion coefficient.

Initial Conditions

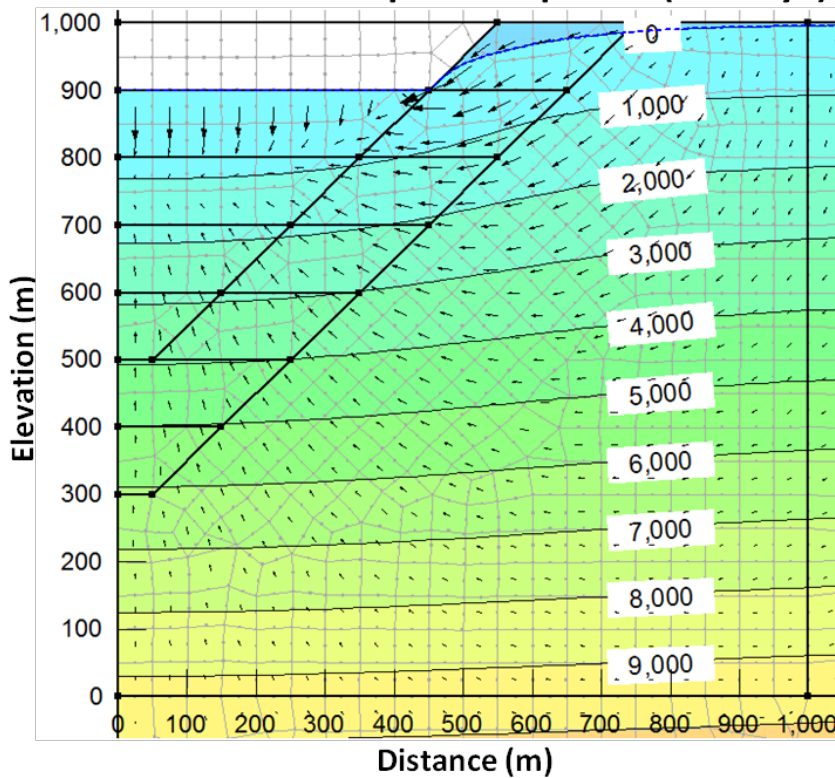


$c_v = 10^{-2} \text{ m}^2/\text{s}$

**PWP
Contours
(kPa)**

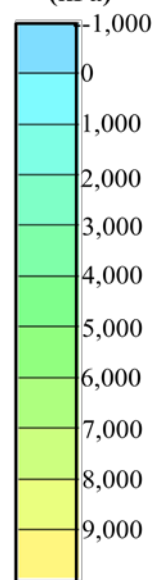


Transient Coupled Response (10 Days)

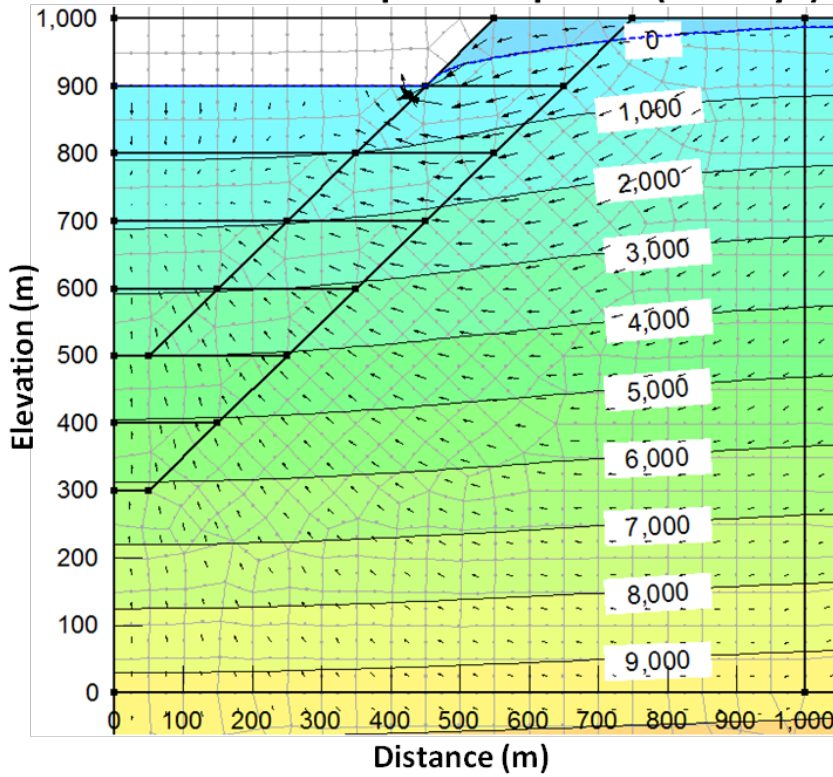


$c_v = 10^{-2} \text{ m}^2/\text{s}$

**PWP
Contours
(kPa)**

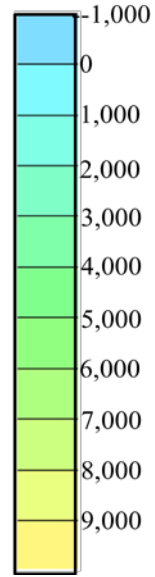


Transient Coupled Response (30 Days)

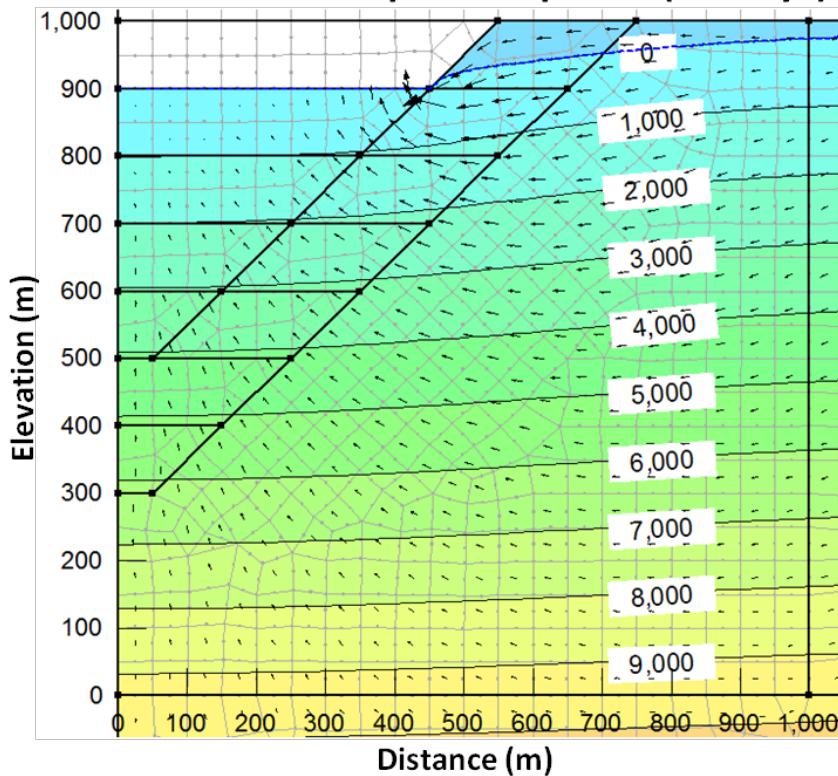


$c_v = 10^{-2} \text{ m}^2/\text{s}$

**PWP
Contours
(kPa)**

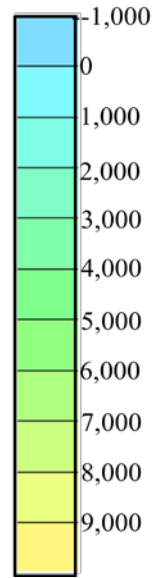


Transient Coupled Response (90 Days)

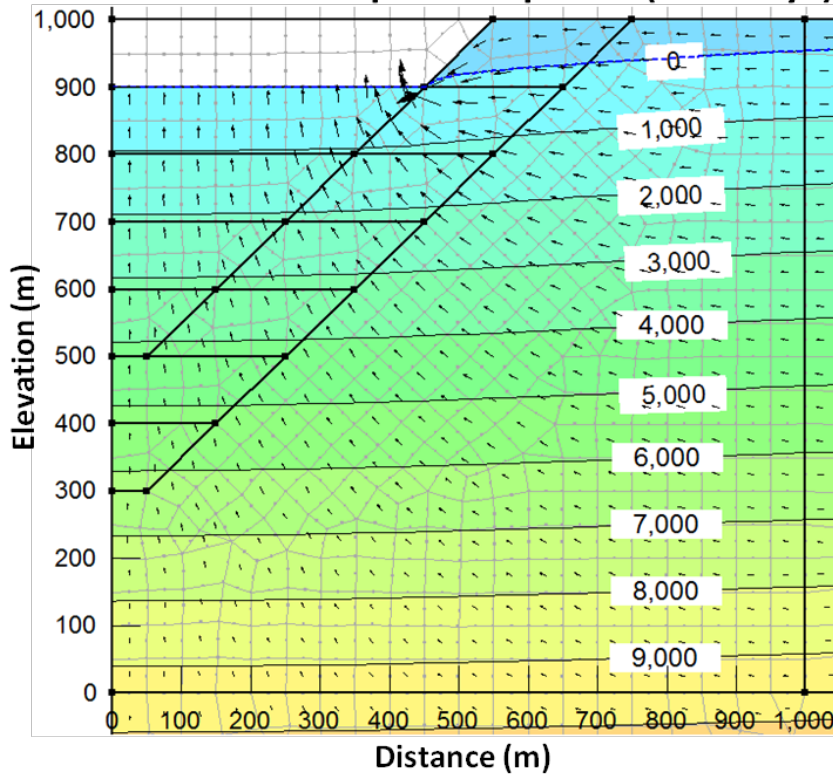


$c_v = 10^{-2} \text{ m}^2/\text{s}$

**PWP
Contours
(kPa)**

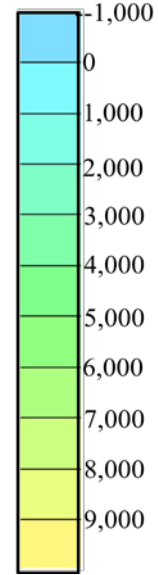


Transient Coupled Response (360 Days)

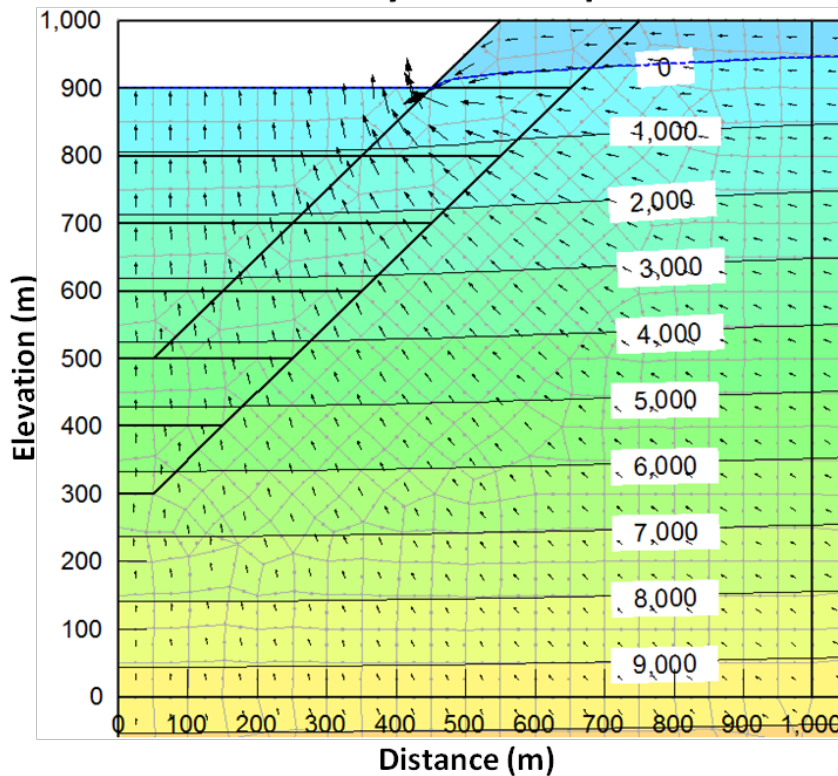


$c_v = 10^{-2} \text{ m}^2/\text{s}$

**PWP
Contours
(kPa)**

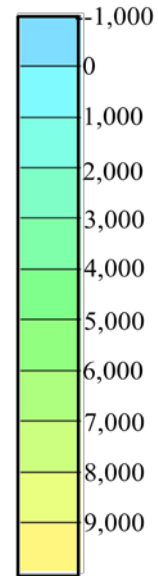


Steady-State Response

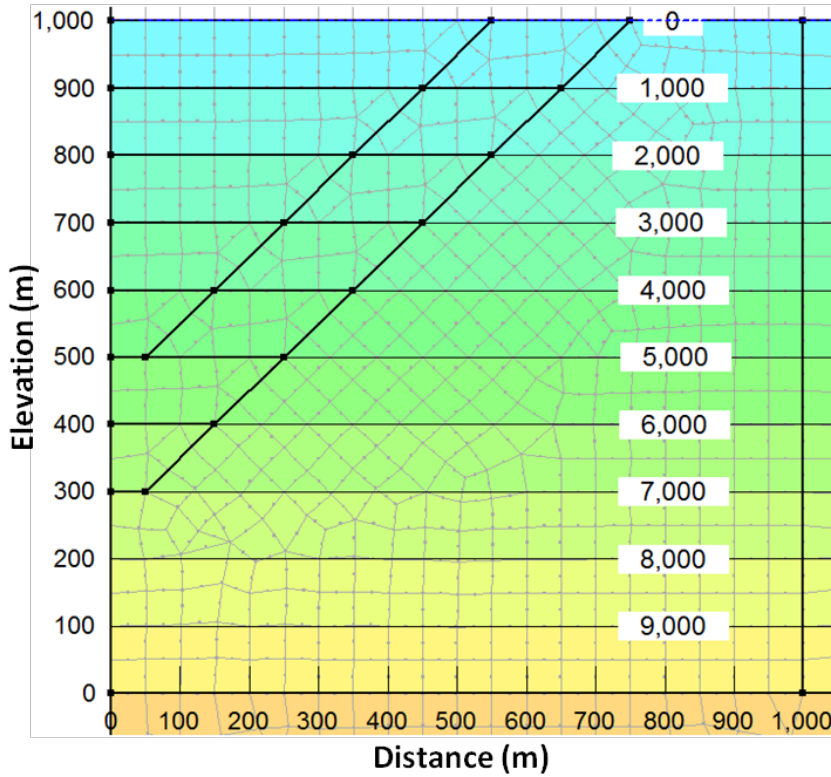


$c_v = 10^{-2} \text{ m}^2/\text{s}$

**PWP
Contours
(kPa)**

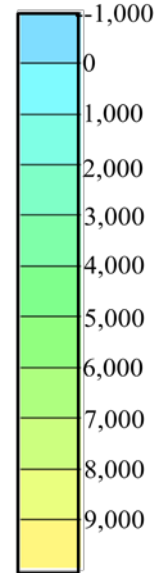


Initial Conditions

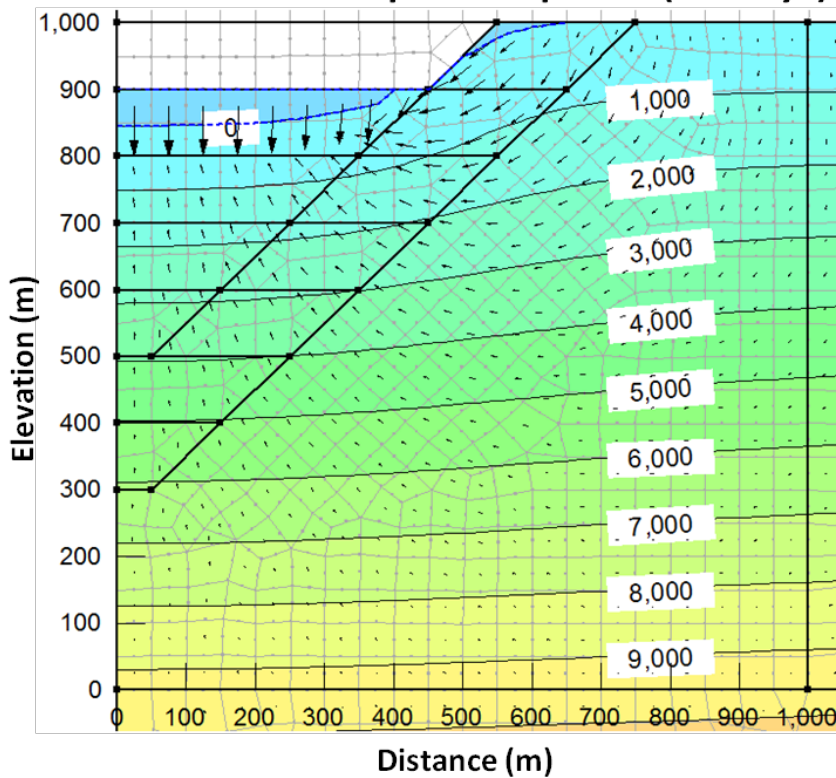


$c_v = 10^{-3} \text{ m}^2/\text{s}$

**PWP
Contours
(kPa)**

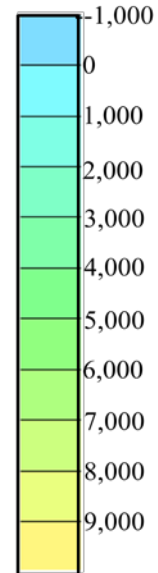


Transient Coupled Response (10 Days)

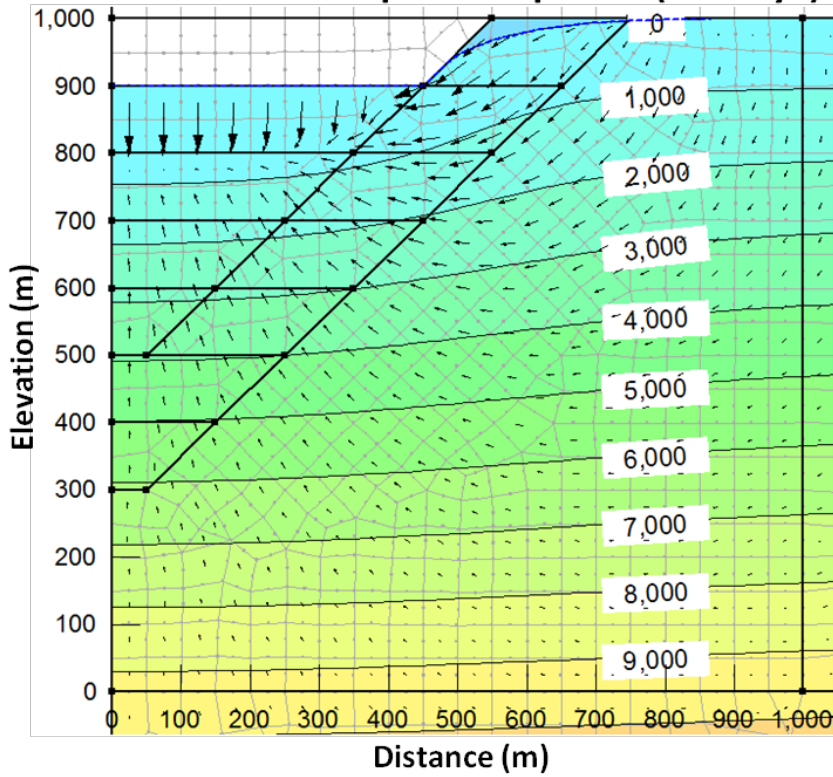


$c_v = 10^{-3} \text{ m}^2/\text{s}$

**PWP
Contours
(kPa)**

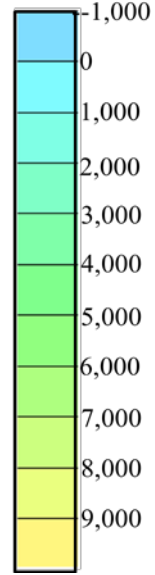


Transient Coupled Response (30 Days)

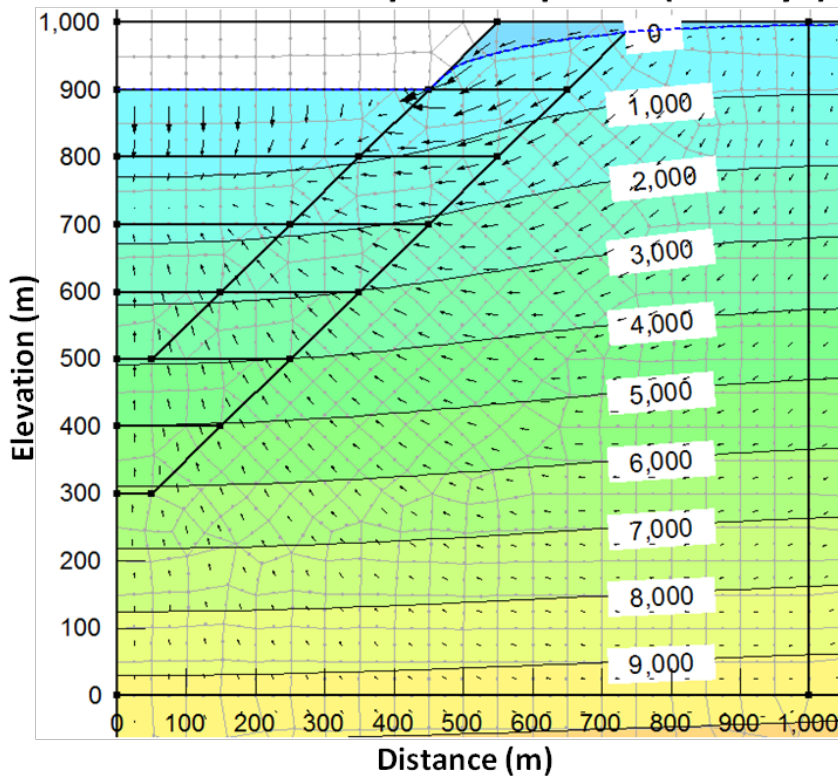


$c_v = 10^{-3} \text{ m}^2/\text{s}$

**PWP
Contours
(kPa)**

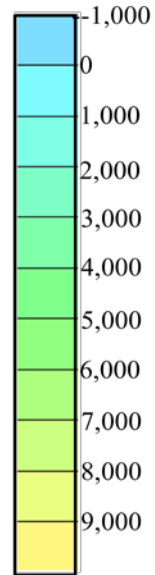


Transient Coupled Response (90 Days)

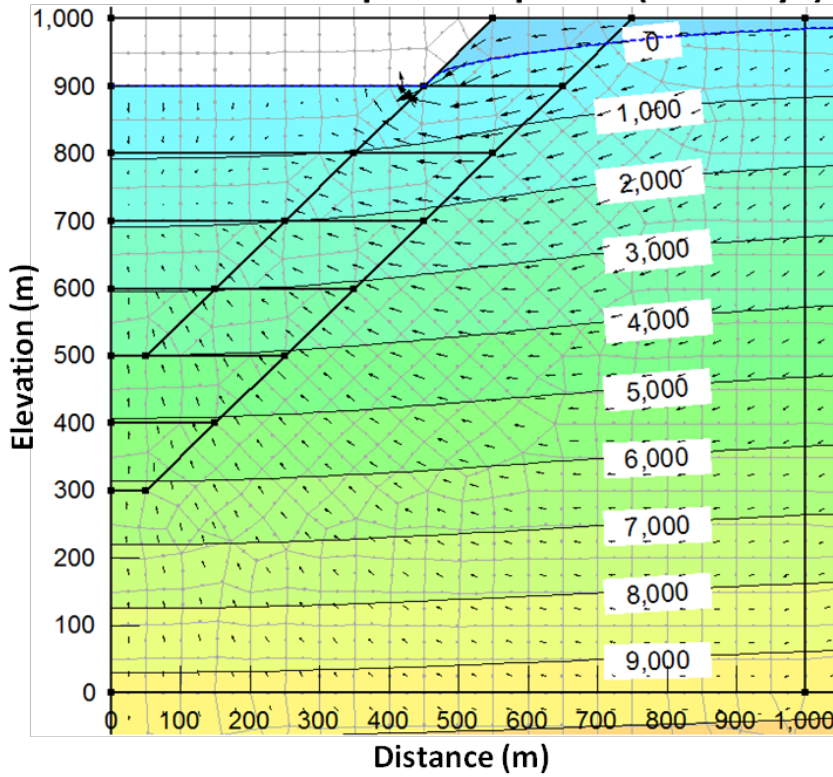


$c_v = 10^{-3} \text{ m}^2/\text{s}$

**PWP
Contours
(kPa)**

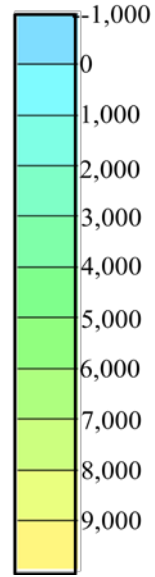


Transient Coupled Response (360 Days)

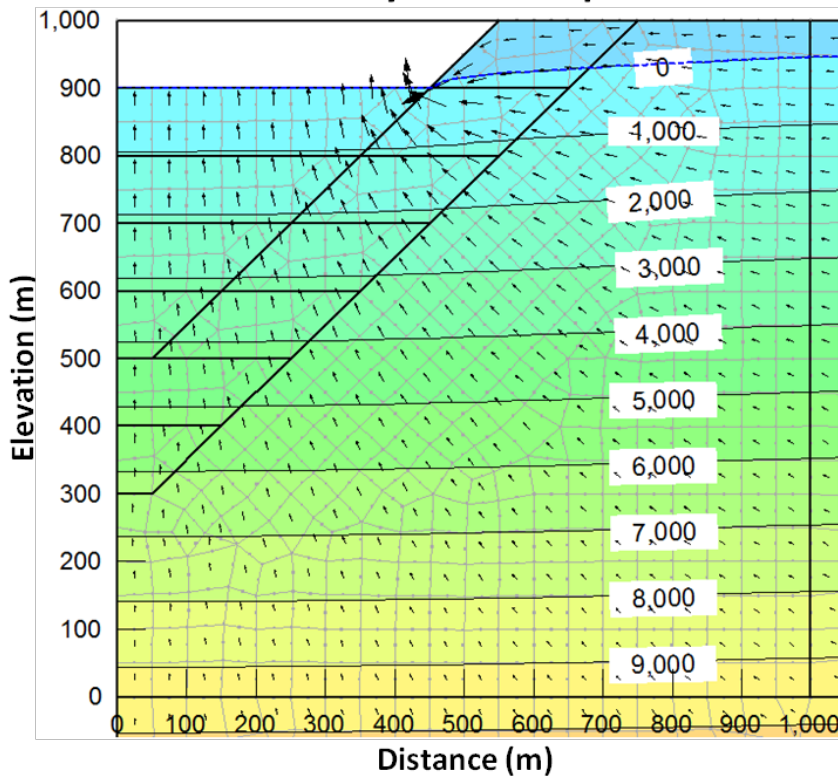


$$c_v = 10^{-3} \text{ m}^2/\text{s}$$

**PWP
Contours
(kPa)**

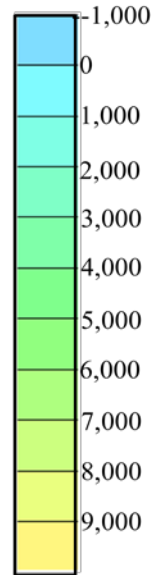


Steady-State Response

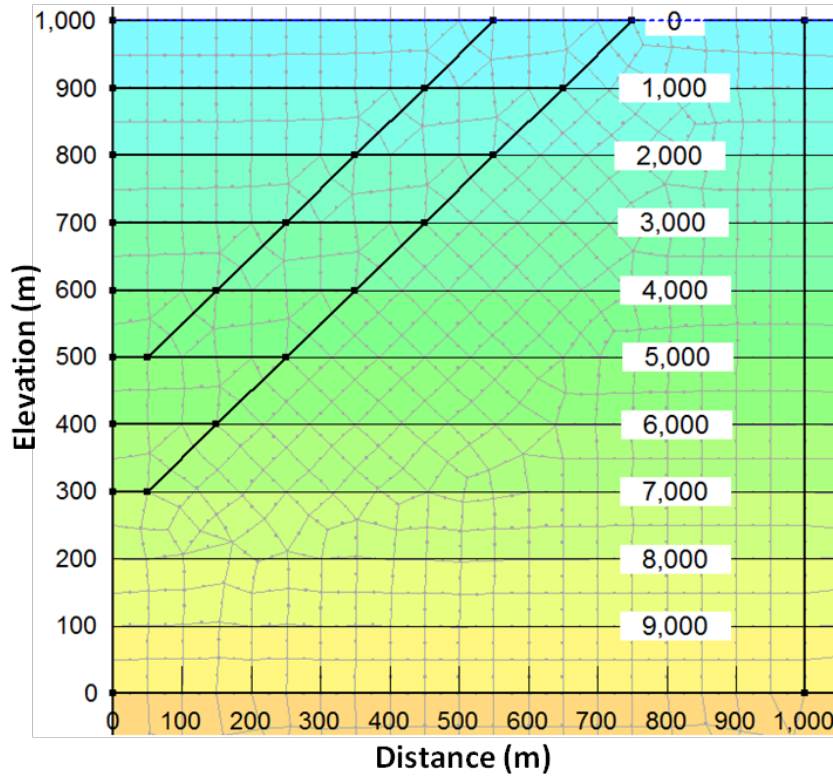


$$c_v = 10^{-3} \text{ m}^2/\text{s}$$

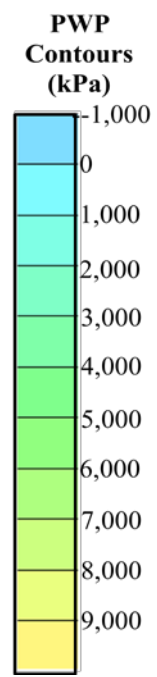
**PWP
Contours
(kPa)**



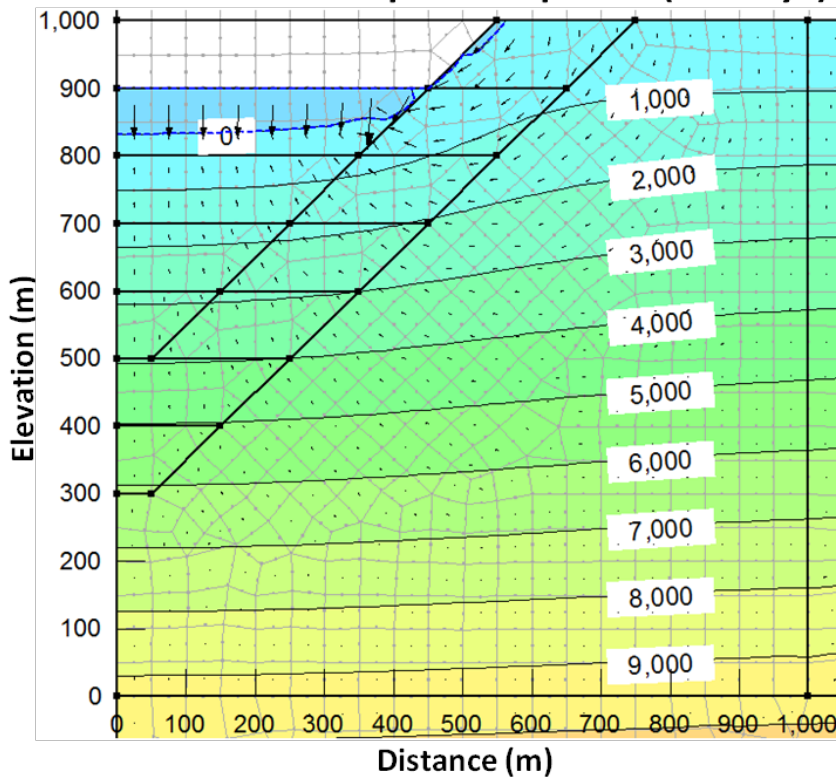
Initial Conditions



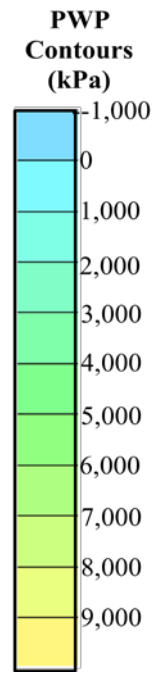
$c_v = 10^{-4} \text{ m}^2/\text{s}$



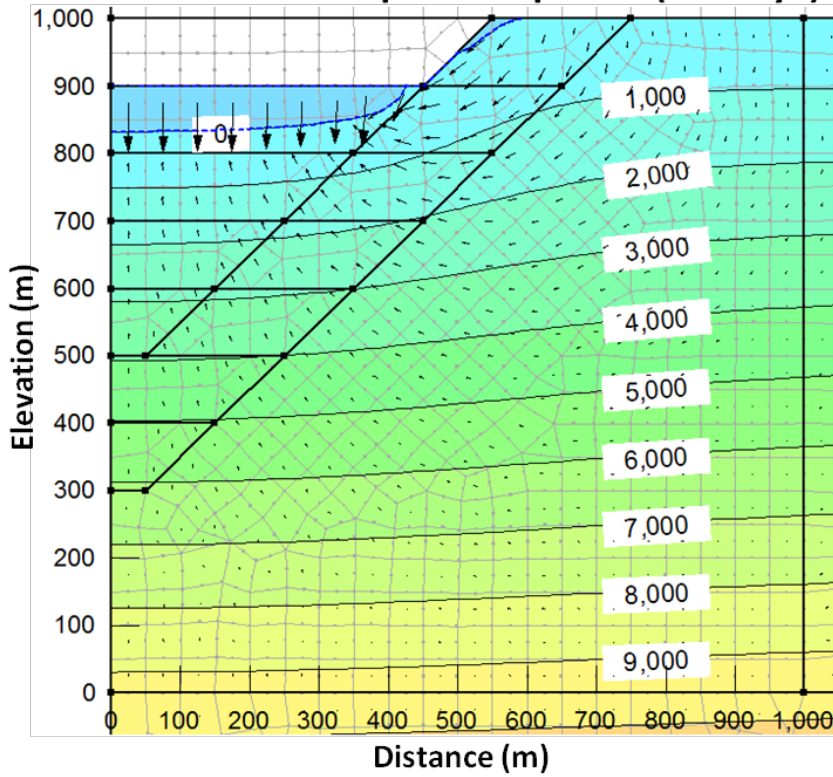
Transient Coupled Response (10 Days)



$c_v = 10^{-4} \text{ m}^2/\text{s}$

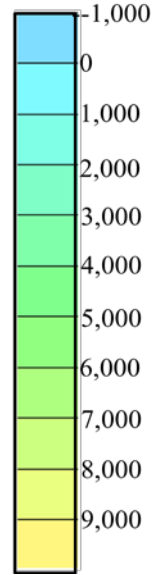


Transient Coupled Response (30 Days)

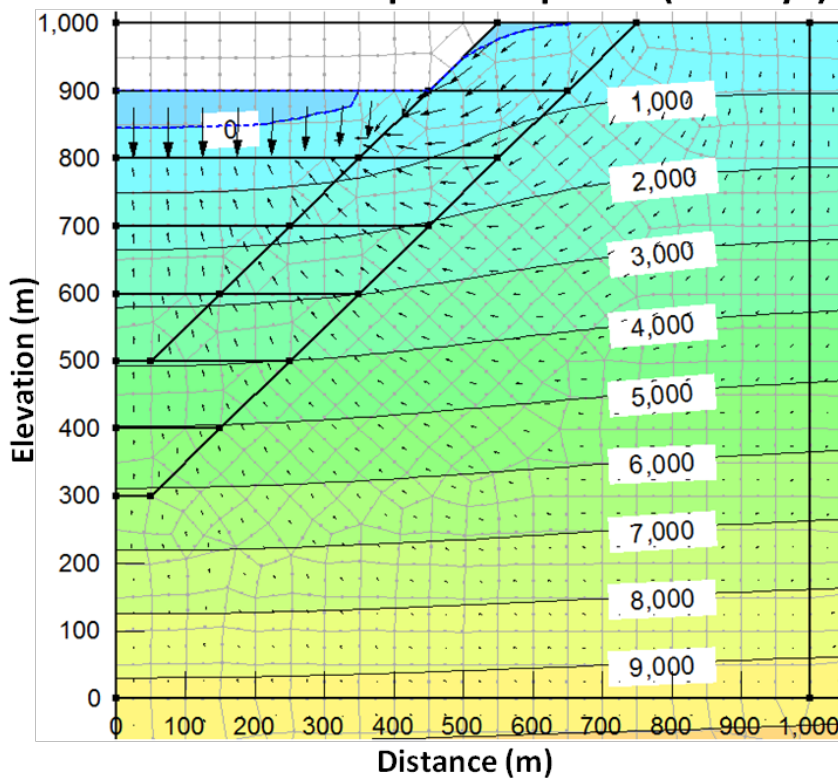


$c_v = 10^{-4} \text{ m}^2/\text{s}$

**PWP
Contours
(kPa)**

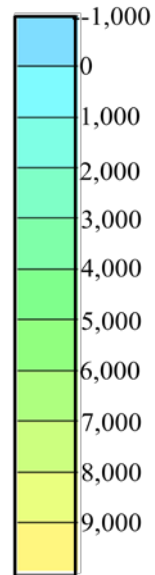


Transient Coupled Response (90 Days)

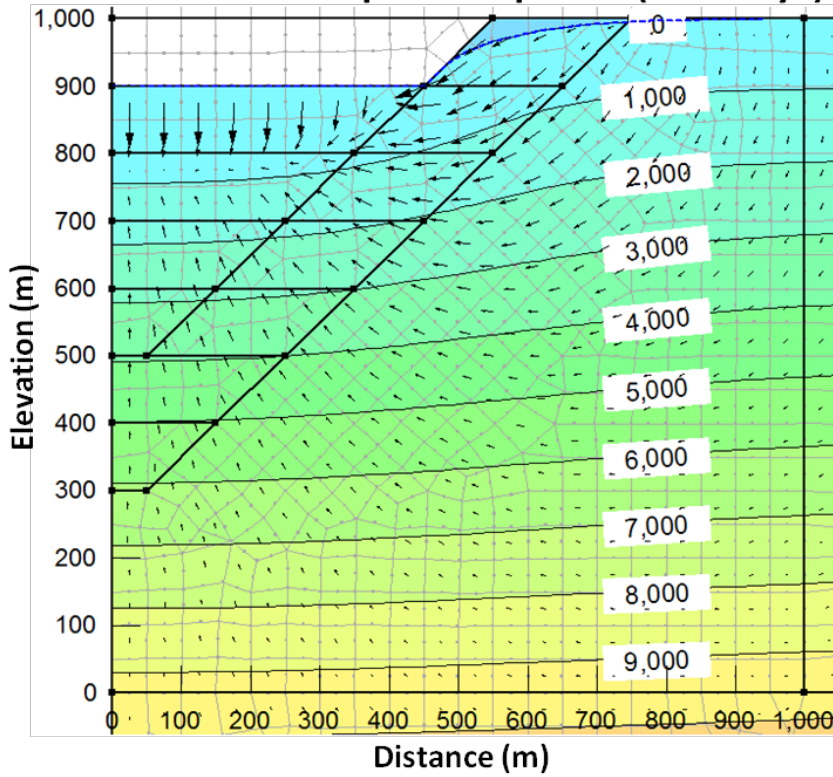


$c_v = 10^{-4} \text{ m}^2/\text{s}$

**PWP
Contours
(kPa)**

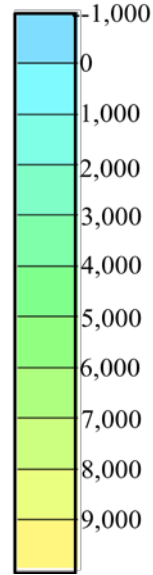


Transient Coupled Response (360 Days)

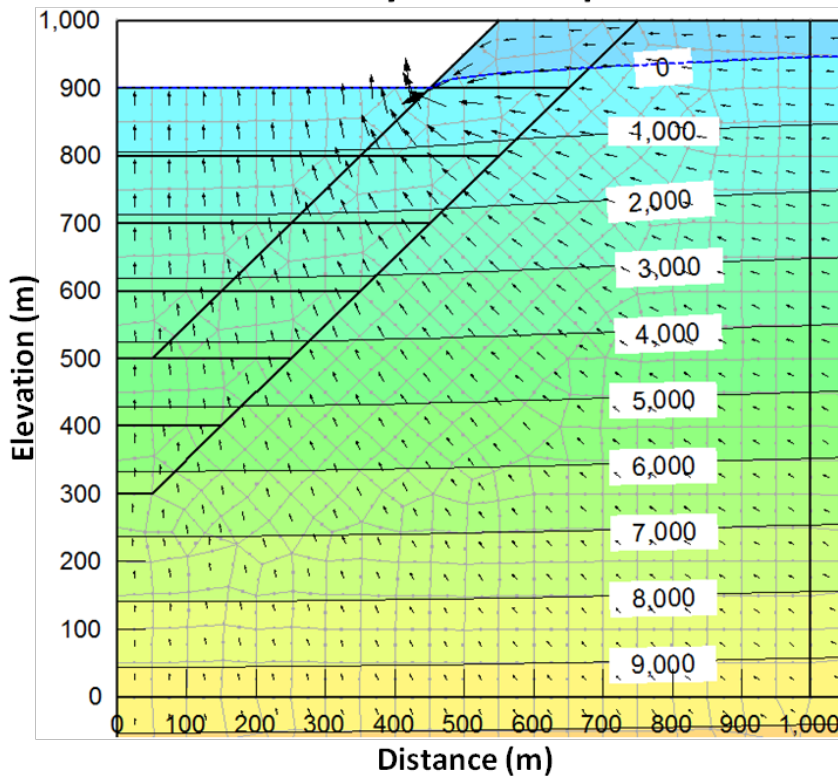


$c_v = 10^{-4} \text{ m}^2/\text{s}$

**PWP
Contours
(kPa)**

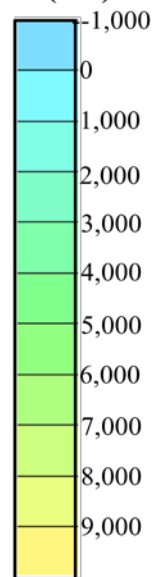


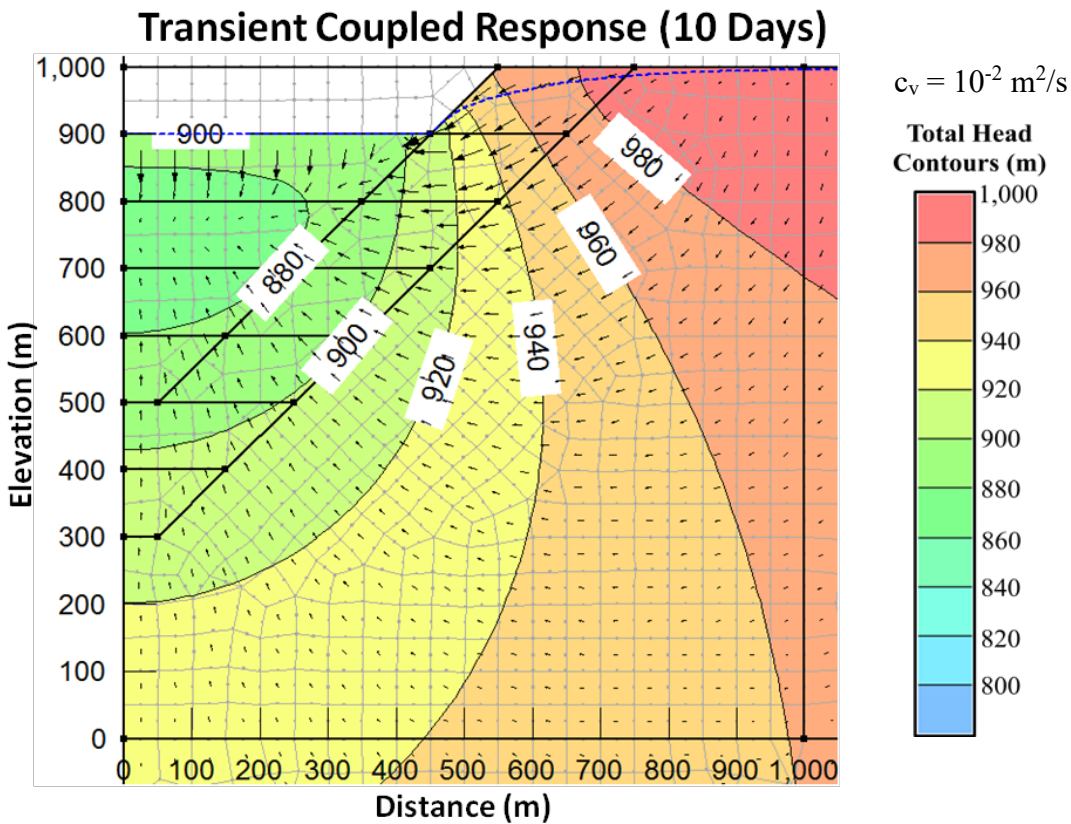
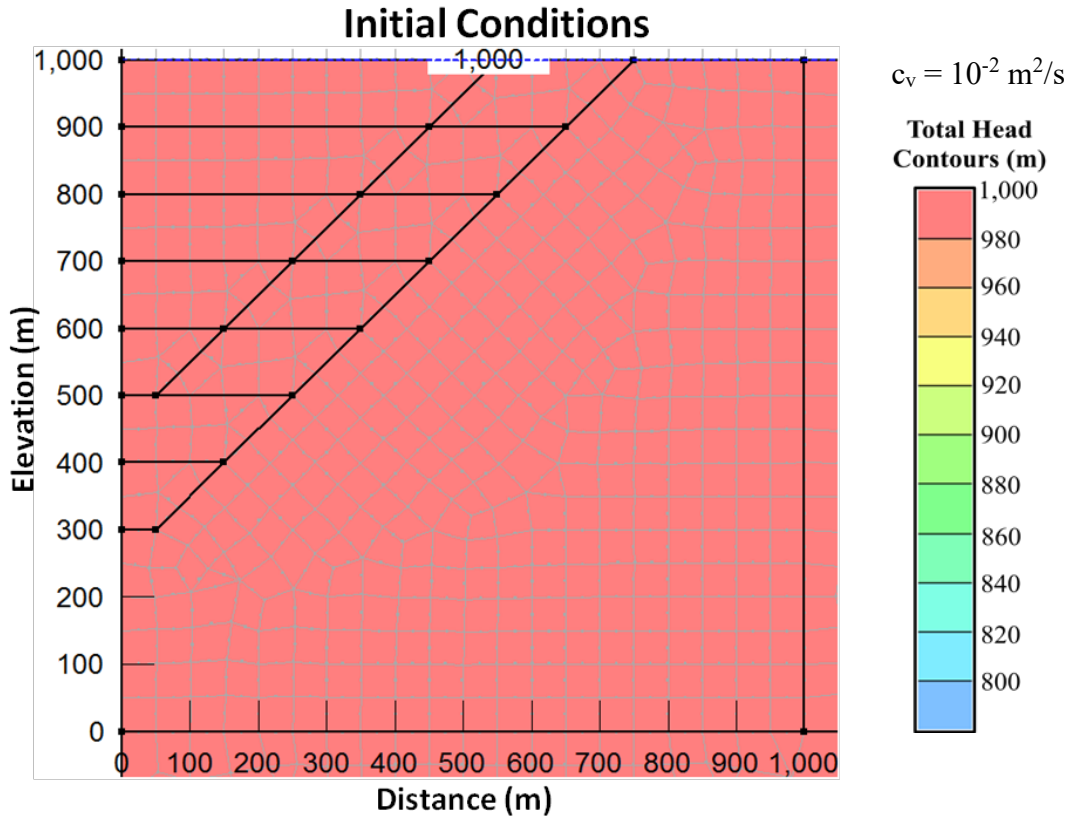
Steady-State Response



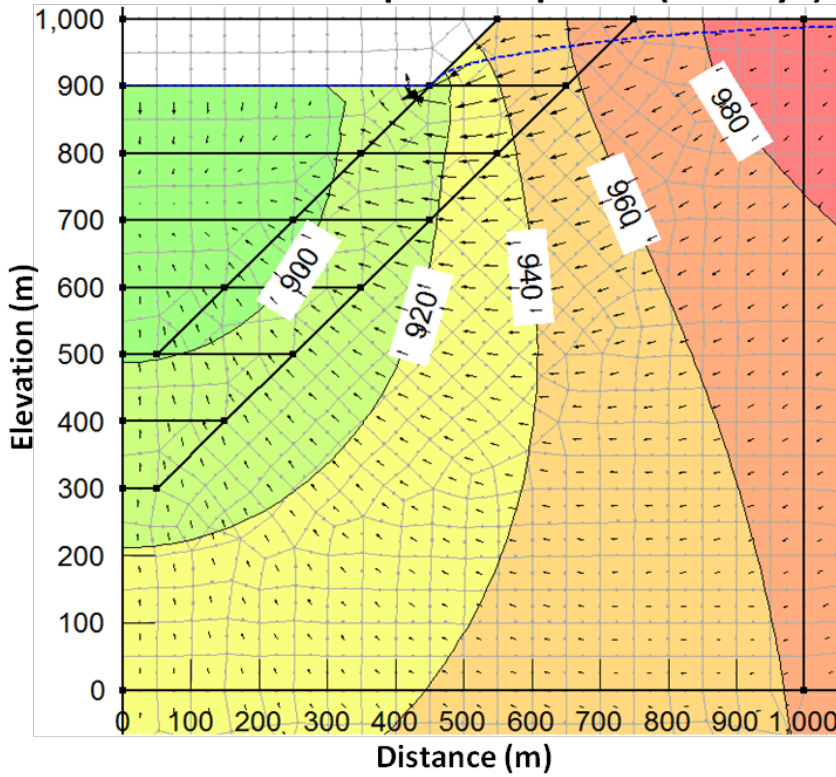
$c_v = 10^{-4} \text{ m}^2/\text{s}$

**PWP
Contours
(kPa)**



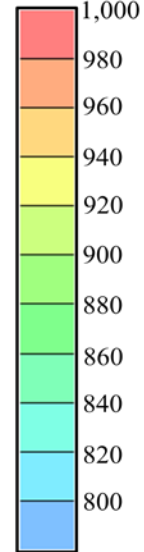


Transient Coupled Response (30 Days)

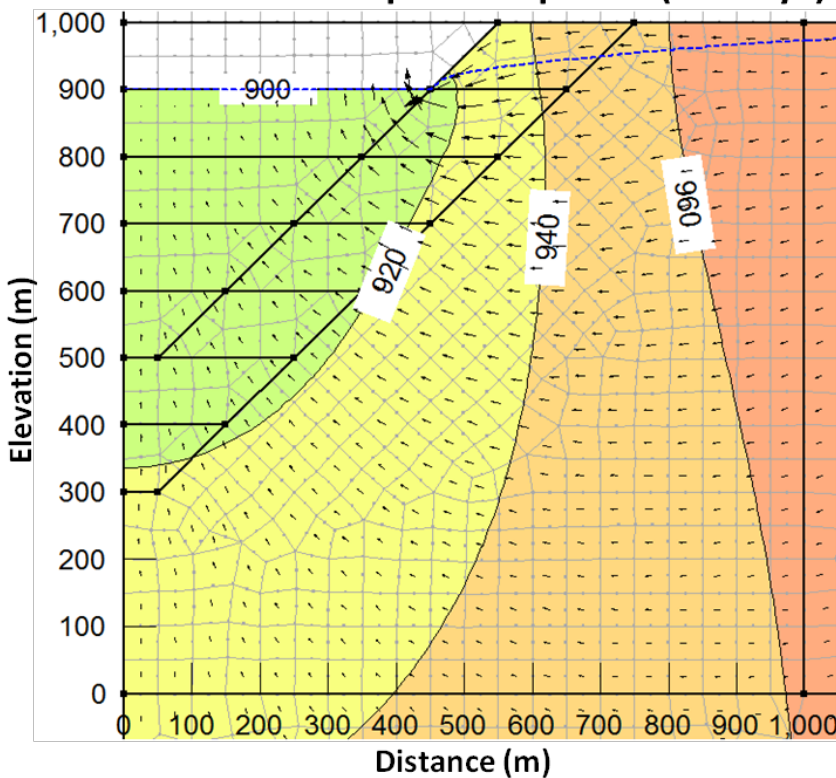


$$c_v = 10^{-2} \text{ m}^2/\text{s}$$

Total Head Contours (m)

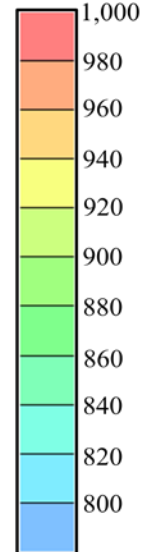


Transient Coupled Response (90 Days)

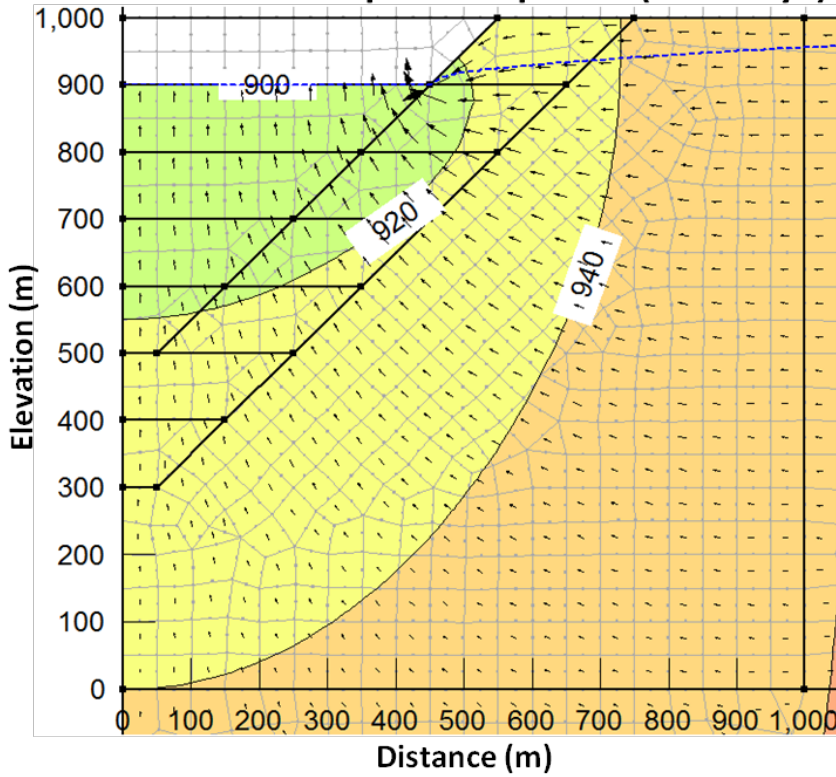


$$c_v = 10^{-2} \text{ m}^2/\text{s}$$

Total Head Contours (m)

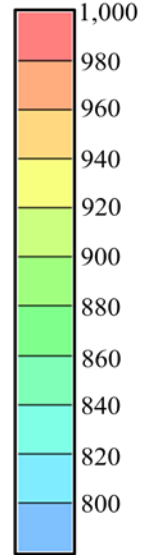


Transient Coupled Response (360 Days)

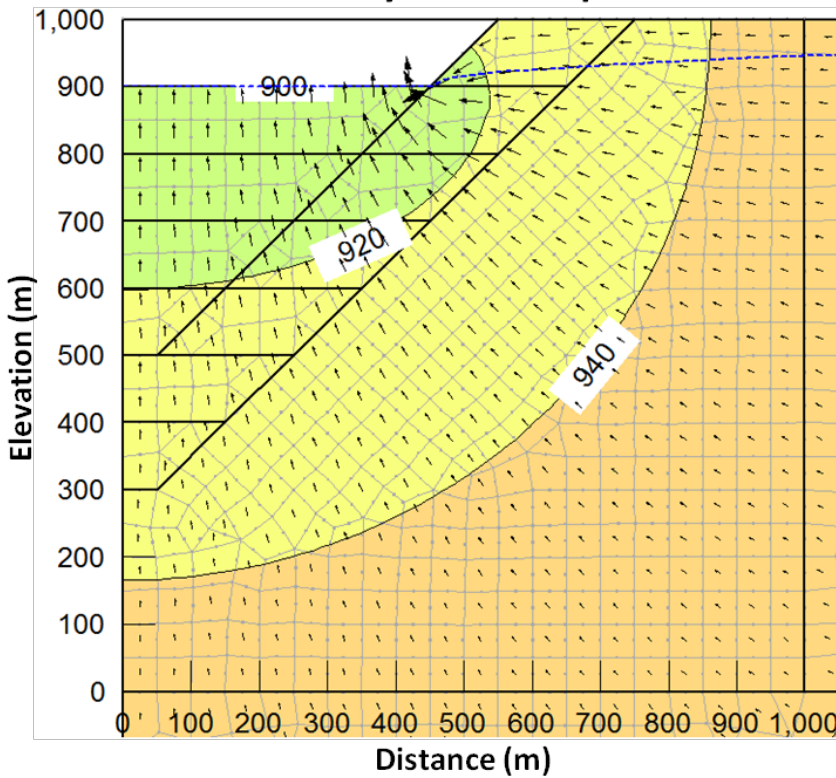


$$c_v = 10^{-2} \text{ m}^2/\text{s}$$

Total Head Contours (m)

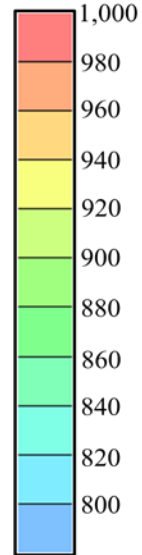


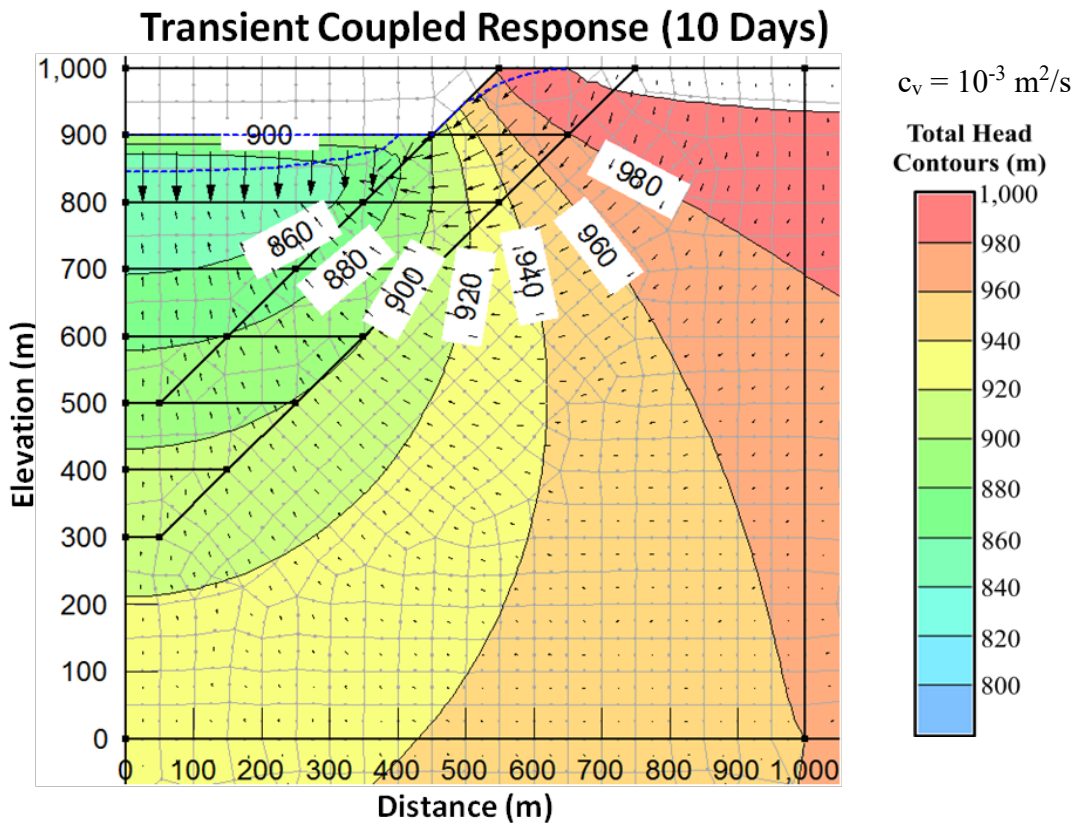
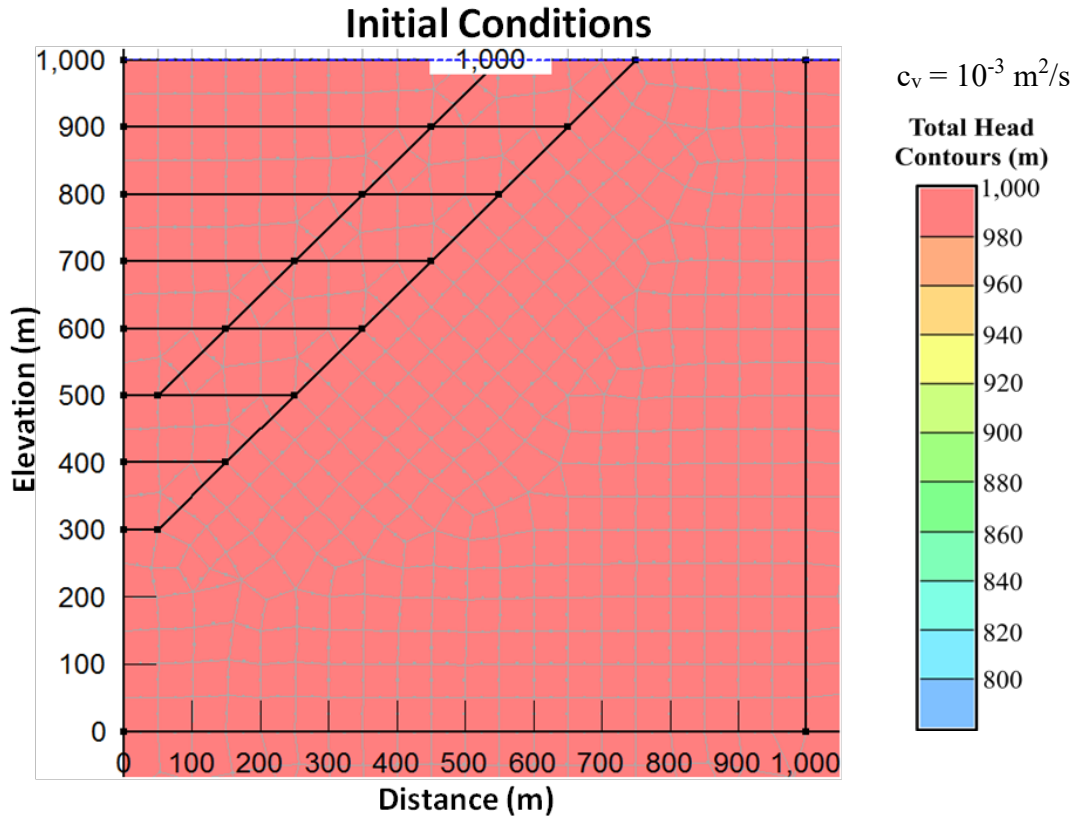
Steady-State Response



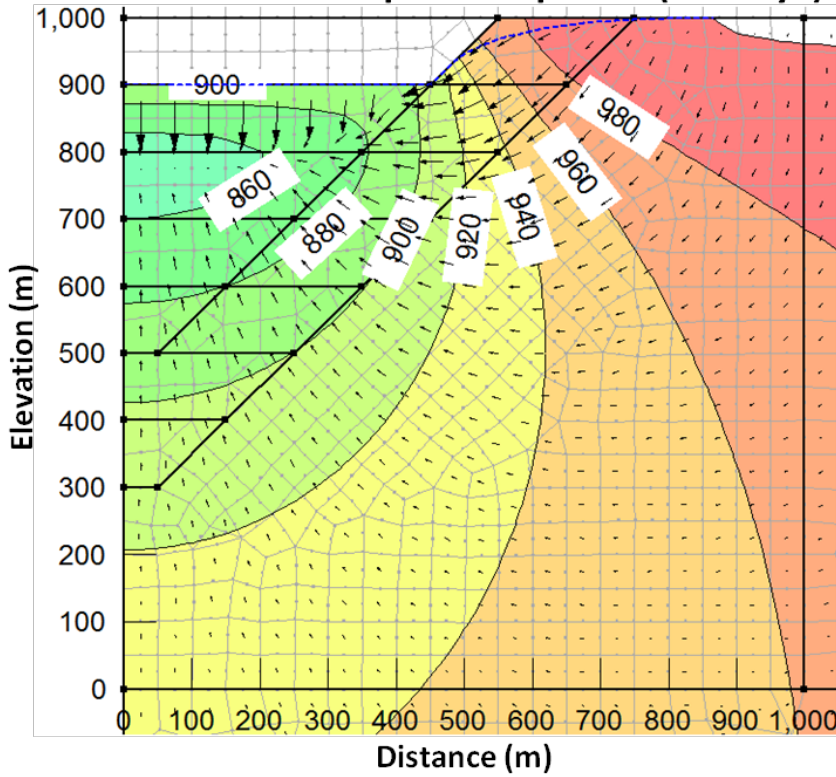
$$c_v = 10^{-2} \text{ m}^2/\text{s}$$

Total Head Contours (m)



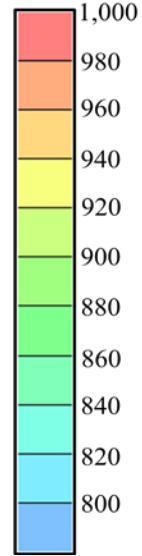


Transient Coupled Response (30 Days)

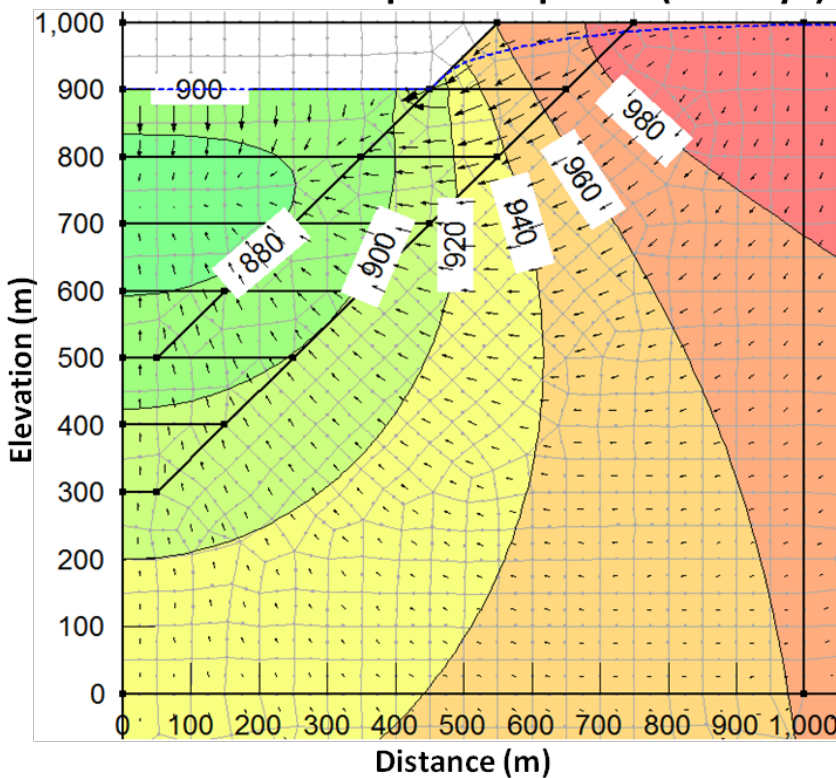


$c_v = 10^{-3} \text{ m}^2/\text{s}$

**Total Head
Contours (m)**

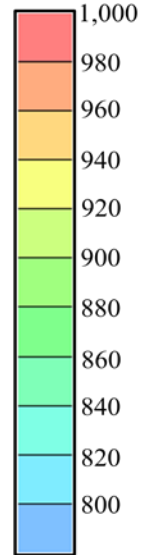


Transient Coupled Response (90 Days)

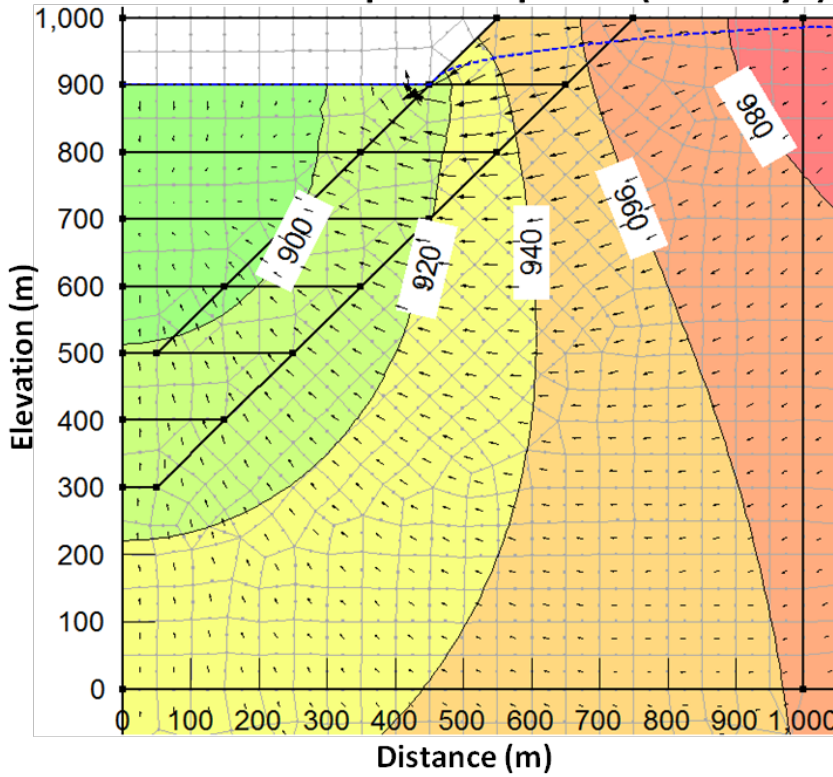


$c_v = 10^{-3} \text{ m}^2/\text{s}$

**Total Head
Contours (m)**

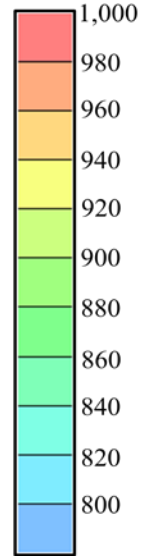


Transient Coupled Response (360 Days)

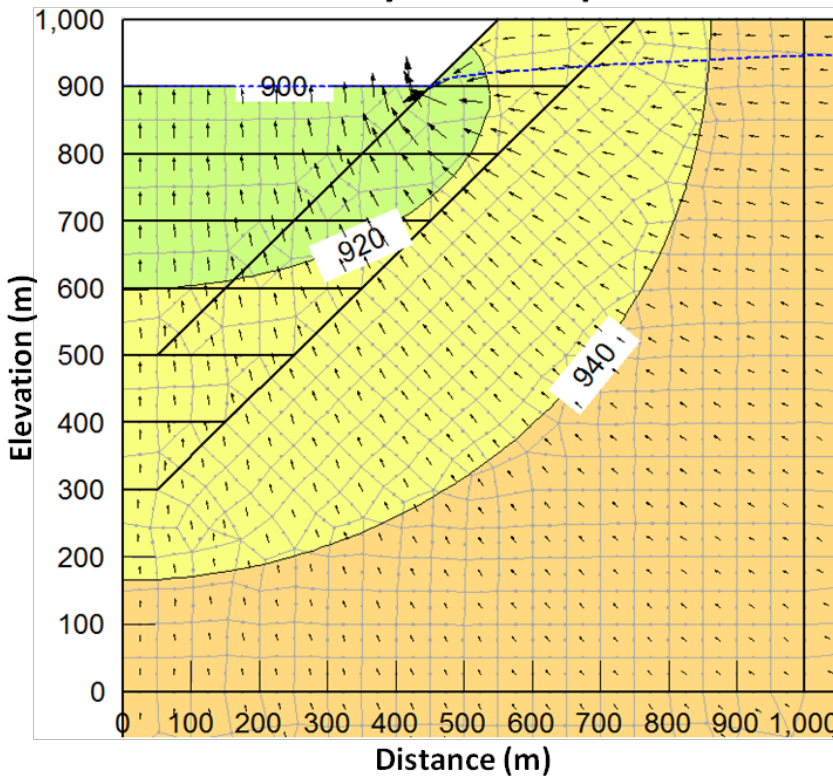


$$c_v = 10^{-3} \text{ m}^2/\text{s}$$

Total Head Contours (m)

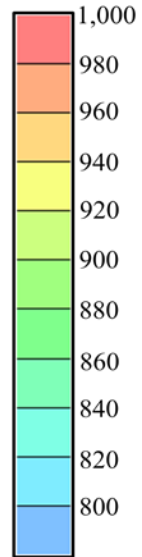


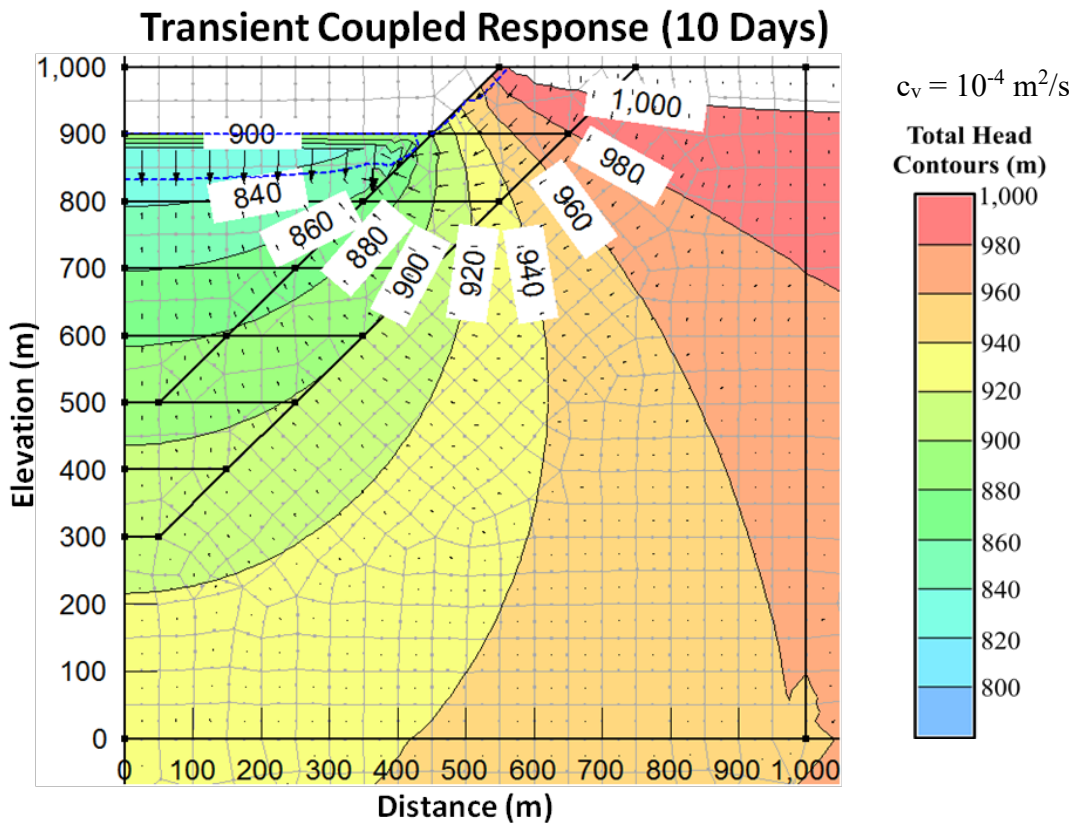
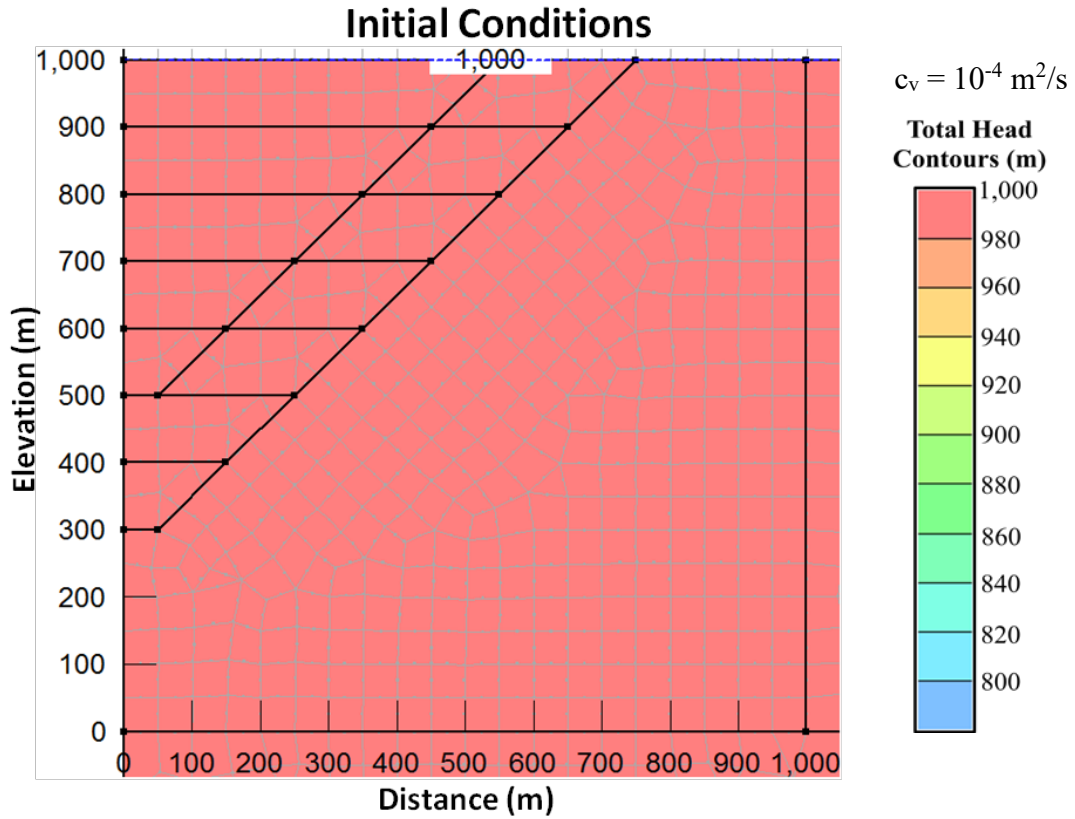
Steady-State Response



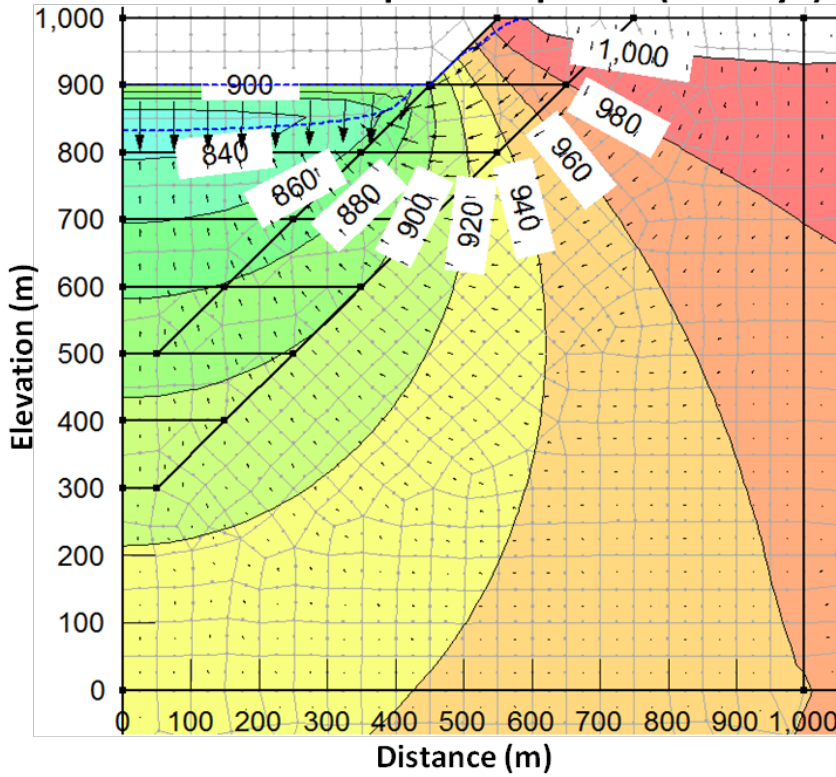
$$c_v = 10^{-3} \text{ m}^2/\text{s}$$

Total Head Contours (m)



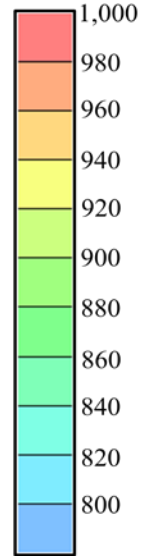


Transient Coupled Response (30 Days)

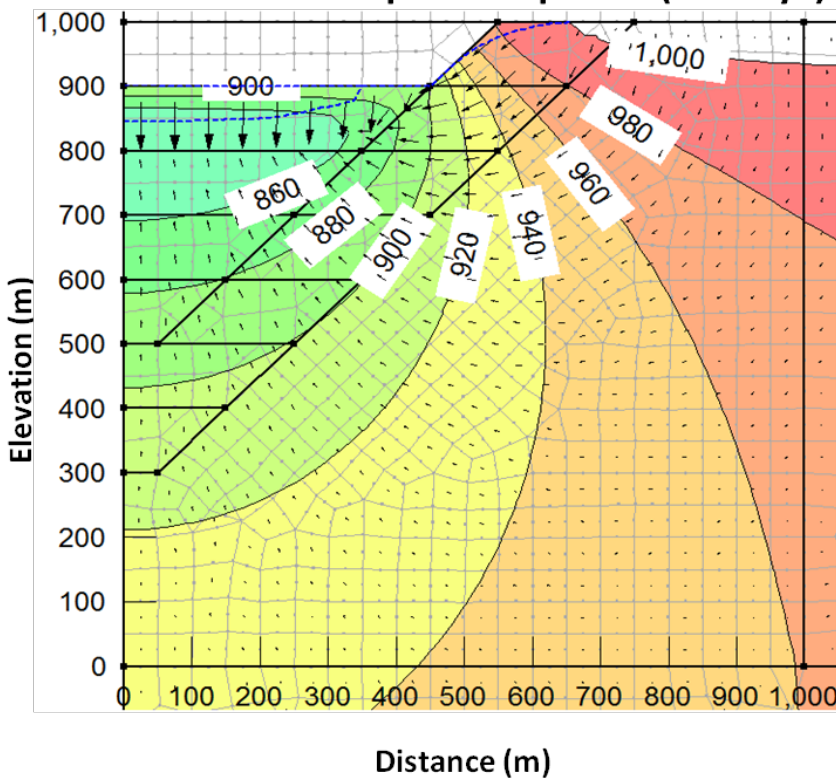


$c_v = 10^{-4} \text{ m}^2/\text{s}$

Total Head Contours (m)

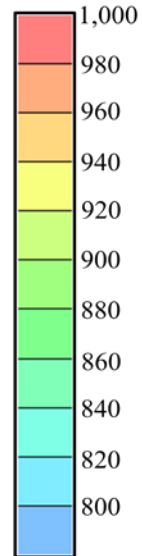


Transient Coupled Response (90 Days)

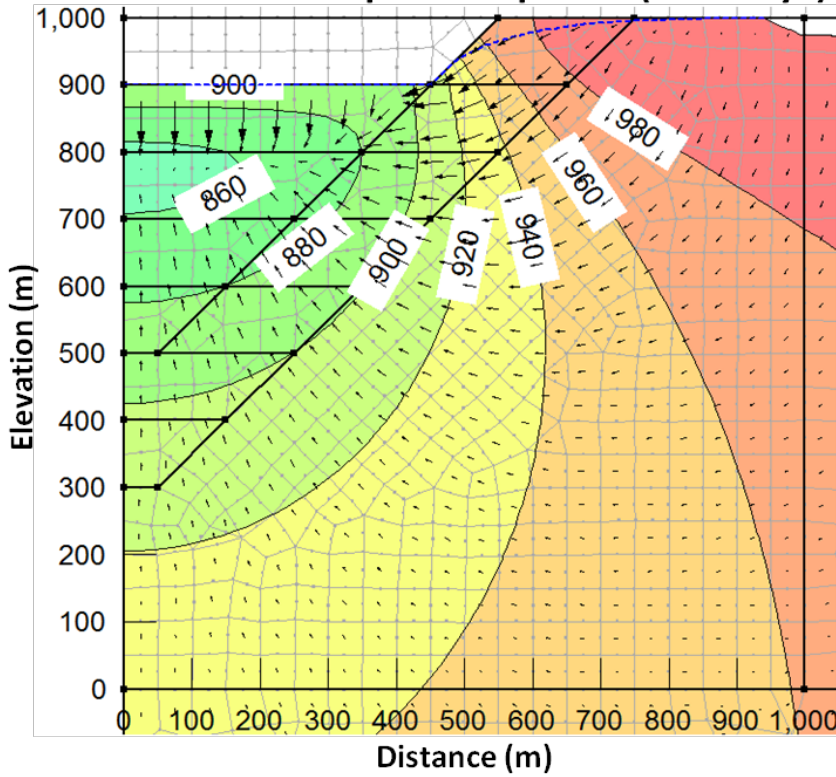


$c_v = 10^{-4} \text{ m}^2/\text{s}$

Total Head Contours (m)

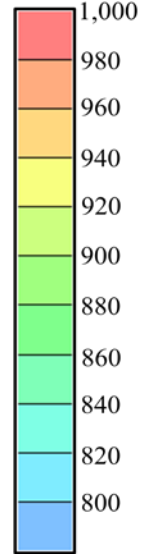


Transient Coupled Response (360 Days)

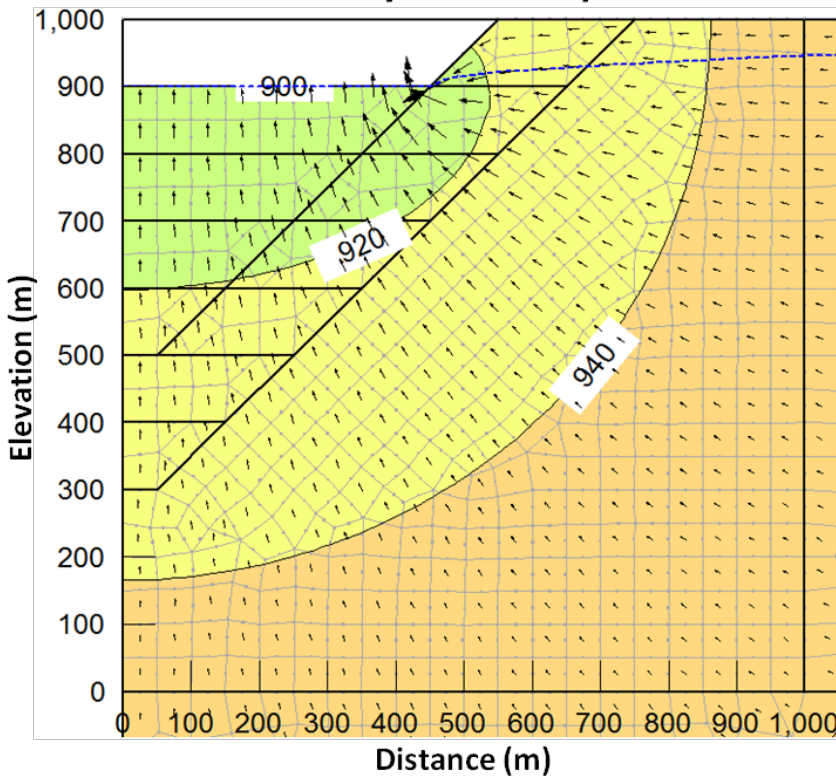


$c_v = 10^{-4} \text{ m}^2/\text{s}$

Total Head Contours (m)

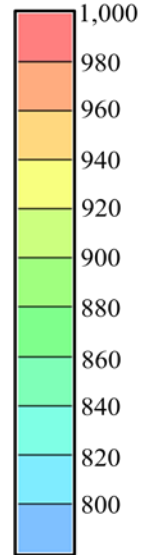


Steady-State Response

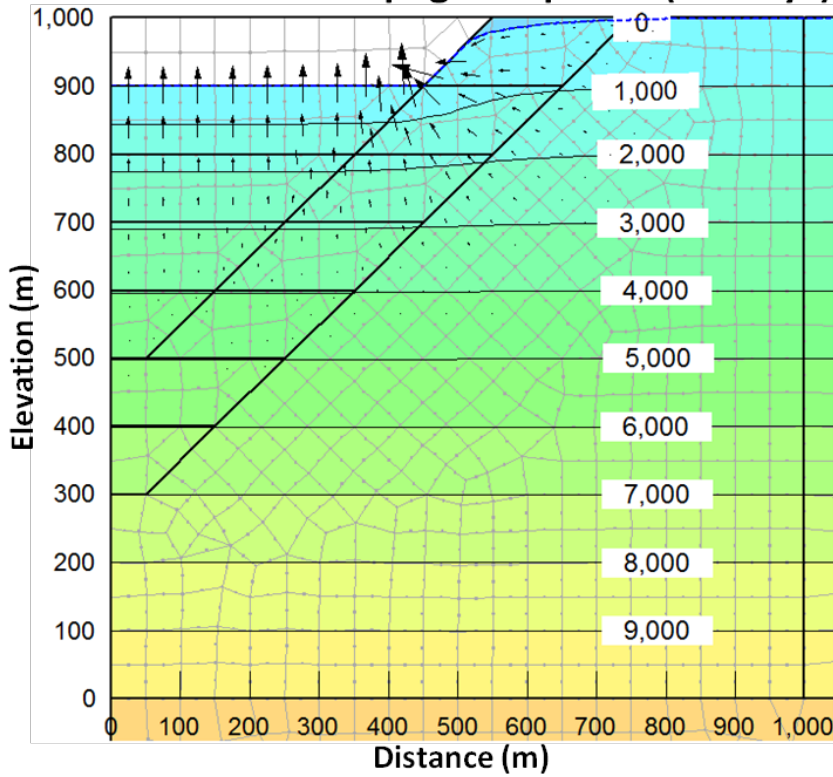


$c_v = 10^{-4} \text{ m}^2/\text{s}$

Total Head Contours (m)

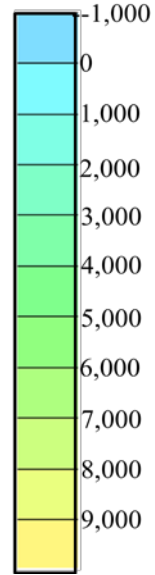


Transient Seepage Response (10 Days)

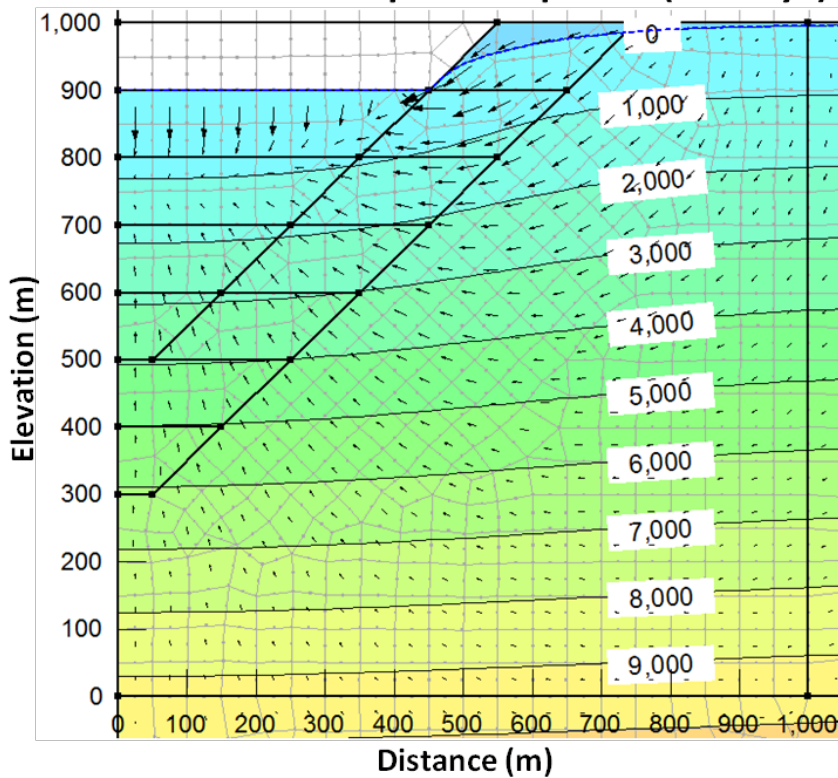


$c_v = 10^{-2} \text{ m}^2/\text{s}$

**PWP
Contours
(kPa)**

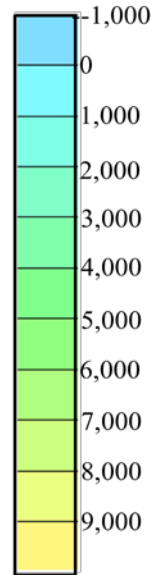


Transient Coupled Response (10 Days)

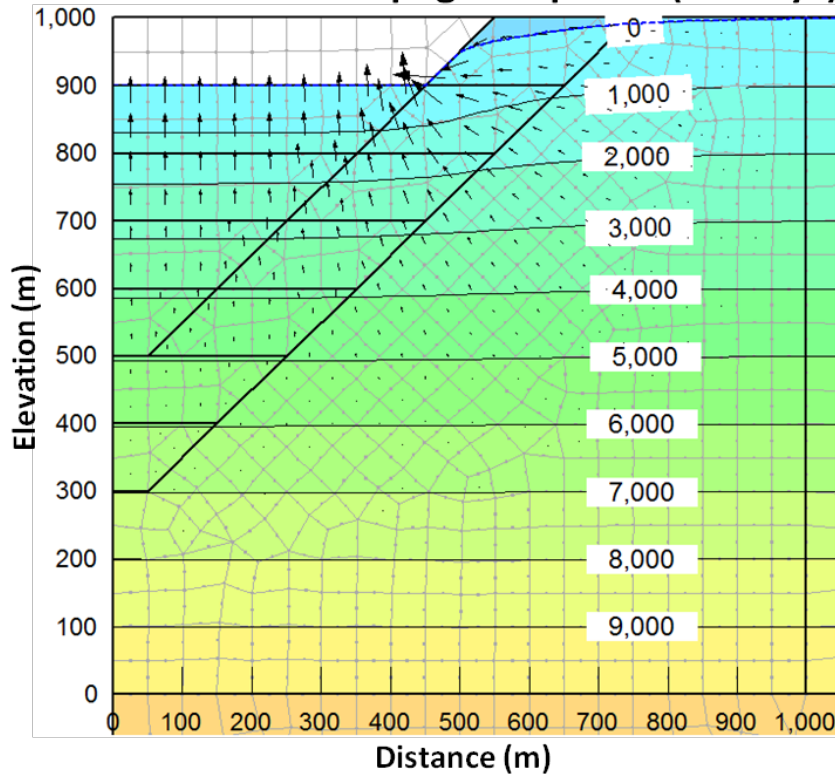


$c_v = 10^{-2} \text{ m}^2/\text{s}$

**PWP
Contours
(kPa)**

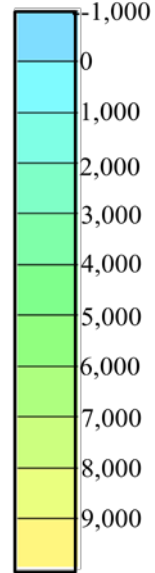


Transient Seepage Response (30 Days)

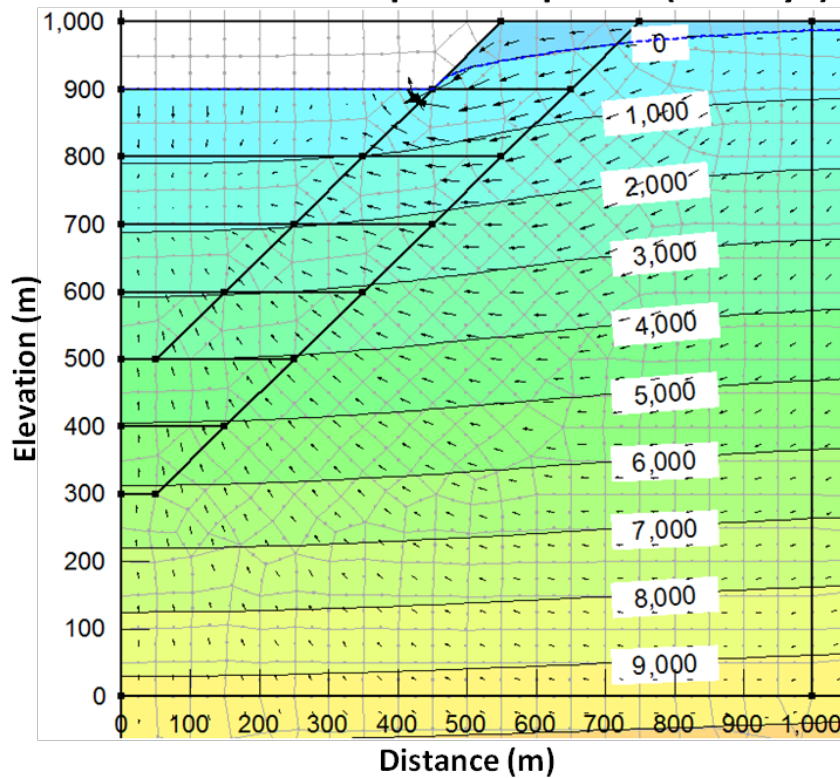


$c_v = 10^{-2} \text{ m}^2/\text{s}$

**PWP
Contours
(kPa)**

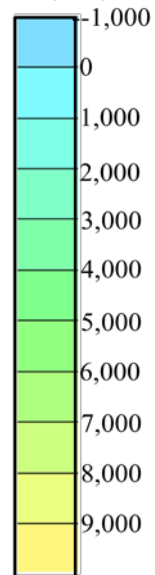


Transient Coupled Response (30 Days)

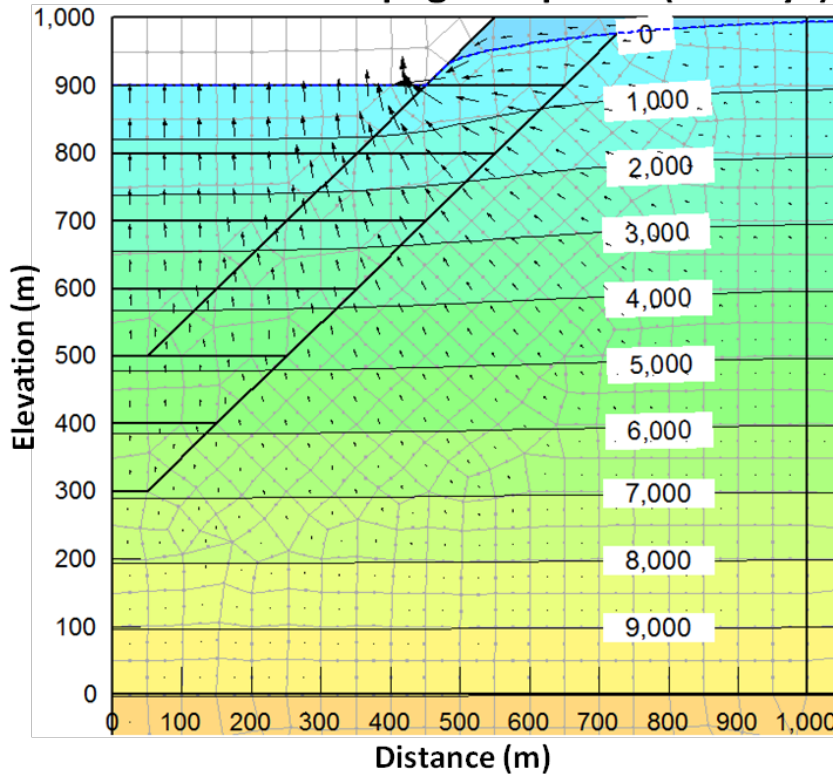


$c_v = 10^{-2} \text{ m}^2/\text{s}$

**PWP
Contours
(kPa)**

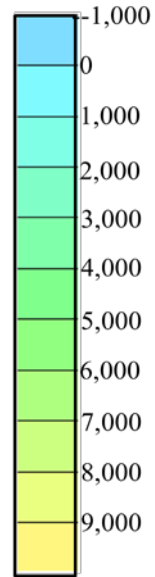


Transient Seepage Response (90 Days)

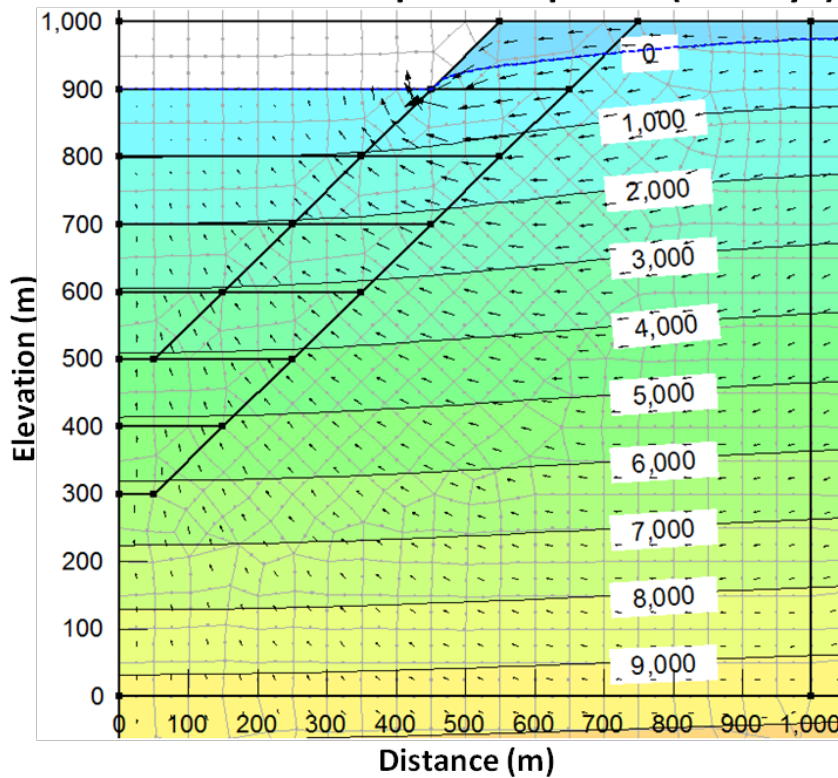


$c_v = 10^{-2} \text{ m}^2/\text{s}$

**PWP
Contours
(kPa)**

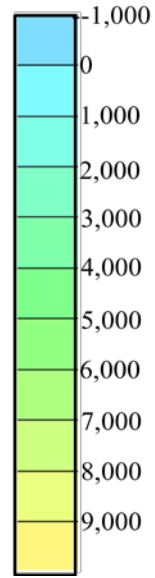


Transient Coupled Response (90 Days)

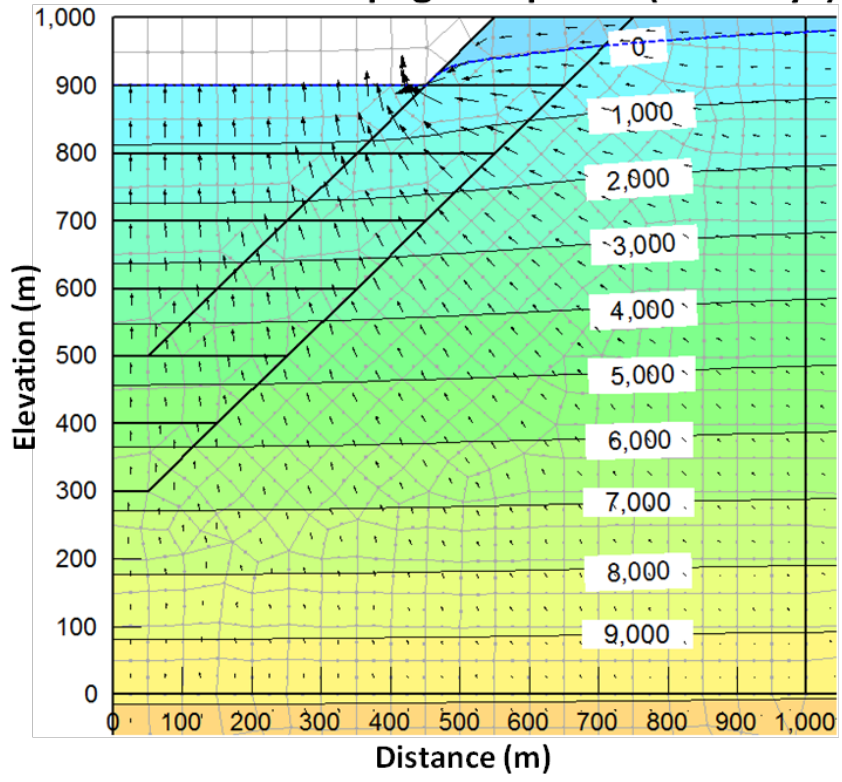


$c_v = 10^{-2} \text{ m}^2/\text{s}$

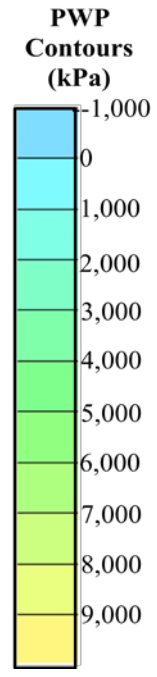
**PWP
Contours
(kPa)**



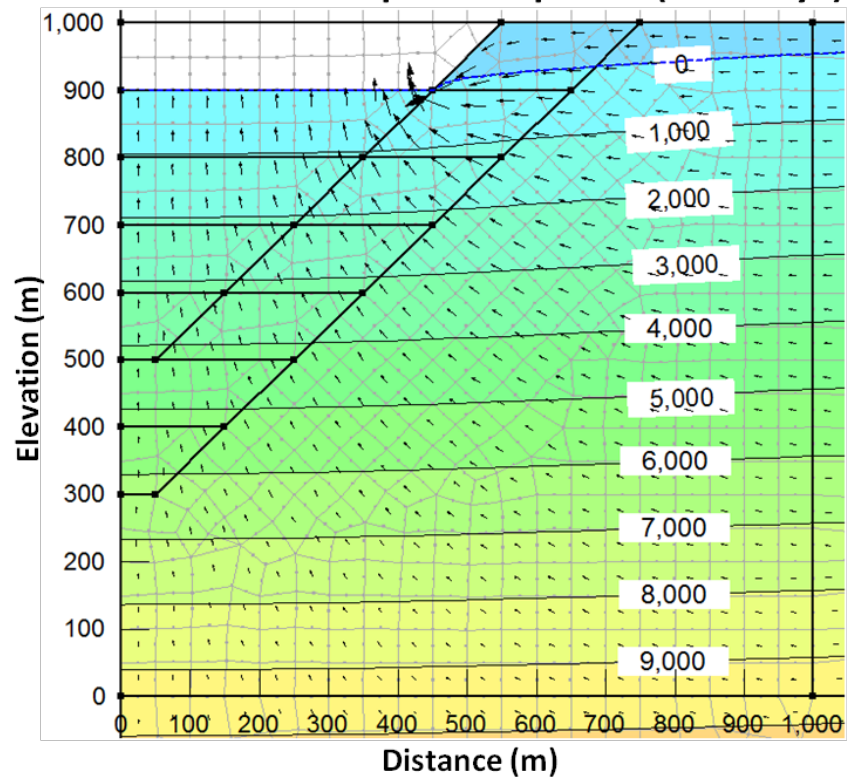
Transient Seepage Response (360 Days)



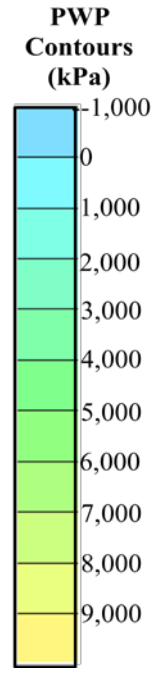
$c_v = 10^{-2} \text{ m}^2/\text{s}$



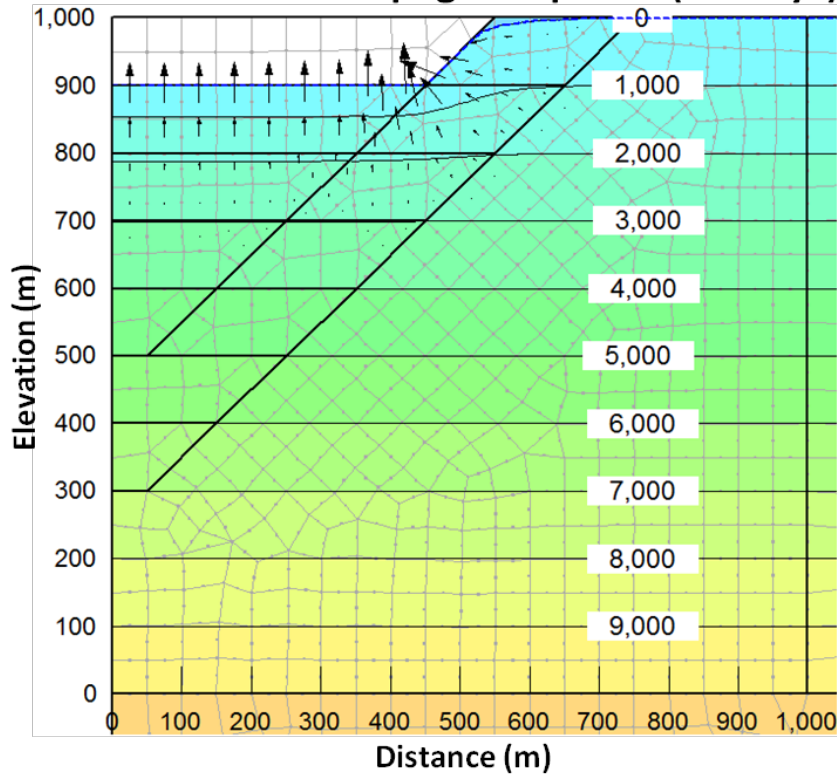
Transient Coupled Response (360 Days)



$c_v = 10^{-2} \text{ m}^2/\text{s}$

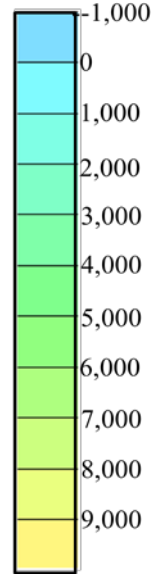


Transient Seepage Response (30 Days)

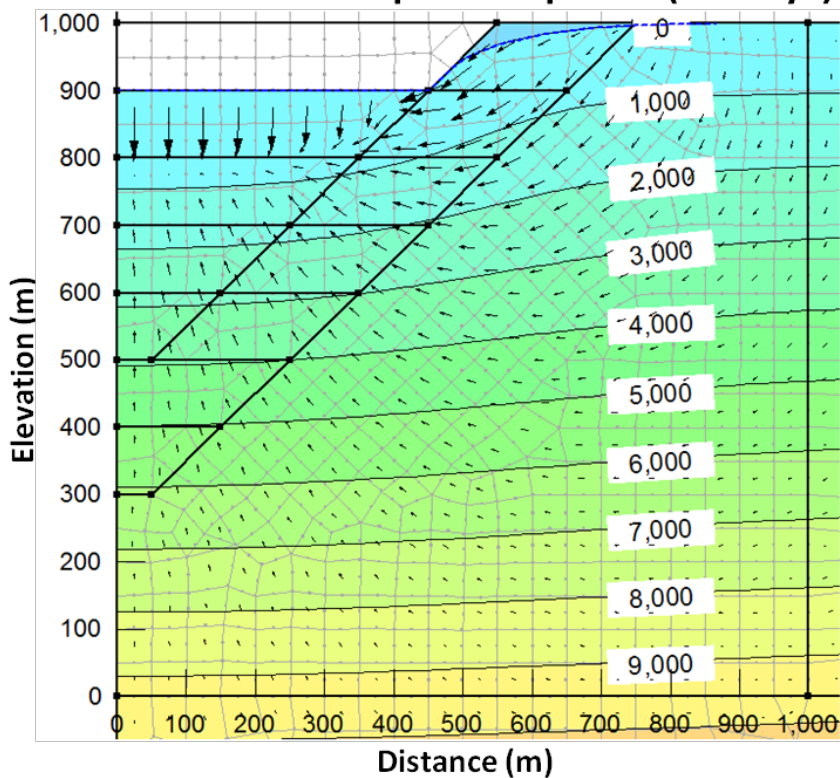


$c_v = 10^{-3} \text{ m}^2/\text{s}$

**PWP
Contours
(kPa)**

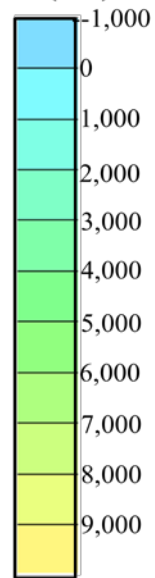


Transient Coupled Response (30 Days)

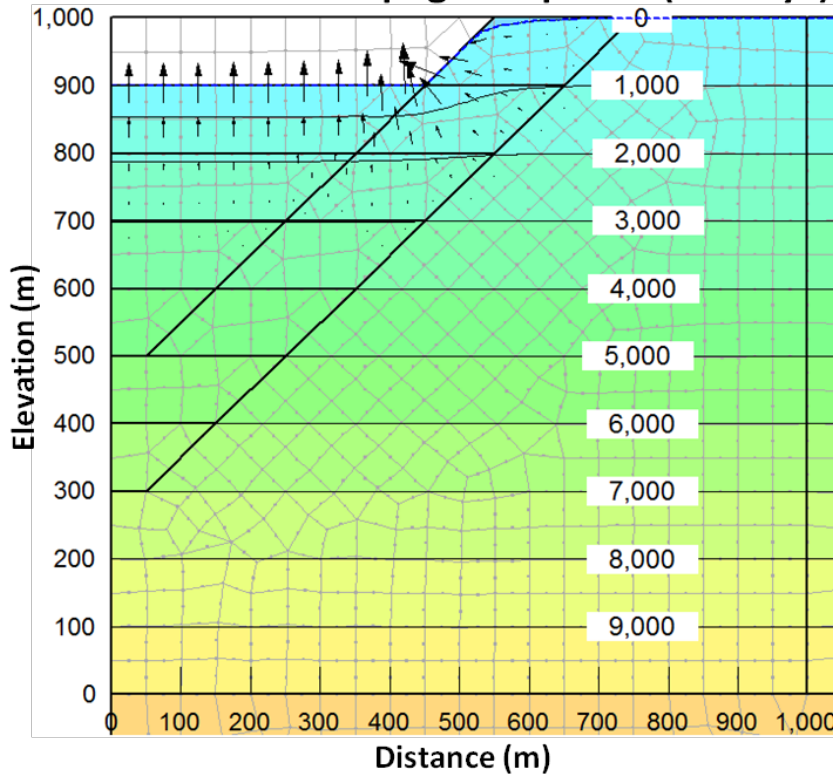


$c_v = 10^{-3} \text{ m}^2/\text{s}$

**PWP
Contours
(kPa)**

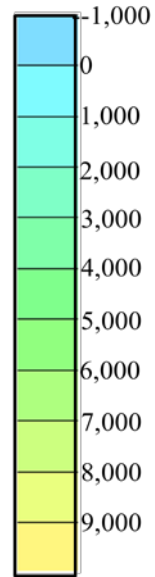


Transient Seepage Response (90 Days)

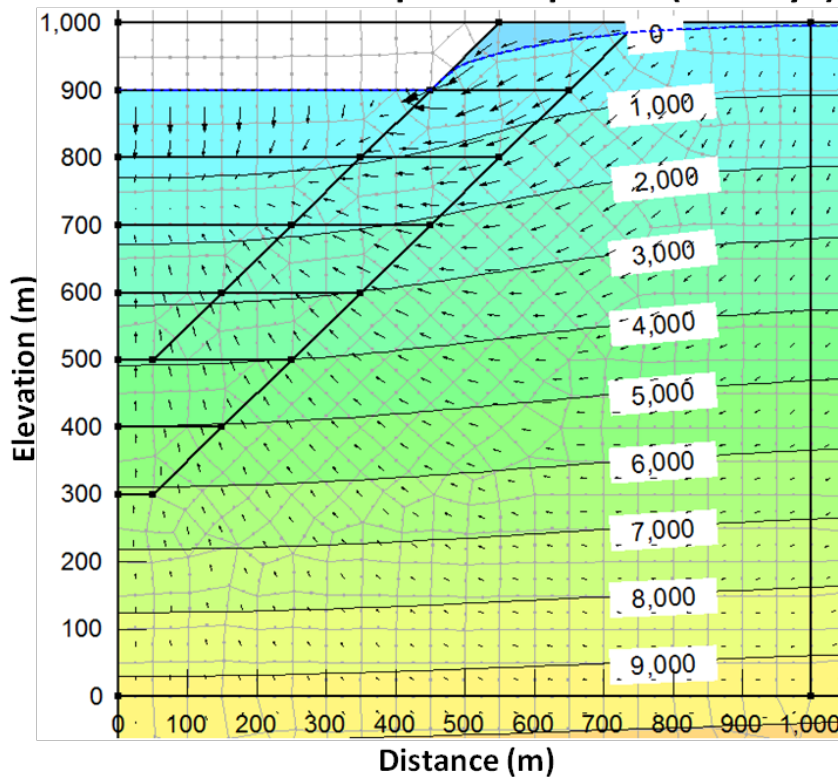


$c_v = 10^{-3} \text{ m}^2/\text{s}$

**PWP
Contours
(kPa)**

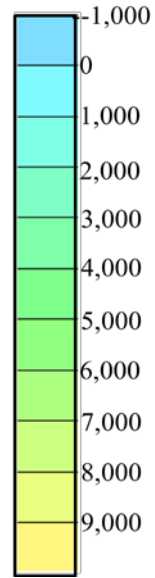


Transient Coupled Response (90 Days)

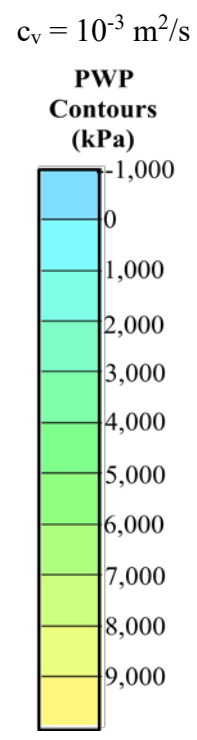
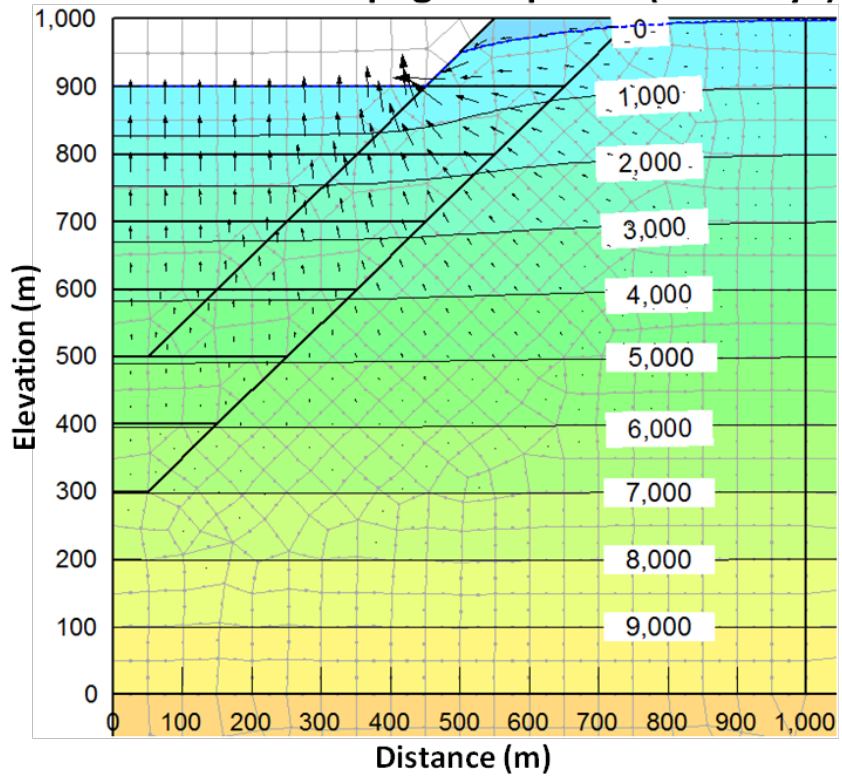


$c_v = 10^{-3} \text{ m}^2/\text{s}$

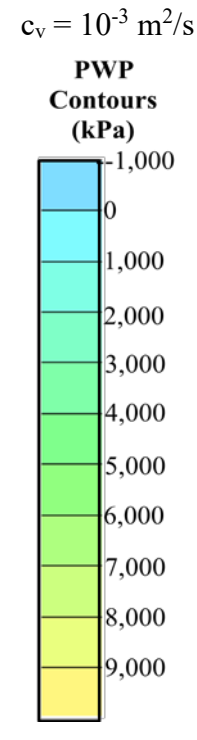
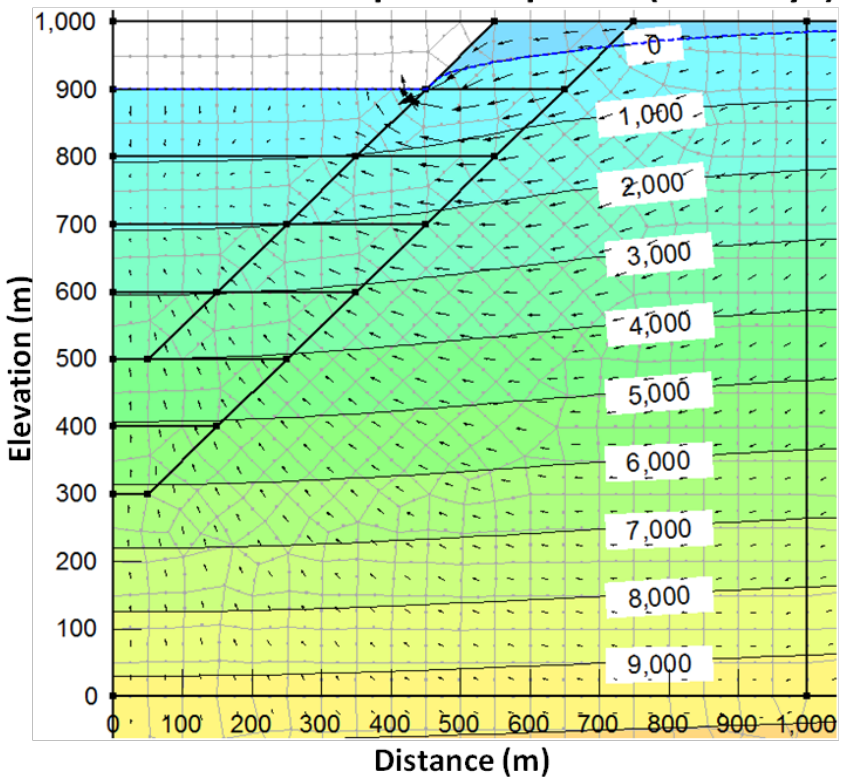
**PWP
Contours
(kPa)**



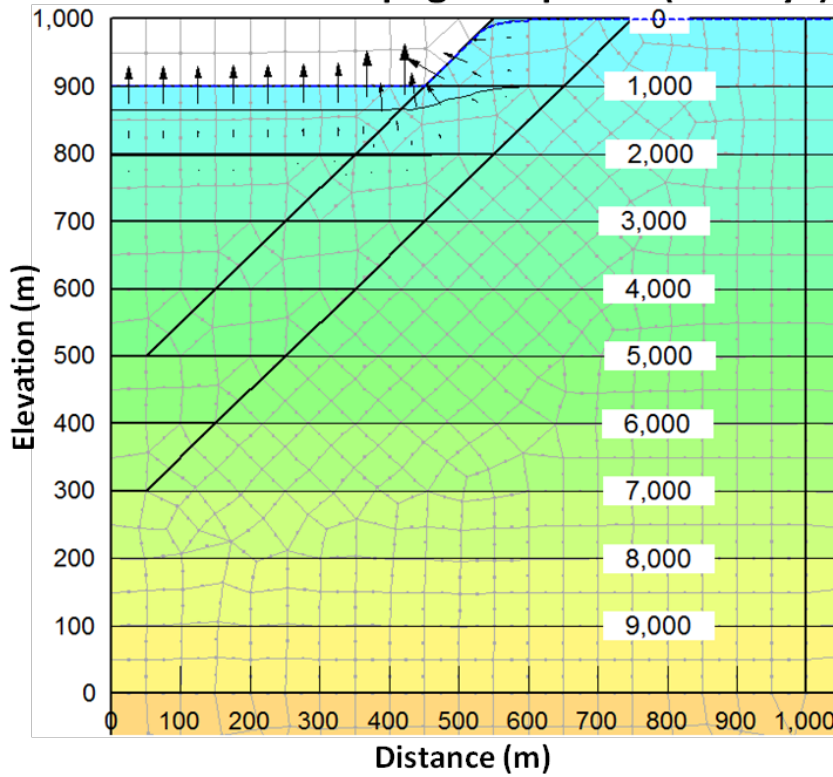
Transient Seepage Response (360 Days)



Transient Coupled Response (360 Days)

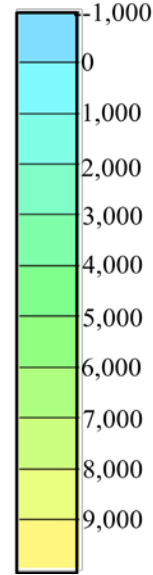


Transient Seepage Response (90 Days)

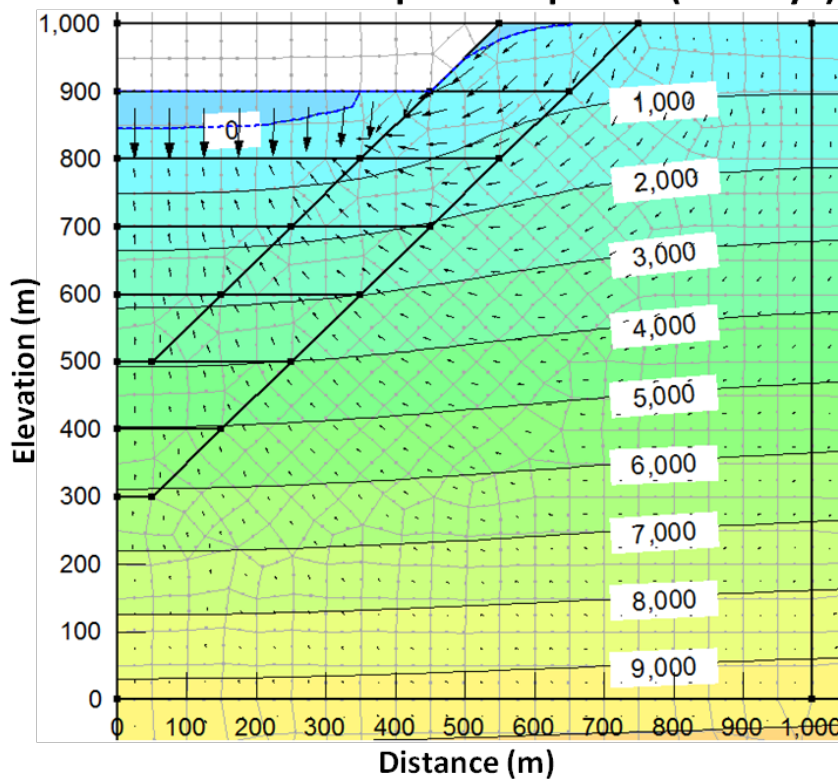


$c_v = 10^{-4} \text{ m}^2/\text{s}$

**PWP
Contours
(kPa)**

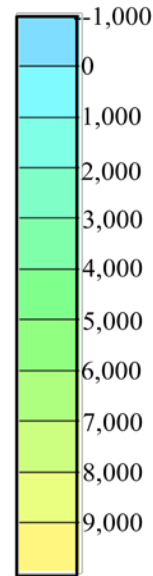


Transient Coupled Response (90 Days)

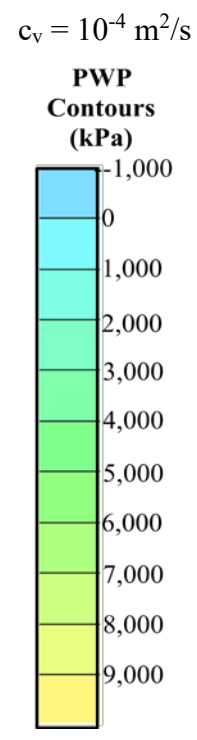
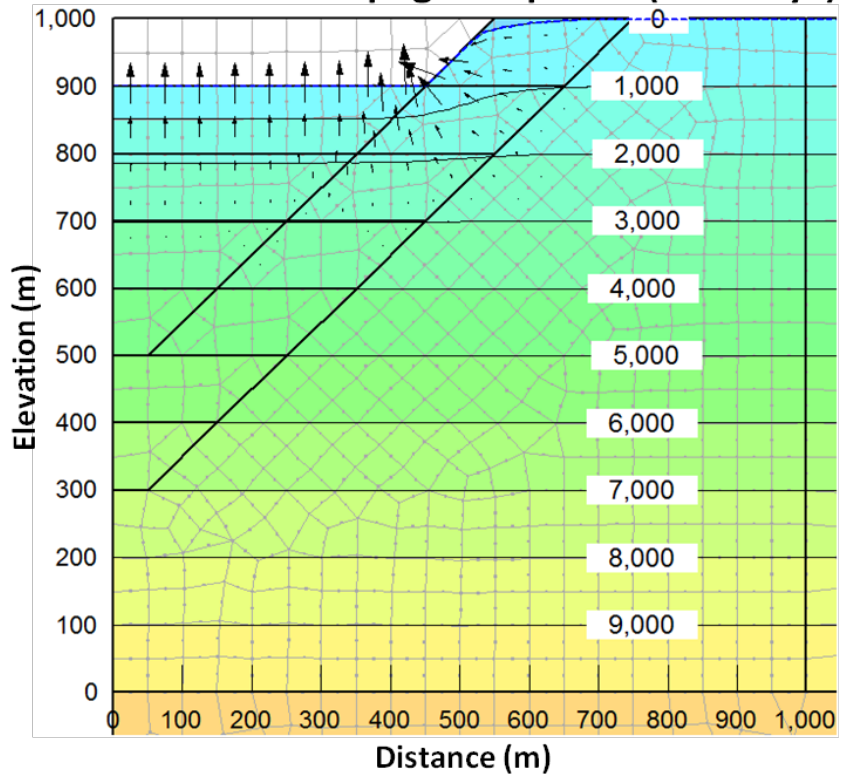


$c_v = 10^{-4} \text{ m}^2/\text{s}$

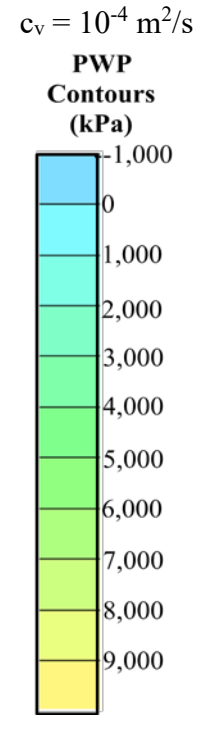
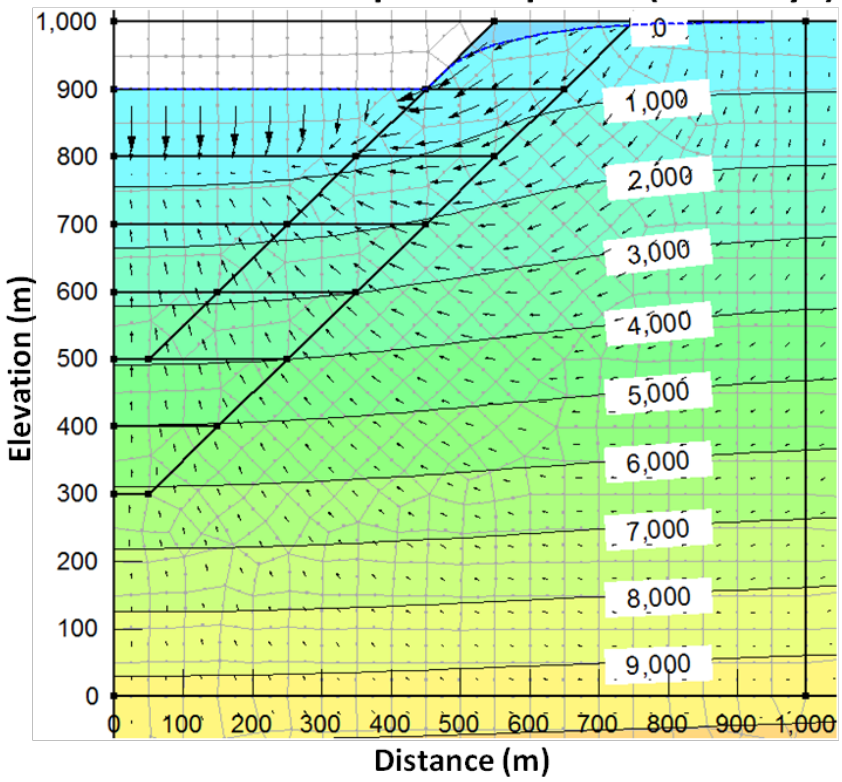
**PWP
Contours
(kPa)**



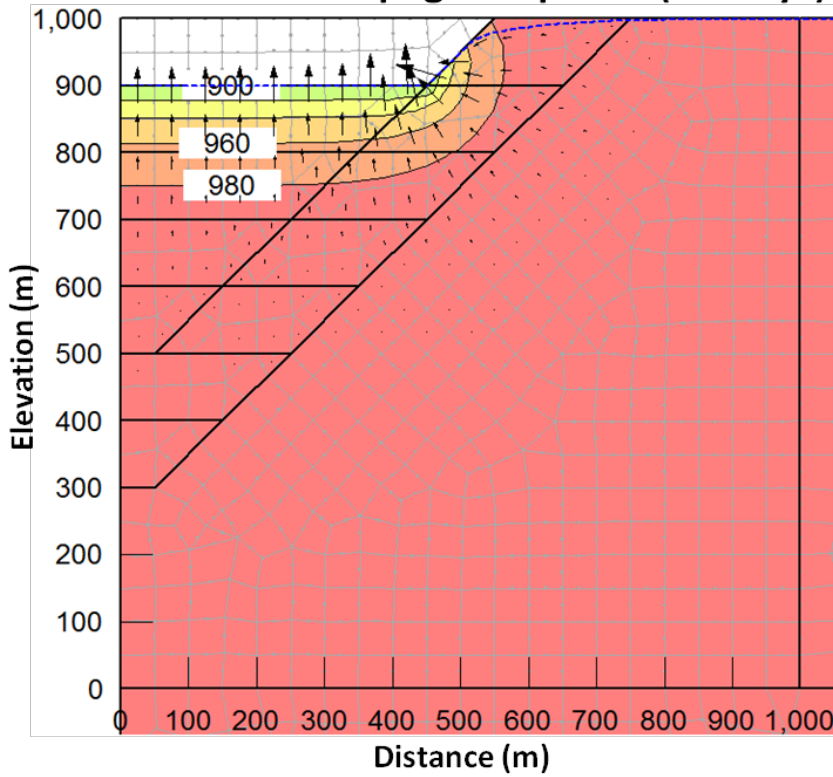
Transient Seepage Response (360 Days)



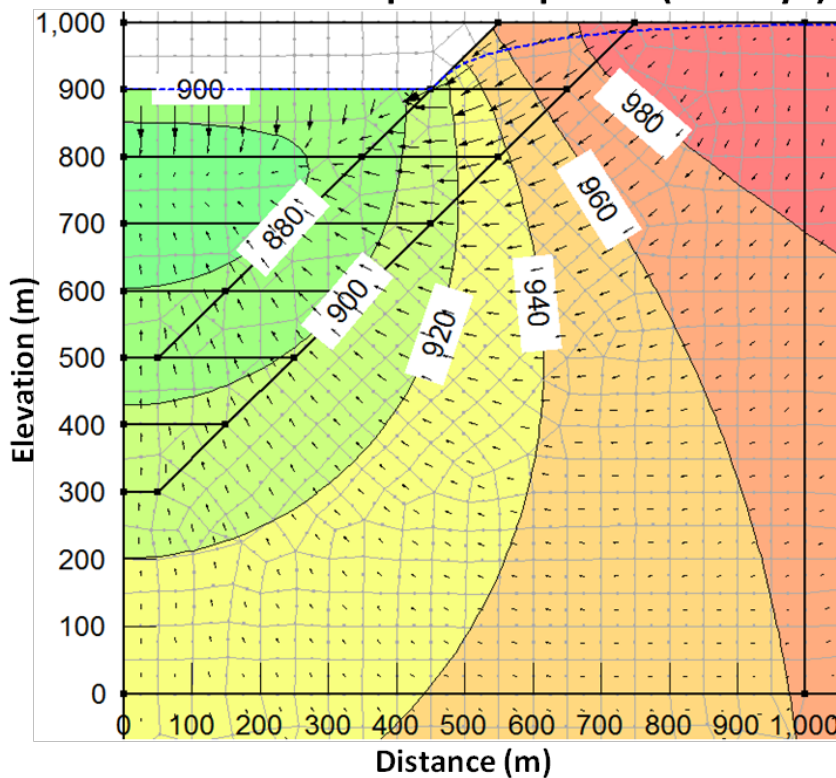
Transient Coupled Response (360 Days)



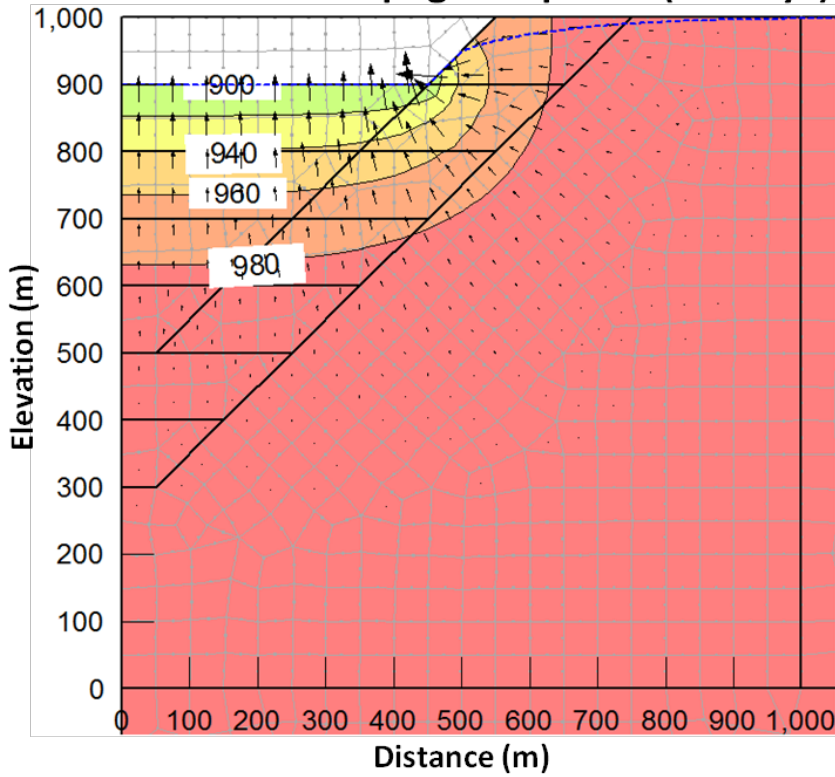
Transient Seepage Response (10 Days)



Transient Coupled Response (10 Days)

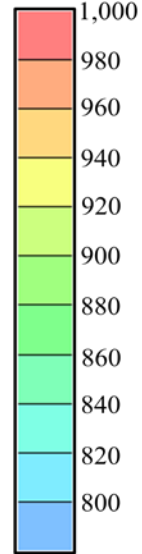


Transient Seepage Response (30 Days)

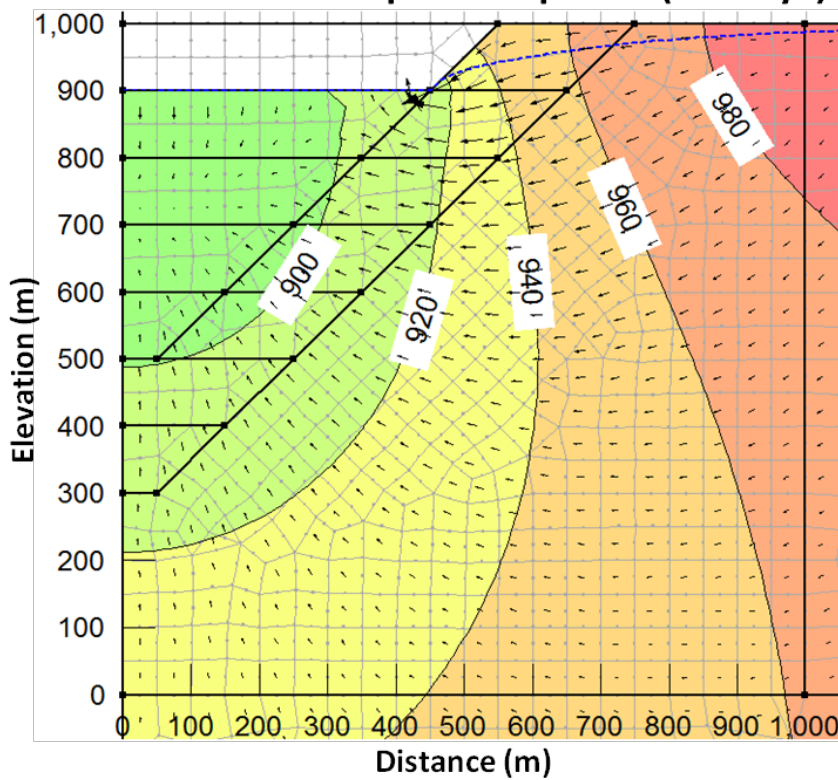


$c_v = 10^{-2} \text{ m}^2/\text{s}$

Total Head Contours (m)

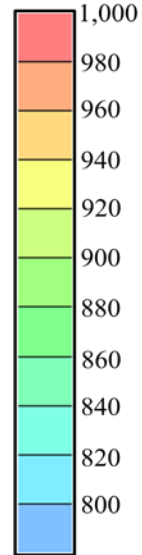


Transient Coupled Response (30 Days)

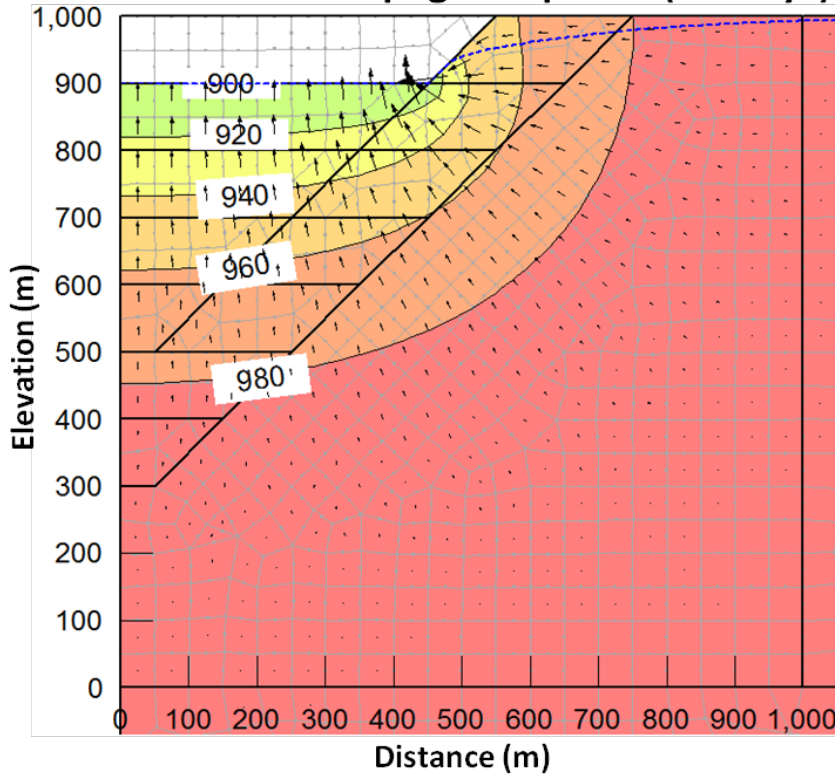


$c_v = 10^{-2} \text{ m}^2/\text{s}$

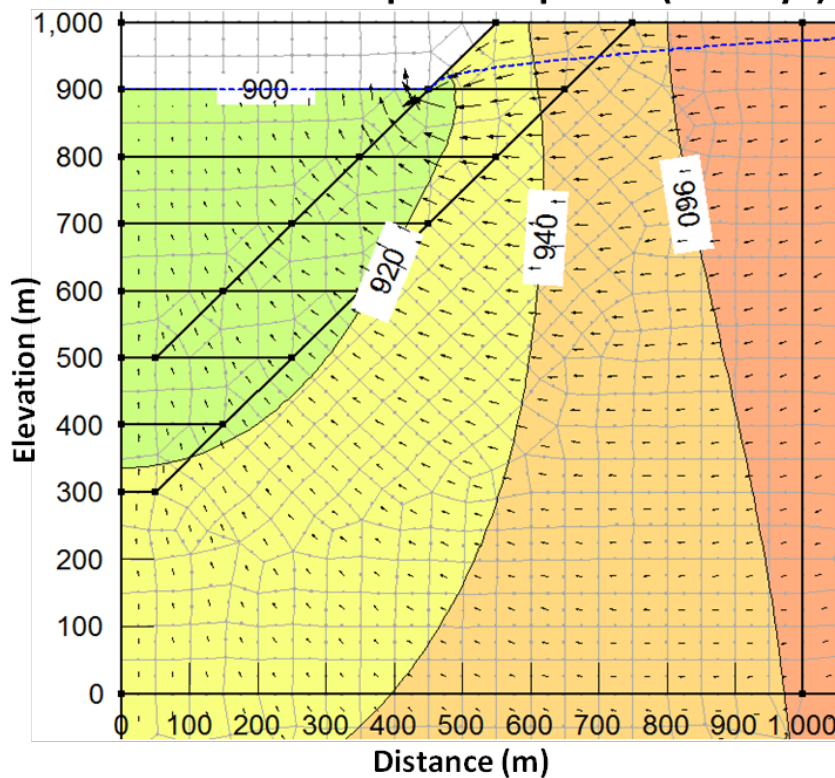
Total Head Contours (m)



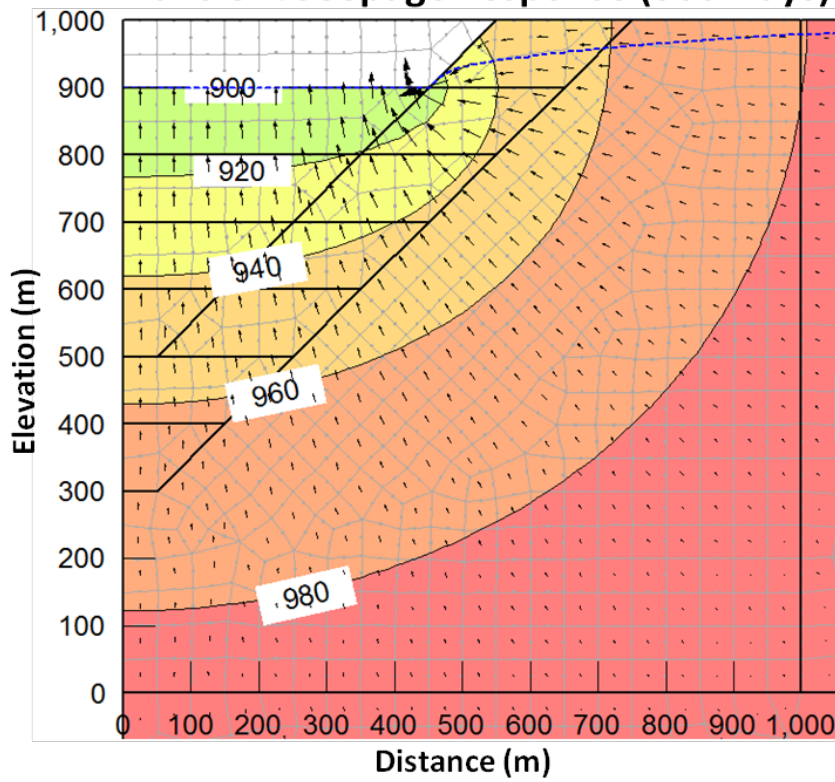
Transient Seepage Response (90 Days)



Transient Coupled Response (90 Days)

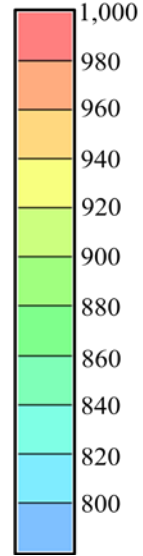


Transient Seepage Response (360 Days)

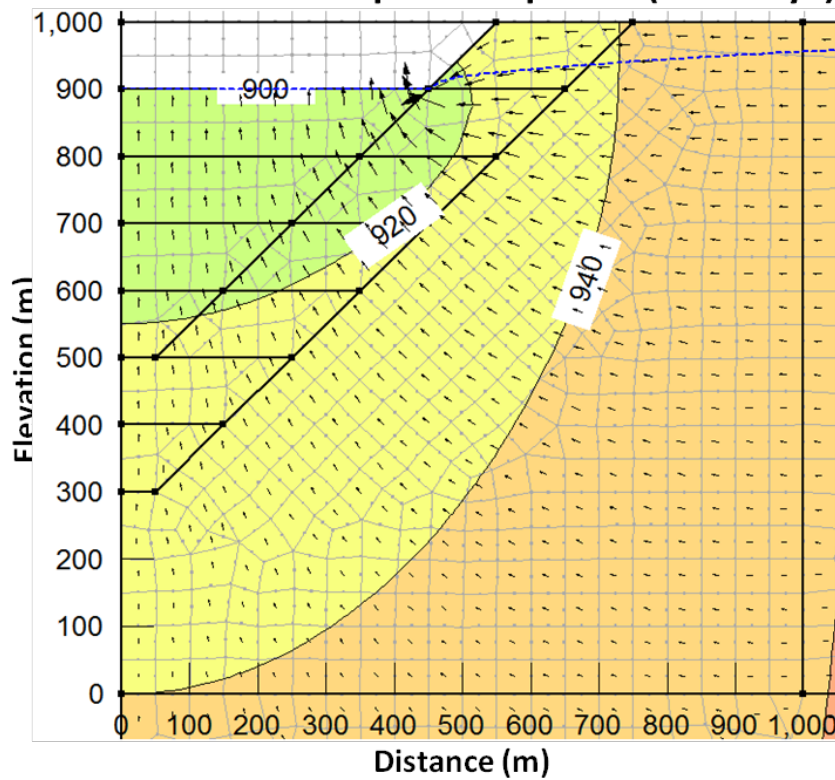


$c_v = 10^{-2} \text{ m}^2/\text{s}$

Total Head Contours (m)

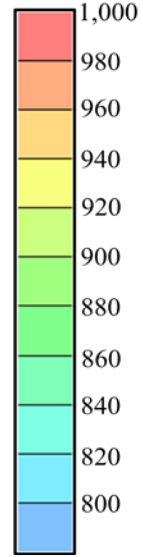


Transient Coupled Response (360 Days)

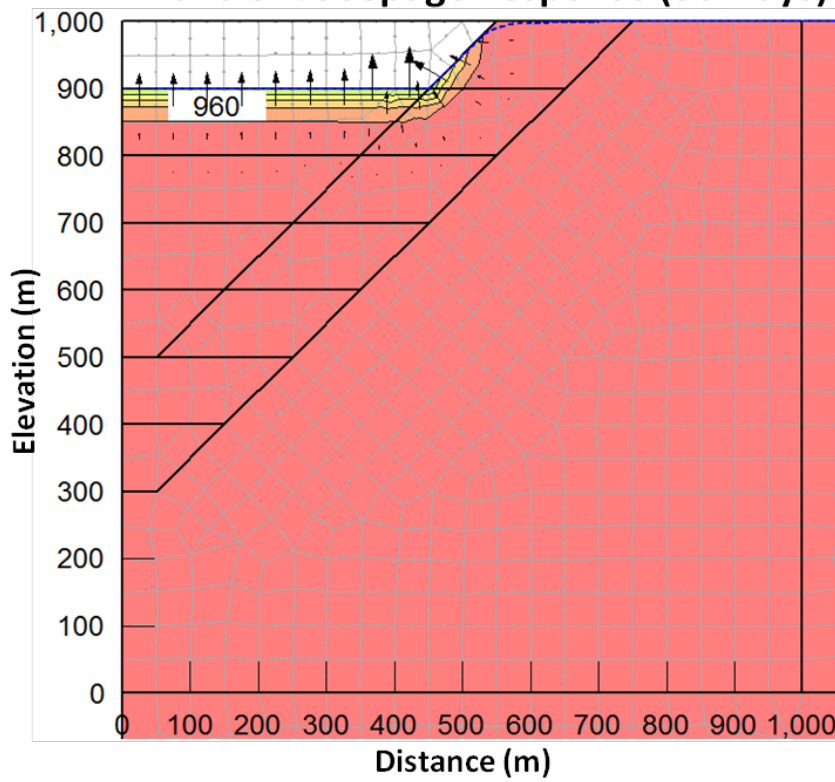


$c_v = 10^{-2} \text{ m}^2/\text{s}$

Total Head Contours (m)

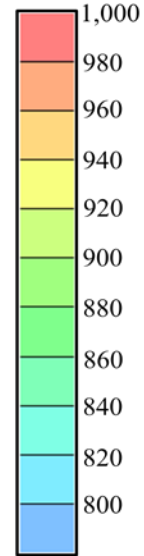


Transient Seepage Response (30 Days)

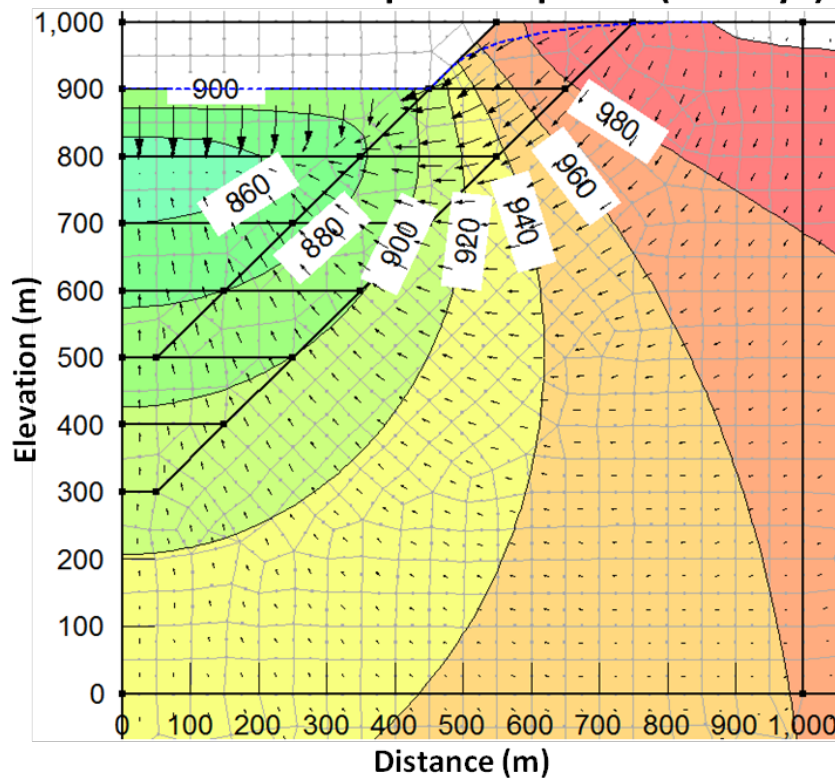


$c_v = 10^{-3} \text{ m}^2/\text{s}$

Total Head Contours (m)

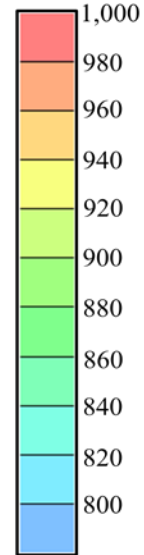


Transient Coupled Response (30 Days)

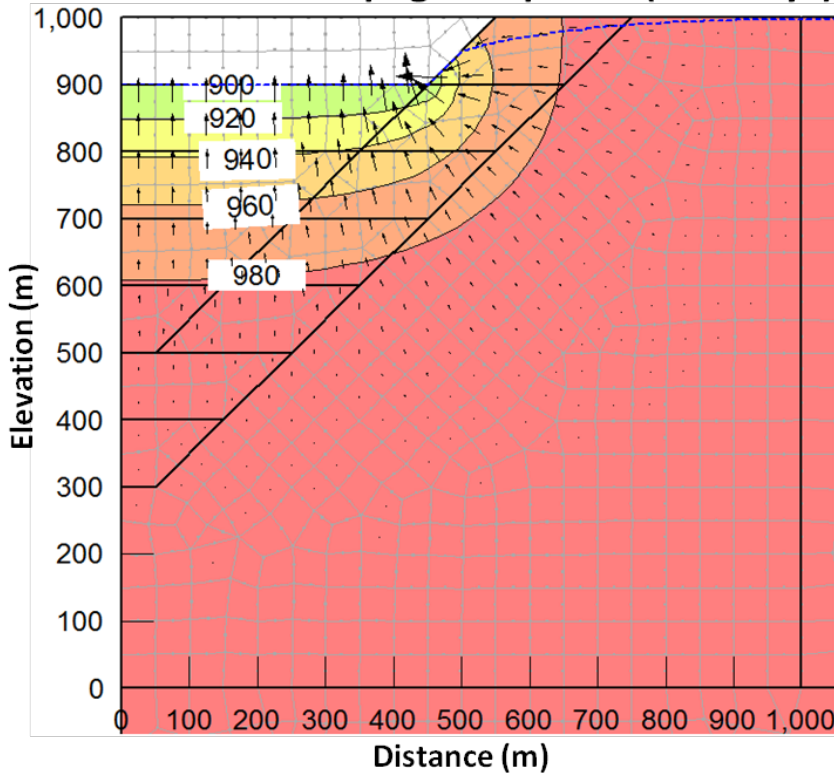


$c_v = 10^{-3} \text{ m}^2/\text{s}$

Total Head Contours (m)

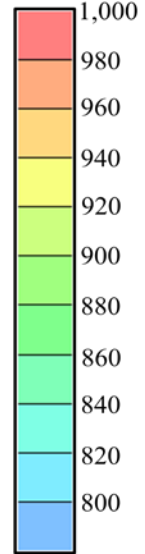


Transient Seepage Response (360 Days)

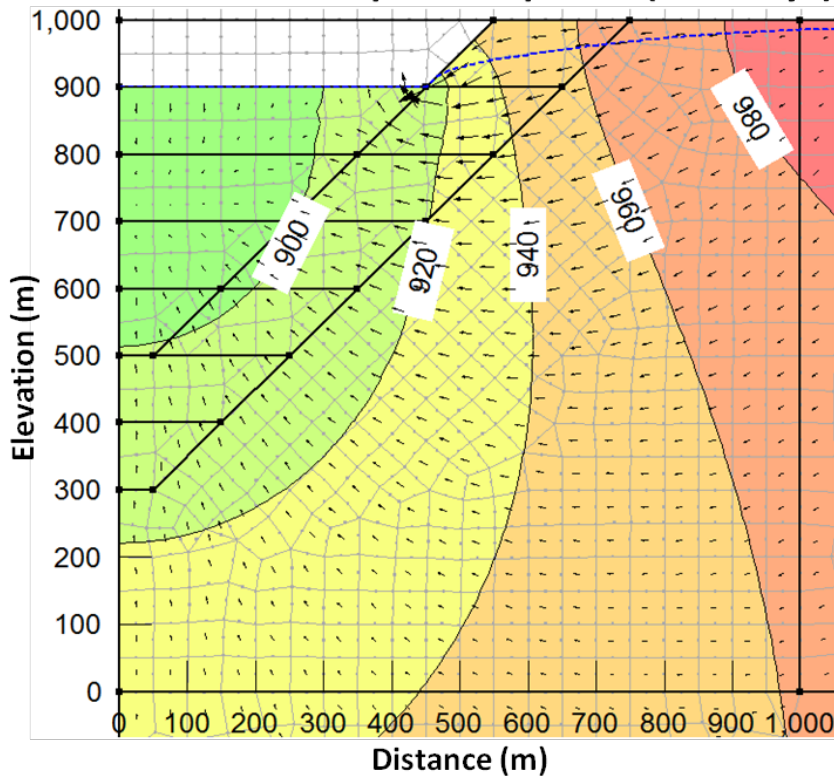


$c_v = 10^{-3} \text{ m}^2/\text{s}$

Total Head Contours (m)

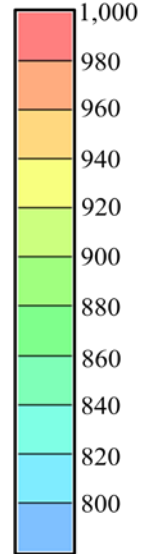


Transient Coupled Response (360 Days)

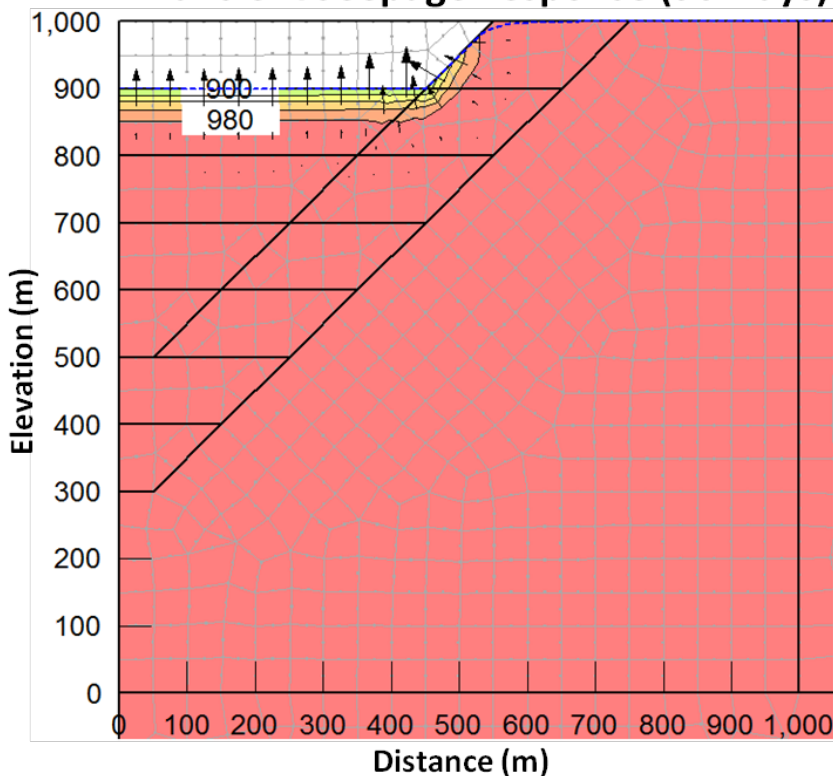


$c_v = 10^{-3} \text{ m}^2/\text{s}$

Total Head Contours (m)

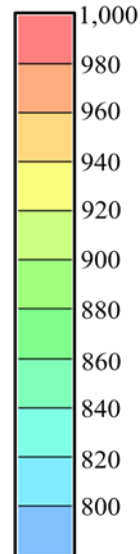


Transient Seepage Response (90 Days)

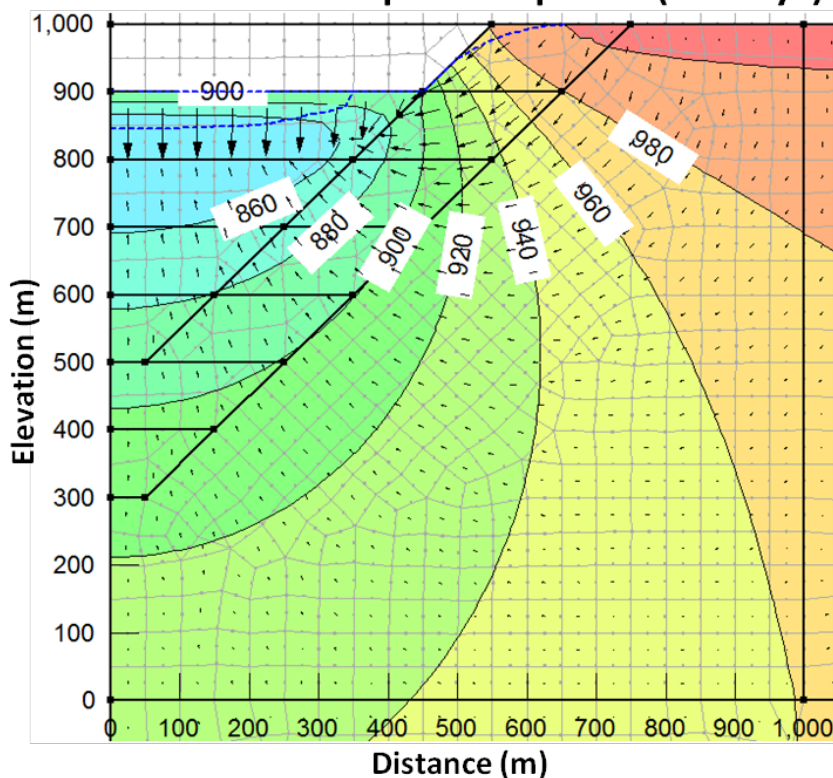


$c_v = 10^{-4} \text{ m}^2/\text{s}$

Total Head Contours (m)

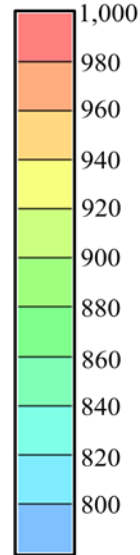


Transient Coupled Response (90 Days)

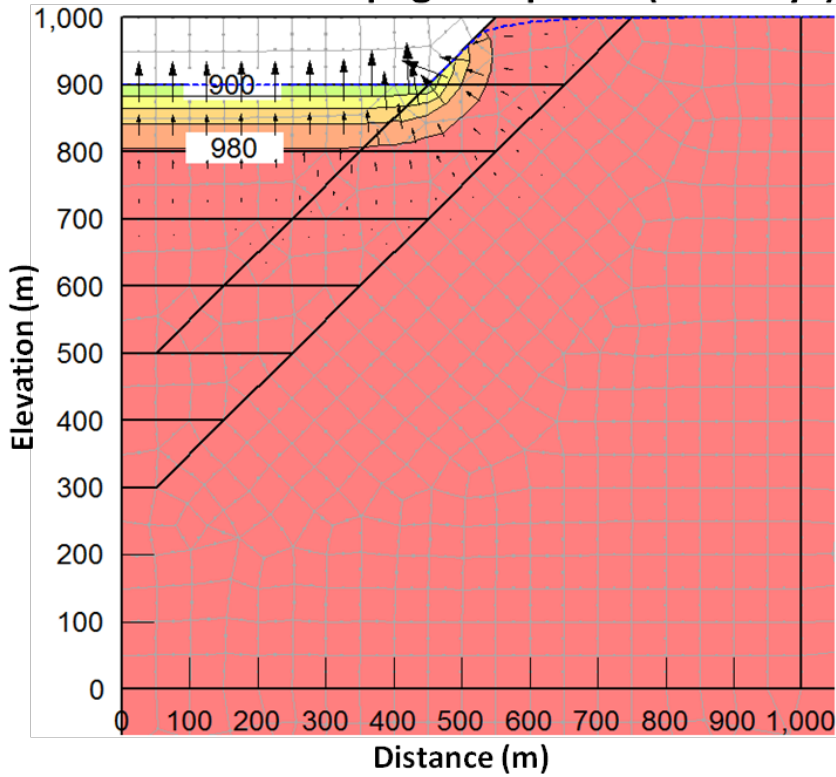


$c_v = 10^{-4} \text{ m}^2/\text{s}$

Total Head Contours (m)



Transient Seepage Response (360 Days)



Transient Coupled Response (360 Days)

